

Dust-Gas Instabilities in Protoplanetary Disks:
Toward Understanding Planetesimal Formation
原始惑星系円盤におけるダスト-ガス不安定性：
微惑星形成過程の解明に向けて

Ryosuke Tominaga

A dissertation submitted for the degree of
Doctor of Science

Laboratory for Theoretical Astronomy & Astrophysics,
Department of Physics, Graduate School of Science, Nagoya University
Furo-cho, Chikusa-ku, Nagoya, Aichi, 464-8602, Japan
February, 2021

Contents

1	Introduction	1
1.1	From Molecular Cloud Cores to Protoplanetary Disks	2
1.2	Dust Dynamics in Protoplanetary Disks	5
1.2.1	Radial drift and vertical sedimentation	7
1.2.2	The effects of turbulence on dust grains	8
1.2.3	Gravitational instability of a dust layer	10
1.2.4	Secular gravitational instability	13
1.3	ALMA Observations of Annular Substructures	19
1.4	Purposes of this thesis	25
2	Revision of Macroscopic Equations for Dust Diffusion	29
2.1	Short introduction: unphysical momentum transport due to the diffusion term	29
2.2	Reformulation of basic equations from the mean-field approximation	32
2.3	Linear analyses	35
2.3.1	Basic equations	35
2.3.2	Linearized equations	36
2.3.3	Results	37
2.4	Discussion: effects of disk thickness	48
2.5	Summary	52
3	Numerical Simulations of Secular Instabilities	54
3.1	Short introduction	54
3.2	Numerical methods	55
3.2.1	Lagrangian-cell method	56
3.2.2	The piecewise exact solution for friction	64
3.2.3	Methods for turbulent diffusion and viscosity	67
3.3	Simulations of radially extended disks	72

3.4	Discussion	84
3.4.1	Linear analyses with dust drift	84
3.4.2	Condition for the thin dense ring formation	89
3.4.3	Subsequent evolution of dusty rings	92
3.4.4	Observational justification	93
3.4.5	Effects on dust-to-gas ratio dependence on the dust coefficient	94
3.5	Summary	96
4	Coagulation Instability: Self-Induced Dust Concentration	98
4.1	Short introduction	98
4.2	Moment method for dust coagulation	102
4.3	One-fluid linear analyses and results	105
4.4	Two-fluid linear analyses and results	107
4.5	Discussion	114
4.5.1	Stabilization due to dust diffusion	114
4.5.2	Effects of other collision velocities	118
4.5.3	Comparison with the drift timescale	119
4.5.4	Effects of fragmentation and erosion	120
4.5.5	Coevolution with other dust-gas instabilities	121
4.6	Summary	122
5	Summary and Future Prospects	124
5.1	Summary of this thesis	124
5.2	Future prospects	126
A	Drift-Limited Stopping Time	130

Abstract

Planets are thought to form in a protoplanetary disk that consists of gas and dust grains. Dust grains first grow into km-sized objects called planetesimals, and planets form through collisional growth of planetesimals. However, planetesimal formation suffers some issues and still under debate. One issue is that mm- and cm-sized dust grains fall onto a central star and depleted. Another issue is collisional fragmentation, which prevents bottom-up coagulation toward planetesimals especially at inner regions.

Recent high-resolution observations with Atacama Large Millimeter/submillimeter Array (ALMA) have been providing detailed dust distributions that can be the key to understand planetesimal formation. One of the most highlighted observational results is the discovery of annular substructures in dust distributions, i.e., rings and gaps. Rings and gaps are found in most of the resolved disks, which indicates ubiquitousness of annular substructures. The existence of such substructures means that mm-sized grains are trapped in rings, which is in contrast to the classical theories that show mm-sized grains are depleted. Thus, revealing dust ring formation will provide important clues to understand planetesimal formation.

In this thesis, we focus on disk evolutions via secular gravitational instability, which is one possible mechanism of ring and planetesimal formation. Secular GI is one of the dust-gas instabilities and originally proposed as a mechanism of planetesimal formation. Previous studies showed that secular GI is stabilized by dust diffusion driven by gas turbulence. However, the previously-used advection-diffusion equation for dust density violates angular momentum conservation. Thus, we first reformulate equations for dust based on the Reynolds averaging. The Reynolds averaging is a method that divides mean flow components and fluctuating components due to turbulence. Averaging usual dust continuity equation introduces an additional advection term of momentum accompanied by diffusion. We find that including the additional advection term recovers angular momentum conservation. Using the reformulated equations, we conduct linear analyses of secular GI. The results show that secular GI is an exponentially growing mode without oscillation while the previous studies found that secular GI is an overstable mode. The overstability in the previous studies is found to be due to the nonconservation of angular momentum. We also found another unstable mode that we name two-component viscous GI (TVGI). TVGI is triggered by a combination of friction and turbulent gas viscosity and grows more easily than secular GI in the absence of dust drift.

Second, we develop numerical methods to investigate long-term linear evolution and subsequent nonlinear evolution of secular GI. We develop a Lagrangian-cell-based method, which is free from the numerical diffusion accompanied by dust drift. We also utilize the symplectic integrator and reduces accumulation of errors due to time integration. Test simulations of secular GI show that combining the method with the piecewise exact solution for dust-gas friction enables long-term simulation for linear/nonlinear secular GI. Using the developed method, we perform numerical simulations of secular GI in radially extended disks while assuming uniform profile of dimensionless stopping time that is a measure of dust sizes. We found that nonlinear growth of secular GI is similar to the gravitational collapse of dust rings whose timescale is well represented in terms of the freefall timescale. The resultant rings will fragment in the azimuthal direction and turn into planetesimals. The nonlinear growth increases dust surface density by an order of magnitude. On the other hand, the gas disk is less affected and show insignificant substructures. Thus, secular GI increases dust-to-gas ratio in rings, which also accelerates dust coagulation and promotes planetesimal formation. When the growth of secular GI is too slow, secular GI only creates transient dust rings and gaps that move inward. Because secular GI creates significant substructures only in a dust disk, gas observations will give hints to understand which ring-forming process operating in the observed disks.

Finally, we investigate a connection between the first bottom-up coagulation and planetesimal formation via secular GI. Secular GI requires high dust-to-gas ratio for mm- or cm-sized grains although the bottom-up coagulation results in depletion of those dust grains. Thus, secular GI requires reaccumulation of mm- and cm-sized dust grains. We propose a new instability as a mechanism of the reaccumulation. The instability we call “coagulation instability” is triggered by a combination of dust coagulation itself and small scale traffic jam. In the absence of dust diffusion, coagulation instability grows faster at shorter wavelengths. This is because a timescale of traffic jam becomes shorter. Coagulation instability still operates in the presence of diffusion and grows within a tens of the Keplerian periods even in a region where dust-to-gas ratio is of the order of 10^{-3} . Therefore, coagulation instability efficiently accumulates mm- and cm-sized dust grains, and connects the first bottom-up coagulation to the top-down planetesimal formation via secular GI.

Acknowledgements

I would like to thank my supervisor Prof. Shu-ichiro Inutsuka for his support and continuous encouragement. He taught me how a theorist should be, the importance of enjoying addressing issues, and a delight in deeply understanding physical processes. He also taught me the importance of making presentations clearer and easier to understand. I would also thank collaborators Hiroshi Kobayashi and Sanemichi Z. Takahashi. They spent their time on discussion and kindly revising papers. I could not accomplish works in this thesis without their kind support. I am also grateful to Tsuyoshi Inoue, Yuri I. Fujii, Kenji Kurosaki, Jiro Shimoda, and all the students in Laboratory for Theoretical Astronomy and Astrophysics. They have been sharing their thoughts, and we had fruitful discussions on various topics. Interaction with them has enriched my daily life. I would also like to appreciate former and present secretaries in the astrophysics group for kindly supporting my research life. I appreciate Kiyotomo Ichiki and Shohei Saga for telling me how fun it is to study physics and astrophysics when I was an undergraduate. That motivated me to start a career in astrophysics. I also thank to former members of the astrophysics groups at Nagoya university: Takeru K. Suzuki, Masanobu Kunitomo, Shinsuke Takasao, Doris Arzoumanian, Yuki A. Tanaka, Masato I. N. Kobayashi, Torsten Stamer, Shoji Mori, Kotaro Maeda, Keisuke Sugiura, Tomoya Miyake, Yuki Ohno, Yutaro Sato, Kenta Nakashima, Shun Arai, Naoya Tokiwa, Kaori Kawamura, Chikako Nishihara, Kensuke Yokosawa, Kouki Matsumoto. Thanks also go to other people whom I had a great time with during my daily life in Nagoya.

Finally, I would like to thank my parents. They have been always supporting and encouraging me. I could not have devoted myself to studying physics and enjoying it for the last nine years without their support. I sincerely appreciate their kind and dedicated support.

This work was supported by JSPS KAKENHI Grant Number JP18J20360.

Chapter 1

Introduction

Over 4000 planets have been found with a wide variety of masses and orbital radii (e.g., hot Jupiters and super Earths) in extra-solar systems ¹. Formation of those planets starts from coagulation of sub-micron-sized dust grains in a gaseous disk around a central star (a “protoplanetary disk”). Such small grains stick to each other through intermolecular force, and their coagulation results in kilometer-sized objects called planetesimals. Resultant planetesimals further coalesce with the help of gravity and grow toward planets. Among this overall scenario, planetesimal formation from tiny dust grains suffers some “barriers”, including a radial drift barrier (e.g., Weidenschilling 1977) and a fragmentation barrier (e.g., Weidenschilling & Cuzzi 1993). Although some theories have been proposed to explain the origin of planetesimals (e.g., Ward 2000; Youdin & Johansen 2007; Okuzumi et al. 2012), planetesimal formation is still under debate.

In addition to theoretical studies of planetesimal formation, recent disk observations have been providing hints to reveal dust growth toward planetesimals. Radio observations can see spatial distributions of dust grains with size \sim mm. High resolution observations with Atacama Large Millimeter/submillimeter Array (ALMA) have shown that most of the resolved disks with ages $<$ a few Myr host bright ring and dark rings (“gaps”) in intensity profiles. These observations indicate that mm-sized dust grains are trapped in such rings, which is in contrast to the classical theories showing that grains are depleted because of the fast radial drift. The observed dust rings are thought to result from planet formation or other processes before planet formation. Therefore, revealing dust ring formation will provide important keys to resolve planetesimal formation. This thesis explores one possibility that dust-gas instabilities in protoplanetary disks explain both dust-ring formation and planetesimal formation.

¹<https://exoplanets.nasa.gov/> , <http://exoplanet.eu/>

In this chapter, we briefly review disk formation from a molecular cloud core, basic dust dynamics, and ALMA observations.

1.1 From Molecular Cloud Cores to Protoplanetary Disks

A protoplanetary disk is a by-product of a star-forming process. Star formation starts from self-gravitational collapse of a molecular cloud core. A molecular cloud core is a gas clump with a size of ~ 0.1 pc, number density of $\sim 10^{4-5}$ cm^{-3} . Gas temperature of molecular cloud cores is about 10 K, which is mainly determined by thermal equilibrium with radiative cooling due to C II fine-structure line and radiative heating due to photoelectric emission from dust grains and PAHs (Wolfire et al. 1995; Koyama & Inutsuka 2000). Those isothermal gas clumps collapse in self-similar manner once their self-gravity dominates thermal pressure gradient force (Larson 1969). This first isothermal collapse proceeds until inner collapsing gas becomes optically thick and behaves as adiabatic gas. Effective specific heat ratio γ_{eff} of the resultant dense region is initially 5/3 although the dense gas consists of H_2 . This behavior originates from high temperature that is required for the lowest rotational transition of H_2 to be excited ($\simeq 510$ K). When compressional heating increases temperature enough, the rotational transition is excited and γ_{eff} becomes 7/5.

These adiabatic gas cores can decelerate self-gravitational collapse as described below. For a polytropic gas, thermal pressure P and gas mass density ρ are related by $P = K\rho^{\gamma_{\text{eff}}}$, where K is a constant. Using this relation, one can estimate a pressure gradient force $-\rho^{-1}\partial P/\partial r \sim K\rho^{\gamma_{\text{eff}}-1}/r$, where r is a radial dimension of the core. Assuming spherical symmetry, one obtains $-\rho^{-1}\partial P/\partial r \propto r^{2-3\gamma_{\text{eff}}}$. On the other hand, self-gravity exerted on the sphere of the core is $GM/r^2 \propto r\rho \propto r^{-2}$, where G and M are the gravitational constant and a core mass, respectively. Thus, when the ratio of the specific heats is larger than 4/3, the pressure gradient force will dominate the self-gravity as the collapse decreases the core radius r , resulting in a hydrostatic core called a “first core”. Larson (1969) performed the first numerical simulation of the core collapse based one dimensional hydrodynamic equations, and showed that the first core initially has a mass of $\sim 0.01M_{\odot}$ and a radius of ~ 4 au.

The resultant first core grows in mass through material infall from a surrounding envelope, and gradually shrinks with help of radiative energy loses from its outer layer. Once the internal temperature reaches ~ 2000 K, molecular gas turns into monoatomic

gas through dissociation of H_2 whose binding energy is $\simeq 4.47$ eV corresponding to $> 10^4$ K (Wolniewicz 1995; Gaustad 1963). The H_2 dissociation plays a role in cooling the gas and triggers the second collapse of the core. Because the energy of collapsing gas is used to dissociate hydrogen molecule, the gas temperature increases insignificantly and the process is closely isothermal ($\gamma_{\text{eff}} < 4/3$). The second collapse is quenched once all hydrogen molecules are dissociated, resulting again in a hydrostatic core called a second core or a “protostar”. The mass of the protostar is about $10^{-3}M_{\odot}$, and its radius is $\sim 10^{-2}$ au corresponding to about 1 solar radius (see, Larson 1969; Masunaga & Inutsuka 2000). The protostar also grows in mass via mass accretion from the surrounding envelope, and finally goes to a (pre-)main-sequence star.

In reality, initial cloud cores have non-zero angular momentum. Gravitational collapse of such a rotating cloud core forms a gaseous disk around a resultant protostar. The resultant disk is called a protostellar disk, and grows toward a protoplanetary disk that is more radially extended than a protostellar disk. Three-dimensional hydrodynamic simulations of the core collapse showed that the first core formed before the second collapse eventually turns into a protostellar disk (Bate 1998; Machida et al. 2010). A protostellar disk is thus initially a few au in size and more massive ($\sim 0.01M_{\odot}$) than a protostar ($\sim 10^{-3}M_{\odot}$). Along with the protostellar evolution through mass accretion from the protostellar disk, the disk also grows in size and mass through magnetic interaction with the surrounding envelope and mass infall.

The disk formation and evolution has also been extensively studied based on (non-)ideal magnetohydrodynamical simulations (e.g., Machida et al. 2014). When inner collapsing gas has a low density and Ohmic dissipation is ineffective, angular momentum of the gas is transferred outward by threaded magnetic fields. This process is called magnetic braking (e.g., Mestel & Spitzer 1956; Mouschovias & Paleologou 1979). Magnetic braking on inner collapsing gas is effective when the outer gas is more massive, which is expected in the early phase of the runaway collapse. Magnetically driven wind and outflow also contributes to extract angular momentum from the very inner region (e.g., Blandford & Payne 1982; Tomisaka 1998, 2002).

The inner gas density increases as the collapse proceeds. Once the gas number density reaches $\sim 10^{11-12}$ cm^{-3} , Ohmic dissipation operates and dissipates magnetic field (Nakano et al. 2002; Machida et al. 2014). Dissipation of magnetic field leads to inefficient angular momentum transfer, and a rotationally supported disk forms around a protostar. Figure 1.1 overviews of disk formation and evolution. The first core, which is a precursor of a protostellar disk, is thermally supported and a few au in size at its formation. The rotationally supported disk where Ohmic dissipation operates (a “magnetically inactive

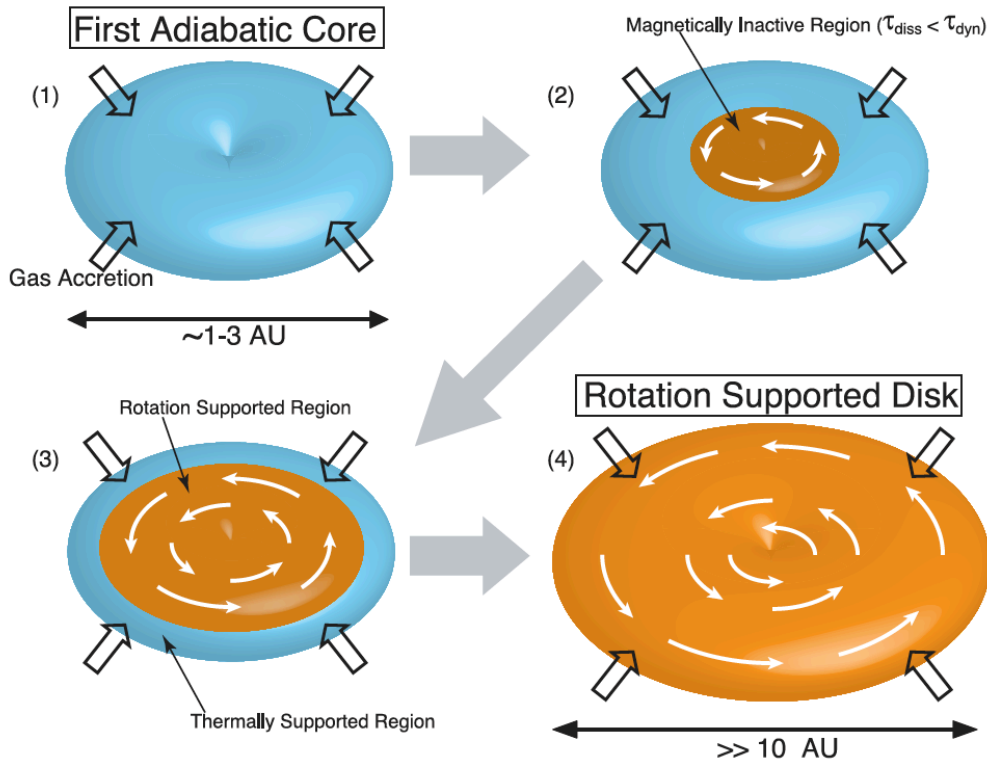


Figure 1.1: Schematic picture of disk evolution. The initially small magnetically inactive region grows in radius because of mass accretion. Further mass accretion from the surrounding envelope results in a rotationally supported disk that is more extended than the first core. This figure is from Fig. 23 of Machida et al. (2014).

region”) is initially (sub-)au scale. Surrounding gas inside of the first core continues to accrete on the inner disk, increasing the gas density of the disk. In addition, accreting gas brings angular momentum to the disk. As a result of the increase in gas density and angular momentum, the inner magnetically inactive region expands radially outward. In other words, the disk radius increases. Machida et al. (2014) showed that a disk radius exceeds 10 au a few thousands year after formation of a protostar. The disk extends further toward $\simeq 100$ au after the infalling gas outside the first core becomes less massive than the inner disk (Machida et al. 2011). Figure 1.2 shows mass evolution of a disk and a protostar, originally shown in Inutsuka et al. (2010). Because of the nature of runaway collapse, the protostellar mass is smaller than the first protostellar disk, denoted by a “circumstellar disk” in Figure 1.2. Such a massive disk evolves not only by magnetic interaction but also by its self-gravity that causes gravitational instability. Gravitational instability creates spiral structures, which drive angular momentum transport and mass

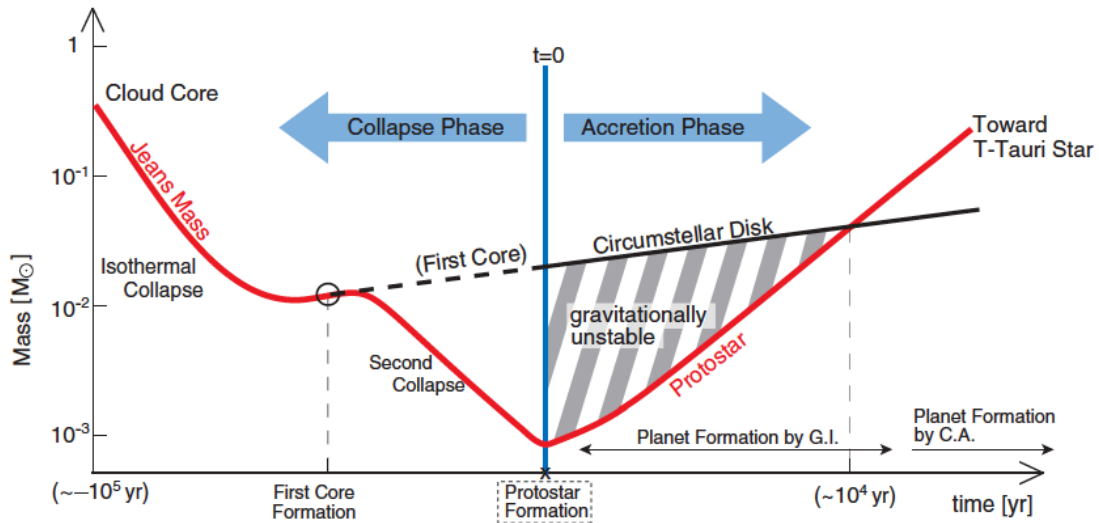


Figure 1.2: Schematic diagram of disk and protostar evolution in time versus mass plane. A protostar is initially less massive than a protostellar disk, denoted as a “circumstellar disk” in this figure. Mass accretion driven by gravitational instability in the disk increases the protostellar mass beyond the disk mass. This figure is from Fig. 2 of Inutsuka et al. (2010).

accretion in magnetically inactive region (e.g., Bate 1998; Machida et al. 2011; Tomida et al. 2017). The protostar grows in mass via resultant mass accretion from the disk, evolving toward a protoplanetary disk less massive than a central star.

1.2 Dust Dynamics in Protoplanetary Disks

Dust grains in a molecular cloud core also accrete with collapsing gas onto a resultant disk. Dust abundance relative to gas was observationally derived for interstellar medium, and dust-to-gas mass ratio is about ~ 0.01 (Bohlin et al. 1978). This small amount of dust grains and their dynamics are important for planetesimal and planet formation in protoplanetary disks. In this section, we briefly review key processes of dust grains in a gas disk.

Dust grains aerodynamically couple with a gas disk. Hereafter, we refer to this dust-gas coupling as “friction”. Characteristic timescale of friction on a dust grain with a size of a and mass of m is called stopping time t_{stop} . Stopping time is determined by surrounding gas density ρ_g , sound velocity c_s , and internal dust mass density ρ_{int} as

follows:

$$t_{\text{stop}} = \begin{cases} \sqrt{\frac{\pi}{8}} \frac{\rho_{\text{int}} a}{\rho_{\text{g}} c_{\text{s}}} & a < \frac{9}{4} \lambda_{\text{mfp}} \\ \sqrt{\frac{\pi}{8}} \frac{4\rho_{\text{int}} a^2}{9\rho_{\text{g}} c_{\text{s}} \lambda_{\text{mfp}}} & a > \frac{9}{4} \lambda_{\text{mfp}} \end{cases}, \quad (1.1)$$

where λ_{mfp} is the mean free path of gas. The former is called the Epstein law while the latter is called the Stokes law. We usually describe how strongly dust grains are coupled to gas using dimensionless stopping time $\tau_{\text{s}} \equiv t_{\text{stop}} \Omega$. Dust with $\tau_{\text{s}} \ll 1$ is tightly coupled while it is decoupled for $\tau_{\text{s}} \gg 1$. Thus, we can use τ_{s} as a measure of dust sizes in a protoplanetary disk. In the following subsections, we summarize dynamical processes mostly based on stopping time.

If we neglect self-gravity of a disk, equations of motion of a dust grain orbiting around a star with mass M_* in cylindrical coordinate (r, ϕ, z) are

$$\frac{dv_r}{dt} = \frac{v_\phi^2}{r} - \frac{GM_* r}{(r^2 + z^2)^{3/2}} - \frac{v_r - u_r}{t_{\text{stop}}}, \quad (1.2)$$

$$\frac{dv_\phi}{dt} = -\frac{v_r v_\phi}{r} - \frac{v_\phi - u_\phi}{t_{\text{stop}}}, \quad (1.3)$$

$$\frac{dv_z}{dt} = -\frac{GM_* z}{(r^2 + z^2)^{3/2}} - \frac{v_z - u_z}{t_{\text{stop}}}, \quad (1.4)$$

where v_r , v_ϕ , and v_z are radial, azimuthal, and vertical velocity of a dust grain. Gas velocities are denoted by u_r , u_ϕ , and u_z . Gas equations are

$$\frac{du_r}{dt} = \frac{u_\phi^2}{r} - \frac{1}{\rho_{\text{g}}} \frac{\partial P}{\partial r} - \frac{GM_* r}{(r^2 + z^2)^{3/2}} - \frac{\rho_{\text{d}}}{\rho_{\text{g}}} \frac{u_r - v_r}{t_{\text{stop}}}, \quad (1.5)$$

$$\frac{du_\phi}{dt} = -\frac{u_r u_\phi}{r} - \frac{1}{\rho_{\text{g}} r} \frac{\partial P}{\partial \phi} - \frac{\rho_{\text{d}}}{\rho_{\text{d}}} \frac{u_\phi - v_\phi}{t_{\text{stop}}}, \quad (1.6)$$

$$\frac{du_z}{dt} = -\frac{1}{\rho_{\text{g}}} \frac{\partial P}{\partial z} - \frac{GM_* z}{(r^2 + z^2)^{3/2}} - \frac{\rho_{\text{d}}}{\rho_{\text{g}}} \frac{u_z - v_z}{t_{\text{stop}}}, \quad (1.7)$$

where we neglect turbulent viscosity, magnetic fields, and self-gravity. Gas pressure P is given by $P = c_{\text{s}}^2 \rho_{\text{g}}$, and dust density is denoted by ρ_{d} .

In the absence of frictional backreaction to the gas, we can derive some gas disk properties used as a zeroth-order background field. For simplicity, we consider axisymmetric disk. We then obtain a steady vertical gas density profile from Equation (1.7):

$$\ln \rho_{\text{g}} = C + \frac{GM_*}{c_{\text{s}}^2 \sqrt{r^2 + z^2}} - \frac{GM_*}{c_{\text{s}}^2 r}, \quad (1.8)$$

where C is an integral constant, and we consider a vertically isothermal structure that is expected in the interior of stellar-irradiated disks (see Chiang & Goldreich 1997). For $z \ll r$, one obtains the following Gaussian density distribution

$$\rho_g = \frac{\Sigma_g}{\sqrt{2\pi}H} \exp\left(-\frac{z^2}{2H^2}\right), \quad (1.9)$$

where the integral constant is chosen as gas surface density. The vertical thickness H is called a gas scale height and given by $H \equiv c_s/\Omega$ where $\Omega \equiv \sqrt{GM_*/r^3}$ is the Keplerian angular velocity at the disk midplane.

We can also derive azimuthal gas velocity for a steady axisymmetric disk and in the absence of the frictional backreaction. Equation (1.5) shows that radial force balance leads to sub-Keplerian gas velocity: $u_\phi < v_{\text{Kep}} \equiv r\Omega$. At the disk midplane ($z = 0$), one obtains

$$u_\phi = \left(1 + \frac{c_s^2}{v_{\text{Kep}}^2} \frac{\partial \ln P}{\partial \ln r}\right)^{1/2} v_{\text{Kep}} \simeq (1 - \eta)v_{\text{Kep}}, \quad (1.10)$$

$$\eta \equiv -\frac{1}{2} \left(\frac{c_s}{v_{\text{Kep}}}\right)^2 \frac{\partial \ln P}{\partial \ln r}. \quad (1.11)$$

The factor η is usually used as a measure of gas pressure gradient force (e.g., Nakagawa et al. 1986). If gas is barotropic $P = P(\rho_g)$ and we neglect friction force on gas, Equations (1.5) and (1.7) give a steady gas solution whose angular velocity is uniform in the vertical direction.

Based on the above equations and the derived ‘‘zeroth-order’’ gas profile, we will describe basic processes of dust in a gas disk.

1.2.1 Radial drift and vertical sedimentation

One important consequence of frictional interaction with gas is radial drift of dust grain (e.g., Whipple 1972; Weidenschilling 1977; Adachi et al. 1976; Nakagawa et al. 1986). Since dust grains move with Keplerian velocity in the absence of gas, they counter a head wind in a sub-Keplerian gas disk. Friction force causes angular momentum transfer from dust grains to gas, and thus dust grains fall toward a central star. In a steady sub-Keplerian gas disk ($u_r = u_z = 0$ and $u_\phi = (1 - \eta)v_{\text{Kep}}$), terminal velocity of dust is

$$v_r = -\frac{2\tau_s}{1 + \tau_s^2} \eta v_{\text{Kep}}, \quad (1.12)$$

$$v_\phi = v_{\text{Kep}} - \frac{\eta v_{\text{Kep}}}{1 + \tau_s^2}. \quad (1.13)$$

When we include the backreaction to the gas, we obtain

$$v_r = -\frac{2\tau_s}{(1+\epsilon)^2 + \tau_s^2} \eta v_{\text{Kep}}, \quad (1.14)$$

$$v_\phi = v_{\text{Kep}} - \frac{(1+\epsilon)}{(1+\epsilon)^2 + \tau_s^2} \eta v_{\text{Kep}}, \quad (1.15)$$

where $\epsilon \equiv \rho_d/\rho_g$ is dust-to-gas ratio. Equation (1.12) shows that dust grains with $\tau_s = 1$ has the fastest drift speed. Once pressure profile is specified, one can estimate the drift rate of dust grains in a gas disk. A model often used in the literature is the “minimum mass solar nebula” (MMSN) model where the disk mass is minimal for the solar system planets to form (Kusaka et al. 1970; Hayashi 1981). Based on power-law disk models including the MMSN model, Weidenschilling (1977) showed that drift velocity of meter-sized dust can reach $10^4 \text{ cm sec}^{-1} \sim 10^{-2} \text{ au yr}^{-1}$. Thus, dust grains located at $r = 1 \text{ au}$ fall onto a central star within just 100 yr, which is shorter by an order of magnitude than one orbital period of protoplanetary disks $\sim 100 \text{ au}$ in size. In other words, this fast drift results in dust depletion and introduces a “barrier” against dust coagulation beyond meter sizes (e.g., Weidenschilling 1977) while Brauer et al. (2008) found that the issue is sensitive to the initial dust abundance in disks.

Another important process is vertical sedimentation. Equation (1.4) shows that dust grains settle toward the midplane at the following terminal velocity

$$v_z - u_z = -t_{\text{stop}} \frac{GM_* z}{(r^2 + z^2)^{3/2}}. \quad (1.16)$$

For the thin disk limit ($z \ll r$), one obtains

$$v_z - u_z \simeq -\tau_s \Omega z. \quad (1.17)$$

In a hydrostatic gas disk, dust grains settle at the velocity $v_z = -\tau_s \Omega z$. Small grains with $\tau_s \ll 1$ take longer time to settle than larger grains with $\tau_s \sim 1$. Note that when too large grains $\tau_s \gg 1$ show vertical oscillation with a frequency Ω rather than settling with the above terminal velocity. The following extrapolated velocity formula to a maximum velocity of large grains is often used (Brauer et al. 2008):

$$v_z = -\frac{\tau_s \Omega}{1 + \tau_s} z. \quad (1.18)$$

1.2.2 The effects of turbulence on dust grains

Gas in a protoplanetary disk is thought to be turbulent to some extent, leading to angular momentum transfer and mass accretion via “turbulent viscosity”. Strength of

turbulence is usually measured by the dimensionless parameter α (Shakura & Sunyaev 1973), and turbulent viscosity coefficient is given by $\nu = \alpha c_s H$. The value α depends on a driving mechanism of gas turbulence. Origins of gas turbulence in protoplanetary disks can be various hydrodynamical or magnetohydrodynamical instabilities including convective overstability (e.g., Lin & Papaloizou 1980; Klahr & Hubbard 2014) and vertical shear instability (e.g., Urpin & Brandenburg 1998; Urpin 2003; Nelson et al. 2013), and magnetorotational instability (e.g., Balbus & Hawley 1991, 1998).

Dust grains in turbulent gas suffer diffusion, which prevents vertical settling introduced in the previous subsection. An equilibrium profile of dust density can be derived from the continuity equation with mass diffusion term:

$$\frac{\partial \rho_d}{\partial t} + \frac{\partial \rho_d v_z}{\partial z} = \frac{\partial}{\partial z} \left(D_z \frac{\partial \rho_d}{\partial z} \right), \quad (1.19)$$

where D_z is a vertical diffusion coefficient, and we ignore radial and azimuthal gradient for simplicity. For steady density profile, ρ_d satisfies

$$\rho_d v_z = D_z \frac{\partial \rho_d}{\partial z}. \quad (1.20)$$

Adopting $v_z = -\tau_s \Omega z$ for dust tightly coupled to turbulence, we obtain the following Gaussian profile (e.g., Dubrulle et al. 1995; Cuzzi et al. 1993; Carballido et al. 2006):

$$\rho_d = \frac{\Sigma_d}{\sqrt{2\pi} H_d} \exp\left(-\frac{z^2}{2H_d^2}\right) \quad (1.21)$$

$$H_d \equiv \sqrt{\frac{D_z}{\tau_s \Omega}}, \quad (1.22)$$

where we use a dust surface density Σ_d for an integral constant, and H_d called dust scale height represents a vertical thickness of a dust disk. The diffusion coefficient has been estimated analytically (e.g., Cuzzi et al. 1993; Youdin & Lithwick 2007). For tightly coupled dust grains, D_z is equal to a gas diffusion coefficient $D_g = \alpha c_s H$.

Using the Langevin equation that includes orbital motion of dust grains, Youdin & Lithwick (2007) derived diffusion coefficients and dust scale height that are also applicable for large dust grains ($\tau_s \gtrsim 1$). For uniform turbulence, the dust scale height is

$$H_d = H \sqrt{\frac{\alpha}{\tau_s} \left(1 + \frac{\text{St} \tau_e^2}{1 + \text{St}}\right)^{-1}}, \quad (1.23)$$

where $\tau_e \equiv t_{\text{eddy}} \Omega$ is dimensionless turnover time of the largest eddies, and $\text{St} \equiv t_{\text{stop}}/t_{\text{eddy}}$ is so-called Stokes number. For eddies in protoplanetary disks, we often assume $\tau_{\text{eddy}} = 1$,

and thus $St = \tau_s$. They also modify Equation (1.23) derived for constant ρ_g in order to make the formula applicable for stratified disks:

$$H_d = H \sqrt{\frac{\alpha}{\alpha + \tau_s} \left(1 + \frac{St\tau_e^2}{1 + St}\right)^{-1}}, \quad (1.24)$$

For $\tau_{\text{eddy}} = 1$ and $St = \tau_s$, the above equation is reduced to the following

$$H_d = H \sqrt{\frac{\alpha}{\alpha + \tau_s} \left(\frac{1 + 2\tau_s}{1 + \tau_s}\right)^{-1}}, \quad (1.25)$$

$$\simeq H \left(1 + \frac{\tau_s}{\alpha} \frac{1 + 2\tau_s}{1 + \tau_s}\right)^{-1/2}. \quad (1.26)$$

Dust diffusion also occurs in the radial direction. Youdin & Lithwick (2007) derived the radial diffusion coefficient given as follows

$$D = \frac{1 + \tau_s + 4\tau_s^2}{(1 + \tau_s^2)^2} \alpha c_s H, \quad (1.27)$$

where we assumed isotropic turbulence (see also Youdin 2011). For small dust grains with $\tau_s \ll 1$, diffusion coefficient becomes $D \simeq \alpha c_s H$. The right hand side corresponds to a rate of gas diffusion via its eddy motion. Thus, dust grains are mixed by gas eddies when they are well coupled to gas. Relatively large grains do not follow gas eddy's motion, and their trajectories are determined by a combination of the Coriolis force and stochastic kicks by gas eddies. The Coriolis force dominates the kicks for $\tau_s \gtrsim 1$, and the diffusion coefficient monotonically decreases.

Along with the diffusion, gas turbulence generates non-zero velocity dispersion c_d . The velocity dispersion is also derived in Youdin & Lithwick (2007). For isotropic turbulence, c_d^2 is given by

$$c_d^2 = \frac{1 + 2\tau_s^2 + (5/4)\tau_s^3}{(1 + \tau_s^2)} \alpha c_s^2. \quad (1.28)$$

The non-zero velocity dispersion acts as Reynolds stress and affects evolution of mean dust flow. The process is often modeled by effective pressure gradient force proportional to c_d^2 (e.g., Youdin 2005a, 2011; Shariff & Cuzzi 2011).

1.2.3 Gravitational instability of a dust layer

In the standard scenario of planet formation, planetesimals are thought to form via gravitational instability (GI) and fragmentation of a dust disk around the midplane

1.2. DUST DYNAMICS IN PROTOPLANETARY DISKS

(e.g., Safronov 1969; Goldreich & Ward 1973). We review basic properties of GI based on one-dimensional linear analyses.

GI can be found in infinitesimally thin disks. We first review GI in such thin disks based on vertically integrated continuity equation and equations of motion of dust in local shearing sheet coordinates (Goldreich & Lynden-Bell 1965b):

$$\frac{\partial \Sigma_d}{\partial t} + \frac{\partial \Sigma_d v_x}{\partial x} = 0, \quad (1.29)$$

$$\frac{\partial v_x}{\partial t} + v_x \frac{\partial v_x}{\partial x} = 3\Omega^2 x + 2\Omega v_y - \frac{c_d^2}{\Sigma_d} \frac{\partial \Sigma_d}{\partial x} - \frac{\partial \Phi}{\partial x}, \quad (1.30)$$

$$\frac{\partial v_y}{\partial t} + v_x \frac{\partial v_y}{\partial x} = -2\Omega v_x, \quad (1.31)$$

$$\frac{\partial^2 \Phi}{\partial x^2} = -4\pi G \Sigma_d \delta(z), \quad (1.32)$$

where $(x, y) = (r - R, R(\phi - \Omega t))$ is the co-orbital coordinate with a reference radius R and angular velocity $\Omega = \sqrt{GM_*/R^3}$. Self-gravitational potential of a dust disk is denoted by Φ . We also assumed that a disk is axisymmetric and dust grains are free from diffusion and friction, for simplicity. Taking a uniform density profile $\Sigma_d = \Sigma_{d,0}$ and Keplerian velocity field $(v_x, v_y) = (0, -3\Omega x/2)$ as an unperturbed state, we introduce linear perturbations and linearize the continuity equation and the equations of motion:

$$\frac{\partial \delta \Sigma_d}{\partial t} + \Sigma_{d,0} \frac{\partial \delta v_x}{\partial x} = 0, \quad (1.33)$$

$$\frac{\partial \delta v_x}{\partial t} = 2\Omega \delta v_y - \frac{c_d^2}{\Sigma_{d,0}} \frac{\partial \delta \Sigma_d}{\partial x} - \frac{\partial \delta \Phi}{\partial x}, \quad (1.34)$$

$$\frac{\partial \delta v_y}{\partial t} = -\frac{\Omega}{2} \delta v_x, \quad (1.35)$$

where the unperturbed value is represented by subscripts “0”, and linear perturbations are denoted with δ . We assume perturbations proportional to $\exp(ikx + nt)$ and perform Fourier transformation of the above equations:

$$n\delta \Sigma_d + ik\Sigma_{d,0}\delta v_x = 0, \quad (1.36)$$

$$n\delta v_x = 2\Omega \delta v_y - ikc_d^2 \frac{\delta \Sigma_d}{\Sigma_{d,0}} - ik\delta \Phi, \quad (1.37)$$

$$n\delta v_y = -\frac{\Omega}{2} \delta v_x. \quad (1.38)$$

Perturbed self-gravitational potential is given by $\delta \Phi = -2\pi G \delta \Sigma_d / k$, which satisfies a boundary condition that $\delta \Phi$ diminishes outside the disk (e.g., see Shu 1992). Equations

(1.36)-(1.38) and $\delta\Phi = -2\pi G\delta\Sigma_d/k$ have nontrivial solutions only when $n = 0$ for arbitrary wavenumber k or the following dispersion relation is satisfied:

$$-n^2 = \Omega^2 - 2\pi G\Sigma_{d,0}k + c_d^2k. \quad (1.39)$$

The solution of $n = 0$ is called a static mode or a neutral mode, and corresponds to a steady solution of the linearized equations. Equation (1.39) is a dispersion relation of GI mode. GI can grow if n has positive real parts. The criterion is given by

$$Q_d \equiv \frac{c_d\Omega}{\pi G\Sigma_{d,0}} < 1, \quad (1.40)$$

where Q_d is the Toomre's Q value for a dust disk (Toomre 1964).

Explicitly including vertical structures reduces growth rate and makes the critical mass larger. Goldreich & Lynden-Bell (1965a) showed that GI of uniformly rotating gas disks grows when $\pi G\rho_{\text{mid}}/4\Omega^2 > 0.73$ is satisfied, where ρ_{mid} is midplane gas density. Applying this criterion for Keplerian dust disks with the midplane dust density $\rho_{d,\text{mid}}$, one obtains

$$Q_{3D} \equiv \frac{\Omega^2}{\pi G\rho_{d,\text{mid}}} \lesssim (0.73)^{-1} \simeq 1.3. \quad (1.41)$$

Assuming the vertical Gaussian profile for dust density distribution, the midplane density is related to $\Sigma_{d,0}$ by $\rho_{d,\text{mid}} = \Sigma_{d,0}/\sqrt{2\pi}H_d$. In this diffusion-less arguments, the vertical thickness of a dust disk is determined by balance of effective pressure gradient force and vertical gravity as in the case of a gas disk shown in the beginning of this section. Thus, the vertical thickness H_d in this case is given by $H_d = c_d/\Omega$. We then have

$$Q_d = \frac{Q_{3D}}{\sqrt{2\pi}} \lesssim 0.55. \quad (1.42)$$

This criterion shows that twice larger disk-mass is required for GI to operate in vertically stratified disks.

Since dust grains settle toward the midplane as a result of frictional interaction with gas, the midplane dust density monotonically increases in the absence of gas turbulence. However, dust settling itself can trigger Kelvin-Helmholtz instability that stirs dust grains up. Dust sedimentation is more difficult in the presence of vertical dust diffusion, which is not considered in the above derivation of the critical Q_d . Kelvin-Helmholtz instability in this context is self-regulated because the instability is powered by vertical shear resultant from dust sedimentation. If dust grains are diffused too much to lead to vertical shear, Kelvin-Helmholtz instability and resultant turbulence become weak. This implies an equilibrium dust density profile. Sekiya (1998) calculated the equilibrium profiles under

the influence of Kelvin-Helmholtz instability. They showed that vertical diffusion driven by Kelvin-Helmholtz instability makes the midplane dust density much lower than the critical value required of GI. Sekiya (1998) also showed that a high dust-to-gas ratio weakens Kelvin-Helmholtz instability, and the midplane dust layer can be GI-unstable. For example, for GI to operate at $r = 1$ au, a dust-to-gas ratio should be about 0.07-0.08 (see Fig. 2 and Table 1 therein). Nevertheless, turbulence powered by other instabilities will prevent dust sedimentation. Thus, the direct formation of planetesimals via GI still seems difficult unless other processes locally concentrate dust grains.

1.2.4 Secular gravitational instability

Pure gravitational instability requires Toomre’s Q value less than unity. Toomre’s Q value represents the magnitude of Coriolis force and pressure gradient force relative to self-gravity. If some processes weaken either Coriolis force or pressure gradient force, GI will grow even in a disk with $Q > 1$. For example, radiative cooling weakens pressure gradient force and augments GI (e.g., Gammie 2001; Lin & Kratter 2016).

Dust-gas friction modifying dust and gas mean flows is another process that can make dust GI more unstable. Dust grains frictionally interacting with gas can not freely move with epicyclic frequency but tend to follow gas flow around their positions. In other words, friction weakens rotational support due to Coriolis force, which is one of the restoring forces exerted on dust. This process augments dust GI and makes its growth faster.

In addition to the augmentation of dust GI, the friction triggers another instability called “dissipative GI” or “secular GI”. Secular GI is a process that most of my thesis focuses on. We thus review properties of secular GI in detail based on previous studies.

The idea of secular GI was pointed out by Ward (2000). Ward (2000) and subsequent works by Youdin (2005a, 2005b) analyzed stability of a self-gravitating dust disk embedded in a static gas disk. Thus, their analyses are based on one-fluid equations. Secular GI originates from a static mode that is present in friction-free self-gravitating disks (see the previous subsection). The static mode represents an equilibrium state that holds radial force balance of self-gravity, Coriolis force, and effective pressure gradient force. At shorter wavelength ($kc_d/\Omega \gg 1$), self-gravity and effective pressure gradient force are dominant, and the radial force balance is mainly achieved by these two. Perturbations with such short wavelengths are insignificantly affected by friction because stabilizing effects due to Coriolis force are small. On the other hand, the static mode at longer wavelengths shows the force balance mainly determined by Coriolis force and

self-gravity, and thus significantly affected by friction. Youdin (2005a) showed that long-wavelength perturbations are unconditionally unstable, which also can be shown in the following.

Another feature of secular GI is its slow growth in contrast to pure GI that grows at timescale of $\sim \Omega^{-1}$. Here, we derived growth rate based on terminal velocity approximation. Considering that velocity perturbations damp at a timescale t_{stop} , we use the following linearized equation of motion:

$$n\delta v_x = 2\Omega\delta v_y - ikc_d^2 \frac{\delta\Sigma_d}{\Sigma_{d,0}} - ik\delta\Phi - \frac{\delta v_x}{t_{\text{stop}}}, \quad (1.43)$$

$$n\delta v_y = -\frac{\Omega}{2}\delta v_x - \frac{\delta v_y}{t_{\text{stop}}}. \quad (1.44)$$

Terminal approximation and $\delta\Phi = -2\pi G\delta\Sigma_d/k$ give

$$2\Omega\delta v_y - ikc_d^2 \frac{\delta\Sigma_d}{\Sigma_{d,0}} + i2\pi G\delta\Sigma_d - \frac{\delta v_x}{t_{\text{stop}}} = 0, \quad (1.45)$$

$$\delta v_y = -\frac{\tau_s}{2}\delta v_x. \quad (1.46)$$

From Equations (1.36), (1.45), and (1.46), we obtain the following approximated dispersion relation:

$$n = \frac{1}{t_{\text{stop}}} \frac{2\pi G\Sigma_{d,0}k - c_d^2 k^2}{\Omega^2 + t_{\text{stop}}^{-2}}. \quad (1.47)$$

This shows that perturbations with $k < 2\pi G\Sigma_{d,0}/c_d^2$ are unconditionally unstable. For small dust with $\tau_s = t_{\text{stop}}\Omega \ll 1$ and sufficiently long wavelengths so that the numerator can be approximated as $2\pi G\Sigma_{d,0}k$, the growth rate is reduced to

$$n \simeq t_{\text{stop}} 2\pi G\Sigma_{d,0}k = 2\pi \left(\frac{\lambda}{t_{\text{stop}} \times 2\pi G\Sigma_{d,0}} \right)^{-1}, \quad (1.48)$$

where $\lambda = 2\pi/k$ is a wavelength of perturbations. The last equality of Equation (1.48) shows that the growth rate is roughly given by a timescale for dust grains to transverse one wavelength with terminal velocity $t_{\text{stop}} 2\pi G\Sigma_{d,0}$ (see also Section 2 of Youdin 2011). Growth rate relative to Ω is $n/\Omega \sim \tau_s \times (kc_d\Omega^{-1})/Q_d$, which is less than unity because of the factor τ_s . Therefore, secular GI grows much slower than dust GI. Regardless of its slow growth, secular GI was proposed as a possible mechanism of planetesimal formation because “one-fluid” secular GI can grow without thresholds in contrast to GI (see also, Sekiya 1998).

In the presence of radial diffusion of dust grains, secular GI is found to be significantly stabilized. Youdin (2011) and Shariff & Cuzzi (2011) performed linear analyses using

hydrodynamic equations of motions for dust as in the above description and continuity equation with diffusion term:

$$\frac{\partial \Sigma_d}{\partial t} + \frac{\partial \Sigma_d v_x}{\partial x} = D \frac{\partial^2 \Sigma_d}{\partial x^2}. \quad (1.49)$$

Michikoshi et al. (2012) analyzed secular GI with diffusion in a more rigorous manner using Langevin equations, and showed consistent results with Youdin (2011) and Shariff & Cuzzi (2011). Dispersion relation in the presence of radial diffusion is as follows (see also Equation (22) in Youdin (2011) and Equation (15) in Shariff & Cuzzi (2011)):

$$n^3 + C_2 n^2 + C_1 n + C_0 = 0, \quad (1.50)$$

$$C_2 = Dk^2 + 2/t_{\text{stop}}, \quad (1.51)$$

$$C_1 = 2Dk^2/t_{\text{stop}} + 1/t_{\text{stop}}^2 + \Omega^2 + c_d^2 k^2 - 2\pi G \Sigma_{d,0} k, \quad (1.52)$$

$$C_0 = Dk^2 (\Omega^2 + t_{\text{stop}}^{-2}) + (c_d^2 k^2 - 2\pi G \Sigma_{d,0} k) / t_{\text{stop}}. \quad (1.53)$$

Adopting the MMSN model (e.g., Hayashi 1981) for calculating disk properties, Youdin (2011) derived growth timescale, unstable wavelengths, and masses of dust grains accumulated via the instability into one ring. Figure 1.3 originally from Youdin (2011) shows their results for dust grain size $a = 1$ mm and dust-to-gas surface density ratio is 0.01. Kinks of lines seen in each panel are due to transition from Epstein region to Stokes region of dust-gas friction. Growth timescale decreases toward the outer region because Toomre's Q also decreases. For significantly weak turbulence with $\alpha = 10^{-10}$, secular GI can grow in wide radial region from 0.1 au to 100 au. On the other hand, turbulence with $\alpha = 10^{-6}$ significantly stabilizes secular GI especially in the inner region. They concluded that secular GI creates dust rings with a mass of $\sim 0.1 M_\oplus$ and resultant rings will fragment into planetesimals.

Shariff & Cuzzi (2011) compared growth timescale of secular GI and a timescale of radial drift:

$$t_{\text{drift}} = \frac{r}{|v_r|}. \quad (1.54)$$

Figure 1.4 originally from Shariff & Cuzzi (2011) shows their results for $r = 3$ au and the MMSN disk model. Larger grains show faster growth, and the growth timescale of secular GI is shorter than t_{drift} when turbulence is weak ($\alpha = 10^{-6}, 10^{-7}$). On the other hand, growth timescale becomes comparable to t_{drift} for $\alpha = 10^{-5}$ even when dust grains are 1 m in size. Therefore, secular GI can be a mechanism for creating planetesimals at the outer region ($r \sim 10^{1-2}$ au) rather than the inner region ($r \sim 1$ au), and weakly turbulent disks are preferable.

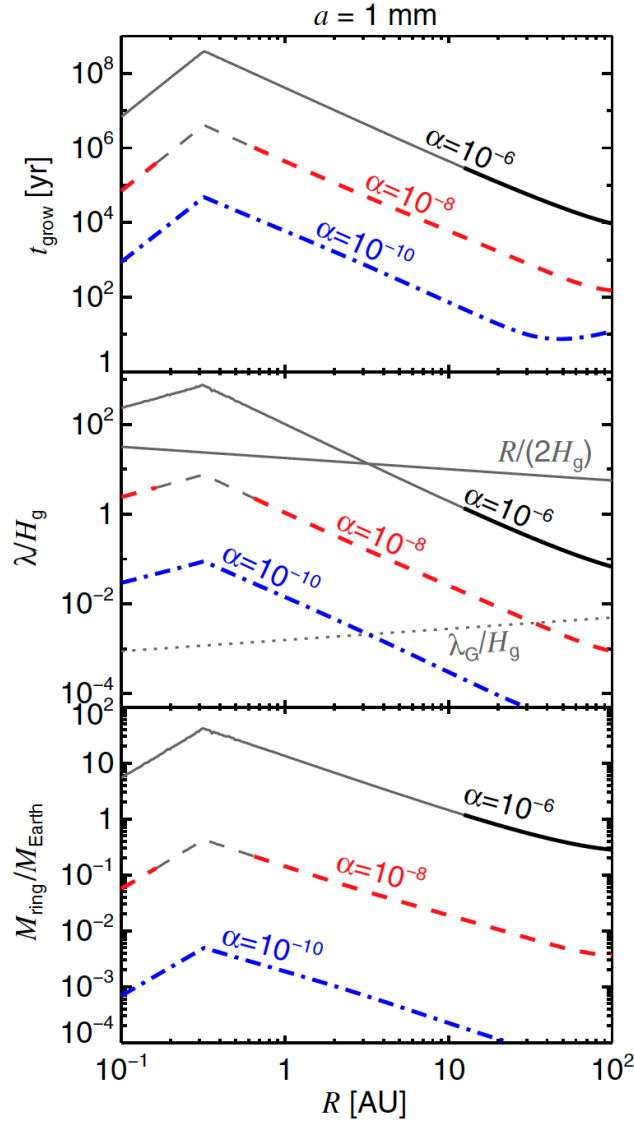


Figure 1.3: Properties of “one-fluid” secular GI in the presence of radial diffusion of dust. Horizontal axis is a radial distance from a central star. Top panel shows growth timescale of the instability for different strength of turbulence α . Gray sections of solid and dashed lines represent a region where the growth time is longer than a typical lifetime of protoplanetary disks $\sim 10^{6-7}$ yr (e.g., Strom et al. 1989; Beckwith et al. 1990). Middle panel shows unstable wavelength in the unit of gas scale height. The half disk radius $R/2$ and the most unstable wavelength of pure GI $\lambda_G = 2\pi^2 G \Sigma_{d,0} / \Omega^2$ are also plotted. Bottom panel shows mass of concentrating dust grains during the growth of secular GI. Because dust grains are concentrated into a ring, the mass is referred to as a ring mass M_{ring} . This figure is from Fig. 2 of Youdin (2011).

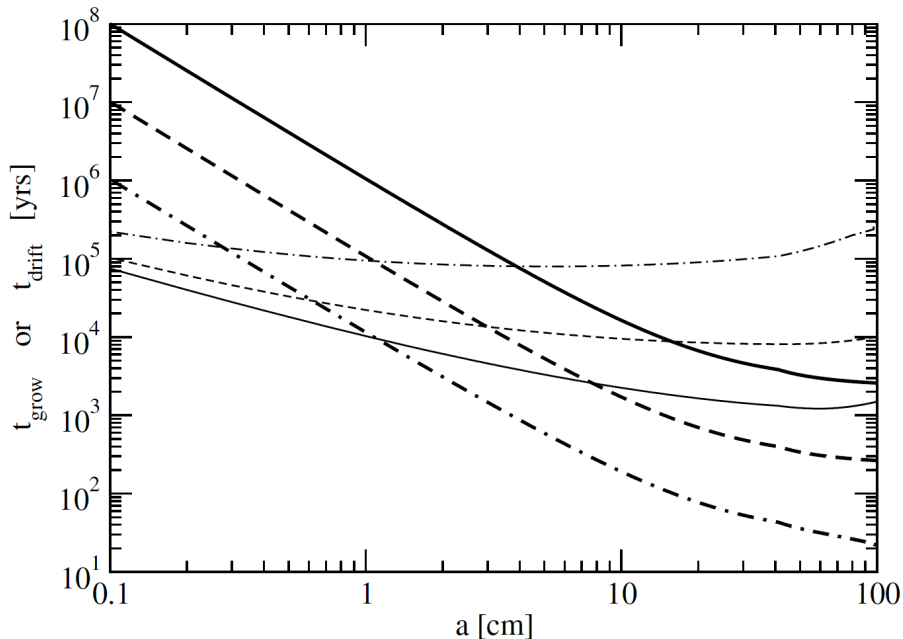


Figure 1.4: Growth timescale of secular GI t_{grow} and drift timescale t_{drift} as a function of dust sizes a in the case of MMSN disk. The radial position is fixed at 3 au. Solid, dotted, and dashed lines correspond to results for $\alpha = 10^{-5}$, 10^{-6} , and 10^{-7} , respectively. Thin and thick lines denote t_{drift} and t_{grow} , respectively. Although larger dust grains show faster growth, the growth timescale is still longer than the drift timescale if strength of turbulence is $\alpha = 10^{-5}$ for MMSN disks. This figure is from Fig. 4 of Shariff & Cuzzi (2011).

We should emphasize that the above findings of Youdin (2011) and Shariff & Cuzzi (2011) are based on the MMSN model where disk masses are set to be minimal. Disk masses significantly affect growth timescale of secular GI through Toomre’s Q value. According to disk formation and evolution reviewed in the previous section, disk masses decrease from its formation time. In other words, increasing disk masses adopted corresponds to considering early-phase disks. Therefore, early massive disks will be one site where secular GI grows.

The previous studies reviewed above are based on one-fluid equations for dust. Including gas equations and frictional backreaction to gas introduces another property of secular GI. Takahashi & Inutsuka (2014) performed two-fluid analyses of secular GI, and showed that long-wavelength perturbations are stabilized as a result of backreaction, which is in contrast to the previous studies showing unconditionally unstable secular GI. Figure 1.5 originally from Takahashi & Inutsuka (2014) shows growth rate of “two-fluid” secular GI for $c_d = 0$, $D = 10^{-4}c_s H$, $Q = 3$, $\tau_s = 10^{-2}$, and unperturbed dust-to-gas surface density ratio $\Sigma_{d,0}/\Sigma_{g,0} = 0.1$. Long-wavelength perturbations show negative

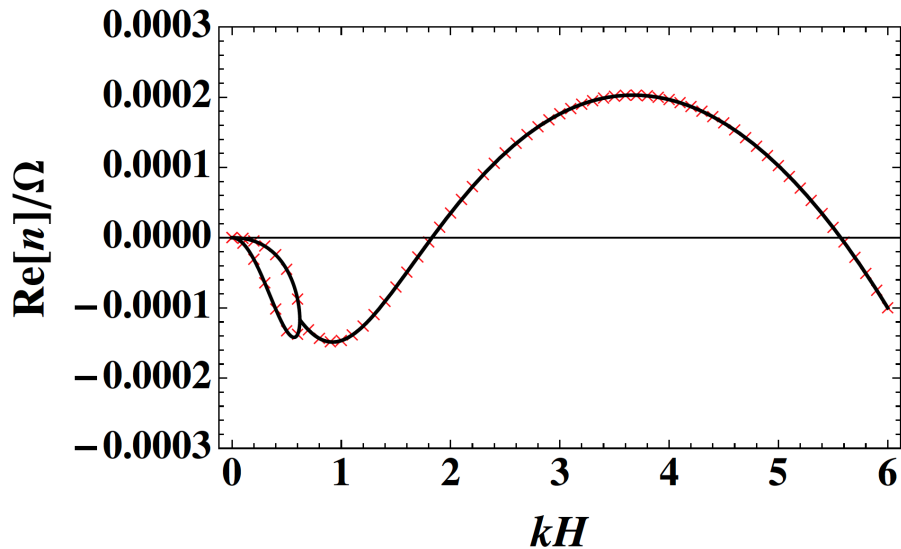


Figure 1.5: Growth rate of “two-fluid” secular GI for $c_d = 0$, $D = 10^{-4}c_s H$, $Q = 3$, $\tau_s = 10^{-2}$, and $\Sigma_{d,0}/\Sigma_{g,0} = 0.1$. Horizontal axis is wavenumber normalized by gas scale height H . This figure is from Fig. 1 of Takahashi & Inutsuka (2014).

growth rates, meaning that the mode is a damping mode for those wavelengths. Takahashi & Inutsuka (2014) showed that the stabilization of long-wavelength perturbations are accounted for Coriolis force exerted on dust. In contrast to one-fluid analyses, gas slightly moves and follows radial concentration of dust grains as a result of backreaction. Radially concentrating flows in positive x -direction induce Coriolis force in the negative y -direction, and decelerate the azimuthal velocity of gas. Dust grains are also decelerated because of the azimuthal friction. This deceleration tends to reduce the radially concentrating flows, and quenches at long wavelengths (see also Latter & Rosca 2017). In this way, backreaction renders secular GI operational only at intermediate wavelengths comparable to gas scale height.

Takahashi & Inutsuka (2014) also derived the following growth condition for secular GI in the absence of velocity dispersion c_d :

$$\frac{D\Omega^2}{(\pi G\Sigma_{g,0})^2} < \varepsilon(1 + \varepsilon)\tau_s, \quad (1.55)$$

where $\varepsilon \equiv \Sigma_{d,0}/\Sigma_{g,0}$ is dust-to-gas surface density ratio (see Equation (21) in Takahashi & Inutsuka 2014). They also numerically calculated maximum growth rate with the inclusion of velocity dispersion, turbulent gas viscosity, and the stabilizing effect due to a finite disk thickness (Vandervoort 1970; Shu 1984). Figure 1.6 originally from Takahashi & Inutsuka (2014) shows their results for $Q = 3$ and $\varepsilon = 0.1$. One can see that “two-

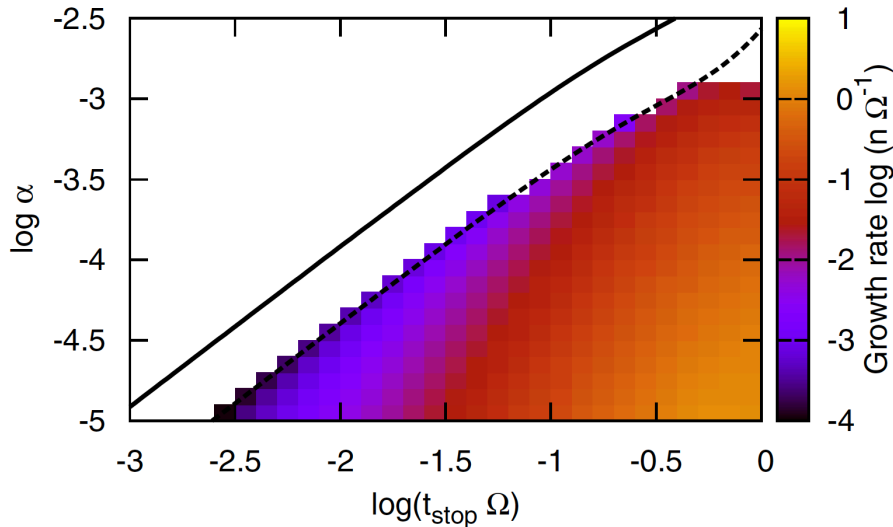


Figure 1.6: Maximum growth rate of “two-fluid” secular GI for $Q = 3$ and $\varepsilon = \Sigma_{d,0}/\Sigma_{g,0} = 0.1$ as a function of strength of turbulence α and dimensionless stopping time τ_s . Solid line shows maximum α derived from the growth condition (Equation (1.55)), and dashed line shows three times lower α . Because they include the gas turbulent viscosity and the stabilizing effect due to the disk thickness to plot this figure, the maximum α is smaller than one shown by the solid line. This figure is from Fig. 3 of Takahashi & Inutsuka (2014).

fluid” secular GI is operational for $\alpha \sim 10^{-4}$ when dust-to-gas ratio is high and Toomre’s Q for gas is 3.

Although their linear analyses does not include collective dust drift as in the previous studies, they estimated condition for secular GI to grow in the presence of dust drift comparing the growth rate and the drift timescale. They found that secular GI can grow when the following condition is satisfied (see Equation (39) therein):

$$\left(\frac{\alpha}{4 \times 10^{-5}}\right) \left(\frac{\varepsilon}{0.1}\right)^{-2} \left(\frac{Q}{10}\right)^2 \left(\frac{\eta}{0.01}\right) \lesssim 1. \quad (1.56)$$

Even for high dust-to-gas ratio, turbulence should be weak ($\alpha \sim 10^{-5}$). When Toomre’s Q is ~ 5 during the disk evolution from its formation, disks with turbulence of $\alpha \sim 10^{-4}$ marginally host secular GI although high dust-to-gas ratio is still required.

1.3 ALMA Observations of Annular Substructures

Classically, the presence of protoplanetary disks was observationally confirmed based on infrared excesses in spectral energy distributions (SEDs). Based on SEDs at μm -wavelengths, Lada (1987) proposed three classes that would divide the evolutionary

timeline of stars and disks (see Figure 1.7). Class I refers to embedded objects that show wider SED relative to stellar black body radiations because of a surrounding envelope. Class II objects show infrared excess relative to stellar black body radiation. The infrared excess is responsible for emissions from dusty-gas disks, i.e., protoplanetary disks. Class III objects correspond to a star with a fairly dispersed disk. In addition to the three classes, Andre et al. (1993) introduced Class 0 as a group of very young objects embedded in dense envelopes (see also Andre & Montmerle 1994).

Recent observational developments enable us to directly see disks and their structures of ~ 10 -au scales. For example, optical and near-infrared observations with Subaru telescope and Very Large Telescope (VLT) with SPHERE² have detected disks with rings, spirals, and shadows casted on disk surfaces (e.g., Muto et al. 2012; Benisty et al. 2015; Hashimoto et al. 2015; Momose et al. 2015; Stolker et al. 2016; van Boekel et al. 2017; Avenhaus et al. 2018). Those observations see scattered light from small dust grains floating in an upper layer of a disk.

Atacama Large Millimeter/submillimeter Array (ALMA) has also been showing observational results on detailed disk structures. ALMA observations at (sub-)mm wavelengths trace dust grains around the midplane. High resolution disk observations with ALMA revealed that most of the observed and resolved disks have annular substructures, i.e., rings and gaps (e.g., ALMA Partnership et al. 2015; Andrews et al. 2016; Tsukagoshi et al. 2016; Isella et al. 2016; Fedele et al. 2017; Long et al. 2018; Andrews et al. 2018). Those rings and gaps have been observed not only in relatively old disks (~ 10 Myr; e.g., TW Hya, Andrews et al. 2016, Tsukagoshi et al. 2016; HD169142, Fedele et al. 2017, Pérez et al. 2019) but also in very young disks ($\lesssim 1$ Myr; e.g., HL Tau, ALMA Partnership et al. 2015; WL 17, Sheehan & Eisner 2017). It is reported by a very recent study that Class 0/I object also hosts a dust ring (e.g., Sheehan & Eisner 2018; Nakatani et al. 2020).

The Disk Substructures at High Angular Resolution Project (DSHARP) is a Class-II-disk survey for statistical studies of dust substructures (e.g., Andrews et al. 2018). They observed 20 disks at 5-au resolutions. Figure 1.8 shows the disk images from Andrews et al. (2018). The observed disks show various substructures including rings/gaps and spirals. 18 disks show annular structures and thus rings and gaps seem common in their samples. Although their observations are targeted to large bright disks, the other disk observations also indicate the ubiquitousness of ring-gap structures in protoplanetary disks (e.g., ALMA Partnership et al. 2015; Andrews et al. 2016; Tsukagoshi et al. 2016; Isella et al. 2016; Fedele et al. 2017; Long et al. 2018).

²Spectro-Polarimetric High-contrast Exoplanet REsearch

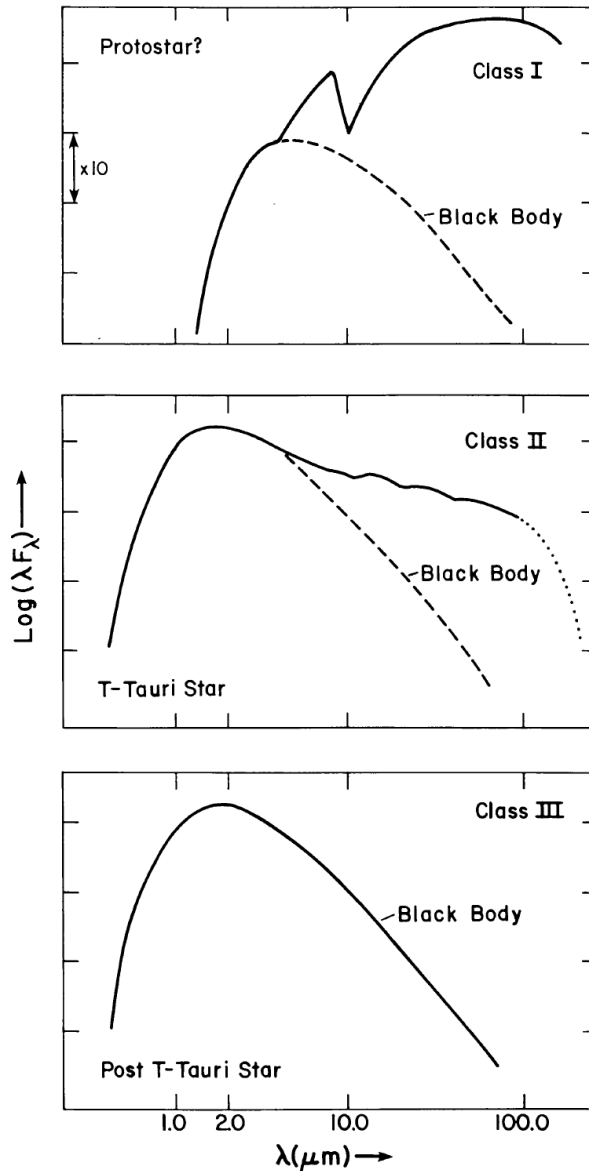


Figure 1.7: SED classifications proposed by Lada (1987). Top panel shows a schematic SED of a Class I object, which has wider energy distribution compared to one of a stellar black body. Middle panel shows a Class-II SED. Class II objects show infrared excess relative to a stellar black body radiation with a flat or negative slope. Bottom panel shows a most evolved objects among these, referred to as Class III. This figure is from Fig. 2 of Lada (1987).

Huang et al. (2018) studied properties of rings and gaps of the DSHARP disks. Based on mean intensities around a gap I_d and a ring I_b , they define widths of those structures as a radial distance between radii of the intensity $I = 0.5(I_d + I_b)$. The intensity variation of adjacent rings and gaps are typically less than 20% (see Section 3.2 of their paper).

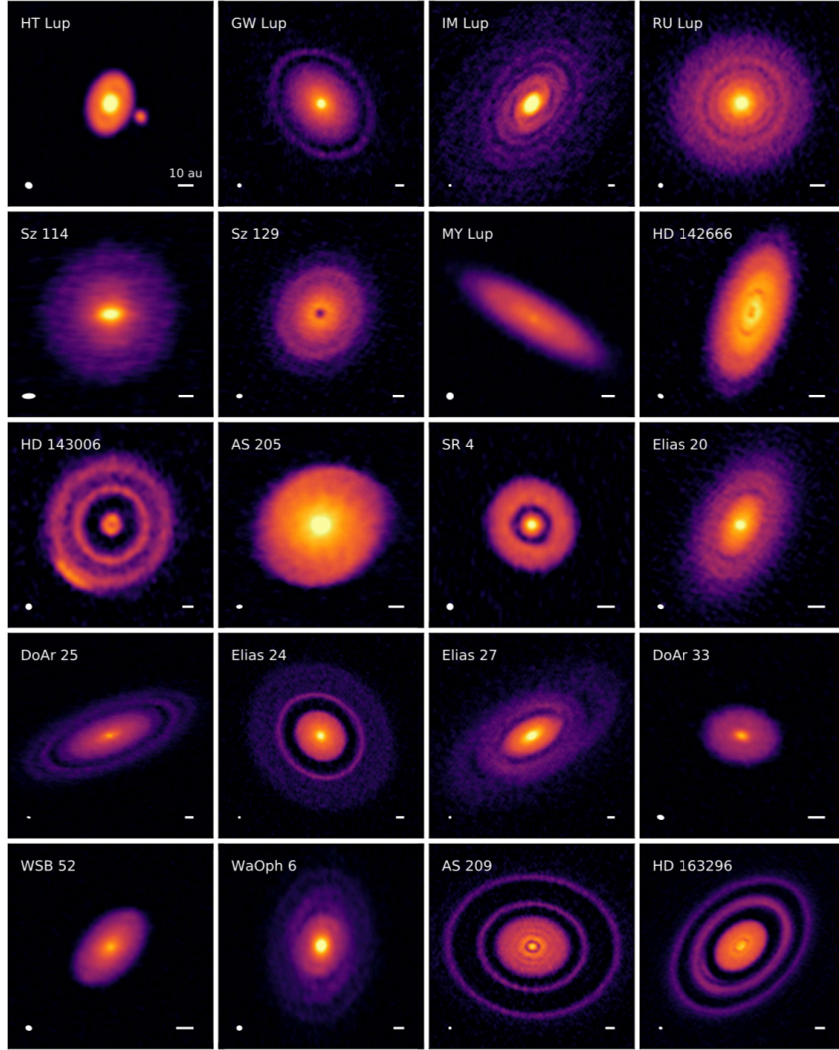


Figure 1.8: Disk images at wavelength of 1.25 mm presented by the DSHARP project. White scalebars shown on the right bottom corners of each panel represent 10 au scale. Beam sizes are shown on the left corners of each panel. This figure is from Fig. 3 of Andrews et al. (2018).

Measured widths are shown in Figure 1.9 that is originally from Figure 4 of Huang et al. (2018). The observed rings and gaps are marginally resolved. They found that the widths of most of their targets are smaller than 10 au. Assuming that disk temperature is determined by stellar irradiation, Dullemond et al. (2018) showed that the observed ring-widths are comparable to or less than the gas scale height H .

Figure 1.9 also shows that the observed rings and gaps are widely distributed from ~ 10 au to 160 au. The dependence of ring- and gap-radius on stellar properties are shown in Figure 1.10 originally from Figure 10 of Huang et al. (2018). One can see that substructures are present across a wide parameter space, and there is no clear trend with

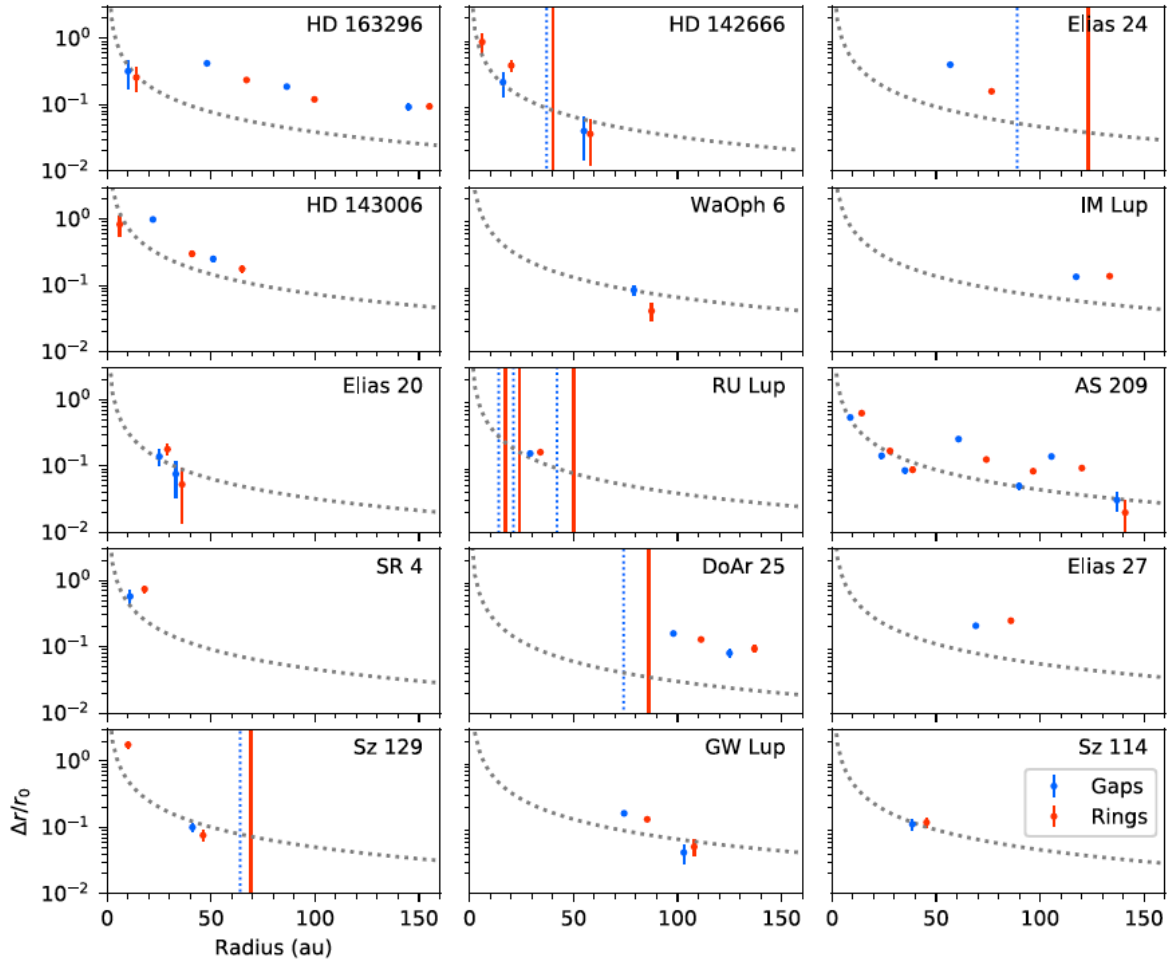


Figure 1.9: Radial distribution of measured widths of rings (red) and gaps (blue) in each object. The vertical axis in each panel is the widths normalized by the locations of the substructures. The vertical red and blue lines show locations of rings and gaps that are too shallow to allow the measurement of those widths. The gray curves show the resolution limit. This figure is from Fig. 4 of Huang et al. (2018).

stellar mass, mass accretion rate, and stellar age.

Possible origins of the observed substructures

Many studies have proposed mechanisms to explain the origins of the observed rings and gaps, and the origins are still in debate. One possible mechanism is “planet-based” and that (sub-)Jupiter mass planets already exist in the observed disks (e.g., Gonzalez et al. 2015; Kanagawa et al. 2015; Zhang et al. 2018). A planet embedded in a disk gravitationally interacts with gas and dust, leading to angular momentum transport. Gas and dust

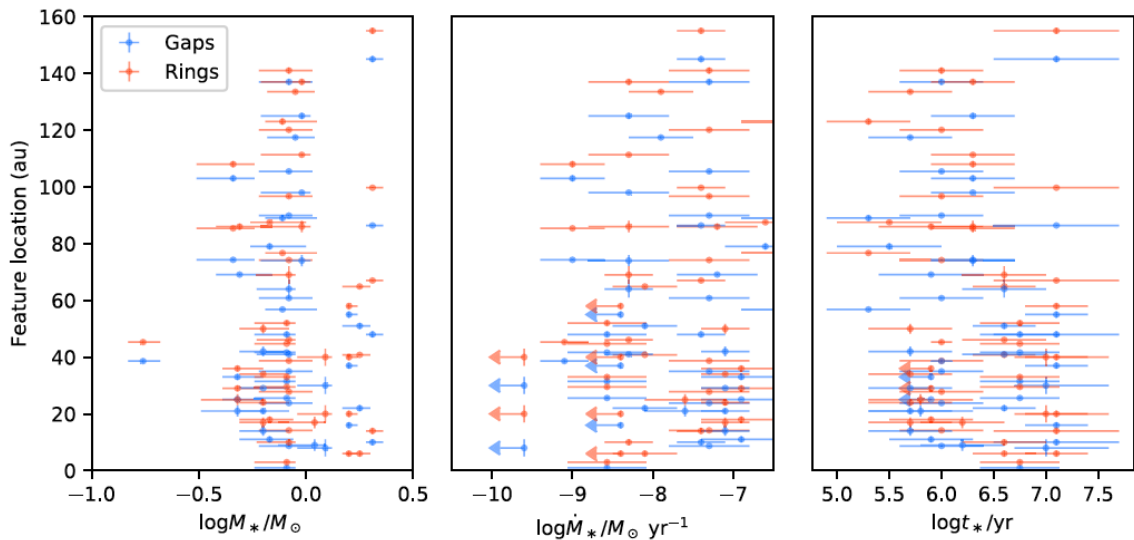


Figure 1.10: Radial distribution of the detected rings and gaps as a function of stellar mass (left figure), mass accretion rate onto a star (middle panel), and stellar age (right panel). Error bars correspond to 1σ error from the stellar properties and the locations of the substructures. This figure is from Fig. 10 of Huang et al. (2018).

around the planetary orbit are then cleared out. This planet-driven clearing makes a gap in the disk. In addition, such a planet excites waves called density waves. Propagating density waves eventually steepen into shocks at radii away from the planetary orbit. Bae et al. (2017) shows that even low-mass planets induce multiple waves (spiral arms) and shocks due to the steepening create multiple gaps.

Although recent works reported kinematic signatures of Jupiter-mass planets at the observed gaps in some disks (Pinte et al. 2018; Teague et al. 2018; Pinte et al. 2019; Pérez et al. 2020; Pinte et al. 2020), it is still unknown whether such planets also exist in the other disks. If planets actually exist in younger disks hosting annular substructures, this gives strong time-constraints on planet formation (within ~ 1 Myr; e.g., Sheehan & Eisner 2018). It is not still understood how to form planets within only 1 Myr at larger radii where gaps are observed. Such a fast planet formation seems difficult at least in the core accretion model (Mizuno 1980; Pollack et al. 1996). For example, collisional fragmentation of planetesimals delays formation of planetary cores necessary to accrete gas at radii $\gtrsim 10$ au (Kobayashi et al. 2010; Kobayashi et al. 2011).

Mechanisms without assuming planets have also been proposed. Dullemond et al. (2018) analyzed the DHSARP data using analytical models, and showed that the observed rings can be explained by dust-trapping due to hypothetical “pressure bumps”

(e.g., Whipple 1972). A pressure bump has a positive and negative pressure gradient at inner and outer radii. According to the formula of the drift velocity (Equation (1.14)), dust grains tend to accumulate at pressure maxima, which creates dust rings. The boundary of magnetically dead and active zones is one possible location where a pressure bump exists (Flock et al. 2015). The magnetic activity itself is also found to form ring-like substructures through reconnection of the toroidal magnetic fields (Suriano et al. 2018; Suriano et al. 2019). Based on local shearing-box simulations and linear analyses, Riols & Lesur (2019) shows that a disk subject to disk-wind mass loss can be unstable and host rings and gaps as a result of such a “wind-driven instability”.

In the above processes, dust grains just follow the background gas structures and accumulate into rings (e.g., pressure bumps). On the other hand, dust itself can drive processes leading to ring formation. Such “active” processes include secular GI (Takahashi & Inutsuka 2014 2016), which is reviewed in the previous section. Takahashi & Inutsuka (2016) performed linear analyses using disk models consistent with observations of HL Tau. They found that widths of outer rings ($r \simeq 100$ au) are consistent with the most unstable wavelengths of secular GI. The presence of dust leads to another type of instability called viscous ring instability (Dullemond & Penzlin 2018). Instead of the self-gravity, this instability requires the turbulent viscosity dependent on dust abundance (e.g., Sano et al. 2000; Ilgner & Nelson 2006).

Zhang et al. (2015) discussed ring formation by rapid dust growth near snow lines where dust grains evaporate. They showed that the process explains the three prominent gaps in the HL Tau disk ALMA Partnership et al. (2015). Sintering of dust aggregates is another important process that changes dust sizes near the snow lines. Okuzumi et al. (2016) shows that dust aggregates that experience sintering fragment and pile up slightly outside snow lines, and resultant piling-up regions are observed as bright dust rings. Those radially changing dust size results in variations of the ionization degree and mass accretion rate across snow lines, which augments the ring-gap formation (Hu et al. 2019). This process is similar to the instability discussed in Dullemond & Penzlin (2018). However, Huang et al. (2018) showed that expected locations of snow lines of CO, N₂ are not correlated with radii of the DSHARP rings/gaps although some of the substructures may result from the processes with snow lines.

1.4 Purposes of this thesis

As shown in the previous sections, the recent high-resolution observations have been providing detailed information on disk structures, especially on spatial distributions of

dust grains. The revealed annular substructures are some clues to reveal planetesimal formation, and planet formation. For example, if the observed substructures result from radial dust concentration without any planets, those observations indicate ongoing planetesimal formation. The ubiquitousness of dust rings may indicate that ring formation is a common process before planetesimal formation. Therefore, it is important to study ring-forming mechanisms without planets and their connection to planetesimal formation.

According to Zhu et al. (2019), protoplanetary disks having observed at mm-wavelengths can be optically thick because of scattering of thermal radiation, and they indicate that disks are more massive than expected previously. Such self-scattering of dust thermal emissions is indicated from polarization observation by ALMA (e.g., Kataoka et al. 2015; Yang et al. 2016; Kataoka et al. 2017; Stephens et al. 2017). These observational results motivate us to study secular GI, which is one ring-forming process operational in massive disks.

As mentioned in the previous section, there is another possibility that unseen planets create the observed substructures. If this is the case, the observations indicate that formation of planet(esimal)s have occurred at early disk-evolutionary stages. Since the early phase disks are more massive according to the disk formation theories (Section 1.1), understanding physics in relatively massive dusty disks seems to be the key to figure out early planet formation. Secular GI is one possible explanation of early planet formation. Therefore, studies on secular GI is also important even when we discuss formation of planets that finally carve gaps in Class II disks.

Based on the above motivations, we investigate the disk evolution via secular GI in this thesis. The previous studies focused on linear growth of secular GI, and they found that turbulent diffusion is the most efficient process to stabilize secular GI. As reviewed in this chapter, turbulent diffusion is usually modeled by mass diffusion term introduced in the continuity equation. Although this modeling is widely used, just introducing the diffusion term violates the conservation law of angular momentum of a disk (e.g., Goodman & Pindor 2000). Since angular momentum is one fundamental physical property, the violation of its conservation law will affect not only stabilities of dusty-gas disks but also radial transport and mixing of dust grains. In Chapter 2, we revisit dust dynamics in turbulent disks and reformulate macroscopic equations that guarantee the angular momentum conservation and describe turbulent dust diffusion. Our formulation is based on mean-field approximation usually used to model turbulent fluid. Our results show that introducing turbulent effects not only in the continuity equation but also in the momentum equations holds the conservation law. We also study the stability of pro-

toplanetary disks using the reformulated equations and revisit properties of secular GI. The linear analyses also show another instability that is unphysically stabilized because of the diffusion modeling in previous works.

In Chapter 3, we investigate nonlinear growth of secular GI using the reformulated equations. In contrast to the previous works, we perform numerical simulations of secular GI and discuss how secular GI grow under the influence of radial dust drift and to what extent the instability accumulates dust grains into rings. To simplify the problem and separately consider multiple processes, we assume dust sizes limited by radial drift in the simulations presented in Chapter 3 rather than explicitly include dust growth. Our simulations show that perturbations growing via secular GI move inward with the so-called drift velocity. The drifting properties can be understood from linear analyses including dust drift in an unperturbed state. Our numerical results also show two types of growth of secular GI: formation of thin dense rings, and formation of transient rings. In the former case, secular GI grows into the nonlinear phase and accumulates over 50% of dust grains into multiple rings. In the latter case, a growth timescale of secular GI is too long for the instability to show nonlinearity. Once amplified density perturbations enter a stable region, those start to decay, that is, rings become transient. Thus, planetesimal formation via secular GI requires that perturbations grow into the nonlinear phase before they enter a stable region.

Secular GI requires higher dust-to-gas ratio than interstellar values ($\simeq 0.01$) although the required dust-to-gas ratio depends on other parameters including strength of turbulence. Dust-to-gas ratio in protoplanetary disks is not constrained observationally. Nevertheless, theoretical studies showed that if a disk is isolated dust coagulation and radial drift decrease dust surface density because of its inside-out nature (e.g., Brauer et al. 2008). Such an isolated disk may correspond to a disk of a very late stage at which we can not expect mass infall from an envelope. Even when dust and gas accrete onto a disk from the envelope, dust coagulation may proceed from the inner region and inner large dust grains fall onto a central star. Thus, dust would tend to be depleted to some extent regardless of the mass infall. Since secular GI also requires large dust (e.g., $\tau_s \sim 0.1$), the dust depletion resulting from coagulation is problematic. In Chapter 4, we propose another instability triggered by coagulation as a re-accumulation process of large dust grains. We call the instability ‘‘coagulation instability’’. Based on linear analyses with a single-sized coagulation equation, we show that coagulation instability can grow at tens orbital periods even when dust-to-gas ratio decreases down to 10^{-3} . We also investigate effects of diffusion and find that coagulation instability overcomes the diffusion and concentrates dust grains at a spatial scale $\sim H$ that is comparable to

1.4. PURPOSES OF THIS THESIS

the most unstable wavelength of secular GI. Therefore, coagulation instability will set up dust-rich circumstances and assist the growth of secular GI and its further development toward planetesimal formation.

In Chapter 5, we summarize the present thesis and discuss issues to be addressed in the future work.

Chapter 2

Revision of Macroscopic Equations for Dust Diffusion

This chapter is based on a published paper, Tominaga, Takahashi, & Inutsuka 2019, *The Astrophysical Journal*, Volume 881, pp. 53-69 (Tominaga et al. 2019).

2.1 Short introduction: unphysical momentum transport due to the diffusion term

In Chapter 2, we revisit macroscopic description of dust disk evolution. Most of studies use the advection-diffusion equation for dust density to describe dust evolution in a turbulent gas disk (e.g., see Equations (1.19) and (1.49)). This widely-used equation for dust does not conserve the total angular momentum. We first analytically show the violation of the angular momentum conservation due to the diffusion and a possible solution to recover the conservation law.

The following statement is independent from spatial dimensions one adopts. In this chapter, we use equations of a two-dimensional disk (a razor thin disk) because we also consider such a disk in Chapters 3 and 4. The continuity equation and the azimuthal equation of motion for the dust in the cylindrical coordinates are as follows:

$$\frac{\partial \Sigma_d}{\partial t} + \frac{1}{r} \frac{\partial (r \Sigma_d v_r)}{\partial r} = \frac{1}{r} \frac{\partial}{\partial r} \left(r D \frac{\partial \Sigma_d}{\partial r} \right), \quad (2.1)$$

$$\Sigma_d \left[\frac{\partial v_\phi}{\partial t} + v_r \frac{\partial v_\phi}{\partial r} \right] = -\Sigma_d \frac{v_\phi v_r}{r} - \Sigma_d \frac{v_\phi - u_\phi}{t_{\text{stop}}}, \quad (2.2)$$

where we assume axisymmetric disks. This assumption does not change the following statement. As introduced in the previous Chapter, the right hand side of Equation

2.1. SHORT INTRODUCTION: UNPHYSICAL MOMENTUM TRANSPORT DUE TO THE DIFFUSION TERM

(2.1) models turbulent dust diffusion (e.g., Youdin 2011). Using the above equations, we obtain an equation for angular momentum of dust $\Sigma_d j_d \equiv \Sigma_d r v_\phi$:

$$\frac{\partial(\Sigma_d j_d)}{\partial t} + \frac{1}{r} \frac{\partial}{\partial r} (r v_r \Sigma_d j_d) = -r \Sigma_d \frac{v_\phi - u_\phi}{t_{\text{stop}}} + j_d \frac{1}{r} \frac{\partial}{\partial r} \left(r D \frac{\partial \Sigma_d}{\partial r} \right). \quad (2.3)$$

The first term on the right hand side represents a torque due to dust-gas friction. If we take into account the frictional backreaction to gas, the frictional torque term unchange total angular momentum of dust and gas as shown in the following. The continuity equation and the azimuthal equation of motion for gas are

$$\frac{\partial \Sigma_g}{\partial t} + \frac{1}{r} \frac{\partial (r \Sigma_g u_r)}{\partial r} = 0, \quad (2.4)$$

$$\Sigma_g \left[\frac{\partial u_\phi}{\partial t} + u_r \frac{\partial u_\phi}{\partial r} \right] = -\Sigma_g \frac{u_\phi u_r}{r} + \Sigma_d \frac{v_\phi - u_\phi}{t_{\text{stop}}}, \quad (2.5)$$

These equations give an equation for angular momentum of gas $\Sigma_g j_g \equiv \Sigma_g r u_\phi$:

$$\frac{\partial(\Sigma_g j_g)}{\partial t} + \frac{1}{r} \frac{\partial}{\partial r} (r u_r \Sigma_g j_g) = r \Sigma_d \frac{v_\phi - u_\phi}{t_{\text{stop}}}. \quad (2.6)$$

We thus obtain an evolutionary equation of total angular momentum summing Equations (2.3) and (2.6):

$$\frac{\partial}{\partial t} (\Sigma_g j_g + \Sigma_d j_d) + \frac{1}{r} \frac{\partial}{\partial r} (r u_r \Sigma_g j_g + r v_r \Sigma_d j_d) = j_d \frac{1}{r} \frac{\partial}{\partial r} \left(r D \frac{\partial \Sigma_d}{\partial r} \right). \quad (2.7)$$

The term on the right hand side cannot be written in the form of divergence of an angular momentum flux. Thus, the volume integral of this term has non-zero values in general, meaning that the set of the above equations violates the total angular momentum conservation. One can immediately see that this ‘‘unphysical’’ nonconservation originates from the mass diffusion term in Equation (2.1) because the right hand side is proportional to the diffusion coefficient. The diffusion term directly changes the dust angular momentum and affects orbital evolution of dust. Gas motion is also affected by the unphysical angular momentum changes because gas and dust always exchange their angular momentums through friction. The effect on gas motion is, however, smaller than that on dust motion by a factor of dust-to-gas mass ratio Σ_d/Σ_g because the angular momentum transport via friction is proportional to the dust surface density (Equation (2.6)). Thus, the violation of the momentum conservation mainly affects on dust evolution.

We can see how the angular momentum nonconservation affects dust motion through the following rearrangement of Equation (2.3):

$$\frac{\partial(\Sigma_d j_d)}{\partial t} + \frac{1}{r} \frac{\partial}{\partial r} \left[r \left(v_r - \frac{D}{\Sigma_d} \frac{\partial \Sigma_d}{\partial r} \right) \Sigma_d j_d \right] = -r \Sigma_d \frac{v_\phi - u_\phi}{t_{\text{stop}}} - D \frac{\partial \Sigma_d}{\partial r} \frac{\partial j_d}{\partial r}. \quad (2.8)$$

2.1. SHORT INTRODUCTION: UNPHYSICAL MOMENTUM TRANSPORT DUE TO THE DIFFUSION TERM

The second term on the left hand side vanishes when one integrate the equation over all space. On the other hand, the second term on the right hand side remains and changes the angular momentum. We here consider a Keplerian disk for further discussion. For such a disk, the second term on the right hand side represents a negative (positive) torque when the dust surface density gradient is positive (negative). In a dust-piling-up region, an inner dust ($\partial\Sigma_d/\partial r > 0$) loses its angular momentum and goes inward, and vice versa. Thus, the unphysical torque prevents dust accumulation, and the previous studies underestimated it. To discuss dust accumulating process precisely, it is necessary to revise the often-used equations with the dust diffusion term.

When dust grains are so small that their stopping time satisfies $\tau_s = t_{\text{stop}}\Omega \ll 1$, dust diffusion is mainly driven by radial friction (“kicks”) due to turbulent gas (Youdin & Lithwick 2007). In that case, specific angular momentum of dust grains remains constant during the radial displacements although they will exchange their angular momentum at a place to which they are going. Equation (2.1) is rearranged to

$$\frac{\partial\Sigma_d}{\partial t} + \frac{1}{r} \frac{\partial}{\partial r} \left[r \left(v_r - \frac{D}{\Sigma_d} \frac{\partial\Sigma_d}{\partial r} \right) \Sigma_d \right] = 0, \quad (2.9)$$

which shows that the dust advection velocity due to diffusion is $-D\Sigma_d^{-1}\partial\Sigma_d/\partial r$. Considering the advection velocity and the fact that small dust grains are displaced with their angular momentum being constant, we experimentally consider the following equation

$$\Sigma_d \left[\frac{\partial j_d}{\partial t} + \left(v_r - \frac{D}{\Sigma_d} \frac{\partial\Sigma_d}{\partial r} \right) \frac{\partial j_d}{\partial r} \right] = -r\Sigma_d \frac{v_\phi - u_\phi}{t_{\text{stop}}}, \quad (2.10)$$

where we add the advection velocity $-D\Sigma_d^{-1}\partial\Sigma_d/\partial r$ to the usual advection term. From this equation, we obtain an equation for dust angular momentum

$$\frac{\partial(\Sigma_d j_d)}{\partial t} + \frac{1}{r} \frac{\partial}{\partial r} \left[r \left(v_r - \frac{D}{\Sigma_d} \frac{\partial\Sigma_d}{\partial r} \right) \Sigma_d j_d \right] = -r\Sigma_d \frac{v_\phi - u_\phi}{t_{\text{stop}}}. \quad (2.11)$$

This equation shows that dust angular momentum changes only through friction. Using Equations (2.6) and (2.11), we can show that the total angular momentum is conserved

$$\frac{\partial}{\partial t} (\Sigma_g j_g + \Sigma_d j_d) + \frac{1}{r} \frac{\partial}{\partial r} \left[r u_r \Sigma_g j_g + r \left(v_r - \frac{D}{\Sigma_d} \frac{\partial\Sigma_d}{\partial r} \right) \Sigma_d j_d \right] = 0. \quad (2.12)$$

The above experimental discussion indicates that considering momentum advection associated with mass diffusion guarantees angular momentum conservation.

In the next section, we derive such an advection term based on the mean-field approximation.

2.2 Reformulation of basic equations from the mean-field approximation

The mean-field approximation is sometimes used to derive macroscopic equations governing evolution of mean-fields. We use the Reynolds averaging, which is one technique to analyze turbulent fluid based on averaging physical properties over a timescale longer than a typical turnover time of turbulent eddies. We decompose a physical variable A into a time-averaged term $\langle A \rangle$ and a short-term fluctuation originating from turbulence $\Delta A \equiv A - \langle A \rangle$, where $\langle \Delta A \rangle = 0$. We average the following equations for dust:

$$\frac{\partial \Sigma_d}{\partial t} + \frac{1}{r} \frac{\partial (r \Sigma_d v_r)}{\partial r} = 0, \quad (2.13)$$

$$\frac{\partial (\Sigma_d v_r)}{\partial t} + \frac{1}{r} \frac{\partial (r \Sigma_d v_r^2)}{\partial r} = \Sigma_d \frac{v_\phi^2}{r} - \Sigma_d \frac{\partial}{\partial r} \left(\Phi - \frac{GM_*}{r} \right) - \Sigma_d \frac{v_r - u_r}{t_{\text{stop}}}, \quad (2.14)$$

$$\frac{\partial (\Sigma_d v_\phi)}{\partial t} + \frac{1}{r} \frac{\partial (r \Sigma_d v_\phi v_r)}{\partial r} = -\Sigma_d \frac{v_\phi v_r}{r} - \Sigma_d \frac{v_\phi - u_\phi}{t_{\text{stop}}}. \quad (2.15)$$

Substituting $\Sigma_d = \langle \Sigma_d \rangle + \Delta \Sigma_d$ and $v_r = \langle v_r \rangle + \Delta v_r$ to Equation (2.13) and averaging both side of the equation in time, we obtain an equation for the mean density:

$$\frac{\partial \langle \Sigma_d \rangle}{\partial t} + \frac{1}{r} \frac{\partial (r \langle \Sigma_d \rangle \langle v_r \rangle)}{\partial r} = -\frac{1}{r} \frac{\partial (r \langle \Delta \Sigma_d \Delta v_r \rangle)}{\partial r}. \quad (2.16)$$

We model the term $\langle \Delta \Sigma_d \Delta v_i \rangle$ based on the “gradient diffusion hypothesis” (see Cuzzi et al. 1993):

$$\langle \Delta \Sigma_d \Delta v_r \rangle = -D \frac{\partial \langle \Sigma_d \rangle}{\partial r}, \quad (2.17)$$

$$\langle \Delta \Sigma_d \Delta v_\phi \rangle = -\frac{D}{r} \frac{\partial \langle \Sigma_d \rangle}{\partial \phi} = 0. \quad (2.18)$$

In the last equality of Equation (2.18), we make use of the assumption of axisymmetric disks. Finally, we obtain the Reynolds-averaged continuity equation

$$\frac{\partial \langle \Sigma_d \rangle}{\partial t} + \frac{1}{r} \frac{\partial (r \langle \Sigma_d \rangle \langle v_r \rangle)}{\partial r} = \frac{1}{r} \frac{\partial}{\partial r} \left(r D \frac{\partial \langle \Sigma_d \rangle}{\partial r} \right). \quad (2.19)$$

This equation is equivalent to Equation (2.1).

In the same way, we obtain equations for mean velocity fields averaging Equations

2.2. REFORMULATION OF BASIC EQUATIONS FROM THE MEAN-FIELD APPROXIMATION

(2.14) and (2.15)

$$\begin{aligned}
& \frac{\partial (\langle \Sigma_d \rangle \langle v_r \rangle)}{\partial t} + \frac{1}{r} \frac{\partial}{\partial r} \left[r \langle \Sigma_d \rangle \left(\langle v_r \rangle - \frac{D}{\langle \Sigma_d \rangle} \frac{\partial \langle \Sigma_d \rangle}{\partial r} \right) \langle v_r \rangle \right] \\
&= \langle \Sigma_d \rangle \frac{\langle v_\phi \rangle^2}{r} - \langle \Sigma_d \rangle \frac{\partial}{\partial r} \left(\langle \Phi \rangle - \frac{GM_*}{r} \right) - \left\langle \Delta \Sigma_d \frac{\partial \Delta \Phi}{\partial r} \right\rangle - \langle \Sigma_d \rangle \frac{\langle v_r \rangle - \langle u_r \rangle}{t_{\text{stop}}} \\
&+ \frac{1}{r} \frac{\partial (r \sigma_{rr})}{\partial r} - \frac{\sigma_{\phi\phi}}{r} \\
&+ \frac{\partial}{\partial t} \left(D \frac{\partial \langle \Sigma_d \rangle}{\partial r} \right) + \frac{1}{r} \frac{\partial}{\partial r} \left(r \langle v_r \rangle D \frac{\partial \langle \Sigma_d \rangle}{\partial r} \right) - \frac{\langle \Delta \Sigma_d (\Delta v_r - \Delta u_r) \rangle}{t_{\text{stop}}}, \quad (2.20)
\end{aligned}$$

$$\begin{aligned}
& \frac{\partial (\langle \Sigma_d \rangle \langle v_\phi \rangle)}{\partial t} + \frac{1}{r} \frac{\partial}{\partial r} \left[r \langle \Sigma_d \rangle \left(\langle v_r \rangle - \frac{D}{\langle \Sigma_d \rangle} \frac{\partial \langle \Sigma_d \rangle}{\partial r} \right) \langle v_\phi \rangle \right] \\
&= - \frac{\langle \Sigma_d \rangle \langle v_\phi \rangle}{r} \left(\langle v_r \rangle - \frac{D}{\langle \Sigma_d \rangle} \frac{\partial \langle \Sigma_d \rangle}{\partial r} \right) - \langle \Sigma_d \rangle \frac{\langle v_\phi \rangle - \langle u_\phi \rangle}{t_{\text{stop}}} \\
&+ \frac{1}{r} \frac{\partial (r \sigma_{r\phi})}{\partial r} + \frac{\sigma_{r\phi}}{r} - \frac{\langle \Delta \Sigma_d (\Delta v_\phi - \Delta u_\phi) \rangle}{t_{\text{stop}}}. \quad (2.21)
\end{aligned}$$

where

$$\sigma_{rr} \equiv - \langle \Sigma_d \rangle \langle \Delta v_r^2 \rangle - \langle \Delta \Sigma_d \Delta v_r^2 \rangle, \quad (2.22)$$

$$\sigma_{r\phi} \equiv - \langle \Sigma_d \rangle \langle \Delta v_r \Delta v_\phi \rangle - \langle \Delta \Sigma_d \Delta v_r \Delta v_\phi \rangle, \quad (2.23)$$

$$\sigma_{\phi\phi} \equiv - \langle \Sigma_d \rangle \langle \Delta v_\phi^2 \rangle - \langle \Delta \Sigma_d \Delta v_\phi^2 \rangle, \quad (2.24)$$

represent the so-called Reynolds stress. Using a closure relation $\langle \Delta v_r^2 \rangle = \langle \Delta v_\phi^2 \rangle = c_d^2$ adopted in Shariff & Cuzzi (2011), we obtain the effective pressure gradient force as follows:

$$\frac{1}{r} \frac{\partial (r \sigma_{rr})}{\partial r} - \frac{\sigma_{\phi\phi}}{r} = - \frac{\partial (c_d^2 \langle \Sigma_d \rangle)}{\partial r} + \frac{1}{r} \frac{\partial (r \sigma'_{rr})}{\partial r} - \frac{\sigma'_{\phi\phi}}{r}, \quad (2.25)$$

$$\sigma'_{rr} \equiv - \langle \Delta \Sigma_d \Delta v_r^2 \rangle, \quad (2.26)$$

$$\sigma'_{\phi\phi} \equiv - \langle \Delta \Sigma_d \Delta v_\phi^2 \rangle. \quad (2.27)$$

In this thesis, we neglect the terms $\sigma'_{rr}, \sigma_{r\phi}, \sigma'_{\phi\phi}$ for simplicity since a closure relation on these terms is uncertain. Moreover, we only consider cases that dust grains are so small that we can assume $\Delta v_r = \Delta u_r, \Delta v_\phi = \Delta u_\phi$. Adopting these assumptions, we obtain

$$\begin{aligned}
& \frac{\partial (\langle \Sigma_d \rangle \langle v_r \rangle)}{\partial t} + \frac{1}{r} \frac{\partial}{\partial r} \left[r \langle \Sigma_d \rangle \left(\langle v_r \rangle - \frac{D}{\langle \Sigma_d \rangle} \frac{\partial \langle \Sigma_d \rangle}{\partial r} \right) \langle v_r \rangle \right] \\
&= \langle \Sigma_d \rangle \frac{\langle v_\phi \rangle^2}{r} - \frac{\partial (c_d^2 \langle \Sigma_d \rangle)}{\partial r} - \langle \Sigma_d \rangle \frac{\partial}{\partial r} \left(\langle \Phi \rangle - \frac{GM_*}{r} \right) - \left\langle \Delta \Sigma_d \frac{\partial \Delta \Phi}{\partial r} \right\rangle \\
&- \langle \Sigma_d \rangle \frac{\langle v_r \rangle - \langle u_r \rangle}{t_{\text{stop}}} + \frac{\partial}{\partial t} \left(D \frac{\partial \langle \Sigma_d \rangle}{\partial r} \right) + \frac{1}{r} \frac{\partial}{\partial r} \left(r \langle v_r \rangle D \frac{\partial \langle \Sigma_d \rangle}{\partial r} \right), \quad (2.28)
\end{aligned}$$

2.2. REFORMULATION OF BASIC EQUATIONS FROM THE MEAN-FIELD APPROXIMATION

$$\begin{aligned} \frac{\partial (\langle \Sigma_d \rangle \langle v_\phi \rangle)_t}{\partial t} + \frac{1}{r} \frac{\partial}{\partial r} \left[r \langle \Sigma_d \rangle \left(\langle v_r \rangle - \frac{D}{\langle \Sigma_d \rangle} \frac{\partial \langle \Sigma_d \rangle}{\partial r} \right) \langle v_\phi \rangle \right] \\ = - \frac{\langle \Sigma_d \rangle \langle v_\phi \rangle}{r} \left(\langle v_r \rangle - \frac{D}{\langle \Sigma_d \rangle} \frac{\partial \langle \Sigma_d \rangle}{\partial r} \right) - \langle \Sigma_d \rangle \frac{\langle v_\phi \rangle - \langle u_\phi \rangle}{t_{\text{stop}}}. \end{aligned} \quad (2.29)$$

The fourth term on the right hand side of Equation (2.28) represents a fluctuated component of self-gravity originating from density fluctuations due to turbulence. In this thesis, we assume that volume-integrated density fluctuations are so small that we can neglect the term. In addition, following Cuzzi et al. (1993), we neglect the sixth term on the right hand side assuming the term is smaller than the time derivative of $\langle \Sigma_d \rangle \langle v_r \rangle$. The seventh term represents the advection of the linear momentum $\langle \Delta \Sigma_d \Delta v_r \rangle$ with the mean velocity $\langle v_r \rangle$. This term is the same order of the advection of $\langle \Sigma_d \rangle \langle v_r \rangle$ along diffusive flow. Adopting these assumptions, we rearrange Equations (2.28) and (2.29), and obtain the following equations for the mean velocities:

$$\begin{aligned} \langle \Sigma_d \rangle \left[\frac{\partial \langle v_r \rangle}{\partial t} + \left(\langle v_r \rangle - \frac{D}{\langle \Sigma_d \rangle} \frac{\partial \langle \Sigma_d \rangle}{\partial r} \right) \frac{\partial \langle v_r \rangle}{\partial r} \right] = \langle \Sigma_d \rangle \frac{\langle v_\phi \rangle^2}{r} - \frac{\partial (c_d^2 \langle \Sigma_d \rangle)}{\partial r} \\ - \langle \Sigma_d \rangle \frac{\partial}{\partial r} \left(\langle \Phi \rangle - \frac{GM_*}{r} \right) \\ - \langle \Sigma_d \rangle \frac{\langle v_r \rangle - \langle u_r \rangle}{t_{\text{stop}}} + \frac{1}{r} \frac{\partial}{\partial r} \left(r \langle v_r \rangle D \frac{\partial \langle \Sigma_d \rangle}{\partial r} \right), \end{aligned} \quad (2.30)$$

$$\begin{aligned} \langle \Sigma_d \rangle \left[\frac{\partial \langle v_\phi \rangle}{\partial t} + \left(\langle v_r \rangle - \frac{D}{\langle \Sigma_d \rangle} \frac{\partial \langle \Sigma_d \rangle}{\partial r} \right) \frac{\partial \langle v_\phi \rangle}{\partial r} \right] = - \frac{\langle \Sigma_d \rangle \langle v_\phi \rangle}{r} \left(\langle v_r \rangle - \frac{D}{\langle \Sigma_d \rangle} \frac{\partial \langle \Sigma_d \rangle}{\partial r} \right) \\ - \langle \Sigma_d \rangle \frac{\langle v_\phi \rangle - \langle u_\phi \rangle}{t_{\text{stop}}} \end{aligned} \quad (2.31)$$

Equation (2.31) yields

$$\langle \Sigma_d \rangle \left[\frac{\partial (r \langle v_\phi \rangle)}{\partial t} + \left(\langle v_r \rangle - \frac{D}{\langle \Sigma_d \rangle} \frac{\partial \langle \Sigma_d \rangle}{\partial r} \right) \frac{\partial (r \langle v_\phi \rangle)}{\partial r} \right] = - \langle \Sigma_d \rangle r \frac{\langle v_\phi \rangle - \langle u_\phi \rangle}{t_{\text{stop}}}, \quad (2.32)$$

which is equivalent to Equation (2.10) since the mean specific angular momentum is $r \langle v_\phi \rangle$. One can also obtain an equation equivalent to Equation (2.11) using Equations (2.19) and (2.32):

$$\frac{\partial (\langle \Sigma_d \rangle r \langle v_\phi \rangle)}{\partial t} + \frac{1}{r} \frac{\partial}{\partial r} \left[r \left(\langle v_r \rangle - \frac{D}{\langle \Sigma_d \rangle} \frac{\partial \langle \Sigma_d \rangle}{\partial r} \right) \langle \Sigma_d \rangle r \langle v_\phi \rangle \right] = - r \langle \Sigma_d \rangle \frac{\langle v_\phi \rangle - \langle u_\phi \rangle}{t_{\text{stop}}}. \quad (2.33)$$

Using the gas equation (Equations (2.6)), one can derive an equation equivalent to Equation (2.12), showing total angular momentum conservation.

It is also possible to model diffusion with the following closure relation

$$\langle \Delta \Sigma_d \Delta v_r \rangle = -D \langle \Sigma_g \rangle \frac{\partial}{\partial r} \left(\frac{\langle \Sigma_d \rangle}{\langle \Sigma_g \rangle} \right), \quad (2.34)$$

which is another often-used diffusion model (e.g., Dubrulle et al. 1995). Even in this case, adopting this closure relation to the momentum equations leads to similar equations that hold momentum conservations. One can derive the equations just replacing $D \partial \langle \Sigma_d \rangle / \partial r$ in the above equations by $D \langle \Sigma_g \rangle \partial (\langle \Sigma_d \rangle / \langle \Sigma_g \rangle) / \partial r$.

In subsequent parts of this thesis, we use the reformulated equations for dust but omit the brackets representing the averaged value for convenience.

2.3 Linear analyses

To investigate to what extent the revised equations affect dust dynamics, we perform linear analyses of secular GI and compare the previous studies.

2.3.1 Basic equations

We summarize a set of basic equations including the newly formulated dust equations. We use the following equations for gas and the Poisson equation, which were also used in Takahashi & Inutsuka (2014 2016):

$$\frac{\partial \Sigma_g}{\partial t} + \frac{1}{r} \frac{\partial (r \Sigma_g u_r)}{\partial r} = 0, \quad (2.4)$$

$$\begin{aligned} \Sigma_g \left(\frac{\partial u_i}{\partial t} + u_j \frac{\partial u_i}{\partial x_j} \right) &= -c_s^2 \frac{\partial \Sigma_g}{\partial x_i} - \Sigma_g \frac{\partial}{\partial x_i} \left(\Phi - \frac{GM_*}{r} \right) \\ &+ \frac{\partial}{\partial x_j} \left[\Sigma_g \nu \left(\frac{\partial u_i}{\partial x_j} + \frac{\partial u_j}{\partial x_i} - \frac{2}{3} \delta_{ij} \frac{\partial u_k}{\partial x_k} \right) \right] + \Sigma_d \frac{v_i - u_i}{t_{\text{stop}}}, \end{aligned} \quad (2.35)$$

$$\nabla^2 \Phi = 4\pi G (\Sigma_g + \Sigma_d) \delta(z), \quad (2.36)$$

where u_i, v_i are the i -th component of gas and dust velocities, and Φ is the gravitational potential of the dust-gas disk, respectively. The third term on the right hand side of Equation (2.35) is turbulent viscosity with viscosity coefficient $\nu = \alpha c_s H$ (Shakura & Sunyaev 1973).

The reformulated dust equations with dust diffusion are summarized as follows:

$$\frac{\partial \Sigma_d}{\partial t} + \frac{1}{r} \frac{\partial (r \Sigma_d v_r)}{\partial r} = \frac{1}{r} \frac{\partial}{\partial r} \left(r D \frac{\partial \Sigma_d}{\partial r} \right), \quad (2.1)$$

$$\begin{aligned} \Sigma_d \left[\frac{\partial v_r}{\partial t} + \left(v_r - \frac{D}{\Sigma_d} \frac{\partial \Sigma_d}{\partial r} \right) \frac{\partial v_r}{\partial r} \right] &= \Sigma_d \frac{v_\phi^2}{r} - c_d^2 \frac{\partial \Sigma_d}{\partial r} - \Sigma_d \frac{\partial}{\partial r} \left(\Phi - \frac{GM_*}{r} \right) \\ &\quad - \Sigma_d \frac{v_r - u_r}{t_{\text{stop}}} + \frac{1}{r} \frac{\partial}{\partial r} \left(r v_r D \frac{\partial \Sigma_d}{\partial r} \right), \end{aligned} \quad (2.37)$$

$$\Sigma_d \left[\frac{\partial v_\phi}{\partial t} + \left(v_r - \frac{D}{\Sigma_d} \frac{\partial \Sigma_d}{\partial r} \right) \frac{\partial v_\phi}{\partial r} \right] = -\Sigma_d \frac{v_\phi}{r} \left(v_r - \frac{D}{\Sigma_d} \frac{\partial \Sigma_d}{\partial r} \right) - \Sigma_d \frac{v_\phi - u_\phi}{t_{\text{stop}}}, \quad (2.38)$$

We again note that we omit the brackets representing the averaged value for convenience.

We investigate mode properties in the local shearing sheet (x, y) . In the local frame, the above continuity equations and the equations of motion yield

$$\frac{\partial \Sigma_g}{\partial t} + \frac{\partial \Sigma_g u_x}{\partial x} = 0, \quad (2.39)$$

$$\frac{\partial u_x}{\partial t} + u_x \frac{\partial u_x}{\partial x} = 3\Omega^2 x + 2\Omega u_y - \frac{c_s^2}{\Sigma_g} \frac{\partial \Sigma_g}{\partial x} - \frac{\partial \Phi}{\partial x} + \frac{1}{\Sigma_g} \frac{\partial}{\partial x} \left(\Sigma_g \nu \frac{4}{3} \frac{\partial u_x}{\partial x} \right) + \frac{\Sigma_d}{\Sigma_g} \frac{v_x - u_x}{t_{\text{stop}}}, \quad (2.40)$$

$$\frac{\partial u_y}{\partial t} + u_x \frac{\partial u_y}{\partial x} = -2\Omega u_x + \frac{\partial}{\partial x} \left(\Sigma_g \nu \frac{\partial u_y}{\partial x} \right) + \frac{\Sigma_d}{\Sigma_g} \frac{v_y - u_y}{t_{\text{stop}}}, \quad (2.41)$$

$$\frac{\partial \Sigma_d}{\partial t} + \frac{\partial \Sigma_d v_x}{\partial x} = \frac{\partial}{\partial x} \left(D \frac{\partial \Sigma_d}{\partial x} \right), \quad (2.42)$$

$$\frac{\partial v_x}{\partial t} + v_x \frac{\partial v_x}{\partial x} = 3\Omega^2 x + 2\Omega v_y - \frac{c_d^2}{\Sigma_d} \frac{\partial \Sigma_d}{\partial x} - \frac{\partial \Phi}{\partial x} - \frac{v_x - u_x}{t_{\text{stop}}}, \quad (2.43)$$

$$\frac{\partial v_y}{\partial t} + v_x \frac{\partial v_y}{\partial x} = -2\Omega v_x - \frac{v_y - u_y}{t_{\text{stop}}}. \quad (2.44)$$

Solving the above equations corresponds to an eigenvalue problem. We derive a dispersion relation ($n = n(k)$) under the condition that the eigenfunctions are nontrivial.

2.3.2 Linearized equations

We choose an unperturbed state with uniform surface densities and radial velocities of $u_{x,0} = v_{x,0} = 0$, where subscripts “0” represent unperturbed state values. The Keplerian rotational velocities $u_{y,0} = v_{y,0} = -3\Omega x/2$ satisfy the steady condition with the above basic equations.

Considering axisymmetric perturbations $\delta\Sigma, \delta\Sigma_d, \delta u_x, \delta u_y, \delta v_x, \delta v_y, \delta\Phi$ proportional to $\exp[nt + ikx]$, we linearize Equations (2.36) and (2.39)-(2.44) and obtain the following linearized equations

$$n\delta\Sigma_g + ik\Sigma_{g,0}\delta u_x = 0, \quad (2.45)$$

$$n\delta u_x = 2\Omega\delta u_y - \frac{c_s^2}{\Sigma_{g,0}} ik\delta\Sigma_g - ik\delta\Phi - \frac{4}{3}\nu k^2\delta u_x + \varepsilon \frac{\delta v_x - \delta u_x}{t_{\text{stop}}}, \quad (2.46)$$

$$n\delta u_y = -\frac{\Omega}{2}\delta u_x - \nu k^2\delta u_y - ik\frac{3\nu\Omega}{2\Sigma_{g,0}}\delta\Sigma + \varepsilon\frac{\delta v_y - \delta u_y}{t_{\text{stop}}}, \quad (2.47)$$

$$n\delta\Sigma_d + ik\Sigma_{d,0}\delta v_x = -Dk^2\delta\Sigma_d, \quad (2.48)$$

$$n\delta v_x = 2\Omega\delta v_y - \frac{c_d^2}{\Sigma_{d,0}}ik\delta\Sigma_d - ik\delta\Phi - \frac{\delta v_x - \delta u_x}{t_{\text{stop}}}, \quad (2.49)$$

$$n\delta v_y = -\frac{\Omega}{2}\left(\delta v_x - \frac{ikD}{\Sigma_{d,0}}\delta\Sigma_d\right) - \frac{\delta v_y - \delta u_y}{t_{\text{stop}}}, \quad (2.50)$$

$$\delta\Phi = -\frac{2\pi G}{k}(\delta\Sigma_g + \delta\Sigma_d), \quad (2.51)$$

where $\varepsilon \equiv \Sigma_{d,0}/\Sigma_{g,0}$ is the dust-to-gas mass ratio.

2.3.3 Results

In this section, we present linear analyses and results with and without the turbulent viscosity separately. In both cases, there are six modes in the system considered because the basic equations include six time-derivatives. In the absence of the dust-gas friction, the dust diffusion and the turbulent gas viscosity, there are two density waves for dust and gas disks respectively, and two static modes. A static mode is a steady solution of linearized equations. Figure 2.1 shows how the six modes change by adding three physical processes step by step and which mode becomes unstable. As shown in Figure 2.1, the two static modes become unstable, which we will explain in more detail.

Without turbulent viscosity

In the absence of turbulent viscosity, we find one static mode ($n = 0$) and one unstable mode (the modes B' and C in Figure 2.1) besides four density waves. The static mode is a perturbed state where dust has the same azimuthal velocity with gas, and the radial force balance holds. The latter mode corresponds to the secular GI.

Adopting the terminal velocity approximation ($t_{\text{stop}} \ll n^{-1}$) and assuming $t_{\text{stop}} \ll \Omega^{-1} \ll n^{-1}$, we obtain the following approximate dispersion relation of the secular GI:

$$A_1 n + A_0 = 0, \quad (2.52)$$

$$A_1 \equiv \left\{ \Omega^2 + \left(\frac{1 + \varepsilon}{t_{\text{stop}}} \right)^2 \right\} \omega_{\text{gd}}^2 + \frac{\varepsilon D k^2}{t_{\text{stop}}} c_s^2 k^2, \quad (2.53)$$

$$A_0 \equiv \frac{\omega_g^2}{1 + \varepsilon} \left\{ \left(\frac{1 + \varepsilon}{t_{\text{stop}}} \right)^2 D k^2 + \frac{1 + \varepsilon}{t_{\text{stop}}} c_d^2 k^2 \right\} + \omega_d^2 \frac{\varepsilon c_s^2 k^2}{t_{\text{stop}}}, \quad (2.54)$$

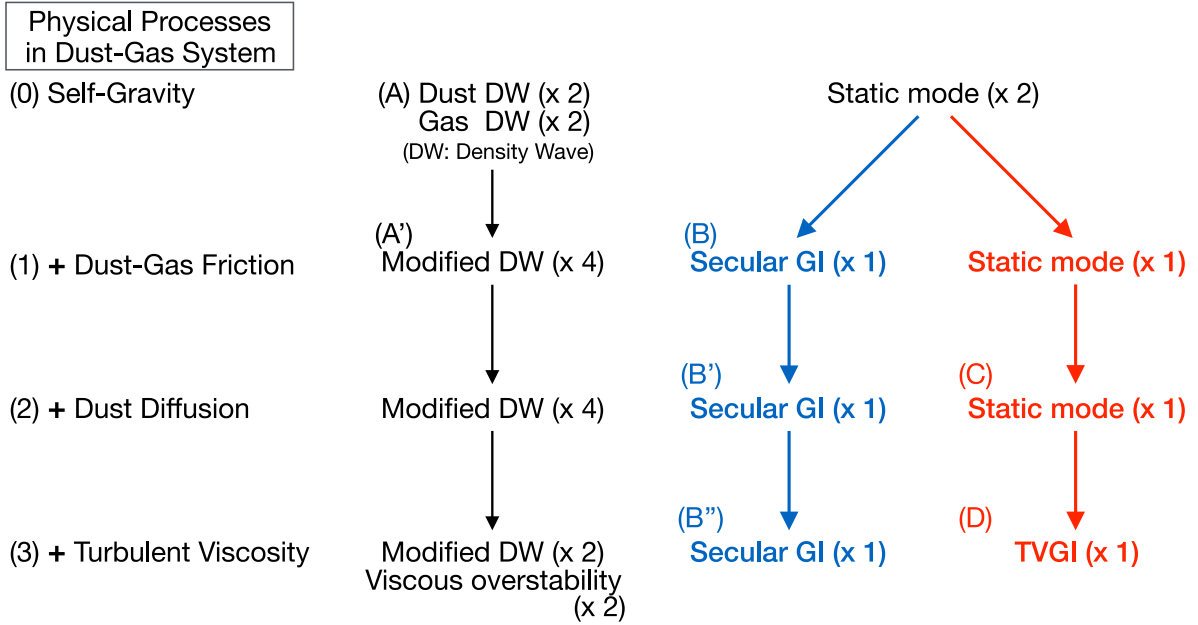


Figure 2.1: A schematic diagram showing mode classes. There are six modes in our analysis: four density waves and unstable mode stemming from independent static modes. The modes on the top line are those obtained in the absence of friction, dust diffusion, and turbulent gas viscosity. (Step 1, the second line) The friction couples the dust and gas density waves, resulting in modified density waves (DWs, the mode A'). The modified density waves become unstable when self-gravity is large enough, which are referred to as the classical GI. One of the static modes becomes secular GI because of friction (the mode B). (Step 2, the third line) The dust diffusion does not qualitatively change properties of those six modes although growth rates for each mode change. (Step 3, the bottom line) The turbulent viscosity destabilizes the remaining static mode (the mode D). This destabilized static mode is referred to as two-component viscous gravitational instability (TVGI). Two of the modified DWs become viscous overstable modes. This figure is originally from Figure 1 of the published paper, Tominaga et al. (2019).

2.3. LINEAR ANALYSES

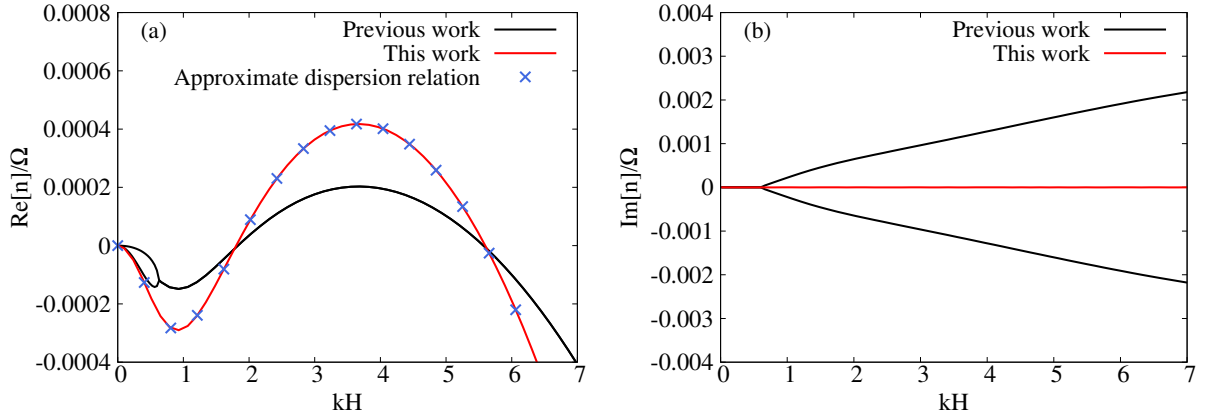


Figure 2.2: Growth rate (left) and frequency (right) of secular GI for $D = 10^{-4}c_s^2\Omega^{-1}$, $c_d = 0$, $\epsilon = 0.1$, $\tau_s = 0.01$, $Q = 3$ as a function of dimensionless wavenumber kH . The vertical axis of the both panels is normalized by the Keplerian frequency Ω . The black line is the dispersion relation obtained in the previous work (Takahashi & Inutsuka 2014; Latter & Rosca 2017), while the red line shows the results of the present analysis. The blue cross mark on the left panel is growth rates obtained from Equation (2.52). The imaginary part $\text{Im}[n]$ is zero for the secular GI mode obtained in our analysis in contrast to the previous work. This figure is originally from Figure 2 of the published paper, Tominaga et al. (2019).

where

$$\omega_{\text{gd}}^2 \equiv \Omega^2 + \frac{c_s^2 + \epsilon c_d^2}{1 + \epsilon} k^2 - 2\pi G (1 + \epsilon) \Sigma_{\text{g},0} k, \quad (2.55)$$

$$\omega_{\text{g}}^2 \equiv \Omega^2 + c_s^2 k^2 - 2\pi G (1 + \epsilon) \Sigma_{\text{g},0} k, \quad (2.56)$$

$$\omega_{\text{d}}^2 \equiv \Omega^2 + c_d^2 k^2 - 2\pi G (1 + \epsilon) \Sigma_{\text{g},0} k. \quad (2.57)$$

Figure 2.2 compares the dispersion relations of secular GI obtained in the present analyses and the previous work (Takahashi & Inutsuka 2014) for $D = 10^{-4}c_s^2\Omega^{-1}$, $c_d = 0$, $\epsilon = 0.1$, $\tau_s \equiv t_{\text{stop}}\Omega = 0.01$, and Toomre's Q value for gas

$$Q \equiv \frac{c_s \Omega}{\pi G \Sigma_{\text{g},0}} \quad (2.58)$$

is set to be 3. As in Takahashi & Inutsuka (2014), secular GI obtained in this work is also stabilized at long wavelengths by the Coriolis force exerted on dust. In contrast, short wavelength perturbations are stabilized by turbulent diffusion. At intermediate wavelengths where secular GI is unstable, the gas pressure gradient force dominates the Coriolis force exerted on gas. As a result, an azimuthal zonal flow form (see, Latter & Rosca 2017), and dust accumulates by the self-gravity of itself. The growth rate of secular GI obtained in the present analyses is several times larger than that obtained in

the previous work. The most remarkable difference is that secular GI is a monotonically growing mode in the present analyses while it is an overstable mode in the previous studies (Takahashi & Inutsuka 2014; Latter & Rosca 2017). This shows that the overstability in the previous work originate from the unphysical torque acting on dust (Equation (2.3)).

We derive an approximate unstable condition of the secular GI from Equation (2.52). The condition is that at least two solutions for $n = 0$ exist in a region $k > 0$. This is equivalent to the condition that $A_0/k^2 = 0$ has two distinct positive real solutions. We then obtain the following approximate unstable condition:

$$\frac{Q^2 (t_{\text{stop}} c_d^2 + D)}{(1 + \varepsilon) [t_{\text{stop}} (\varepsilon c_s^2 + c_d^2) + D (1 + \varepsilon)]} < 1. \quad (2.59)$$

Equation (2.59) is equivalent to the condition derived in Latter & Rosca (2017) in the case of $D = 0$ (see Equation (43) in their paper). If we assume $c_d = 0$ and $(1 + \varepsilon)D \ll \varepsilon c_s^2 t_{\text{stop}}$, Equation (2.59) yields

$$Q < \sqrt{\frac{\varepsilon (1 + \varepsilon) t_{\text{stop}} c_s^2}{D}}. \quad (2.60)$$

Equation (2.60) is equivalent to Equation (50) in Latter & Rosca (2017) for $(1 + \varepsilon)D \ll \varepsilon c_s^2 t_{\text{stop}}$. Thus, our formulation does not change the condition for secular GI if D is so small that $(1 + \varepsilon)D \ll \varepsilon c_s^2 t_{\text{stop}}$ is satisfied.

We find mode exchange between secular GI and dust GI at $k = k_{c,-}, k_{c,+}$ where the growth rate of dust GI becomes zero (Figure 2.3). Mode exchange is reconnection of curves in the $k - n$ plane of dispersion relations for two different modes. Youdin (2011) also found the mode exchange even in the one-fluid linear analyses (see Figure 10 therein). To distinguish the different mode on the same branch of the dispersion relation, we designate the growing mode in the limited range of wavenumbers where dust GI remains unstable even for $t_{\text{stop}} \rightarrow \infty$ as ‘‘dust GI’’. On the other hand, we designate the growing mode in the disconnected curves in the regions of wavenumbers where dust GI is stable for $t_{\text{stop}} \rightarrow \infty$ as ‘‘secular GI’’.

Figure 2.4 shows the maximum growth rate of secular GI and dust GI as a function of τ_s and α for $\varepsilon = 0.1$, $Q = 3$. To plot this figure, we use Equations (1.27) and (1.28) for the diffusion coefficient D and the velocity dispersion c_d . The short-dashed line in Figure 2.4 represents the approximated maximum value of α for the growth of secular GI, which is obtained from Equation (2.59). The exact upper limit of α is well represented by Equation (2.59). Secular GI is the fastest growing mode in the colored region above the long-dashed line, while dust GI grows faster in the region below the long-dashed line. On the long-dashed line, the most unstable wavelengths are $k_{c,-}$. Dust GI becomes the

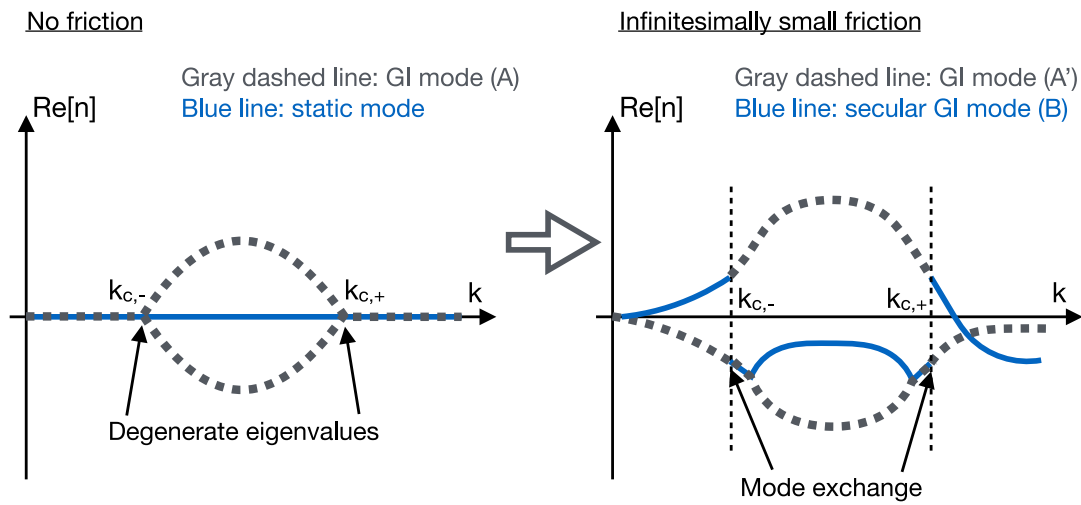


Figure 2.3: Schematic picture of mode exchange between secular GI and dust GI. The left figure shows the dispersion relations of the static mode and dust GI in the absence of friction. The right figure shows the dispersion relations obtained with friction. The gray dashed line represents a growth rate of the dust GI mode, and the blue solid line is that of the static mode or secular GI. The labels (A), (A') and (B) shown in the legends correspond to the labels shown in Figure 2.1. The mode exchange occurs at wavelengths where the eigenvalue and eigenfunction degenerate in the absence of friction. This figure is originally from Figure 3 of the published paper, Tominaga et al. (2019).

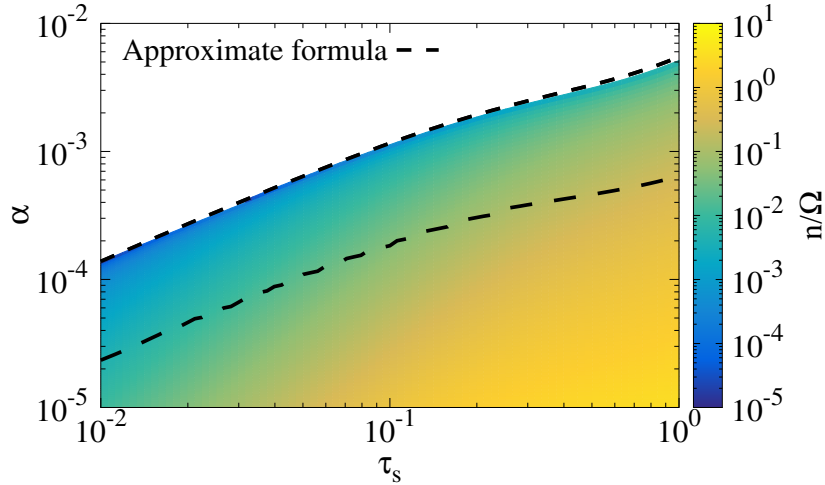


Figure 2.4: Maximum growth rate of secular GI and dust GI for $\varepsilon = 0.1$ and $Q = 3$ as a function of dimensionless stopping time τ_s and strength of turbulence α . The color represents the growth rate normalized by the Keplerian angular velocity Ω . We note that $\text{Im}[n]$ is zero in the whole parameter space. The short-dashed line represents the approximate condition for the instability (Equation (2.59)). Dust GI is the most unstable mode below the long-dashed line. In the colored region above the long-dashed line, secular GI is the fastest growing mode. Both instabilities are stable in the white region. This figure is originally from Figure 4 of the published paper, Tominaga et al. (2019).

fastest growing mode for smaller α cases since effects of the diffusion and the velocity dispersion is smaller.

With turbulent viscosity

Next, we show the linear stability in the presence of turbulent viscosity exerted on the gas (Step 3 in Figure 2.1). In this case, we find a new instability that is different from secular GI. We name this new instability “two-component viscous gravitational instability (TVGI)”. TVGI originates from the static mode that appears in the absence of turbulent viscosity (the mode labeled (C) in Figure 2.1). The static mode is a steady solution where gas and dust have the same azimuthal velocity ($\delta u_y = \delta v_y$). In this steady state, the radial force balance is maintained mainly by self-gravity and the Coriolis force, that is, $2\Omega\delta u_y - ik\delta\Phi = 2\Omega\delta v_y - ik\delta\Phi \simeq 0$. This radial force balance is not realized once turbulent viscosity is taken into account. The viscosity decreases δu_y , resulting in the azimuthal relative motion between dust and gas. Since dust is interacting with gas through friction, the azimuthal velocity perturbation δv_y also decreases. The decrease of both δu_y and δv_y breaks the radial force balance, and thus both dust and gas accumulate

2.3. LINEAR ANALYSES

by the self-gravity. This is the physical interpretation of TVGI. The decrease of the Coriolis force due to both viscosity and friction is important for the growth of TVGI. In the absence of friction, this unstable mode becomes a static mode that satisfies the radial force balance for both components and

$$\delta u_x = 0, \quad (2.61)$$

$$-\nu k^2 \delta u_y - ik \frac{3\nu\Omega}{2\Sigma_{g,0}} \delta \Sigma_g = 0, \quad (2.62)$$

$$\delta v_x - \frac{ikD}{\Sigma_{d,0}} \delta \Sigma_d = 0. \quad (2.63)$$

This indicates that TVGI is different from the so-called viscous instability, which grows even in the one-fluid system and does not require friction (e.g., Lynden-Bell & Pringle 1974; Schmit & Tscharnuter 1995; Gammie 1996; Lin & Kratter 2016).

Adopting the terminal velocity approximation and assuming $t_{\text{stop}} \ll \Omega^{-1} \ll n^{-1}$, we derive the reduced dispersion relation as a quadratic function of n :

$$B_2 n^2 + B_1 n + B_0 = 0, \quad (2.64)$$

$$\begin{aligned} B_2 \equiv & \left\{ \Omega^2 + \left(\frac{1+\varepsilon}{t_{\text{stop}}} \right)^2 \right\} \omega_{\text{gd}}^2 + \frac{\varepsilon D k^2}{t_{\text{stop}}} c_s^2 k^2 \\ & + \frac{\nu k^2}{(1+\varepsilon)^2} \left[\frac{(1+\varepsilon)^2}{t_{\text{stop}}} \varepsilon \omega_{\text{gd}}^2 + \varepsilon D k^2 \{ 3(1+\varepsilon) \Omega^2 + \varepsilon c_s^2 k^2 \} \right. \\ & \left. + \frac{(1+\varepsilon)^3}{t_{\text{stop}}^2} D k^2 + \frac{1+\varepsilon}{t_{\text{stop}}} (c_d^2 + \varepsilon c_s^2) k^2 \right] \\ & + \frac{4\nu k^2}{3} \frac{1+\varepsilon}{t_{\text{stop}}} \left(\frac{D k^2}{t_{\text{stop}}} + \frac{\varepsilon \Omega^2}{1+\varepsilon} + c_d^2 k^2 - 2\pi G \varepsilon \Sigma_{g,0} k \right), \end{aligned} \quad (2.65)$$

$$\begin{aligned} B_1 \equiv & \frac{\omega_g^2}{1+\varepsilon} \left\{ \left(\frac{1+\varepsilon}{t_{\text{stop}}} \right)^2 D k^2 + \frac{1+\varepsilon}{t_{\text{stop}}} c_d^2 k^2 + \varepsilon \nu k^2 \left(2\pi G \Sigma_{g,0} k + \frac{D k^2}{t_{\text{stop}}} \right) \right\} \\ & + \frac{\varepsilon \omega_d^2}{1+\varepsilon} \left\{ \frac{1+\varepsilon}{t_{\text{stop}}} c_s^2 k^2 + \nu k^2 (3\Omega^2 + c_s^2 k^2 - 2\pi G \Sigma_{g,0} k) \right\} \\ & + \frac{\varepsilon \nu k^2}{(1+\varepsilon) t_{\text{stop}}} \left\{ \frac{1+\varepsilon}{t_{\text{stop}}} (c_d^2 - c_s^2) k^2 + D k^2 (c_s^2 k^2 - \Omega^2) \right\} \\ & + \frac{\nu k^2}{1+\varepsilon} \left\{ \Omega^2 + \left(\frac{1+\varepsilon}{t_{\text{stop}}} \right)^2 \right\} \{ 3\Omega^2 + c_s^2 k^2 - 2\pi G (1+\varepsilon) \Sigma_{g,0} k \}, \end{aligned} \quad (2.66)$$

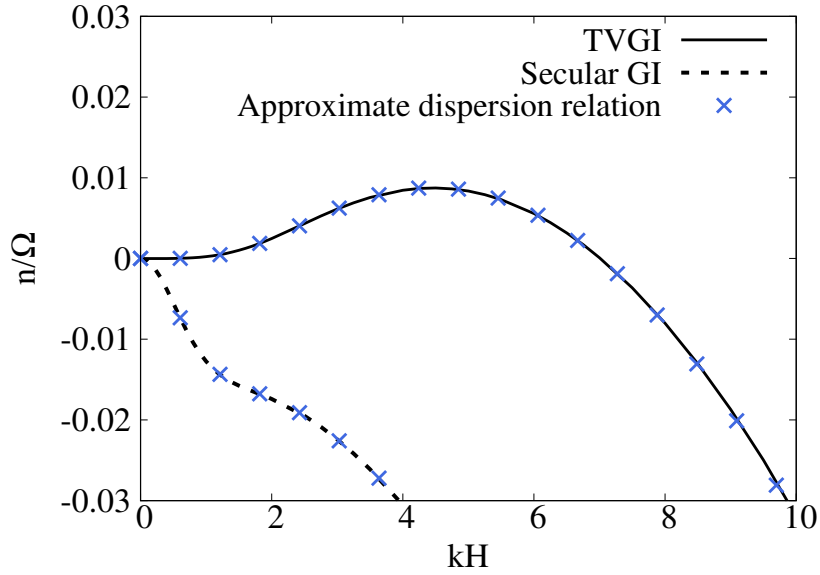


Figure 2.5: Growth rates $\text{Re}[n]/\Omega$ of TVGI and secular GI for $\alpha = 10^{-3}$, $\varepsilon = 0.1$, $\tau_s = 0.3$ and $Q = 5$ as a function of dimensionless wavenumbers kH . The solid and dashed lines represent the dispersion relation of TVGI and secular GI, respectively. The blue cross mark represents the approximated growth rates obtained from Equation (2.64). In this case, the secular GI is stable.

$$\begin{aligned}
 B_0 \equiv & \frac{\nu k^2}{1 + \epsilon} \left\{ \left(\frac{1 + \epsilon}{t_{\text{stop}}} \right)^2 Dk^2 + \frac{1 + \epsilon}{t_{\text{stop}}} c_d^2 k^2 \right\} (3\Omega^2 + c_s^2 k^2 - 2\pi G \Sigma_{g,0} k) \\
 & - \nu k^2 \frac{\epsilon c_s^2 k^2}{t_{\text{stop}}} \left(2\pi G \Sigma_{g,0} k + \frac{Dk^2}{t_{\text{stop}}} \right). \quad (2.67)
 \end{aligned}$$

When reducing the dispersion relation, we neglected the second and higher order terms of νk^2 assuming weak turbulence ($\alpha \ll 1$). Equation (2.64) yields growth rates of two modes: secular GI and TVGI. In fact, the solutions of Equation (2.64) gives the static mode ($n = 0$) and the growth rate of secular GI (Equation (2.52)) in the absence of turbulent viscosity ($\nu = 0$).

Figure 2.5 shows the dispersion relations of TVGI and secular GI for $\alpha = 10^{-3}$, $\varepsilon = 0.1$, $\tau_s = 0.3$ and $Q = 5$. For those parameters, secular GI is stable, and only TVGI is unstable. Note that n is real for both TVGI and secular GI, and thus they are not oscillating modes. The growth rate of TVGI is very small at long wavelengths because the angular momentum transport via turbulent viscosity becomes ineffective as k decreases.

We derive the condition for the growth of TVGI from the approximate dispersion relation (Equation (2.64)). We consider a case where secular GI is stable and also assume

2.3. LINEAR ANALYSES

that a disk is self-gravitationally stable and $\omega_{\text{gd}}^2 > 0$, that is,

$$\frac{(1 + \varepsilon)^{3/2}}{\sqrt{1 + \varepsilon (c_d/c_s)^2}} < Q. \quad (2.68)$$

For $\omega_{\text{gd}}^2 > 0$ and weak turbulence that satisfies $\varepsilon \nu k^2 / t_{\text{stop}} \ll \Omega^2$, one finds $B_2 > 0$. In such a case, the unstable condition is that Equation (2.64) has one negative solution and one positive solution for a certain wavenumber k . This is equivalent to the condition for wavenumbers satisfying $B_0 < 0$ to exist. From Equation (2.67), we obtain the following quadratic equation for $k > 0$:

$$\frac{B_0 t_{\text{stop}}}{\nu k^4} = 3 \left(\frac{1 + \varepsilon}{t_{\text{stop}}} D + c_d^2 \right) \Omega^2 - 2\pi G \Sigma_{\text{g},0} \left(\frac{1 + \varepsilon}{t_{\text{stop}}} D + c_d^2 + \varepsilon c_s^2 \right) k + \left(\frac{D}{t_{\text{stop}}} + c_d^2 \right) c_s^2 k^2. \quad (2.69)$$

Thus, such wavelengths exist if the discriminant of the right hand side of Equation (2.69) is positive. We then find the following condition for the instability:

$$\frac{3Q^2 (t_{\text{stop}} c_d^2 + D) [t_{\text{stop}} c_d^2 + (1 + \varepsilon) D]}{[t_{\text{stop}} (c_d^2 + \varepsilon c_s^2) + (1 + \varepsilon) D]^2} < 1. \quad (2.70)$$

The left hand side of Equation (2.70) is independent from ν . This is partly because we assume weak turbulence. Another reason is that infinitesimally small viscosity is enough for TVGI. Leaving the lading term in Equation (2.70) under the assumptions of $\alpha \ll \tau_s \ll 1$ and $c_d^2/c_s^2 \sim D\Omega/c_s^2 \sim \alpha$ gives

$$3(1 + \varepsilon) \left(\frac{QD}{\varepsilon t_{\text{stop}} c_s^2} \right)^2 \lesssim 1, \quad (2.71)$$

or

$$(t_{\text{stop}} \pi G \Sigma_{\text{g},0} H^{-1})^{-1} \lesssim \frac{(DH^{-2})^{-1}}{\sqrt{3(1 + \varepsilon)}}. \quad (2.72)$$

The left hand side of Equation (2.72) represents a timescale at which dust grains travel across a length of $H = c_s \Omega^{-1}$ with the terminal velocity. The right hand side represents a diffusion timescale of dust surface density perturbation with the length scale $\sim H$. Thus, Equation (2.70) represents that TVGI can grow if dust grains can accumulate with the terminal velocity overcoming turbulent diffusion. This physical picture is analogous to that of the one-component secular GI discussed in Youdin (2011).

We can also estimate the most unstable wavelength if the higher order terms of νk^2 are negligibly small. The growth rate of TVGI is also small since its growth is determined by the efficiency of viscous angular momentum transport. Hence, the growth

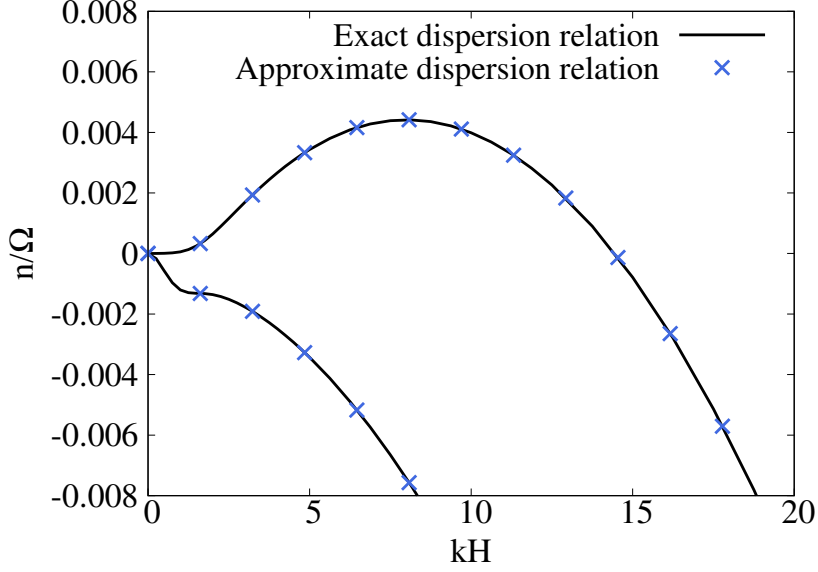


Figure 2.6: Growth rates $\text{Re}[n]/\Omega$ of TVGI and secular GI for $\alpha = 10^{-4}$, $\varepsilon = 0.1$, $\tau_s = 0.03$ and $Q = 4$ as a function of dimensionless wavenumbers kH . The solid lines show the exact dispersion relations. The blue cross mark is the approximated growth rates (Equation (2.64)). In this case, both TVGI and the secular GI grow. This figure is originally from Figure 6 of the published paper, Tominaga et al. (2019).

rate is approximately given by $-B_0/B_1$ (see Equation (2.64)). Neglecting the higher order terms of νk^2 , we obtain the reduced growth rate:

$$n \simeq -\nu k^2 \frac{3\Omega^2 D(1+\varepsilon) - 2\pi G \Sigma_{g,0} \{t_{\text{stop}} \varepsilon c_s^2 + D(1+\varepsilon)\} k + D c_s^2 k^2}{\{t_{\text{stop}} \varepsilon c_s^2 + D(1+\varepsilon)\} \Omega^2 - 2\pi G(1+\varepsilon) \Sigma_{g,0} \{t_{\text{stop}} \varepsilon c_s^2 + D(1+\varepsilon)\} k + D(1+\varepsilon) c_s^2 k^2} \quad (2.73)$$

Here, we neglect $c_d^2 k^2$ since this term has a smaller effect to stabilize TVGI than dust diffusion. The most unstable wavenumber k_{max} is of the order of a wavenumber at which $n/\nu k^2$ has the local maximum, which is

$$\begin{aligned} k_{\text{max}} &\sim \frac{\pi G \Sigma_{g,0} [t_{\text{stop}} \varepsilon c_s^2 + D(1+\varepsilon)]}{D c_s^2} \\ &= \frac{1+\varepsilon}{Q} H^{-1} + \frac{\varepsilon \tau_s}{(D \Omega c_s^{-2}) Q} H^{-1}. \end{aligned} \quad (2.74)$$

The right hand side of the Equation (2.74) is about $4.5H^{-1}$ for $\alpha = 10^{-3}$, $\varepsilon = 0.1$, $\tau_s = 0.3$ and $Q = 5$, which is consistent with the most unstable wavenumber seen in Figure 2.5. Note that the unstable condition depends on ν when the higher order terms of νk^2 are not negligible.

In the case that both TVGI and secular GI are unstable, those appear on one branch of the dispersion relation. Figure 2.6 shows the dispersion relations for $\alpha = 10^{-4}$, $\varepsilon =$

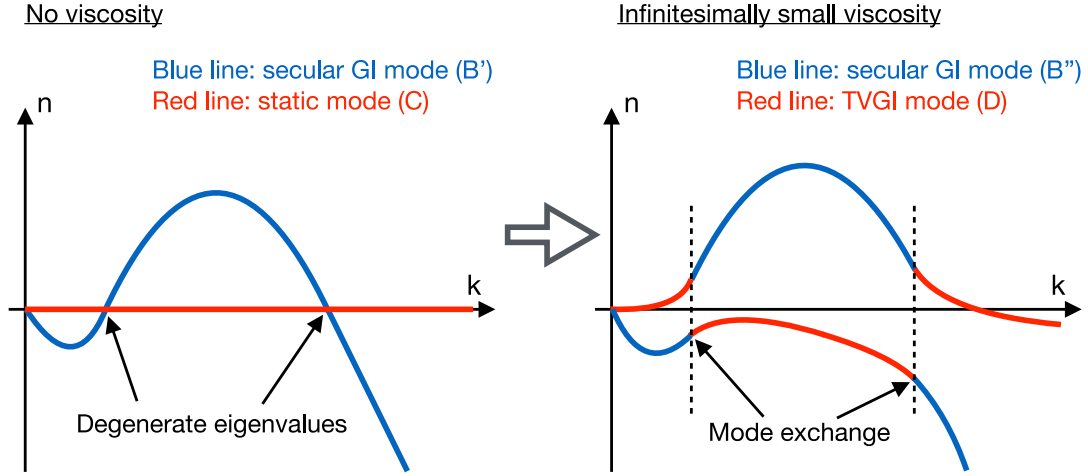


Figure 2.7: Schematic picture of the mode exchange between TVGI and secular GI. The mode exchange occurs because of turbulent viscosity. Left figure shows the dispersion relations of secular GI and the static mode in the absence of turbulent viscosity, and right figure shows those obtained in the presence of the turbulent viscosity. The blue line shows a branch of secular GI, and the red line shows the static mode or TVGI. The labels (B'), (B''), (C) and (D) shown in the legends correspond to the labels in Figure 2.1. The mode exchange occurs at wavelengths where eigenvalues and eigenfunctions degenerate in the absence of turbulent viscosity. This figure is originally from Figure 7 of the published paper, Tominaga et al. (2019).

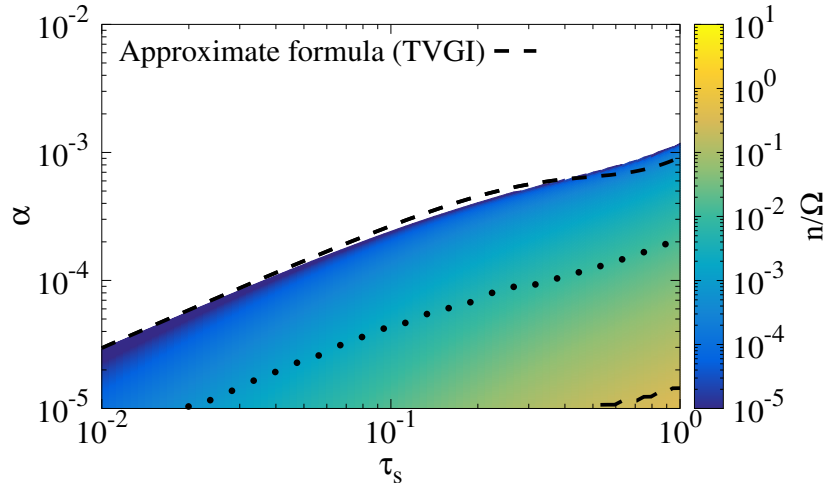


Figure 2.8: Maximum growth rates of TVGI and secular GI as a function of τ_s and α for $\epsilon = 0.05$ and $Q = 10$. The short-dashed line shows the maximum α for which TVGI can grow (Equation (2.70)). TVGI is the fastest growing mode in the colored region above the dotted line. In the region between the dotted and long-dashed lines, secular GI grows the fastest. Dust GI is the most unstable mode below the long-dashed line as in Figure 2.4. This figure is originally from Figure 8 of the published paper, Tominaga et al. (2019).

0.1, $\tau_s = 0.03$ and $Q = 3$. Those parameters satisfy the unstable conditions of TVGI and secular GI (Equations (2.59) and (2.70)). However, Figure 2.6 only shows one growing mode. We find that this apparent “single” unstable mode results from mode exchange between TVGI and secular GI (Figure 2.7). In the absence of turbulent viscosity, eigenvalues and eigenfunctions of the static mode and secular GI degenerate at wavenumbers where the growth rate of the secular GI is zero. In the presence of small but finite turbulent viscosity, curves of the dispersion relations of the destabilized static mode (i.e., TVGI) and secular GI reconnect at their crossing points, which results in single unstable branch. As shown in Figure 2.7, we designate the growing mode as secular GI at wavenumbers where secular GI is unstable for $\nu = 0$. On the other hand, we call the mode TVGI at wavenumbers where secular GI is stable for $\nu = 0$.

Figure 2.8 shows the maximum growth rate of TVGI and secular GI for $\varepsilon = 0.05$ and $Q = 10$ as a function of τ_s and α . TVGI is the fastest growing mode in the colored region above the dotted line. The dotted line almost coincides with the maximum α for which secular GI can grow (Equation (2.59)). Secular GI is the fastest growing mode in the parameter space enclosed by the dotted and long-dashed lines. Figure 2.8 also shows that TVGI can grow in a parameter space where turbulence and friction are so strong that secular GI is stable. We thus expect that TVGI grows earlier than secular GI since the stopping time becomes larger as dust grains grow in protoplanetary disks. As described above, the dust grains accumulate through the growth of TVGI. Therefore, TVGI should be a promising mechanism to form planetesimals.

We should note that the above analyses do not include the radial drift of dust grains at the unperturbed state. In the presence of the significant radial drift, secular GI is more important than TVGI. Linear analyses with the radial drift are shown in the next Chapter.

2.4 Discussion: effects of disk thickness

In the previous section, we assume that a disk is infinitesimally thin. The vertical thickness however stabilizes unstable modes to some extent because the thickness reduces self-gravity estimated for an infinitesimally thin disk. In this section, we investigate such effects on growth rates of secular GI and TVGI.

According to Vandervoort (1970) and Shu (1984), the self-gravitational potential $\delta\Phi$ reduced by the disk thickness is approximately given by

$$\delta\Phi = -\frac{2\pi G}{k} \left(\frac{\delta\Sigma_g}{1+kH} + \frac{\delta\Sigma_d}{1+kH_d} \right), \quad (2.75)$$

2.4. DISCUSSION: EFFECTS OF DISK THICKNESS

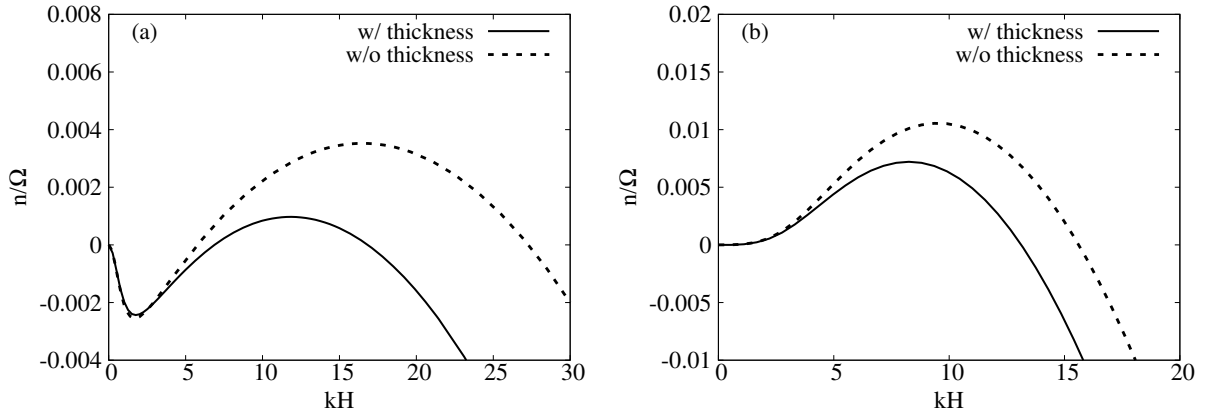


Figure 2.9: Dispersion relations of secular GI (left panel) and TVGI (right panel) for $\epsilon = 0.05$ and $Q = 10$. The dimensionless stopping time and strength of turbulence (τ_s, α) are set to be $(0.1, 2.5 \times 10^{-5})$ for the left panel and $(1, 2.5 \times 10^{-4})$ for the right panel (see also, Figure 2.10). We neglect the turbulent viscosity in the left panel so that only the secular GI grows. The solid lines represent the dispersion relation for a disk with finite thickness while the dashed lines are those for a razor thin disk. The growth rates and the most unstable wavenumbers become smaller as a result of the reduced self-gravity due to the disk thickness. This figure is originally from Figure 9 of the published paper, Tominaga et al. (2019).

where H_d is the dust scale height (Equation (1.26)). Using this equation rather than Equation (2.51) gives the reduced growth rate.

Figure 2.9 shows how introducing the thickness changes the dispersion relations of secular GI and TVGI for $\epsilon = 0.05$ and $Q = 10$. The dimensionless stopping time and strength of turbulence (τ_s, α) are set to be $(0.1, 2.5 \times 10^{-5})$ for the left panel of Figure 2.9 and $(\tau_s, \alpha) = (1, 2.5 \times 10^{-4})$ for the right panel. The most unstable mode is secular GI and TVGI in the former and latter cases, respectively. In both cases, introducing the disk thickness decreases the maximum growth rates by a factor of a few. Figure 2.10 shows the maximum growth rate as a function of τ_s and α for the same parameters as in Figure 2.8. Although the maximum growth rates are smaller than those in Figure 2.8, the extent of the unstable region is almost the same, and the maximum α for which the instabilities can grow does not change more than a factor of two.

Equation (1.26) shows that a dust disk is generally thinner than a gas disk. In reality, gas above a dust disk hardly interact with dust grains via friction because of less dust abundance at the upper layer. In the above analysis, the back reaction is assumed to be exerted on all of gas. Thus, we may need to exclude gas located above a dust disk from our analysis (see also, Latter & Rosca 2017). We should note that, even though gas above a dust disk is frictionally decoupled from dust, upper gas and the midplane dust

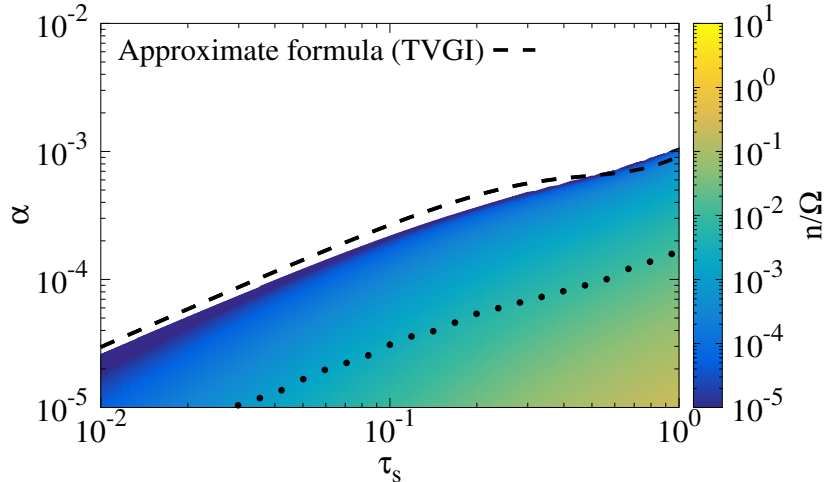


Figure 2.10: Maximum growth rate obtained when we introduce the disk thickness. Toomre’s Q for gas and dust-to-gas ratio ϵ are set to be the same value as those of Figure 2.8. The horizontal and vertical axes are the dimensionless stopping time τ_s and strength of turbulence α . The color represents the maximum growth rate normalized by Ω . The short-dashed line is the same as that shown in Figure 2.8. TVGI grows the fastest in the colored region above the dotted line. In the region below the dotted line, secular GI is the fastest growing mode. Both instabilities are stable in the white region.

interact with each other through their self-gravity. Thus, it is unclear to what vertical extent dust and gas should be considered. Although multidimensional analyses will give solutions to this problem, we focus on one-dimensional analyses in this work and discuss with some simplifications, which is described below.

Assuming the following Gaussian functions for the unperturbed density structures, we investigate stability in a dust disk:

$$\rho_{g,0} \equiv \frac{\Sigma_{g,0}}{\sqrt{2\pi}H} \exp\left(-\frac{z^2}{2H^2}\right), \quad (2.76)$$

$$\rho_{d,0} \equiv \frac{\Sigma_{d,0}}{\sqrt{2\pi}H_d} \exp\left(-\frac{z^2}{2H_d^2}\right), \quad (2.77)$$

where $\rho_{g,0}$ and $\rho_{d,0}$ are the mass density of gas and dust, respectively. Vertically integrating these density profiles gives surface densities within a dust disk although there is a large uncertainty in the appropriate range of the vertical integration. Here, we integrate these densities in $-3H_d \leq z \leq 3H_d$. Although the dust density at $z = 3H_d$ is smaller by orders of magnitudes than that at the midplane, the dust-to-gas mass ratio is still large because the dust scale height is much smaller than the gas scale height and dust concentrates around the midplane. In addition, friction force per unit mass exerted on

dust grains is independent from dust density, which means that the dust even at a low density region can take part in instabilities. The vertical integration of the mass densities gives

$$\Sigma'_{g,0} \equiv \int_{-3H_d}^{3H_d} \rho_{g,0} dz = \Sigma_{g,0} \operatorname{erf} \left(\frac{3H_d}{\sqrt{2}H} \right), \quad (2.78)$$

$$\Sigma'_{d,0} \equiv \int_{-3H_d}^{3H_d} \rho_{d,0} dz = \Sigma_{d,0} \operatorname{erf} \left(\frac{3}{\sqrt{2}} \right) \simeq 0.997 \Sigma_{d,0}, \quad (2.79)$$

where $\operatorname{erf}(x)$ is the error function. The relation between the mid-plane dust-to-gas mass ratio and $\Sigma'_{d,0}/\Sigma'_{g,0}$ is

$$\frac{\rho_{d,0}(z=0)}{\rho_{g,0}(z=0)} = \frac{\Sigma'_{d,0}H}{\Sigma'_{g,0}H_d} \operatorname{erf} \left(\frac{3H_d}{\sqrt{2}H} \right) \left[\operatorname{erf} \left(\frac{3}{\sqrt{2}} \right) \right]^{-1}. \quad (2.80)$$

We perform linear analyses using these surface densities and the dust-to-gas mass ratio $\Sigma'_{d,0}/\Sigma'_{g,0}$. In these analyses, we introduce the modified Toomre's Q parameter for a gas disk $\tilde{Q} \equiv c_s \Omega / \pi G \Sigma'_{g,0}$. We also modify the self-gravitational potential using H_d for both gas and dust:

$$\delta\Phi = -\frac{2\pi G}{k} \frac{\delta\Sigma'_g + \delta\Sigma'_d}{1 + kH_d}. \quad (2.81)$$

Figure 2.11 shows the maximum growth rates as a function of total dust-to-gas mass ratio $\Sigma_{d,0}/\Sigma_{g,0}$ and $Q = c_s \Omega / \pi G \Sigma_{g,0}$ for $\tau_s = 0.1$ and $\alpha = 10^{-4}$. In this case, H_d/H is about 0.03, and, thus, \tilde{Q}/Q is about 14, meaning that \tilde{Q} is 14 times larger than Q in the whole parameter space of Figure 2.11. The dust-to-gas mass ratio in the dust disk $\Sigma'_{d,0}/\Sigma'_{g,0}$ is also about 10 times larger than $\Sigma_{d,0}/\Sigma_{g,0}$. Secular GI grows the fastest in the parameter space bounded by the dotted and dashed lines. This is because \tilde{Q} is too large and dust GI grows faster than secular GI. TVGI can grow in a larger parameter space. Since the self-gravity of dust is important for its growth, TVGI grows even for large \tilde{Q} . Thus, at least in the absence of the radial drift, TVGI can grow even when we consider the vertical structures.

We again note that gas above the dust disk will affect the motion in the dust disk through the gravitational interaction. Thus, we may underestimate the self-gravity in this analysis. Increasing the vertical extent of the integration results in smaller \tilde{Q} and a larger parameter space where secular GI is the most unstable. To examine the effects of the upper gas on the instabilities in the dust disk, we need to perform multidimensional analyses, which are beyond the scope of this thesis. Moreover, dust is less diffusive in dust rich regions Schreiber & Klahr (2018). The less radial diffusivity makes the disk more unstable to secular GI than in Figure 2.11.

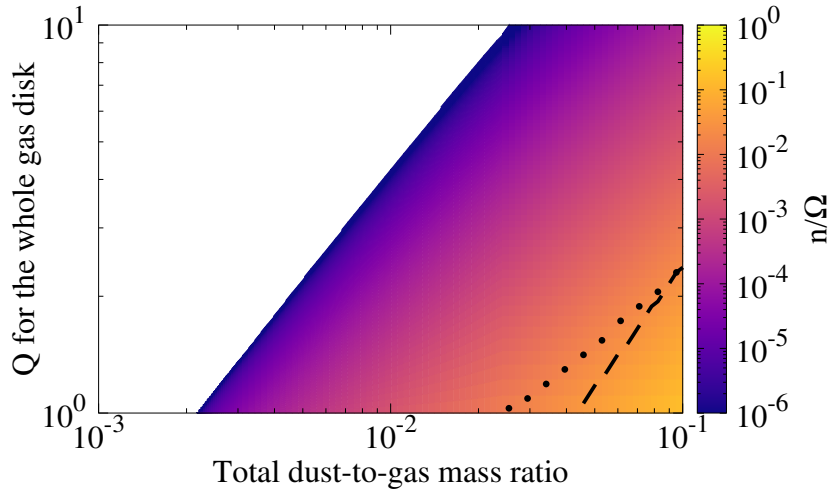


Figure 2.11: Maximum growth rates of secular GI, TVGI, and dust GI as a function of total dust-to-gas mass ratio $\Sigma_{d,0}/\Sigma_{g,0}$ and $Q = c_s\Omega/\pi G\Sigma_0$ for $\tau_s = 0.1$ and $\alpha = 10^{-4}$. The color represents the maximum growth rate normalized by the angular velocity Ω . In the colored region above the dotted line, TVGI is the most unstable mode. Secular GI grows the fastest in the region enclosed by the dotted and dashed lines. Dust GI is the most unstable mode below the dashed line. This figure is originally from Figure 11 of the published paper, Tominaga et al. (2019).

2.5 Summary

In Chapter 2, we revisit dust dynamics in turbulent gas and reformulate the macroscopic equations of dust based on the mean-field approximation (the Reynolds-averaging). The reformulated equations conserve total angular momentum, which is in contrast to the previous studies that simply use the advection-diffusion equation for dust density. The difference comes from the fact that we introduce the advection terms originating from the diffusive flow in momentum equations. The reformulated equations can be used for various studies because of its simplicity.

Using the reformulated equations, we perform linear stability analyses on secular GI. We find that secular GI grows monotonically with a few times larger growth rate than expected in the previous studies. The property of the monotonic growth is in contrast to the previous studies that found overstabilized secular GI. Our linear analyses show that the overstability in the previous studies is resultant from the violation of angular momentum conservation.

The present linear analyses show that turbulent viscosity introduces a new instability that we refer to as TVGI. TVGI grows for larger α and smaller τ_s for which secular GI can not grow. Because τ_s increases as dust grains grow, we may expect that TVGI

becomes operational earlier than secular GI at least in the absence of significant radial drift (cf. Chapter 3).

The vertical structure is a possible source stabilizing the instabilities. Simply assuming the Gaussian density profiles, we investigate its effect on the maximum growth rates of secular GI and TVGI. Although it is unclear to what vertical extent dust and gas should be considered, we consider the extent of $-3H_d \leq z \leq 3H_d$ and perform linear analyses. Results show that secular GI grows the fastest in a region bounded by the dotted and dashed lines in Figure 2.11. This is because gas mass in $-3H_d \leq z \leq 3H_d$ is about 10 times smaller than the overall gas mass. On the other hand, TVGI can grow even larger Q and smaller dust-to-gas mass ratio. We should note that increasing the vertical extent in consideration expands unstable regions of those instabilities. Because upper gas interacts with the midplane dust through gravity, we may underestimate the growth rate and extents of parameter space unstable to secular GI. To explore more precisely, we need to perform linear analyses where vertical structures are explicitly considered. Those multidimensional analyses are our future work.

Chapter 3

Numerical Simulations of Secular Instabilities

This chapter is based on published papers, Tominaga, Inutsuka, & Takahashi 2018, *Publication of the Astronomical Society of Japan*, Volume 70, pp. 3 (1-15) (Tominaga et al. 2018), and Tominaga, Takahashi, & Inutsuka 2020, *The Astrophysical Journal*, Volume 900, pp. 182-198 (Tominaga et al. 2020).

3.1 Short introduction

Chapter 2 and the previous studies on secular GI focused on linear growth of the instability (e.g., Ward 2000; Youdin 2005a; Youdin 2011; Takahashi & Inutsuka 2014; Latter & Rosca 2017). The linear analyses showed the possibility that secular GI creates some observed ring-like structures (Takahashi & Inutsuka 2014). Moreover, resultant dust concentration is expected to lead to planetesimal formation (e.g., Youdin 2011; Takahashi & Inutsuka 2016). However, the process from ring formation to planetesimal formation is a nonlinear process, which has not been studied. Studies on nonlinear secular GI are necessary toward understanding planetesimal formation.

Although the linear growth at the local frame is well studied (e.g., Youdin 2011; Takahashi & Inutsuka 2014; Tominaga et al. 2019 and Chapter 2), it is also necessary to investigate the growth of secular GI toward planetesimal formation as a global problem. This is because dust grains drift inward throughout a disk where the growth efficiency of secular GI varies radially. Numerical simulations are useful to study such a nonlinear global problem. We thus perform numerical simulations of secular GI and explore how the instability grows in a radially extended disk and to what extent the instability

concentrates dust grains into rings.

For numerical simulations of secular GI, it seems necessary to take notice especially of numerical errors and diffusion. A growth timescale of secular GI is typically about 100 times longer than one Keplerian period. Such a slow process will suffer numerical diffusion during long-term integrations. In addition, numerical diffusion due to spatial discretization and advection prevents growth of secular GI because dust grains drift inward in a disk and the associated advection numerically smoothes out seed perturbations of secular GI.

Motivated by these numerical issues, we develop a Lagrangian-cell method that utilizes a symplectic integrator for time integrations (Tominaga et al. 2018). Using Lagrangian cells, we avoid numerical diffusion due to the spatial advection. A symplectic integrator is one method used in N-body simulations for orbital evolutions because the method preserves an error in total energy throughout a calculation for Hamiltonian systems. Since secular GI requires frictional dissipation and the system is not exactly Hamiltonian, we adopt the operator splitting and use a symplectic integrator only for time integration with Hamiltonian part. We solve momentum evolution due to friction using the piecewise exact solution (Inoue & Inutsuka 2008) that is free from time-step requirement due to small $t_{\text{stop}}\Omega$. Adopting these methods, we perform radially one-dimensional simulations secular GI (Tominaga et al. 2020).

In Section 3.2, we describe numerical methods and show some test calculations. We then show results of simulations of secular GI in Section 3.3. Discussions and summary are given in Sections 3.4 and 3.5.

3.2 Numerical methods

As in the previous chapter, we consider the following gas and dust equations:

$$\frac{\partial \Sigma_{\text{g}}}{\partial t} + \frac{1}{r} \frac{\partial (r \Sigma_{\text{g}} u_r)}{\partial r} = 0, \quad (2.4)$$

$$\begin{aligned} \Sigma_{\text{g}} \left(\frac{\partial u_i}{\partial t} + u_j \frac{\partial u_i}{\partial x_j} \right) &= -c_s^2 \frac{\partial \Sigma_{\text{g}}}{\partial x_i} - \Sigma_{\text{g}} \frac{\partial}{\partial x_i} \left(\Phi - \frac{GM_*}{r} \right) \\ &+ \frac{\partial}{\partial x_j} \left[\Sigma_{\text{g}} \nu \left(\frac{\partial u_i}{\partial x_j} + \frac{\partial u_j}{\partial x_i} - \frac{2}{3} \delta_{ij} \frac{\partial u_k}{\partial x_k} \right) \right] + \Sigma_{\text{d}} \frac{v_i - u_i}{t_{\text{stop}}}, \end{aligned} \quad (2.35)$$

$$\frac{\partial \Sigma_{\text{d}}}{\partial t} + \frac{1}{r} \frac{\partial (r \Sigma_{\text{d}} v_r)}{\partial r} = \frac{1}{r} \frac{\partial}{\partial r} \left(r D \frac{\partial \Sigma_{\text{d}}}{\partial r} \right), \quad (2.1)$$

$$\begin{aligned} \Sigma_d \left[\frac{\partial v_r}{\partial t} + \left(v_r - \frac{D}{\Sigma_d} \frac{\partial \Sigma_d}{\partial r} \right) \frac{\partial v_r}{\partial r} \right] &= \Sigma_d \frac{v_\phi^2}{r} - c_d^2 \frac{\partial \Sigma_d}{\partial r} - \Sigma_d \frac{\partial}{\partial r} \left(\Phi - \frac{GM_*}{r} \right) \\ &\quad - \Sigma_d \frac{v_r - u_r}{t_{\text{stop}}} + \frac{1}{r} \frac{\partial}{\partial r} \left(r v_r D \frac{\partial \Sigma_d}{\partial r} \right), \end{aligned} \quad (2.37)$$

$$\Sigma_d \left[\frac{\partial v_\phi}{\partial t} + \left(v_r - \frac{D}{\Sigma_d} \frac{\partial \Sigma_d}{\partial r} \right) \frac{\partial v_\phi}{\partial r} \right] = -\Sigma_d \frac{v_\phi}{r} \left(v_r - \frac{D}{\Sigma_d} \frac{\partial \Sigma_d}{\partial r} \right) - \Sigma_d \frac{v_\phi - u_\phi}{t_{\text{stop}}}, \quad (2.38)$$

$$\nabla^2 \Phi = 4\pi G (\Sigma_g + \Sigma_d) \delta(z), \quad (2.36)$$

where the numbering of the equations are the same as in the previous chapter. We solve these equations utilizing the operator splitting method. In the following, we describe the methods in detail.

3.2.1 Lagrangian-cell method

First, we formulate the Lagrangian-cell method adopted for dissipationless parts of hydrodynamic equations. For the simplicity, we first consider a one-dimensional sound wave in gas in the Cartesian coordinates and demonstrate that our method is free from the numerical diffusion due to the advection. Next, we formulate the method in the cylindrical coordinates.

Our formulation starts from the action principle. The Lagrangian of a certain fluid is given by

$$L = \int dx \left[\rho \left(\frac{\dot{x}^2}{2} - u \right) \right], \quad (3.1)$$

where x and \dot{x} denote position and velocity, ρ denotes mass density, and u denotes specific internal energy. Assuming a barotropic relation $P = P(\rho)$, one obtains

$$u = \int \frac{P}{\rho^2} d\rho. \quad (3.2)$$

Next, we discretize the Lagrangian as the following:

$$L = \sum_{i=1}^{N-1} \left(m_{i+1/2} \frac{\dot{x}_{i+1/2}^2}{2} \right) - \sum_{i=1}^N m_i u_i, \quad (3.3)$$

$$m_{i+1/2} = \frac{m_{i+1} + m_i}{2}, \quad (3.4)$$

where N denotes the number of cells, physical properties defined in the i th cell are represented with the index i . $x_{i+1/2}$ denotes a boundary position between the i th and

3.2. NUMERICAL METHODS

$(i + 1)$ th cells. Our Lagrangian formulation assumes that mass in the i -th cell m_i is constant in time. The density ρ_i is given by

$$\rho_i = \frac{m_i}{x_{i+1/2} - x_{i-1/2}}. \quad (3.5)$$

Substituting Equation (3.3) into the Euler-Lagrange equation

$$\frac{d}{dt} \left(\frac{\partial L}{\partial \dot{x}_{i+1/2}} \right) - \frac{\partial L}{\partial x_{i+1/2}} = 0, \quad (3.6)$$

we obtain

$$m_{i+1/2} \ddot{x}_{i+1/2} = - \frac{\partial}{\partial x_{i+1/2}} \sum_{j=1}^N m_j u_j. \quad (3.7)$$

With the use of Equation (3.2), the right hand side of Equation (3.7) is

$$\begin{aligned} - \frac{\partial}{\partial x_{i+1/2}} \sum_{j=1}^N m_j u_j &= - \frac{\partial}{\partial x_{i+1/2}} (m_{i+1} u_{i+1} + m_i u_i), \\ &= - \frac{\partial \rho_{i+1}}{\partial x_{i+1/2}} \frac{\partial (m_{i+1} u_{i+1})}{\partial \rho_{i+1}} - \frac{\partial \rho_i}{\partial x_{i+1/2}} \frac{\partial (m_i u_i)}{\partial \rho_i}, \\ &= -P_{i+1} + P_i. \end{aligned} \quad (3.8)$$

Finally, we obtain the following equation of motion of cell boundaries:

$$m_{i+1/2} \ddot{x}_{i+1/2} = -(P_{i+1} - P_i). \quad (3.9)$$

We integrate Equation (3.9) using a symplectic integrator. In this work, we use the leap-frog integrator, which is the second-order symplectic integrator.

Equation (3.9) has the second-order accuracy in Δx_i , which can be shown as follows. Assuming that cell widths are small enough ($\Delta x_i \ll x_i$), we conduct the Taylor-series expansion on the right hand side of Equation (3.9) around $x_{i+1/2}$ and obtain

$$m_{i+1/2} \ddot{x}_{i+1/2} = - \frac{\Delta x_i + \Delta x_{i+1}}{2} \frac{dP}{dx} + \mathcal{O}(\Delta x_i^3), \quad (3.10)$$

where x_i is set to be $(x_{i+1/2} + x_{i-1/2})/2$, and we assume $\Delta x_{i+1} = \Delta x_i + \mathcal{O}(\Delta x_i^2)$. The mass $m_{g,i+1/2}$ can be written as follows:

$$\begin{aligned} m_{i+1/2} &= \frac{1}{2} (m_i + m_{g,i+1}) \\ &= \frac{1}{2} (\rho_i \Delta x_i + \rho_{i+1} \Delta x_{i+1}) \\ &= \frac{\rho_{i+1/2}}{2} (\Delta x_i + \Delta x_{i+1}) + \mathcal{O}(\Delta x_i^3). \end{aligned} \quad (3.11)$$

3.2. NUMERICAL METHODS

Dividing both side of Equation (3.9) by $m_{i+1/2}$ gives

$$\ddot{x}_{i+1/2} = -\frac{1}{\rho_{i+1/2}} \frac{dP}{dx} + \mathcal{O}(\Delta x_i^2). \quad (3.12)$$

Therefore, our method has the second-order accuracy in Δx_i .

We test our method for one-fluid plane wave propagation in a one-dimensional domain with the length L . We equally space the domain using $N = 128$ cells. We assume the isothermal equation of state. A time-step Δt is taken to be $0.5L/Nc_s$. We adopt code units where the unperturbed gas density is 2 and $L = c_s = 1$. We initially displace cells with an amplitude of $\xi = 1.0 \times 10^{-6}$ and a wavelength of $\lambda = 0.5$.

Figure 3.1 shows errors in the total energy as a function of time t and time evolution of the density perturbation $\delta\rho$. The oscillating property in the error is one feature of the symplectic integrator. Although there is a dispersive error in the profile of $\delta\rho$, the amplitude of the sound wave keeps constant over 100 periods, meaning that the method is free from numerical diffusion.

We also check convergence and spatial accuracy of our scheme. The unperturbed density, the wavelength and the amplitude are the same as those of the above test. We conduct two test simulations: (1) propagation of sound wave under the periodic boundary condition, and (2) standing wave under the fixed boundary condition. We let the fluid evolve until $t = 3$ periods using $\Delta t = 0.1L/512c_s$ for both simulations. Figure 3.2 shows the N -dependence of L_2 norm error of the density profile at the end of the simulations. The error is proportional to N^{-2} , meaning that our scheme has the second-order accuracy in space.

We finally formulate methods in the cylindrical coordinates (r, ϕ) for infinitesimally thin axisymmetric disks. We use the following discretized Lagrangian and surface density at each cell:

$$L = \sum_{i=1}^{N-1} m_{i+1/2} \left(\frac{\dot{\mathbf{r}}_{i+1/2}^2}{2} + \Phi(r_{i+1/2}) \right) - \sum_{i=1}^N m_i u_i, \quad (3.13)$$

$$\dot{\mathbf{r}}_{i+1/2}^2 \equiv \dot{r}_{i+1/2}^2 + r_{i+1/2}^2 \dot{\phi}_{i+1/2}^2, \quad (3.14)$$

$$\Sigma_i = \frac{m_i}{\pi (r_{i+1/2}^2 - r_{i-1/2}^2)}, \quad (3.15)$$

where Φ is the gravitational potential. Substituting Equation (3.13) into the Euler-Lagrange equation, we obtain

$$m_{i+1/2} \ddot{r}_{i+1/2} = \frac{J_{i+1/2}^2}{m_{i+1/2} r_{i+1/2}^3} - 2\pi r_{i+1/2} (P_{i+1} - P_i) - m_{i+1/2} \frac{\partial \Phi(r_{i+1/2})}{\partial r_{i+1/2}}, \quad (3.16)$$

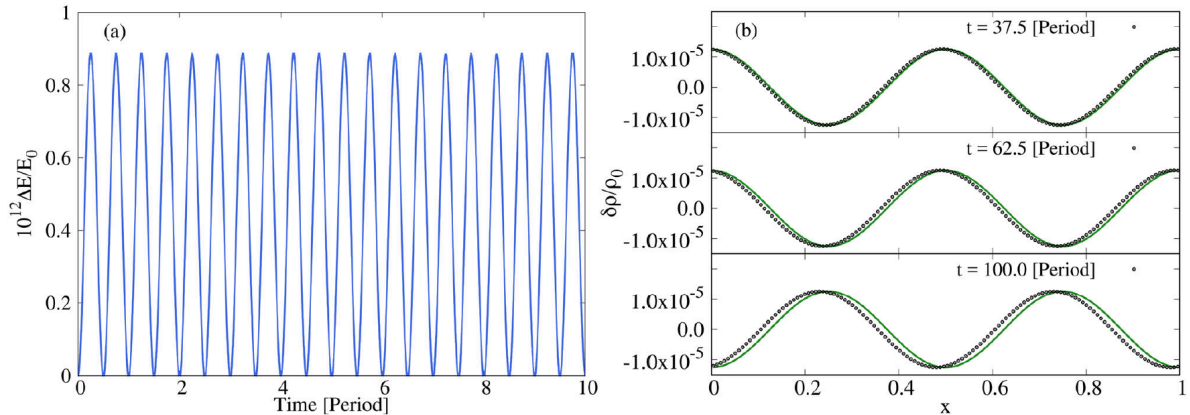


Figure 3.1: Tests on a one-fluid plane wave propagation. The left figure shows a time variation of the error in the total energy. Although we show the time variation only for 10 periods, the amplitude of errors is constant for a longer-term calculation. The right figure shows density perturbations of a plane wave. The solid green lines show the exact solution while the black circles show the numerical simulation. One can see that the perturbation amplitudes keep constant over 100 periods although there are dispersive errors. This figure is originally from Figure 16 of Tominaga et al. (2018).

$$\frac{dJ_{i+1/2}}{dt} = 0, \quad (3.17)$$

$$J_{i+1/2} \equiv \frac{\partial L}{\partial \dot{\phi}_{i+1/2}}, \quad (3.18)$$

where $J_{i+1/2}$ is angular momentum of a cell boundary at $r = r_{i+1/2}$. Figure 3.3 shows where physical variables are defined in the cylindrical coordinates. For two-fluid calculations, we also use the same cell-structures for dust and gas. In the absence of frictional interaction between dust and gas, our method is a symplectic scheme, which is free from numerical diffusion and enables accurate long-term calculations.

Self-gravity solver

We regard self-gravity of a disk as a sum of gravitational forces from infinitesimally thin rings that are (1) coaxial with the center at $(r, \phi) = (0, 0)$, (2) located in $z = 0$ plane, and (3) having uniform line densities. Gravitational potential $\Phi_{\text{ring}}(r, z; R_{\text{ring}})$ due to a ring with a mass of M_{ring} and a radius of R_{ring} is given by

$$\Phi_{\text{ring}}(r, z; a) = M_{\text{ring}} U(r, z; R_{\text{ring}}), \quad (3.19)$$

$$U(r, z; R_{\text{ring}}) \equiv -\frac{2GK(n)}{\pi p}, \quad (3.20)$$

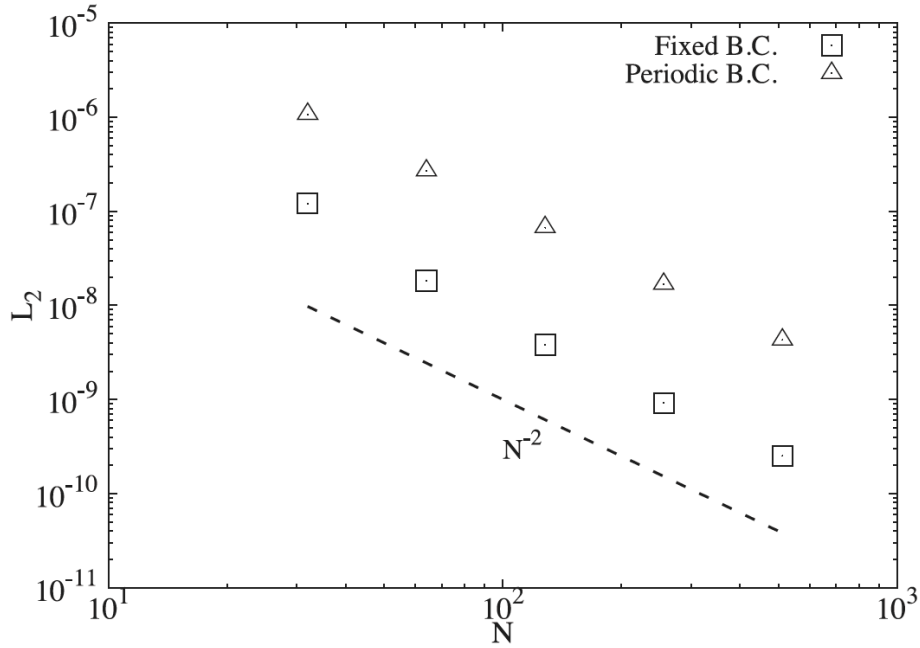


Figure 3.2: N -dependence of L_2 norm error from the convergence tests. The symbols \square and \triangle represent the results of a plane wave propagation and a standing wave tests, respectively. This figure is originally from Figure 17 of Tominaga et al. (2018).

where p and n are

$$p \equiv \sqrt{(r + R_{\text{ring}})^2 + z^2}, \quad (3.21)$$

$$n \equiv \frac{4R_{\text{ring}}r}{p^2}. \quad (3.22)$$

$K(n)$ is the complete elliptic integral of the first kind

$$K(n) \equiv \int_0^{\pi/2} \frac{d\phi}{\sqrt{1 - n \sin^2 \phi}}. \quad (3.23)$$

One obtains the ring gravity per unit mass $F_r(r, z; R_{\text{ring}})$ by differentiating the potential:

$$F_r(r, z; R_{\text{ring}}) \equiv M_{\text{ring}} \tilde{F}(r, z; R_{\text{ring}}) \quad (3.24)$$

$$\tilde{F}(r, z; R_{\text{ring}}) = -\frac{G}{\pi p} \left[\frac{K(n)}{r} + A(r, z; R_{\text{ring}}) \frac{E(n)}{q^2} \right], \quad (3.25)$$

$$A(r, z; R_{\text{ring}}) \equiv \frac{r^2 - z^2 - R_{\text{ring}}^2}{r}, \quad (3.26)$$

$$q \equiv \sqrt{(r - R_{\text{ring}})^2 + z^2}, \quad (3.27)$$

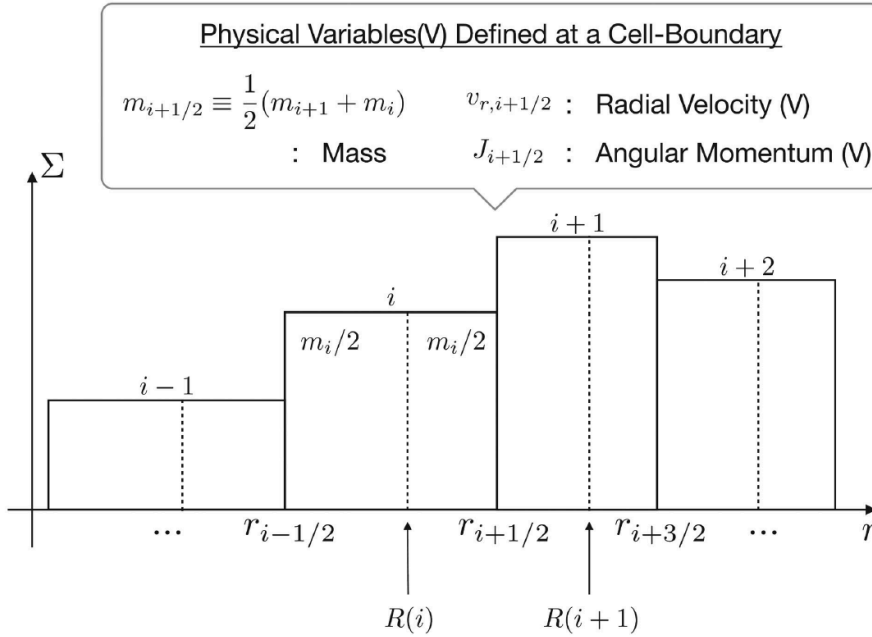


Figure 3.3: Schematic picture to show where variables are defined. The surface density is denoted by Σ , and a radial location of a cell boundary between the i -th and the $(i+1)$ -th cells is denoted by $r_{i+1/2}$. Radial velocity and angular momentum are defined at each cell boundary. $R(i)$ denotes a radius that equally divides a mass in a i th cell. This figure is originally from Figure 1 of Tominaga et al. (2018)

where $E(n)$ is the complete elliptic integral of the second kind

$$E(n) \equiv \int_0^{\pi/2} \sqrt{1 - n \sin^2 \phi} d\phi. \quad (3.28)$$

In this thesis, we use approximated functions to evaluate the elliptic integrals (Hastings et al. 1955).

We approximate self-gravity of a one-fluid disk per unit mass at $r = r_{i+1/2}$ using perturbed ring masses $\delta m_{i+1/2}$ defined in terms of surface density Σ and unperturbed surface density Σ_0 as follows:

$$\delta m_{i+1/2} \equiv \frac{\delta m_{i+1} + \delta m_i}{2}, \quad (3.29)$$

$$\delta m_i \equiv \pi (\Sigma - \Sigma_0) (r_{i+1/2}^2 - r_{i-1/2}^2), \quad (3.30)$$

$$\sum_{i \neq j} \delta m_{j+1/2} \tilde{F}_r(r_{i+1/2}, 0; r_{j+1/2}). \quad (3.31)$$

The above method with δm corresponds to the solution of the Poisson equation with perturbed surface density $\delta \Sigma \equiv \Sigma - \Sigma_0$ as a source term. For a problem with dust and

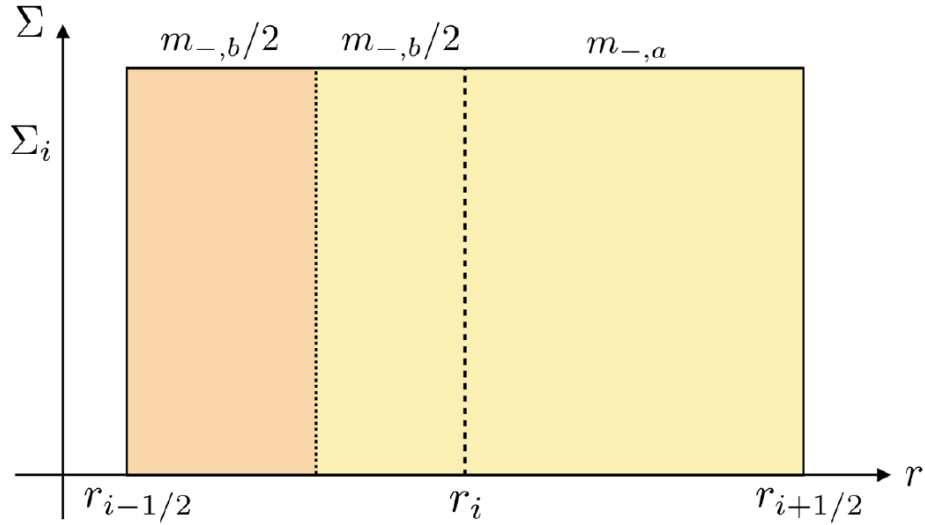


Figure 3.4: This figure shows how to distribute a mass in the i th cell before we calculate the correction terms for self-gravity. The mass assigned at $r = r_i$ is $m_- = m_{-,a} + m_{-,b}/2$, where $m_{-,a} \equiv \pi [r_{i+1/2}^2 - r_i^2] \Sigma_i$ and $m_{-,b} \equiv \pi [r_i^2 - r_{i-1/2}^2] \Sigma_i$. We replace the mass at $r = r_{i-1/2}$, i.e. $m_{i-1/2}$, with $[m_{i-1} + m_{-,b}]/2$. This figure is originally from Figure 18 of Tominaga et al. (2018).

gas, we calculate the self-gravity using this approximation for both dust and gas based on their surface densities Σ_d , Σ_g , unperturbed densities $\Sigma_{d,0}$, $\Sigma_{g,0}$, and their cell masses $m_{d,i}$, $m_{g,i}$. When we use softening length h for self-gravity to avoid divergence at ring positions, we use the following equation

$$\sum_{i \neq j} \delta m_{j+1/2} \tilde{F}_r(r_{i+1/2}, h; r_{j+1/2}). \quad (3.32)$$

We find that including gravity of a ring from itself to calculate self-gravity increases the accuracy. In the following, we consider self-gravity exerted on a ring at $r = r_{i+1/2}$ as an example. In addition to the formula (Equation 3.31), we introduce gravity from rings at $r = r_i$, r_{i+1} as “correction terms”. To calculate gravity from the ring at $r = r_i$, we divide the mass m_i into two parts: $m_{-,a}$ and $m_{-,b}$ (see Figure 3.4):

$$m_{-,a} \equiv \pi [r_{i+1/2}^2 - r_i^2] \Sigma_i, \quad (3.33)$$

$$m_{-,b} \equiv \pi [r_i^2 - r_{i-1/2}^2] \Sigma_i. \quad (3.34)$$

Using these masses, we change masses defined at $r = r_i$ ($m = m_-$), $r_{i-1/2}$ ($m = m_{i-1/2}$)

3.2. NUMERICAL METHODS

as follow

$$m_- = m_{-,a} + \frac{m_{-,b}}{2}, \quad (3.35)$$

$$m_{i-1/2} = \frac{m_{i-1} + m_{-,b}}{2}. \quad (3.36)$$

We also calculate masses m_+ and $m_{i+3/2}$ of rings at $r = r_{i+1}, r_{i+3/2}$ respectively using $m_{+,a}$ and $m_{+,b}$ as follows:

$$m_{+,a} \equiv \pi [r_{i+1}^2 - r_{i+1/2}^2] \Sigma_{i+1}, \quad (3.37)$$

$$m_{+,b} \equiv \pi [r_{i+3/2}^2 - r_{i+1}^2] \Sigma_{i+1}, \quad (3.38)$$

$$m_+ = m_{+,a} + \frac{m_{+,b}}{2}, \quad (3.39)$$

$$m_{i+3/2} = \frac{m_{i+2} + m_{+,b}}{2}. \quad (3.40)$$

With these masses, we calculate gravity exerted on a ring at $r = r_{i+1/2}$ from $r = r_{i-1/2}, r_i, r_{i+1}$, and $r_{i+3/2}$ in the same way as Equation (3.31). For dust-gas systems, we make use of the above correction for both dust and gas based on their cell masses $m_{d,i}, m_{g,i}$.

Using the above method, we test our scheme calculating growth of pure GI. As a test simulation, we consider a Keplerian disk around a solar mass star. A local domain is set around $r = 80$ au with a radial width L of twice the most unstable wavelength. Only in test simulations, we use a piecewise polytropic relation (cf., Machida et al. (2006))

$$P = c_{s,0}^2 \Sigma_0 \left[\frac{\Sigma}{\Sigma_0} + \left(\frac{\Sigma}{\Sigma_0} \right)^{5/3} \right], \quad (3.41)$$

where $c_{s,0}$ is an isothermal sound speed, and Σ_0 is set to be the unperturbed surface density. The most unstable wavelength is scaled by $c_{s,0}/\Omega$. To compare results with ‘‘local’’ linear analyses, we assume small $c_{s,0}$ ($c_{s,0} \simeq 0.18 \text{ m s}^{-1}$) and make the most wavelength $\sim 10^{-4}$ times shorter than the orbital radius. The assumed sound speed is a thousand times smaller than a sound speed with mean molecular weight 2.37 and temperature 10 K. We set the unperturbed surface density Σ_0 for Toomre’s Q value to be 0.999 at $r = 80$ au. We initially put perturbations with the amplitude $\delta\Sigma/\Sigma_0 \sim 10^{-5}$ based on the eigenfunction of the most unstable mode. Although we adopt the fixed boundary condition, we let a surface density outside the domain evolve according to the eigenfunction of GI. The external density perturbations on both sides are resolved by 128 cells. We space the domain using 512 cells. Time interval Δt is set to be $\Delta t = L/512c_s$. We also use the softening length $h = L/4N$ to avoid divergence of ring gravity. Figure 3.5 shows the time evolution of the density peak at the center of the domain. The growth

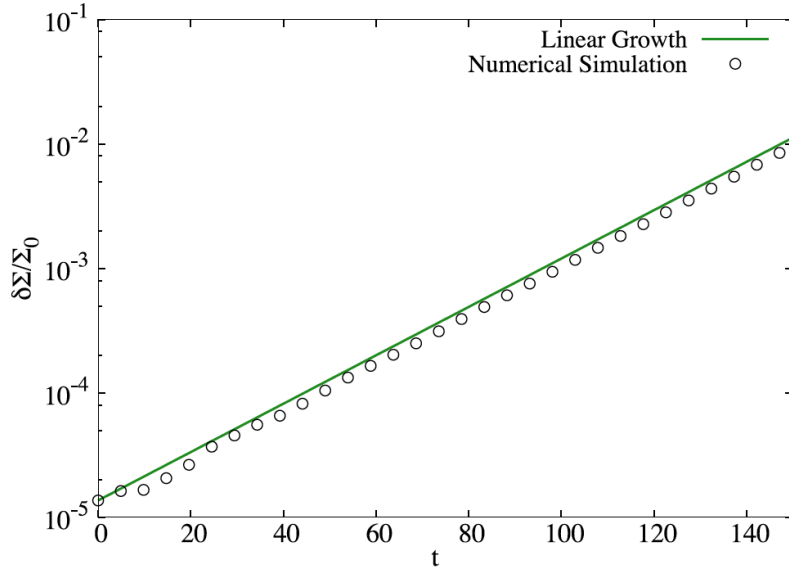


Figure 3.5: Time evolution of the surface density peak via GI. The horizontal axis is normalized by angular velocity Ω . The black circles represent the result of the test simulation, and the solid green line shows the linear growth rate from local linear analyses. The numerical results show good agreement with the linear growth rate, meaning that our scheme can accurately solve such a long-term evolution. This figure is originally from Figure 2 of Tominaga et al. (2018).

rate is about $4.5 \times 10^{-2}\Omega$ for $Q = 0.999$. The numerical results reproduce analytically derived growth rate. In this way, our scheme can accurately solve such a very slow evolution with our symplectic method.

3.2.2 The piecewise exact solution for friction

We adopt the piecewise exact solution to calculate frictional momentum transport (Inoue & Inutsuka 2008). The stopping time is much smaller than one Keplerian period for small dust grains considered in this thesis. In such a case, time stepping for stable simulations is restricted by the small stopping time, which makes long-term simulations difficult. The piecewise exact solution enables us to get rid of such a restriction. The method is based on an operator splitting method. In our cases, we split the equations into time evolutions due to (1) friction, (2) dust diffusion, (3) turbulent viscosity, and (4) the other hydrodynamical force that are solved based on the Lagrangian-cell method (e.g., pressure gradient, self-gravity). In the part (1), the momentum equations can be solve analytically. The piecewise exact solution utilizes the analytical solution and let

3.2. NUMERICAL METHODS

momentums evolve. This method is not only free from the above restriction but also unconditionally stable. In the following, we describe the scheme in more detail. The part (3) is described afterward.

When solving the frictional interaction, we only update linear and angular momentums of dust and gas whose positions are unchanged. Because our method is based on the Lagrangian description, positions of dust cells do not necessarily coincide with gas cells' positions. Thus, we first interpolate physical variables in $r_i \leq r < r_{i+1}$ using the physical values at $r = r_{i+1/2}$. We use linear functions in r for radial velocities, j_g/\sqrt{r} and j_d/\sqrt{r} , where j_d and j_g are specific angular momentum of dust and gas. Coefficients of r^1 and r^0 in the linear functions are determined so that spatial integrations of the interpolation functions give the radial momentum and angular momentum of the cell boundary at $r = r_{i+1/2}$. In this way, we avoid numerical diffusion due to the interpolation.

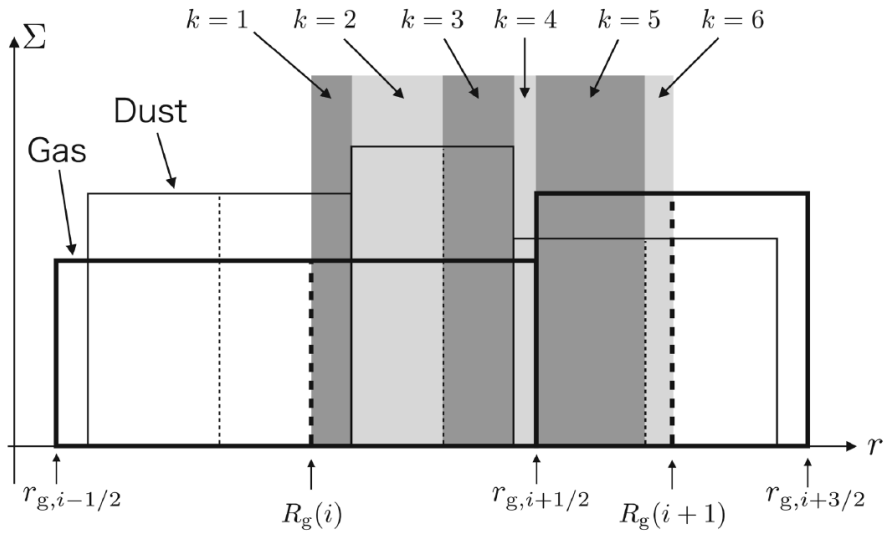


Figure 3.6: Regions used for the piecewise exact solution (colored with dark and light gray). Their boundaries are either the cell boundary or the cell center of gas and dust. The number k characterizes each region. Cells enclosed by thick lines represent gas cells while those enclosed by thin lines represent dust cells. This figure highlights regions used for calculating momentum changes at the gas cell boundary at $r = r_{g,i+1/2}$. This figure is originally from Figure 3 of Tominaga et al. (2018).

We integrate the interpolation functions and calculate masses, radial momentums, and angular momentums in a region where j th dust cell and i th gas cell overlap with each other. Those values are denoted by m_g^k , m_d^k , P_g^k , P_d^k , J_g^k , and J_d^k for gas and dust at k th overlap region (see Figure 3.6). We update these momentums using the following

3.2. NUMERICAL METHODS

equations:

$$\frac{dP_g^k}{dt} = -m_d^k \frac{U^k - V^k}{t_{\text{stop}}^k}, \quad (3.42)$$

$$\frac{dP_d^k}{dt} = -m_d^k \frac{V^k - U^k}{t_{\text{stop}}^k}, \quad (3.43)$$

$$\frac{dJ_g^k}{dt} = -m_d^k \frac{j_g^k - j_d^k}{t_{\text{stop}}^k}, \quad (3.44)$$

$$\frac{dJ_d^k}{dt} = -m_d^k \frac{j_d^k - j_g^k}{t_{\text{stop}}^k}, \quad (3.45)$$

where $U^k \equiv P_g^k/m_g^k$ and $V^k \equiv P_d^k/m_d^k$ denote radial velocity, and $j_g^k \equiv J_g^k/m_g^k$ and $j_d^k \equiv J_d^k/m_d^k$ are specific angular momentum. Assuming m_g^k and m_d^k to be constant, one can analytically solve the above differential equations as follows:

$$P_g^k(t + \Delta t) = P_g^k(t) - [U^k(t) - V^k(t)] f^k(\Delta t), \quad (3.46)$$

$$P_d^k(t + \Delta t) = P_d^k(t) + [U^k(t) - V^k(t)] f^k(\Delta t), \quad (3.47)$$

$$J_g^k(t + \Delta t) = J_g^k(t) - [j_g^k(t) - j_d^k(t)] f^k(\Delta t), \quad (3.48)$$

$$J_d^k(t + \Delta t) = J_d^k(t) + [j_g^k(t) - j_d^k(t)] f^k(\Delta t), \quad (3.49)$$

$$f^k(t) \equiv \frac{m_g^k m_d^k}{m_d^k + m_g^k} \left[1 - \exp\left(\frac{m_d^k + m_g^k}{m_g^k} \frac{t}{t_{\text{stop}}^k} \right) \right], \quad (3.50)$$

where the interval of time integration is from t to $t + \Delta t$. Using these analytical solutions, we update momentums and angular momentums at each region where a dust cell overlaps with a gas cell. Summing up updated values P_g^k , P_d^k , J_g^k , and J_d^k in each cell gives radial linear momentums, $P_{g,i+1/2}^k$ and $P_{d,i+1/2}^k$, and angular momentums, $J_{g,i+1/2}^k$ and $J_{d,i+1/2}^k$, of cell boundaries:

$$P_{g,i+1/2}(t + \Delta t) = \sum_k P_g^k(t + \Delta t), \quad (3.51)$$

$$P_{d,i+1/2}(t + \Delta t) = \sum_k P_d^k(t + \Delta t), \quad (3.52)$$

$$J_{g,i+1/2}(t + \Delta t) = \sum_k J_g^k(t + \Delta t), \quad (3.53)$$

$$J_{d,i+1/2}(t + \Delta t) = \sum_k J_d^k(t + \Delta t), \quad (3.54)$$

This method exactly conserves total linear momentum and total angular momentum.

3.2.3 Methods for turbulent diffusion and viscosity

We implement dust diffusion solver and viscosity solver based on the second-order Runge-Kutta integrator. To calculate the mass flux due to dust diffusion, we first interpolate dust surface density using a quadratic function. We then evaluate $D\partial\Sigma_d/\partial r$ at dust cell boundaries and displace them using velocity $-\Sigma_d^{-1}D\partial\Sigma_d/\partial r$, which corresponds to the diffusion term in Equation (2.1). We keep angular momentums of dust cell boundaries invariant when displacing them because the Lagrangian derivative in the equation for the mean specific angular momentum includes advection along the diffusive flow (Equation (2.32)) and the mass at a cell boundary are constant in time. On the other hand, the radial linear momentum of i th dust cell boundary, $m_{d,i+1/2}v_{r,i+1/2}$, evolves during the diffusion because of the last term on the right hand side of Equation (2.30). We evaluate $F(r) \equiv rv_r D\partial\Sigma_d/\partial r$ at $r = r_{d,i+1}$, $r_{d,i}$, and update $m_{d,i+1/2}v_{r,i+1/2}$ with using $F(r_{d,i+1}) - F(r_{d,i})$, where we omit brackets representing the averaged value for the simplicity. Dust diffusion tends to limit the time step when secular GI collects dust grains in small radial regions and results in spiky structures. To reduce the limitation due to dust diffusion, we adopt the super-time-stepping (STS) (Alexiades et al. 1996) if Δt is limited by dust diffusion. The number of substeps and the stability parameter in the STS scheme are fixed to be 4 and 0.1, respectively. Because the total time step in the STS should be shorter than a timescale “physically” required by dust diffusion, we just moderately accelerate the time stepping.

In the part for viscous evolution, we interpolate radial velocity u_r and specific angular momentum j_g to obtain radial and angular momentum fluxes at $r = r_{g,i+1}$, $r_{g,i}$. In the cylindrical coordinates, the radial and angular momentum changes due to turbulent viscosity are written as follows

$$\left(\frac{\partial\Sigma_g u_r}{\partial t}\right)_{\text{vis}} \equiv \frac{1}{r} \frac{\partial F_{\text{vis},r}}{\partial r} - \frac{2u_r}{3r^3} \frac{\partial r^2 \Sigma \nu}{\partial r}, \quad (3.55)$$

$$\left(\frac{\partial\Sigma_g j_g}{\partial t}\right)_{\text{vis}} \equiv \frac{1}{r} \frac{\partial F_{\text{vis},\phi}}{\partial r}, \quad (3.56)$$

$$F_{\text{vis},r} \equiv \frac{4}{3} r \Sigma \nu \frac{\partial u_r}{\partial r}, \quad (3.57)$$

$$F_{\text{vis},\phi} \equiv r^3 \Sigma \nu \frac{\partial}{\partial r} \left(\frac{u_\phi}{r}\right). \quad (3.58)$$

Spatial integration of the above equations give equations for momentums of i th gas cell boundary $m_{g,i+1/2}u_{r,i+1/2}$ and $m_{g,i+1/2}j_{g,i+1/2}$:

$$\frac{\partial m_{g,i+1/2}u_{r,i+1/2}}{\partial t} = [2\pi F_{\text{vis},r}]_{r_{g,i}}^{r_{g,i+1}} - \frac{4\pi}{3} \int_{r_{g,i}}^{r_{g,i+1}} \frac{u_r}{r^2} \frac{\partial r^2 \Sigma \nu}{\partial r} dr, \quad (3.59)$$

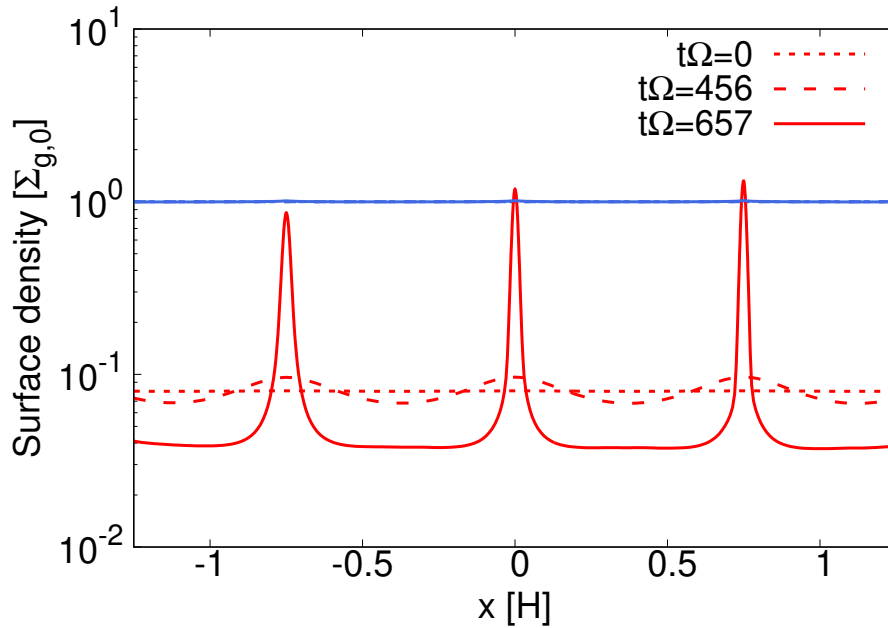


Figure 3.7: Surface density profile normalized by the unperturbed gas surface density and its evolution via secular GI. The horizontal axis is normalized by the assumed gas scale height. Red and blue lines represent surface density of dust and gas, respectively. The short-dashed, long-dashed, and solid lines correspond to the profile at $t\Omega = 0, 456, 657$.

$$\frac{\partial m_{g,i+1/2} j_{g,i+1/2}}{\partial t} = [2\pi F_{\text{vis},\phi}]_{r_{g,i}}^{r_{g,i+1}}, \quad (3.60)$$

where $[A(r)]_{r_1}^{r_2} \equiv A(r_2) - A(r_1)$. We update radial and angular momentums of gas cell boundaries according to Equations (3.59) and (3.60). We evaluate the last term on the right hand side of Equation (3.59) by $-\left(4\pi u_{r,i+1/2}/3r_{g,i+1/2}^2\right) [r^2 \Sigma \nu]_{r_{g,i}}^{r_{g,i+1}}$.

Test simulations on secular GI and TVGI

To validate our numerical methods, we perform test simulations of secular GI and TVGI. As in the test simulations of GI, we use the piecewise polytropic equation of state for gas pressure, and initially set flat surface density profiles for dust ($\Sigma_{d,0}$) and gas ($\Sigma_{g,0}$). The Toomre's Q of gas is set to be 5, and strength of turbulence α is 2×10^{-4} . We also assume that $t_{\text{stop}}\Omega$ is uniform in the domain and set $t_{\text{stop}}\Omega = 0.1$. We consider two values of the dust-to-gas ratio $\Sigma_{d,0}/\Sigma_{g,0}$: 0.08 for a simulation of secular GI and 0.04 for a simulation of TVGI. Although diffusion coefficient D and velocity dispersion c_d have t_{stop} -dependences, those are small for $t_{\text{stop}}\Omega < 1$ and we simply assume $D = \alpha c_s H$ and $c_d = \sqrt{\alpha} c_s$. To guarantee the locality, we place the center of the domain at $r = 80$ au and set 100 time smaller gas scale height H than that for a disk around solar mass

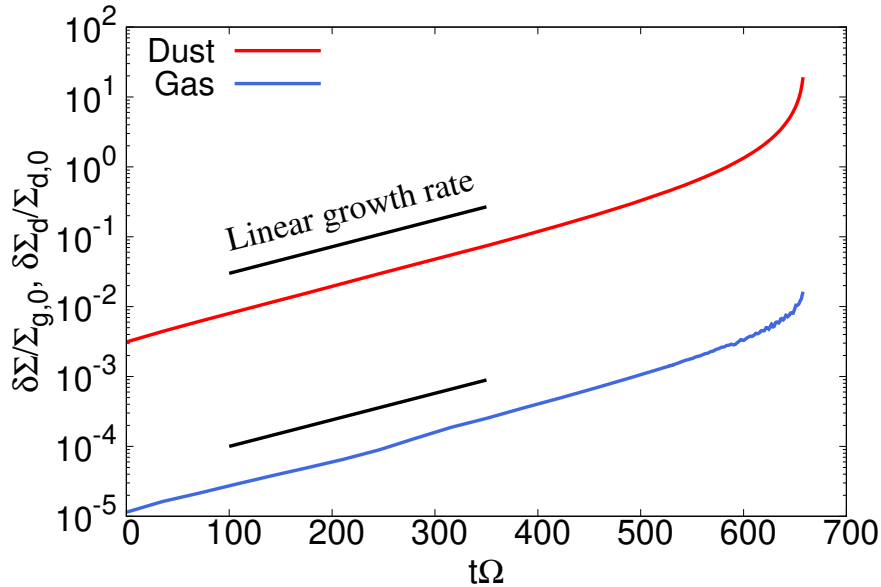


Figure 3.8: Time evolution of surface density peaks of dust (red line) and gas (blue line) via secular GI. The black segments represent the linear growth rate derived from the linear analyses. Numerical simulations reproduce the linear growth of secular GI.

star. The domain width is 4 times the most unstable wavelength. We adopt periodic boundary condition for dust and gas surface density profiles, which we utilize to calculate self-gravity. The number of cells is 512 for both dust and gas, and the domain is equally spaced. The softening length is initially set to be one fourth of the cell width. To follow nonlinear evolution, we change the softening length in time at a region of positive surface density perturbations and reset the length to be one fourth of the cell width at each time. The time step is set based on the following:

$$\Delta t = \min(\Delta t_g, \Delta t_d, \Delta t_{\text{diff}}, \Delta t_{\text{vis}}), \quad (3.61)$$

where Δt_g and Δt_d are the time steps determined by the Courant-Friedrich-Levy (CFL) condition for gas and dust equations without the dust diffusion or the viscosity, Δt_{diff} and Δt_{vis} are those determined by the diffusion term and the viscosity term: $\Delta t_{\text{diff}} = 0.125 \times \min((r_{d,i+1/2} - r_{d,i-1/2})^2/D)$, and $\Delta t_{\text{vis}} = 0.125 \times \min((r_{g,i+1/2} - r_{g,i-1/2})^2/\nu)$. The CFL number is set to be 0.5.

Figure 3.7 shows dust and gas surface density evolution via secular GI. The amplitude $\delta\Sigma_d/\Sigma_{d,0}$ is larger by an order of magnitude than $\delta\Sigma_g/\Sigma_{g,0}$. Secular GI concentrates dust into narrow regions with a width of $\ll H$ while its linear growth proceeds at a wavelength $\sim H$. The resultant concentration increases dust-to-gas ratio above unity in the dust rings. Figure 3.8 shows the time evolution of the surface density peak. The black segment

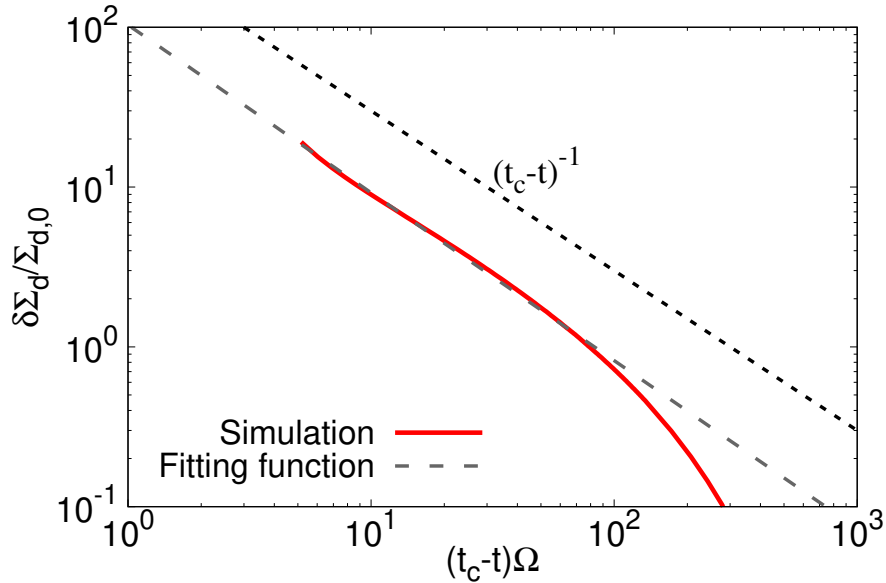


Figure 3.9: Dust surface density evolution at the nonlinear growth phase. The horizontal axis is the looking-back time from the collapse time t_c obtained by fitting the data. The divergent nature with proportional to $(t_c - t)^{-1}$ is consistent with the freefall collapse of a self-gravitating ring.

represents the linear growth rate obtained from the linear analyses. The numerical results at the long-term linear growth until $t\Omega \simeq 500$ are in good agreement with the linear analyses, which validates the efficiency of our scheme for exploring long-term evolution even in the presence of the friction.

The simulation shows divergent behavior at the nonlinear growth phase of secular GI. To understand the physics of the nonlinear growth, we fit the dust surface density evolution in $500 \leq t\Omega \leq 670$ using the power-law function:

$$\frac{\delta\Sigma_d}{\Sigma_{d,0}} = \frac{a}{(t_c\Omega - t\Omega)^b}, \quad (3.62)$$

where a , b , t_c are parameters. The time t_c represents collapse time. The fitting gives $a = 103 \pm 5$, $b = 1.05 \pm 0.01$, and $t_c\Omega = 663.0 \pm 0.1$. Figure 3.9 shows the resultant fitting function and the original data. The density evolution is almost proportional to $(t_c - t)^{-1}$. This behavior originates from gravitational collapse of a ring as explained below. A timescale of self-gravitational collapse is given by the freefall time: $t_{\text{ff}} \sim 1/\sqrt{G\rho_d}$. Assuming $\Sigma_d \sim \rho_d\lambda_J$ where $\lambda_J \sim c_d/\sqrt{G\rho_d}$ is the Jeans length, one obtains $\Sigma_d \sim c_d/G \times t_{\text{ff}}$. Thus, dust surface density increases with being proportional to $(t_c - t)^{-1}$.

Figures 3.10 and 3.11 show results of the test simulation of TVGI. TVGI also concentrates dust into thin rings through its nonlinear growth. Although the growth timescale

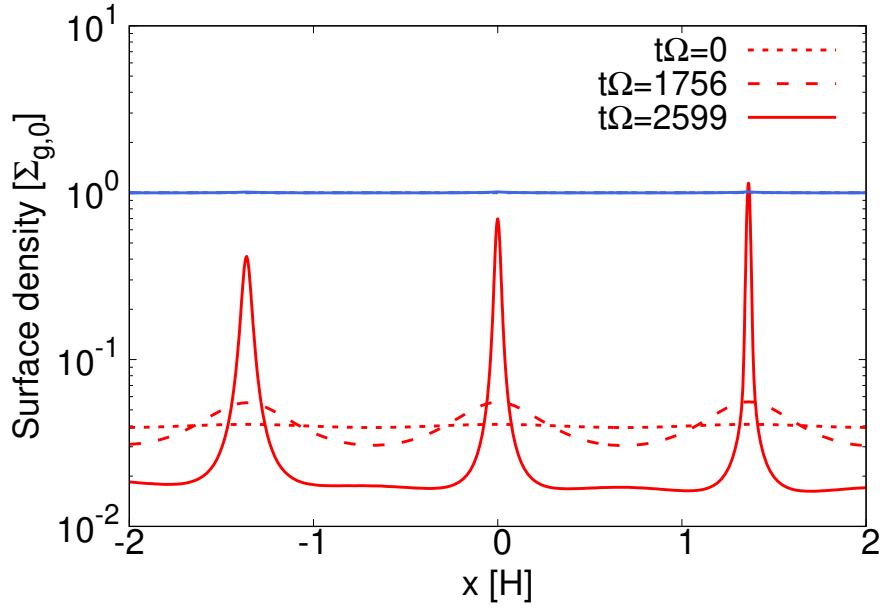


Figure 3.10: Surface density profile normalized by the unperturbed gas surface density and its evolution via secular GI. The horizontal axis is normalized by the assumed gas scale height. Red and blue lines represent surface density of dust and gas, respectively. The short-dashed, long-dashed, and solid lines correspond to the profile at $t\Omega = 0, 1756, 2599$.

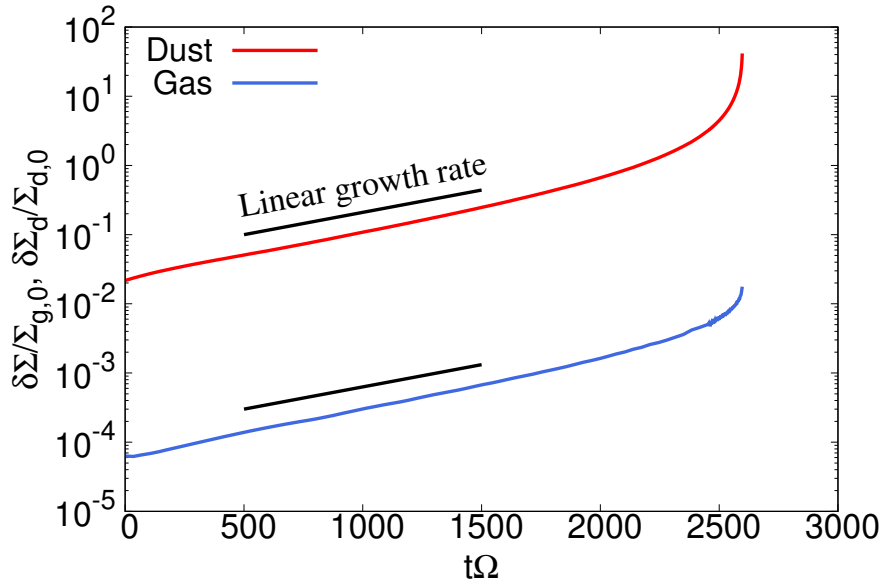


Figure 3.11: Time evolution of surface density peaks of dust (red line) and gas (blue line) via TVGI. The black segments represent the linear growth rate derived from the linear analyses. Numerical simulations reproduce the slow linear growth of TVGI.

of TVGI is much longer than secular GI, our scheme can trace such a long-term linear growth until $t\Omega \simeq 2250$ and the result shows in good agreement with the linear analyses. This validates the efficiency of our scheme.

3.3 Simulations of radially extended disks

Using the method in the previous section, we investigate evolution of radially extended disks via secular GI using Equations (2.4) (2.35), (2.1), (2.37), (2.38), and (2.36), which are summarized at the beginning of this chapter.

Because secular GI requires friction to operate, a dust layer around the midplane seems to be the most important region, which is also discussed in the linear analyses presented in Chapter 2. Gas above the dust layer will also contribute to the growth of secular GI via the gravitational interaction although its frictional interaction with dust is relatively weak. In the present study, we thus adopt Equations (2.4) (2.35), (2.1), (2.37), (2.38), and (2.36) for a “lower layer” that includes those dust and gas driving secular GI. As also mentioned in Section 2.4, the vertical extent of such a lower layer is unknown unless one perform multidimensional analyses. Hereafter, we do not concern the vertical extent since it is beyond the scope of this study.

Setups

The initial inner boundaries for dust and gas are set at 10 au. We use 1024 cells for both dust and gas and space the radial domain so that each cell has the same mass. Such a spacing gives the outer boundaries located at $r \simeq 300$ au. We fixed the gas and dust outer boundaries in simulations. We let the gas inner boundary move so that the inner most gas surface density is constant in time. On the other hand, we allow dust cells to move to the inner region of $r < r_{g,1}$ where $r_{g,1}$ denotes the radius of the first gas cell center. The radial velocities of those inner dust cells are fixed to the steady drift velocity (e.g., Nakagawa et al. 1986) estimated for the initial density profiles at $r = r_{g,1}$. When calculating self-gravity, we weakens the individual-ring gravity using a softening length of half cell’s width (~ 0.1 au), and rescale it when the cell width becomes larger in time.

3.3. SIMULATIONS OF RADIALY EXTENDED DISKS

Table 3.1: Summary of parameters and results originally from Table 1 of Tomi-
naga et al. (2020)

Label	Q_{100}^a	α	Results	t_{fin}^b
Q4a10	4	1×10^{-3}	thin dense dust rings	2.1×10^4 yr
Q4a20	4	2×10^{-3}	transient low-contrast rings	5.9×10^4 yr
Q5a5	5	5×10^{-4}	thin dense dust rings	1.9×10^4 yr
Q5a8	5	8×10^{-4}	transient low-contrast dust rings	5.6×10^4 yr
Q5a8L ^c	5	8×10^{-4}	thin dense dust rings	2.5×10^4 yr
Q6a3	6	3×10^{-4}	thin dense dust rings	2.7×10^4 yr
Q6a5	6	5×10^{-4}	transient low-contrast dust rings	6.2×10^4 yr

^a Toomre’s Q value for the lower layer of a gas disk at $r = 100$ au

^b Time that simulations last for

^c The letter “L” means a run with six times larger perturbations

We consider disks around $1M_{\odot}$ mass star, and set the initial gas and dust surface density profiles by the following power law function:

$$\Sigma_g(r) = \Sigma_{g,100} \left(\frac{r}{100 \text{ au}} \right)^{-q} \exp \left(-\frac{r}{100 \text{ au}} \right), \quad (3.63)$$

$$\Sigma_d(r) = \Sigma_{d,100} \left(\frac{r}{100 \text{ au}} \right)^{-q} \exp \left(-\frac{r}{100 \text{ au}} \right), \quad (3.64)$$

where $\Sigma_{g,100}$ and $\Sigma_{d,100}$ are constants. In this study, we use the Toomre’s Q value of gas ($Q = c_s \Omega / \pi G \Sigma_g$) to show how massive the lower layer is. One obtains Σ_{100} from the Q value at $r = 100$ au (Table 3.1), Keplerian angular velocity and the temperature shown below. The dust surface density at $r = 100$ au is determined by the assumed initial dust-to-gas ratio in the lower layer Σ_d / Σ_g . We note that Σ_d / Σ_g represents the dust-to-gas mass ratio averaged in the lower layer, which is different from $\Sigma_{d,\text{tot}} / \Sigma_{g,\text{tot}}$ where $\Sigma_{d,\text{tot}}$ and $\Sigma_{g,\text{tot}}$ are total surface densities of dust and gas disks including both upper and lower layers. In weakly turbulent gas disks, Σ_d / Σ_g easily becomes higher than $\Sigma_{d,\text{tot}} / \Sigma_{g,\text{tot}}$ by an order of magnitude. In this work, considering dust rich disks $\Sigma_{d,\text{tot}} / \Sigma_{g,\text{tot}} = 0.05$, we assume $\Sigma_d / \Sigma_g = 0.1$. According to Kitamura et al. (2002), disks observed around T Tauri stars have density profiles with the power-law index between 0-1 in most cases. Motivated by this study, we take the median value and fix $q = 0.5$ in the present simulations.

In our simulations, a gas disk is assumed to be locally isothermal, and its temperature profile $T(r)$ is

$$T(r) = 10 \text{ K} \left(\frac{r}{100 \text{ au}} \right)^{-1/2}, \quad (3.65)$$

3.3. SIMULATIONS OF RADIALLY EXTENDED DISKS

where we mimic a disk passively heated by the stellar radiation (e.g., Chiang & Goldreich 1997). We calculate the sound speed c_s at each radius assuming the molecular weight to be 2.34. The gas scale height is $H \simeq 6.3 \text{ au} (r/100\text{au})^{5/4}$. We set the initial azimuthal velocity based on the radial force balance without friction, diffusion or viscosity.

The dimensionless stopping time $t_{\text{stop}}\Omega$ is one important parameter characterizing the growth of secular GI. Although it is important to explicitly implement dust growth in our code and explore the coevolution of dust grains and secular GI, we focus only on secular GI in radially global disks and assume a uniform $t_{\text{stop}}\Omega$ profile to make the problem simple. Because a timescale of the dust coagulation is expected to be shorter than that of secular GI when dust grains are small (see Takahashi & Inutsuka 2014), dust grains will grow up to the drift-limited size (see also, Okuzumi et al. 2012). The drift-limited value can be regarded as a maximum value expected from the direct bottom-up coagulation. We thus adopt the drift-limited $t_{\text{stop}}\Omega$, which is about 0.6 for $\Sigma_{\text{d,tot}}/\Sigma_{\text{g,tot}} = 0.05$ (see Appendix A). We do not consider fragmentation-limited dust sizes because we are focusing on dynamics at outer region in weakly turbulent gas disks (see also, Birnstiel et al. 2009 2012).

Although the diffusion coefficient D and the velocity dispersion c_d depend on $t_{\text{stop}}\Omega$ and α (Youdin & Lithwick 2007), those are well approximated by $D \simeq \alpha c_s^2 \Omega^{-1}$ and $c_d \simeq \sqrt{\alpha} c_s$ for $t_{\text{stop}}\Omega < 1$, which are also used in the test simulations. Thus we use those relations in the present simulations for simplicity. In this study, we perform numerical simulations with different Toomre's Q values and strength of turbulence α . We summarize the parameters in Table 3.1.

Our choice of the parameters is optimistic to study and understand physics of radially global secular GI and its nonlinear outcomes. For example, disks are massive. On the other hand, disk masses and dust-to-gas surface density ratio $\Sigma_{\text{d,tot}}/\Sigma_{\text{g,tot}}$ are not well-constrained by observations partly because of uncertainties in dust opacity. In addition, recent work shows that neglecting scattering effects of dust thermal emissions underestimates dust masses in a disk (Zhu et al. 2019). We thus assume massive disks where secular GI relatively easily grows in our simulations. The situations might correspond to early disks if dust grains can grow up to the drift-limited sizes in the early phase.

We put initially random perturbations to positions of the cell boundaries and their velocity. Amplitudes of the position and velocity perturbations are five percent of the cell widths and c_d , respectively.

3.3. SIMULATIONS OF RADIALLY EXTENDED DISKS

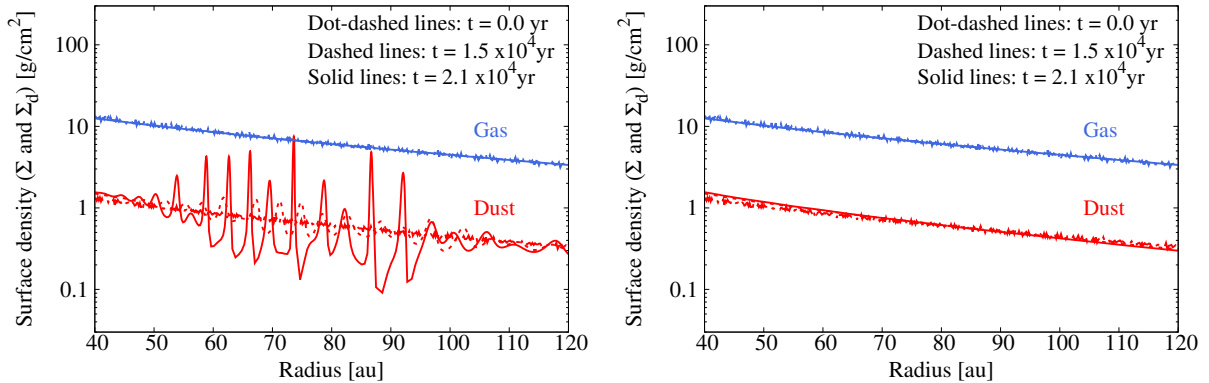


Figure 3.12: (Left panel) Surface density evolution from Q4a10 run. Multiple dust rings and gaps form within 10^4 yr. (Right panel) Surface density evolution from a run where we use the same parameters as in Q4a10 run and switch off self-gravity. In both panels, red and blue lines show dust and gas surface densities. The dotted-dashed, dashed and solid lines show snapshots at $t=0.0$ yr, 1.5×10^4 yr and 2.1×10^4 yr, respectively. We note that the classical GI is stable in this simulation because of the dust diffusion, meaning that the multiple ring-gap formation is result from secular GI. This figure is originally from Figure 1 of Tominaga et al. (2020).

Results

We overview the results of our simulations. The results show two regimes of the disk evolution via secular GI: formation of “thin dense dust rings” and “transient low-contrast dust rings” (see also Table 3.1). In the following, we show those results in detail.

Formation of Thin Dense Dust Rings

Figure 3.12 shows time evolution of dust and gas surface densities from Q4a10 run. We also show the surface density evolution from a run in which we switch off self-gravity to eliminate secular GI. Note that the gas disk is self-gravitationally stable and the dust GI is also stabilized because of dust diffusion within the set of the parameters. The results show formation of multiple dust rings and gaps only when we switch on self-gravity. Thus, the ring-gap formation is associated with secular GI. Secular GI grows at wavelengths $\sim c_s/\Omega$, resulting in the ring-gap formation in the dust disk (see the dashed line in Figure 3.12). Nonlinear growth of secular GI makes the resultant rings much thinner as in the test simulations, and the dust surface density increases by a factor of $\simeq 10$.

On the left panel of Figure 3.13, we show trajectories of dust cells that compose the resultant rings and gaps. The red dashed line shows the trajectory of the 525th cell as a reference cell in one dust ring. We note that a reduced number of cells are shown on the left panel of Figure 3.13. Because our numerical scheme is based on the Lagrangian-cell

3.3. SIMULATIONS OF RADIALY EXTENDED DISKS

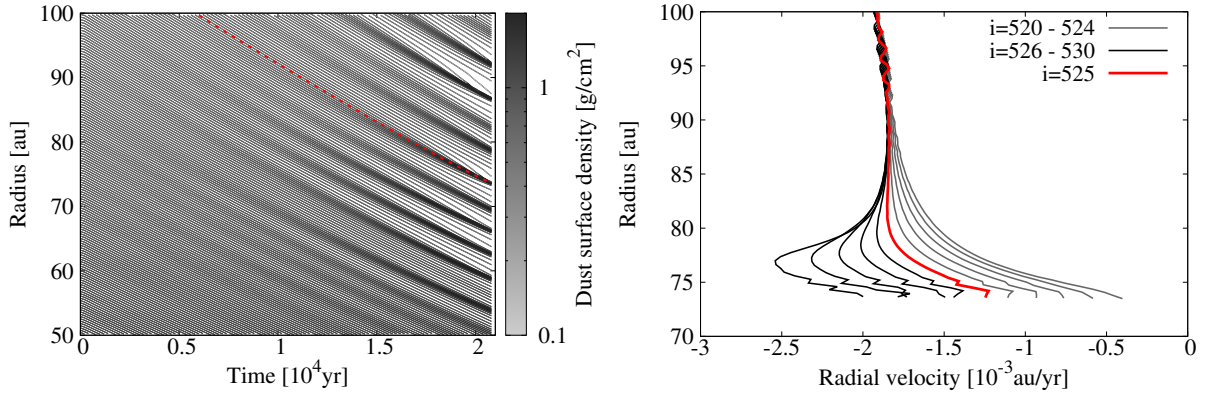


Figure 3.13: (Left) Trajectories of dust cells in Q4a10 run. Color of each line shows dust surface density at each dust cell. We used a reduced number of cells to plot this figure. Red dashed line is the trajectory of the 525th dust cell. (Right) The radial velocity of some dust cell boundaries ($r = r_{d,i+1/2}$ where $i = 520 - 530$) at each radius. The 525th cell boundary whose trajectory is shown in red roughly corresponds to the ring peak position. The inner and outer cells are shown in gray and black, respectively. The spreading of the lines in $v_r - r$ plane represents the collapsing toward the ring center. At the radius $\simeq 77$ au, the gravitational softening suppresses the accelerated collapse. At $r \lesssim 77$ au, the drift speed decreases as Σ_d/Σ_g increases. This figure is originally from Figure 2 of Tominaga et al. (2020)

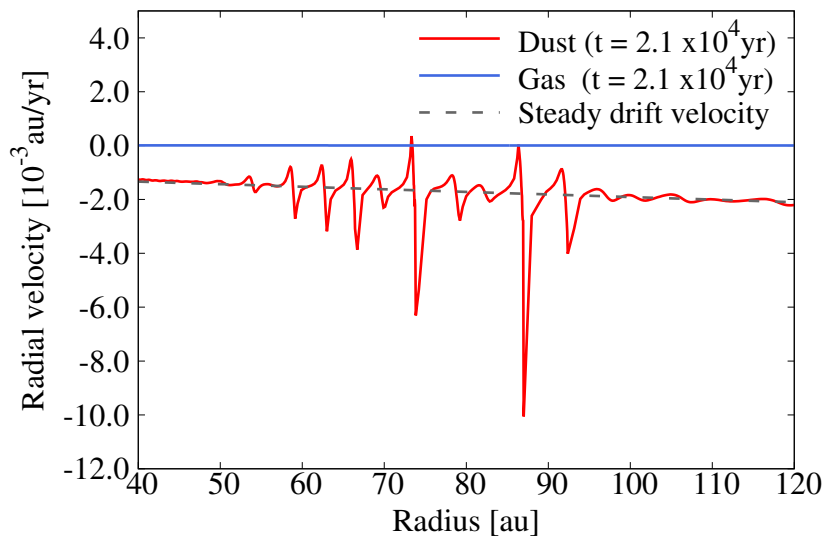


Figure 3.14: Radial velocity profile at $t = 2.1 \times 10^4$ yr in Q4a10 run. Red and blue lines show dust and gas radial velocities, respectively. The gray dashed line shows the steady drift velocity of dust v_{dri} (Nakagawa et al. 1986). The mean dust velocity is in good agreement with the steady drift velocity. The gas has small positive velocity because of frictional back-reaction from the dust drift. This figure is originally from Figure 3 of Tominaga et al. (2020)

3.3. SIMULATIONS OF RADIALLY EXTENDED DISKS

method, the motion of cells represents actual motion of dust, and a cell-concentrating region corresponds to a high density region. The dust initially moves inward with the steady drift velocity v_{dri} (Figure 3.14)

$$v_{\text{dri}} \equiv -\frac{2t_{\text{stop}}\Omega}{(1 + \varepsilon_0)^2 + (t_{\text{stop}}\Omega)^2}\eta' r\Omega, \quad (3.66)$$

where ε_0 is the initial surface density ratio $\Sigma_{\text{d}}/\Sigma_{\text{g}}$ and

$$\eta' \equiv -\frac{c_{\text{s}}^2}{2r^2\Omega^2} \frac{\partial \ln(c_{\text{s}}^2\Sigma)}{\partial \ln r}. \quad (3.67)$$

Note that Equation (3.66) is different from Equation (1.14). Since we use vertically integrated equations, the steady drift velocity depends not on η and ϵ but on η' and ε . Those drifting dust finally concentrates into the rings via secular GI. One can see that the dust density perturbations also move inward with the drift velocity.

The significant dust concentration ($t = 1.3 \times 10^5$ yr) results from the self-gravitational ring collapse that is discussed in the test calculations and in Tominaga et al. (2018). On the right panel of Figure 3.13, we plot radial velocities of dust cell boundaries ($r(t) = r_{\text{d},i+1/2}$) that compose one dust ring ($i = 520 - 530$). The red curve shows trajectory of the 525th dust cell boundary in the $v_r - r$ plane. Those dust cells initially move inward with the drift velocity. As secular GI grows ($r \gtrsim 77$ au), the radial velocities deviate from the drift velocity, and the lines spread in the $v_r - r$ plane. When the dust cell width becomes smaller than the gravitational softening length, the softening weakens the radial collapse (e.g., $r \simeq 77$ au for $i = 526 - 530$). Because the dust-to-gas surface density ratio increases, the radial velocities of those cell boundaries gradually decreases.

Figure 3.15 shows the cumulative dust mass $M_{\text{d}}(< r)$. From the height of “cliffs” on each line, one can roughly evaluate dust-ring masses from Figure 3.15 and find that the large amounts (\sim tens of M_{\oplus}) of dust reside in the individual ring. Summing up masses of dust cells between the adjacent local minima in the dust surface density, we estimate a mass of the i th ring ($M_{\text{ring},i}$) whose radius is defined as the radius of the local maximum in dust surface density. We then compare the dust disk mass M_{d} and the total ring mass $M_{\text{ring,tot}} \equiv \sum_{i=1}^{N_{\text{ring}}} M_{\text{ring},i}$, where N_{ring} is the number of the dust rings whose amplitudes are increasing or saturated at a certain time. In order to discuss the ring mass fraction, we set a certain radius denoted by $R_{\text{d,out}}$ and use dust cells whose initial radii are smaller than $R_{\text{d,out}}$ to calculate M_{d} and $M_{\text{ring,tot}}$. We calculate the ring masses at the time when dust-to-gas mass ratio in one of the dust rings exceeds unity.

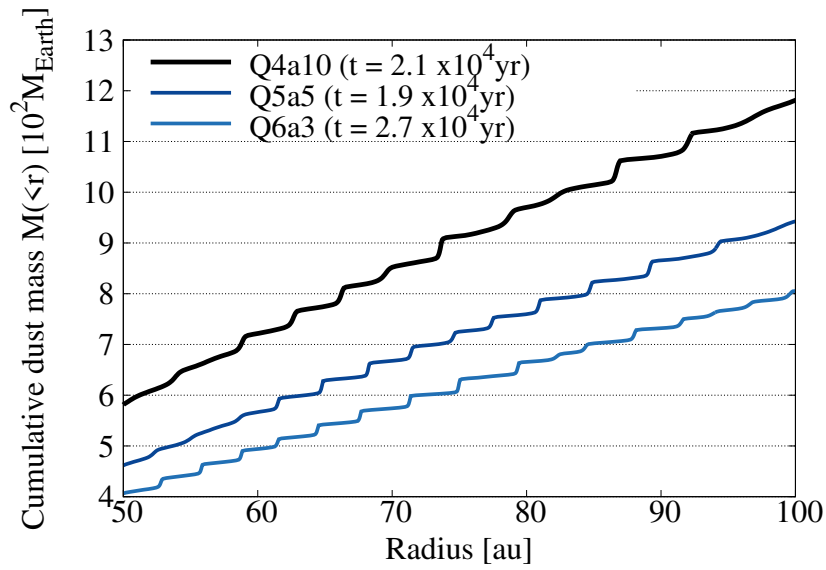


Figure 3.15: Cumulative dust mass $M(< r)$ obtained from Q4a10, Q5a5 and Q6a3 runs. Thick black line corresponds to Q4a10 run, from which we obtain the surface density evolution in Figure 3.12. Positions of cliffs correspond to dust ring radii, and the height of the each cliff corresponds to dust mass in each ring, from which one can see that the mass of the individual dust ring is $\gtrsim 10M_{\oplus}$. This figure is originally from Figure 4 of Tominaga et al. (2020).

3.3. SIMULATIONS OF RADIALLY EXTENDED DISKS

Table 3.2: List of the evaluated masses originally from Table 2 of Tominaga et al. (2020)

Label and Time	$R_{d,out} = 120$ au			$R_{d,out} = 200$ au		
	$M_{ring,tot} [M_{\oplus}]$	$M_d [M_{\oplus}]$	$M_{ring,tot}/M_d$	$M_{ring,tot} [M_{\oplus}]$	$M_d [M_{\oplus}]$	$M_{ring,tot}/M_d$
Q4a10 ($t = 2.0 \times 10^4$ yr)	4.7×10^2	1.2×10^3	0.38	8.5×10^2	1.8×10^3	0.46
Q5a5 ($t = 1.6 \times 10^4$ yr)	4.5×10^2	9.8×10^2	0.46	7.4×10^2	1.4×10^3	0.51
Q5a8L ($t = 2.3 \times 10^4$ yr)	3.2×10^2	9.8×10^2	0.33	6.9×10^2	1.4×10^3	0.47
Q6a3 ($t = 1.8 \times 10^4$ yr)	3.5×10^2	8.1×10^2	0.42	7.3×10^2	1.2×10^3	0.60

Table 3.3: List of the evaluated masses originally from Table 3 of Tominaga et al. (2020)

Label and Time	$R_{d,in} = 60$ au, $R_{d,out} = 120$ au			$R_{d,in} = 60$ au, $R_{d,out} = 200$ au		
	$M_{ring,tot} [M_{\oplus}]$	$M_d [M_{\oplus}]$	$M_{ring,tot}/M_d$	$M_{ring,tot} [M_{\oplus}]$	$M_d [M_{\oplus}]$	$M_{ring,tot}/M_d$
Q4a10 ($t = 2.0 \times 10^4$ yr)	4.7×10^2	6.5×10^2	0.72	8.5×10^2	1.2×10^3	0.68
Q5a5 ($t = 1.6 \times 10^4$ yr)	4.5×10^2	5.2×10^2	0.85	7.4×10^2	9.9×10^2	0.75
Q5a8L ($t = 2.3 \times 10^4$ yr)	3.2×10^2	5.2×10^2	0.62	6.9×10^2	9.9×10^2	0.69
Q6a3 ($t = 1.8 \times 10^4$ yr)	3.5×10^2	4.3×10^2	0.79	7.3×10^2	8.2×10^2	0.88

The results for $R_{d,out} = 120$ au and 200 au are summarized in Table 3.2 originally from Table 2 of Tominaga et al. (2020). We find that secular GI can convert tens of percent of the dust mass into ring mass. The ring mass $M_{ring,tot}$ increases as increasing $R_{d,out}$ because dust drifting from the outer disk are concentrated into rings at inner region (see Figure 3.13).

The mass M_d includes the mass of dust initially located at the secular-GI-stable region (see also Section 3.4). Those dust grains never concentrate into rings. Thus, the mass fraction $M_{ring,tot}/M_d$ will increase if one excludes those dust grains from the estimation. Table 3.3 originally from Table 3 of Tominaga et al. (2020) summarizes $M_{ring,tot}$, M_d and $M_{ring,tot}/M_d$ for dust grains initially at an unstable region $R_{d,in} \leq r \leq R_{d,out}$, where we set $R_{d,in} = 60$ au because secular GI can grow at $r > 60$ au in all runs. Over half of the dust masses are collected into the rings in most of the runs. Especially, 88 percent of the dust grains are saved in the dust rings in the case of Q6a3 run with $R_{d,in} = 60$ au and $R_{d,out} = 200$ au.

The dust-to-gas mass ratio in the ring becomes comparable to or higher than unity, which makes the dust drift velocity smaller (see also the right panel of Figure 3.13). The increase in dust surface density is saturated because of the balance between diffusion and self-gravitational collapse. Figure 3.16 compares two velocities around one dust ring with a radius of $r \simeq 73.6$ au at $t = 2.1 \times 10^4$ yr: (1) dust velocity with respect to the ring velocity $v_{ring} = -1.5 \times 10^{-3}$ au/yr that we measured from the data and (2) the velocity due to dust diffusion $v_{diff} \equiv -D\Sigma_d^{-1}\partial\Sigma_d/\partial r$. The red line shows the sum

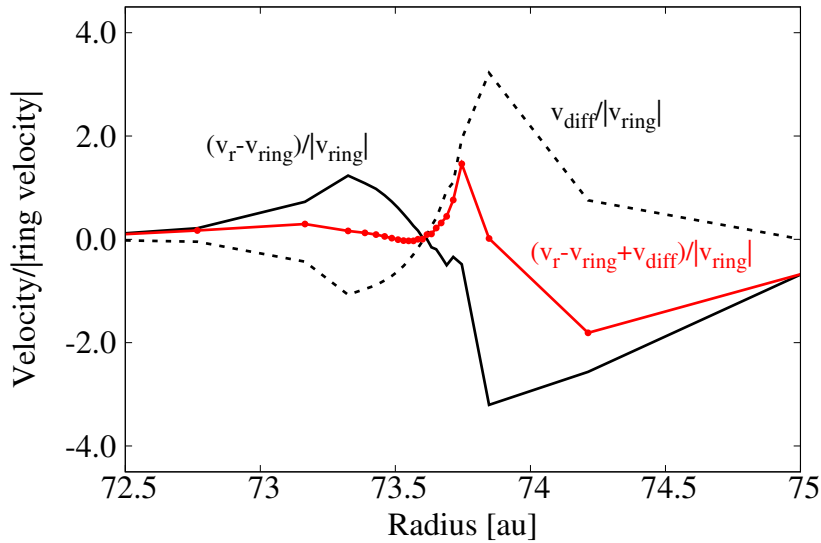


Figure 3.16: Radial velocity profile normalized by the ring velocity v_{ring} at $t = 2.1 \times 10^4$ yr in Q4a10 run. Black solid line shows the dust velocity with respect to the ring velocity, $v_r - v_{\text{ring}}$. Black dashed line shows the velocity $v_{\text{diff}} \equiv -D\Sigma_d^{-1}\partial\Sigma_d/\partial r$. Red line with filled circles showing the data point is the sum $v_r - v_{\text{ring}} + v_{\text{diff}}$. This figure is originally from Figure 5 of Tominaga et al. (2020).

of them. The red filled circles in the Figure 3.16 are the data points, which show that the dusty ring is well resolved while the adjacent gaps are not. In the well-resolved dust ring, we find $|v_r - v_{\text{ring}}| \simeq |v_{\text{diff}}| > |v_r - v_{\text{ring}} + v_{\text{diff}}|$, meaning that dust diffusion prevents further self-gravitational collapse. Especially, one can see the equilibrium at the inner half of the well-resolved ring. At the outer half of the ring, the red line shows an increasing trend. This means that the radially converging flow is slower than the diffusive flow. This slow converging flow results from the deceleration due to the last term on the right hand side of Equation (2.37), i.e., $r^{-1}\partial F(r)/\partial r$ where $F(r) = rv_r D\partial\Sigma_d/\partial r$. Figure 3.17 compares the four forces per mass exerted on dust: self-gravity, pressure gradient force ($\Sigma_d^{-1}c_d^2\partial\Sigma_d/\partial r$), the sum of the curvature term and the stellar gravity, and $\Sigma_d^{-1}r^{-1}\partial F(r)/\partial r$. The magnitude of $\Sigma_d^{-1}r^{-1}\partial F(r)/\partial r$ is comparable to that of the self-gravity, meaning that the term decelerates the radial speed of dust coming from the outer gap toward the ring.

Because the constant gravitational softening term weakens self-gravity, the final dust surface density might be underestimated¹. To check whether the dust surface density

¹The actual finite thickness of the disk slightly weakens the self-gravity for short-wavelength modes (Shu 1984, Vandervoort 1970), and the softening term is expected to account for this effect to some

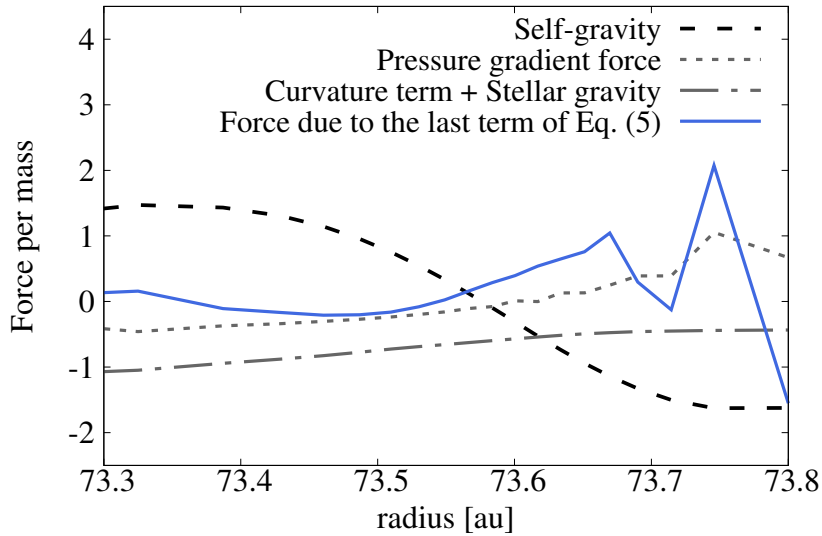


Figure 3.17: Radial profile of the forces per mass exerted on dust in the ring with radius of $\simeq 73.6$ au. The vertical axis is normalized by $10^{-6}GM_{\odot}/(1 \text{ au})^2$. We only plot the self-gravity (black dashed line), the pressure gradient force ($\Sigma_{\text{d}}^{-1}c_{\text{d}}^2\partial\Sigma_{\text{d}}/\partial r$, gray short dashed line), the sum of the curvature term and the stellar gravity (gray dot-dashed line), and the force coming from the last term on the right hand side of Equation (2.37), i.e., $\Sigma_{\text{d}}^{-1}r^{-1}\partial F(r)/\partial r$ where $F(r) = rv_r D\partial\Sigma_{\text{d}}/\partial r$ (blue solid line). At the outer half of the ring, the third term becomes comparable to self-gravity, and decelerates the radial converging speed toward the ring center. This figure is originally from Figure 6 of Tominaga et al. (2020). Note that the legend of the blue line is based on the numbering of equations in Tominaga et al. (2020).

3.3. SIMULATIONS OF RADIALLY EXTENDED DISKS

is underestimated or not, we evaluate a resultant dust surface density $\Sigma_{d,f}$ which one would obtain if the gravitational softening is neglected. The diffusion timescale becomes comparable to the gravitational-collapse timescale when nonlinear growth is saturated:

$$D^2 k_c^4 \sim 2\pi G \Sigma_{d,f} k_c, \quad (3.68)$$

where k_c^{-1} represents the length scale of a spiky ring. This gives $k_c \sim (2\pi G \Sigma_{d,f} / D^2)^{1/3}$. Assuming that a ring mass does not change throughout the linear and nonlinear growth, one has a relation between the dust surface density and the wavenumber: $\Sigma_{d,f} / k_c = \Sigma_{d,0} / k_0$, where $\Sigma_{d,0}$ and k_0 denote the unperturbed dust surface density and the wavenumber at which secular GI grows in the linear phase, respectively. Using this relation and Equation (3.68), one obtains

$$\begin{aligned} \frac{\Sigma_{d,f}}{\Sigma_{d,0}} &= \left(\frac{2\pi G \Sigma_{d,0}}{D^2} \right)^{\frac{1}{2}} k_0^{-\frac{3}{2}} \\ &\simeq 9.3 \left(\frac{\Sigma_{d,0} / \Sigma_{g,0}}{0.1} \right)^{\frac{1}{2}} \left(\frac{\alpha}{1 \times 10^{-3}} \right)^{-1} \left(\frac{Q}{4.5} \right)^{-\frac{1}{2}} \left(\frac{k_0 H}{8} \right)^{-\frac{3}{2}}, \end{aligned} \quad (3.69)$$

where $\Sigma_{g,0}$ is the unperturbed gas surface density. This estimation is in good agreement with the resultant dust density of the ring at $r \simeq 73.6$ au in Q4a10 run (see Figure 3.12). When the assumed α is smaller, numerical simulations with the constant softening length would underestimate $\Sigma_{d,f}$.

Formation of Transient Low-Contrast Dust Rings

Figure 3.18 shows the surface density and radial velocity profiles from Q5a8 run. Dust rings and gaps form at $t = 3.2 \times 10^4$ yr. However, these structures decay as they move inward, which is in contrast to Q4a10 run (Figure 3.12). The mean radial velocity of dust is in good agreement with the steady drift velocity as in the other runs. The relative motion with respect to the radial drift is so low that dust grains are insignificantly concentrated. As a result, the dust rings drift further without achieving a significant increase in dust-to-gas mass ratio.

The decay of the dust substructures can be clearly seen in Figure 3.19 where we show deviation of Σ_d from the initial profile $\Sigma_d(t=0)$ as a function of radius and time. The perturbations with a wavelength of $\simeq 5$ au grow while they drift inward from $r \gtrsim 100$ au. Their amplitudes decrease after they cross $r \simeq 60$ – 70 au. Q4a20 and Q6a5 runs

extent. Thus, the following estimation of the dust surface density might be regarded as a reasonable upper limit.

3.3. SIMULATIONS OF RADIALLY EXTENDED DISKS

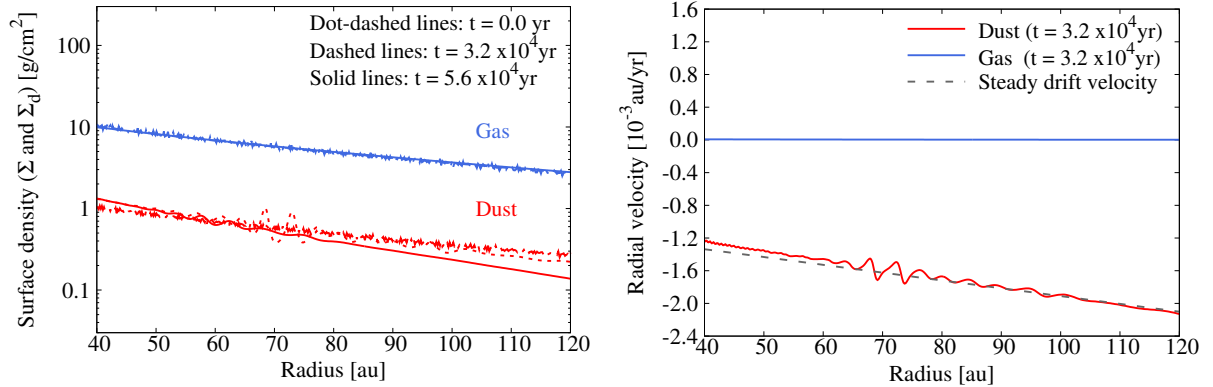


Figure 3.18: (Left panel) Dust and gas surface density profiles at $t = 0.0$ yr (dot-dashed line), 3.2×10^4 yr (dashed line) and 5.6×10^4 yr (solid line) from Q5a8 run. Although dust rings and gaps form, their contrast is low compared to the rings and the gaps in Q4a10 run (Figure 3.12). Those substructures decay while drifting inward. (Right panel) Dust and gas radial velocity profiles at $t = 3.2 \times 10^4$ yr. The gray line is the steady dust drift velocity (Nakagawa et al. 1986). The mean radial velocity of the dust is in good agreement with the steady drift velocity as in Figure 3.14 (Q4a10 run). In contrast, the relative motion with respect to the drift is insignificant. This figure is originally from Figure 7 of Tominaga et al. (2020).

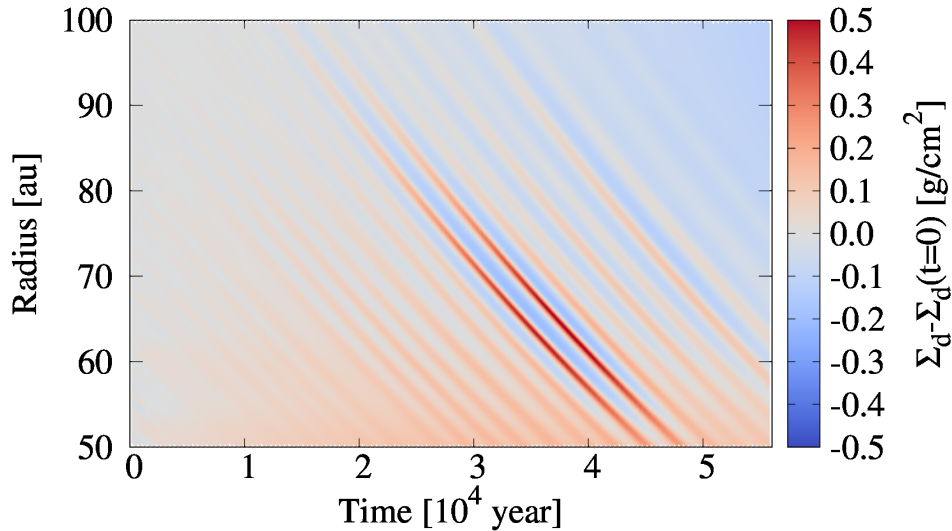


Figure 3.19: Deviation of dust surface density Σ_d from the initial value $\Sigma_d(t=0)$ as a function of radius and time in Q5a8 run. One can see the radial perturbations moving inward. Those patterns become faint after they enter an inner region $r \lesssim 65$ au. This figure is originally from Figure 8 of Tominaga et al. (2020).

also show formation of such transient low-contrast rings and gaps. In those cases, the unstable region is so small that the dust moves across the unstable region without a significant increase in the surface density, which is discussed in the next section.

3.4 Discussion

3.4.1 Linear analyses with dust drift

To understand the physics seen in the numerical results, we perform linear analyses including the radial drift of dust. We also show which mode becomes secular GI in the dust-drifting system. Although the simulations treat both dust and gas, we begin with one-fluid (dust) linear analyses to readily understand mode properties of secular GI. The simplified analysis seems valid for qualitative comparison with two-component simulations because the gas disk does not significantly evolve in our simulations. Two-fluid linear analyses are described later.

As in the previous chapter, we explore the linear stability in the local coordinates (x, y) rotating around the central star with the angular velocity $\Omega_0 = \Omega(r = R)$. Basic equations for dust are the following:

$$\frac{\partial \Sigma_d}{\partial t} + \frac{\partial}{\partial x} (\Sigma_d v_x) = D \frac{\partial^2 \Sigma_d}{\partial x^2}, \quad (3.70)$$

$$\begin{aligned} \frac{\partial v_x}{\partial t} + \left(v_x - \frac{D}{\Sigma_d} \frac{\partial \Sigma_d}{\partial x} \right) \frac{\partial v_x}{\partial x} = & 3\Omega_0^2 x + 2\Omega_0 v_y - \frac{c_d^2}{\Sigma_d} \frac{\partial \Sigma_d}{\partial x} - \frac{\partial \Phi}{\partial x} \\ & - \frac{v_x}{t_{\text{stop}}} + \frac{1}{\Sigma_d} \frac{\partial}{\partial x} \left(v_x D \frac{\partial \Sigma_d}{\partial x} \right), \end{aligned} \quad (3.71)$$

$$\frac{\partial v_y}{\partial t} + \left(v_x - \frac{D}{\Sigma_d} \frac{\partial \Sigma_d}{\partial x} \right) \frac{\partial v_y}{\partial x} = -2\Omega_0 \left(v_x - \frac{D}{\Sigma_d} \frac{\partial \Sigma_d}{\partial x} \right) - \frac{v_y - U_{g,0}}{t_{\text{stop}}}, \quad (3.72)$$

where $U_{g,0} \equiv -3\Omega_0 x/2 - \eta'_0 R \Omega_0$ is an azimuthal velocity of a steady gas disk, and $\eta'_0 \equiv \eta'(r = R)$ (see Equation (3.67)). We include dust diffusion so that dust momentum is conserved in the absence of the drag force (see Chapter 2). As an unperturbed state, we use the steady drift solution, $v_{x,0}, v_{y,0}$, with uniform surface density $\Sigma_d = \Sigma_{d,0}$:

$$v_{x,0} = -\frac{2t_{\text{stop}}\Omega_0}{1 + (t_{\text{stop}}\Omega_0)^2} \eta'_0 R \Omega_0, \quad (3.73)$$

$$v_{y,0} = U_{g,0} + \frac{(t_{\text{stop}}\Omega_0)^2}{1 + (t_{\text{stop}}\Omega_0)^2} \eta'_0 R \Omega_0. \quad (3.74)$$

3.4. DISCUSSION

Assuming that perturbations $\delta\Sigma_d$, δv_x , δv_y are proportional to $\exp[ikx + nt]$, we derive the following linearized equations:

$$(n + ikv_{x,0})\delta\Sigma_d + ik\Sigma_{d,0}\delta v_x = -Dk^2\delta\Sigma_d, \quad (3.75)$$

$$(n + ikv_{x,0})\delta v_x = 2\Omega_0\delta v_y - ikc_d^2\frac{\delta\Sigma_d}{\Sigma_{d,0}} - ik\delta\Phi - \frac{\delta v_x}{t_{\text{stop}}} - v_{x,0}Dk^2\frac{\delta\Sigma_d}{\Sigma_{d,0}}, \quad (3.76)$$

$$(n + ikv_{x,0})\delta v_y = -\frac{\Omega_0}{2}\left(\delta v_x - ikD\frac{\delta\Sigma_d}{\Sigma_{d,0}}\right) - \frac{\delta v_y}{t_{\text{stop}}}. \quad (3.77)$$

Because this analysis consider only the dust motion, we assume that the background gas is not perturbed and $\delta\Phi = -2\pi G\delta\Sigma_d/k$. From the above linearized equations, we obtain the following dispersion relation for $\gamma \equiv n + ikv_{x,0}$:

$$\left(\gamma + \frac{1}{t_{\text{stop}}}\right)\left[F_{\text{DW}}(\gamma, k) + \gamma\left(\frac{1}{t_{\text{stop}}} + Dk^2\right) + Dk^2\left(-ikv_{x,0} + \frac{1}{t_{\text{stop}}}\right)\right] = \frac{\Omega_0^2}{t_{\text{stop}}}, \quad (3.78)$$

$$F_{\text{DW}}(\gamma, k) \equiv \gamma^2 + \Omega_0^2 + c_d^2k^2 - 2\pi G\Sigma_{d,0}k. \quad (3.79)$$

In the absence of the dust diffusion ($D = 0$), Equation (3.78) for γ is equivalent to Equation (1.50) for n derived in Youdin (2011) (see also Equation (22) therein). One of the solutions of Equation (3.78) with $D = 0$ corresponds to the one-component secular GI (e.g., Youdin 2005a, 2011), which is denoted by γ_{SGI} in the following, and we obtain $n = -ikv_{x,0} + \gamma_{\text{SGI}}$. Note that Equation (3.78) for $D = 0$ is a cubic equation of γ with the real coefficients, and $\text{Im}[\gamma_{\text{SGI}}] = 0$. This is mathematically and physically expected because one can remove the drift motion performing the Galilean transformation (see also Youdin 2005a). The phase velocity $\text{Re}[n/(-ik)]$ is equivalent to the steady drift velocity $v_{x,0}$, which is consistent with our numerical simulations (see Figures 3.14 and 3.18). As noted in Chapters 1 and 2, secular GI originates from a static mode, i.e. $\gamma_{\text{SGI}} \rightarrow 0$ for $t_{\text{stop}}\Omega \rightarrow \infty$ (see Figure 2.1). Equation (3.78) also shows $n \rightarrow 0$ for $t_{\text{stop}}\Omega \rightarrow \infty$ because $v_{x,0}$ becomes zero for friction-free cases.

Dust diffusion due to weak turbulence does not qualitatively change the mode properties of secular GI of the drifting dust, and just suppresses the growth rate especially at short wavelengths. Although strong dust diffusion results in non-zero $\text{Im}[\gamma_{\text{SGI}}]$ at short wavelengths, such wavelengths are stable to secular GI ($\text{Re}[\gamma_{\text{SGI}}] < 0$). Note that Equation (3.78) is different from the dispersion relation (Equation (1.50)) derived by Youdin (2011) because the diffusion modeling is different. As mentioned in Chapter 2 Tominaga et al. (2019), the diffusion modeling adopted in Youdin (2011) unphysically changes angular momentum of dust while ours does not. Hence, our dispersion relation (Equation (3.78)) describes the mode properties more precisely. For example, Youdin (2011) found

3.4. DISCUSSION

mode coupling between the static mode and GI mode when including dust diffusion. Our dispersion relation, Equation (3.78), does not show the mode coupling.

We also perform two-fluid analyses assuming the steady drift solution in an unperturbed state. In contrast to the one-fluid analyses, we can not remove the drift motion because dust and gas have different drift speeds. We use the following equations for gas:

$$\frac{\partial \Sigma}{\partial t} + \frac{\partial}{\partial x} (\Sigma u_x) = 0, \quad (3.80)$$

$$\frac{\partial u_x}{\partial t} + u_x \frac{\partial u_x}{\partial x} = 3\Omega_0^2 x + 2\Omega_0 u_y + 2\eta'_0 R \Omega_0^2 - \frac{c_s^2}{\Sigma} \frac{\partial \Sigma}{\partial x} - \frac{\partial \Phi}{\partial x} + \frac{1}{\Sigma} \frac{\partial}{\partial x} \left(\frac{4}{3} \Sigma \nu \frac{\partial u_x}{\partial x} \right) + \frac{\Sigma_d}{\Sigma} \frac{v_x - u_x}{t_{\text{stop}}}, \quad (3.81)$$

$$\frac{\partial u_y}{\partial t} + u_x \frac{\partial u_y}{\partial x} = -2\Omega_0 u_x + \frac{1}{\Sigma} \frac{\partial}{\partial x} \left(\Sigma \nu \frac{\partial u_y}{\partial x} \right) + \frac{\Sigma_d}{\Sigma} \frac{v_y - u_y}{t_{\text{stop}}}. \quad (3.82)$$

The external force $2\eta'_0 R \Omega_0^2$ in the radial equation of motion mimics the global pressure gradient that drives the dust drift (e.g., Youdin & Goodman 2005). The equations for the dust are the almost same as Equations (3.70)-(3.72) except for replacing $U_{g,0}$ by u_y in Equation (3.72).

The unperturbed state is the following steady drift solution where the unperturbed surface densities, $\Sigma_{d,0}$ and $\Sigma_{g,0}$, are spatially constant (Nakagawa et al. 1986):

$$v_{x,0} = -\frac{2t_{\text{stop}}\Omega_0}{(1+\varepsilon)^2 + (t_{\text{stop}}\Omega_0)^2} \eta'_0 R \Omega_0, \quad (3.83)$$

$$v_{y,0} = -\frac{3}{2}\Omega_0 x - \left[1 - \frac{(t_{\text{stop}}\Omega_0)^2}{(1+\varepsilon)^2 + (t_{\text{stop}}\Omega_0)^2} \right] \frac{\eta'_0 R \Omega_0}{1+\varepsilon}, \quad (3.84)$$

$$u_{x,0} = \frac{2t_{\text{stop}}\Omega_0 \varepsilon}{(1+\varepsilon)^2 + (t_{\text{stop}}\Omega_0)^2} \eta'_0 R \Omega_0, \quad (3.85)$$

$$u_{y,0} = -\frac{3}{2}\Omega_0 x - \left[1 + \frac{(t_{\text{stop}}\Omega_0)^2 \varepsilon}{(1+\varepsilon)^2 + (t_{\text{stop}}\Omega_0)^2} \right] \frac{\eta'_0 R \Omega_0}{1+\varepsilon}, \quad (3.86)$$

where $\varepsilon = \Sigma_{d,0}/\Sigma_{g,0}$. We use the fixed t_{stop} for comparison with the numerical simulations². The linearized continuity equation for dust is the same as Equation (3.75). The other linearized equations are as follows:

$$(n + iku_{x,0})\delta\Sigma_g + ik\Sigma_{g,0}\delta u_x = 0, \quad (3.87)$$

²Even if we consider $\Sigma_{g,0}$ -dependence of t_{stop} when linearizing the equation, the mode properties do not change much.

$$\begin{aligned}
 (n + ikv_{x,0})\delta u_x &= 2\Omega_0\delta u_y - ikc_s^2 \frac{\delta\Sigma_g}{\Sigma_{g,0}} - ik\delta\Phi - \frac{4}{3}\nu k^2\delta u_x \\
 &+ \frac{\delta\Sigma_d}{\Sigma_{g,0}} \frac{v_{x,0} - u_{x,0}}{t_{\text{stop}}} - \varepsilon \frac{\delta\Sigma_g}{\Sigma_{g,0}} \frac{v_{x,0} - u_{x,0}}{t_{\text{stop}}} + \epsilon \frac{\delta v_x - \delta u_x}{t_{\text{stop}}}, \quad (3.88)
 \end{aligned}$$

$$\begin{aligned}
 (n + ikv_{x,0})\delta u_y &= -\frac{\Omega_0}{2}\delta u_x - \frac{3}{2}\Omega ik\nu \frac{\delta\Sigma_g}{\Sigma_{g,0}} - \nu k^2\delta u_y \\
 &+ \frac{\delta\Sigma_d}{\Sigma_{g,0}} \frac{v_{y,0} - u_{y,0}}{t_{\text{stop}}} - \varepsilon \frac{\delta\Sigma_g}{\Sigma_{g,0}} \frac{v_{y,0} - u_{y,0}}{t_{\text{stop}}} + \varepsilon \frac{\delta v_y - \delta u_y}{t_{\text{stop}}}, \quad (3.89)
 \end{aligned}$$

$$(n + ikv_{x,0})\delta v_x = 2\Omega_0\delta v_y - ikc_d^2 \frac{\delta\Sigma_d}{\Sigma_{d,0}} - ik\delta\Phi - \frac{\delta v_x - \delta u_x}{t_{\text{stop}}} - v_{x,0} D k^2 \frac{\delta\Sigma_d}{\Sigma_{d,0}}, \quad (3.90)$$

$$(n + ikv_{x,0})\delta v_y = -\frac{\Omega_0}{2} \left(\delta v_x - ikD \frac{\delta\Sigma_d}{\Sigma_{d,0}} \right) - \frac{\delta v_y - \delta u_y}{t_{\text{stop}}}, \quad (3.91)$$

where $\delta\Phi = -2\pi G(\delta\Sigma_g + \delta\Sigma_d)/k$.

Figure 3.20 shows the derived dispersion relation of secular GI. We take the physical values from Q4a10 run to set the unperturbed state. The qualitative properties are the same as in the previous studies that neglected the drift motion. The long-wavelength perturbations are stabilized by the back reaction from dust to gas. The dust diffusion limits the shortest unstable wavelength. Thus, secular GI is operational only at the intermediate wavelengths.

We also show the growth rate of a viscosity-free case (filled circles) and the approximated dispersion relation n_{ap} obtained without turbulent viscosity and drift motion (gray line; Equation (2.52)). The gray line well reproduces the dispersion relation in the dust-drifting system (filled circles). The frequency $-\text{Im}[n]$ is shown on the right panel of Figure 3.20. The frequency $v_{x,0}k$ (black line) well expresses the derived frequency of secular GI (filled circles and cross symbols) as in the one-fluid analyses. At higher wavenumbers, the frequency deviates from $v_{x,0}k$ because of the dust diffusion term.

The drift motion insignificantly modify the growth rate of secular GI significantly, which is similar to the above one-fluid analyses (see the filled circles and the gray line in Figure 3.20). To demonstrate this, we plot dispersion relations of secular GI for various power-law indices q of gas surface density Σ_g in Figures 3.21 and 3.22. We exclude turbulent viscosity when plotting Figure 3.21 because secular GI does not require viscosity. We find that changing q insignificantly change the growth rate. Thus, regardless of the variety of gas surface density distribution, the dust drift insignificantly change the growth rate of secular GI. The oscillation frequencies are well reproduced by $v_{x,0}k/\Omega_0$ for each power-law index q at small wavenumbers (see the right panel of Figure 3.21). Thus,

3.4. DISCUSSION

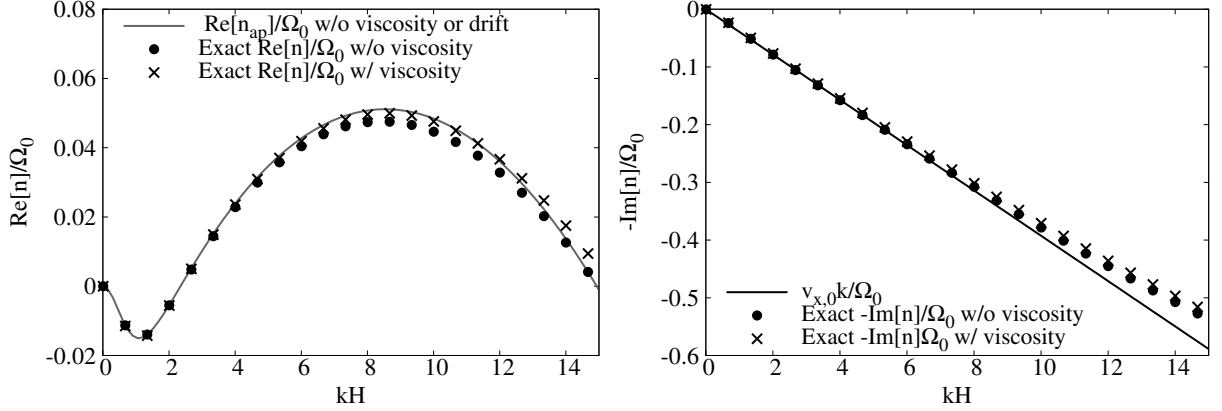


Figure 3.20: Growth rate (left panel) and frequency (right panel) of secular GI as a function of dimensionless wavenumber kH . The physical parameters are $t_{\text{stop}}\Omega_0 = 0.6$, $\varepsilon = 0.1$, $Q = 4.463$ and $\eta' = 0.003014$, which are taken from the initial-state values at $r = 75$ au of Q4a10 run. In both panels, the cross symbols and the filled circles show n calculated with and without the turbulent viscosity, respectively. The gray line on the left panel shows the approximated dispersion relation in the case without the turbulent viscosity or the drift motion (Equation (2.52)). The black line on the right panel shows $v_{x,0}k/\Omega_0$ that reproduces well the frequency of secular GI. This figure is originally from Figure 9 of Tominaga et al. (2020).

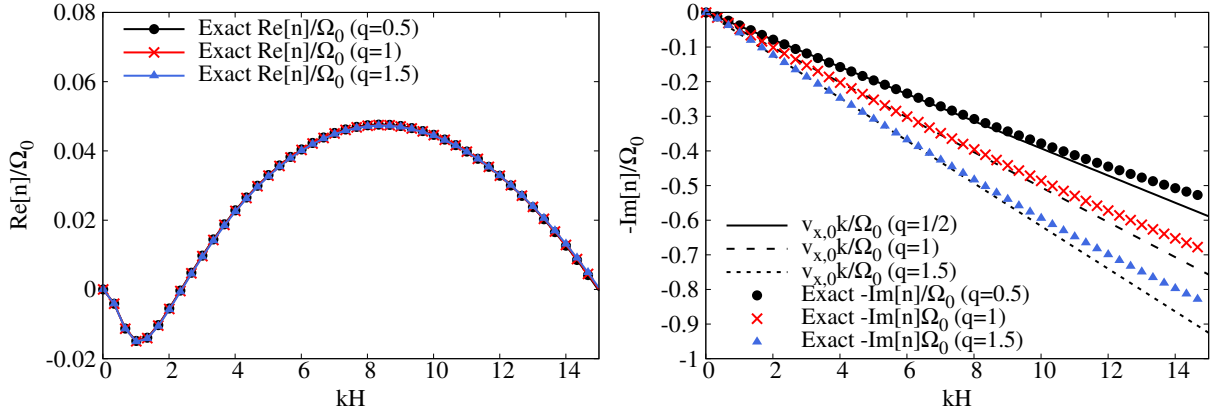


Figure 3.21: Growth rate (left panel) and frequency (right panel) of secular GI as a function of dimensionless wavenumber kH in the absence of turbulent viscosity. We assume $t_{\text{stop}}\Omega = 0.6$, $\Sigma_{d,0}/\Sigma_0 = 0.1$ and $\alpha = 1 \times 10^{-3}$. The Toomre's Q value is fixed to be 4.463, which corresponds to the value at $r = 75$ au in Q4a10 run ($q = 0.5$). The filled circles, the red cross symbols and the blue triangles show dispersion relations for $q = 0.5, 1, 1.5$, respectively. The solid, dashed and short dashed lines on the right panel show $v_{x,0}k/\Omega_0$ for $q = 0.5, 1, 1.5$, respectively. This figure is originally from Figure 13 of Tominaga et al. (2020).

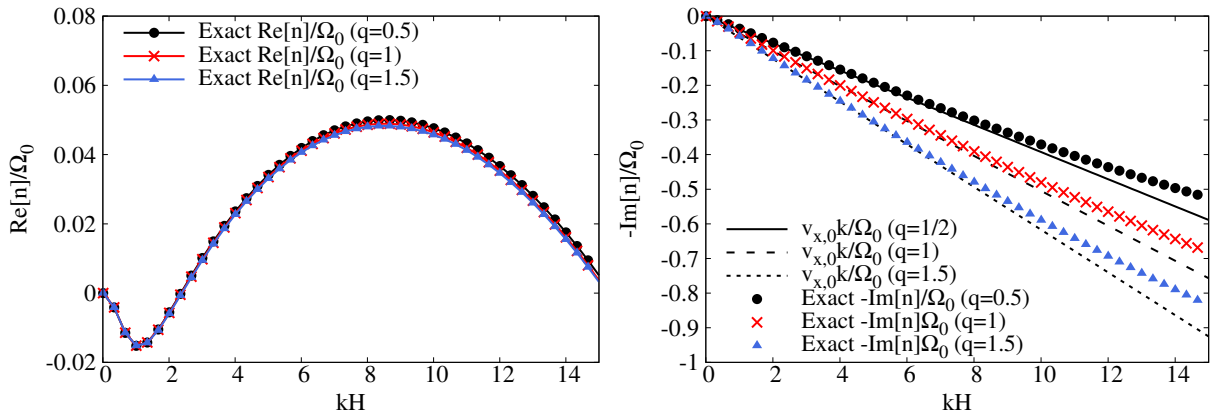


Figure 3.22: Growth rate (left panel) and frequency (right panel) of secular GI as a function of dimensionless wavenumber kH . Here we also consider the turbulent viscosity. We assume $t_{\text{stop}}\Omega = 0.6$, $\Sigma_{d,0}/\Sigma_0 = 0.1$ and $\alpha = 1 \times 10^{-3}$. The Toomre's Q value is fixed to be 4.463 as in Figure 3.21. The filled circles, the red cross symbols and the blue triangles show dispersion relations for $q = 0.5, 1, 1.5$, respectively. The solid, dashed and short dashed lines on the right panel show $v_{x,0}k/\Omega_0$ for $q = 0.5, 1, 1.5$, respectively. This figure is originally from Figure 14 of Tominaga et al. (2020).

the power-law index only change the frequency mostly through the term $v_{x,0}$. Including turbulent viscosity only slightly change the dispersion relation (Figure 3.15).

The present analyses do not show an unstable mode corresponding to TVGI. In the previous analyses in Chapter 2 and Tominaga et al. (2019), TVGI originates from a static mode in which dust velocity perturbations are in phase with gas velocity perturbations. This situation is not realized if dust grains have significant drift velocities, which seems to be the reason for the stabilization of TVGI.

3.4.2 Condition for the thin dense ring formation

For the development from linear growth of secular GI to planetesimal formation, formation of thin dense rings seems important as resultant high dust density will promote dust coagulation or lead to ring fragmentation. We first discuss its condition based on the previous linear analyses.

The condition for the formation of thin dense rings is that the radial drift motion is almost stopped because of resultant high dust-to-gas mass ratio in rings. Q4a10 run shows that the maximum dust-to-gas mass ratio reaches about unity, and the thin dense rings form (Figure 3.12). On the other hand, the maximum dust-to-gas ratio is smaller than unity in Q5a8 run, and the transient low-contrast dust rings form (Figure 3.18).

3.4. DISCUSSION

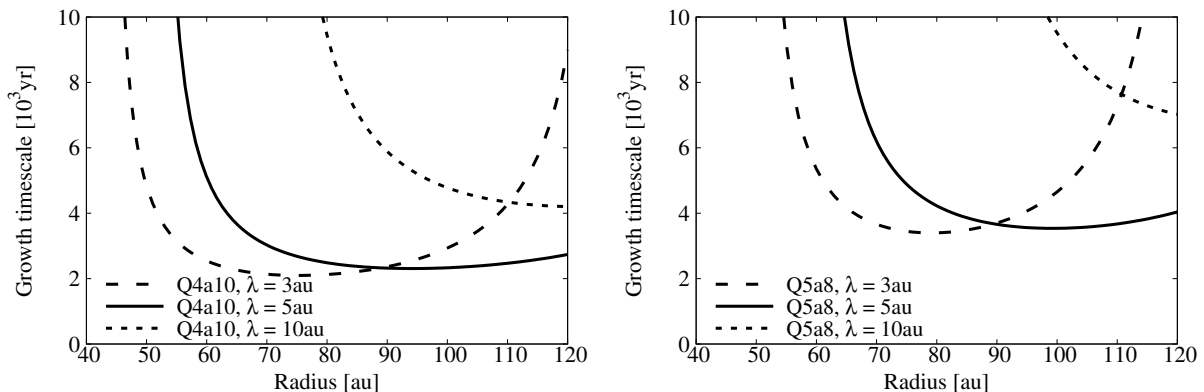


Figure 3.23: Growth timescales of secular GI at wavelengths $\lambda = 3$ au, 5 au, 10 au for disk models in Q4a10 run (left panel) and Q5a8 run (right panel). The unstable region is located at an outer region in Q5a8 run compared to Q4a10 run. Perturbations at long wavelength can grow only at outer radii. This figure is originally from Figure 10 of Tominaga et al. (2020).

Thus, the critical dust-to-gas mass ratio seems to be about unity.

To what extent the dust-to-gas ratio increases depends on the radial extent of an unstable region. Figure 3.23 shows radial dependence of growth timescales of secular GI in Q4a10 and Q5a8 runs. We plot three lines corresponding to different wavelengths: $\lambda = 3$ au, 5 au and 10 au. Q5a8 run shows smaller radial extent of the unstable region for each wavelength than the Q4a10 run. As shown in the previous section, the perturbations with $\lambda \simeq 3-5$ au grow and form the substructures in both cases (see Figures 3.12 and 3.18). In the Q4a10 case, Figure 3.23 shows that those perturbations can grow at $r \gtrsim 50$ au, which is consistent with Figure 3.12. The resultant dust enrichment up to $\Sigma_d/\Sigma_g \simeq 1$ decelerates the drift velocity of the rings before they reach the stable region. As a result, the thin dense rings do not become transient but sustain their dust-concentrating structure. On the other hand, in Q5a8 case the growth timescale at $\lambda = 5$ au starts increasing significantly at $r \simeq 60-70$ au (see the right panel of Figure 3.23). In other words, the growth of perturbations are reduced while those perturbations keep drifting inward. Thus, the perturbations eventually enter the stable region ($r \lesssim 58$ au for $\lambda = 5$ au), and start to decay as shown in Figure 3.19.

Resultant dust-to-gas ratio in rings also depends on the amplitudes of initial perturbations. We performed a simulation in which we set the same parameters as Q5a8 run but initial random perturbations with six times larger amplitudes. We do not initially perturb a region of $10 \text{ au} < r < 20 \text{ au}$ to avoid sudden dust concentrations near the inner boundary due to the initial large perturbations. Figure 3.24 shows surface density profiles of dust and gas and their evolution. Spiky dust rings form before they enter

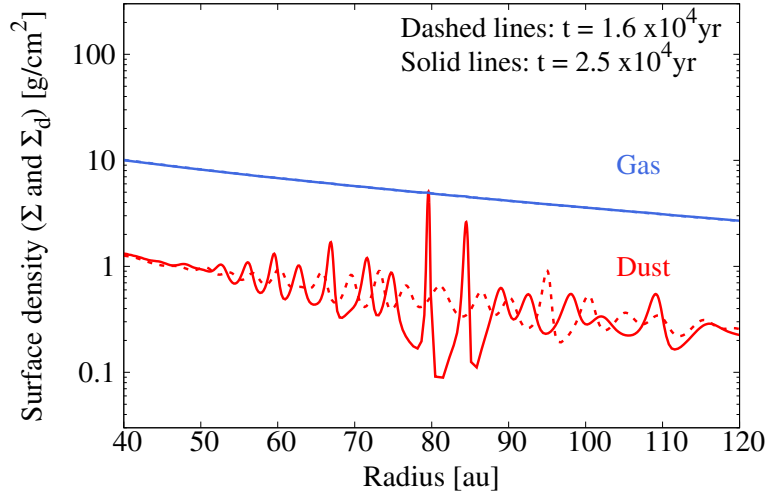


Figure 3.24: Surface density profiles of dust and gas at $t = 1.6 \times 10^4$ yr (dashed lines) and 2.5×10^4 yr (solid lines) from a run in which we put the same parameters as Q5a8 run but initial perturbations with six times larger amplitudes (Q5a8L run). This figure is originally from Figure 11 of Tominaga et al. (2020).

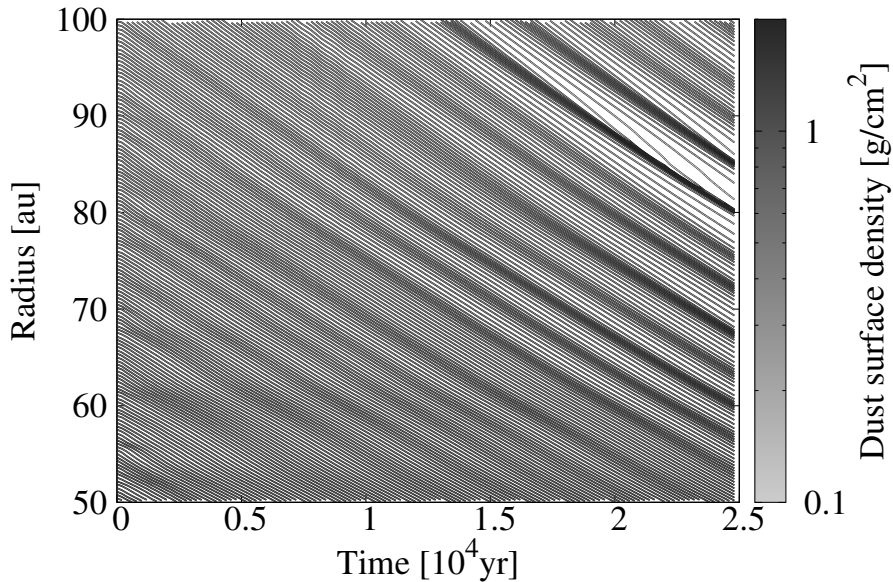


Figure 3.25: Trajectories of dust cells in Q5a8L run. Color on each line represents the dust surface density at each dust cell. We used a reduced number of cells to plot this figure. This figure is originally from Figure 12 of Tominaga et al. (2020).

3.4. DISCUSSION

the stable region, resulting in thin dense rings with $\Sigma_d/\Sigma_g \simeq 1$ (see also Figure 3.25). For instance, amplitudes of perturbations in an actual disk come from disk turbulence or disturbances due to mass accretion from the envelope. However, those are unknown, and we thus do not qualitatively discuss perturbation amplitudes in the present thesis.

In the present simulations, we fix the power-law index q of the surface densities. In disks with larger q , the inner region is more massive than smaller- q disks, and thus the unstable region shifts inward. If α , $t_{\text{stop}}\Omega$, Q and Σ_d/Σ_g are the same, the growth timescale becomes shorter because the power-law index insignificantly changes the growth timescale and the timescale is scaled by the Keplerian period $2\pi\Omega^{-1} \propto r^{3/2}$. Although the drift timescale $r/|v_r|$ also becomes shorter, its change is smaller than that of the growth timescale. The drift speed is faster for larger q . If one neglect the exponential cutoff term, $\eta'r\Omega$ is independent from the radial distance. Thus, the drift timescale is linearly proportional to r . The r -dependence is weaker than that of the growth timescale ($r^{3/2}$). Therefore, secular GI can grow and more easily create thin dense rings in steeper disks. We note that unstable wavelengths become shorter because they are scaled by the gas scale height that decreases inward. The widths of resultant rings are thus smaller than we present in this thesis, which will require higher numerical resolutions.

3.4.3 Subsequent evolution of dusty rings

In dense dusty rings resultant from nonlinear evolution of secular GI, accelerated coagulation and gravitational collapse will form planetesimals. Because the rings are massive with mass of $\gtrsim 10M_\oplus$ and self-gravitational, they will azimuthally fragment into solid bodies. The timescale of the ring fragmentation can be measured by the freefall time t_{ff} . The mean dust surface density in a dust ring $\tilde{\Sigma}_d$ is given by

$$\tilde{\Sigma}_d = \frac{M_{\text{ring}}}{2\pi R_{\text{ring}} w_{\text{ring}}}, \quad (3.92)$$

where M_{ring} , R_{ring} , w_{ring} are mass, radius and width of a dust ring, respectively. Assuming a relation $\tilde{\rho}_d = \tilde{\Sigma}_d/\sqrt{2\pi}H_d$, we obtain $t_{\text{ff}} = \sqrt{3\pi/32G\tilde{\rho}_d}$. For the ring of $M_{\text{ring}} = 49.7M_\oplus$, $R_{\text{ring}} = 73.6$ au and $w_{\text{ring}} = 0.3$ au in Q4a10 run, we have $t_{\text{ff}} \simeq 55$ yr, which is much shorter than one Keplerian period at $r = 73.6$ au ($\simeq 631$ yr).

Both total dust-to-gas ratio $\Sigma_{d,\text{tot}}/\Sigma_{g,\text{tot}}$ and the dust-to-gas ratio Σ_d/Σ_g in a lower layer around the midplane increase in a growing dusty ring. Because the coagulation timescale t_{grow} is inversely proportional to the total dust-to-gas ratio $\Sigma_{d,\text{tot}}/\Sigma_{g,\text{tot}}$ in the Epstein regime (see Equation (A.3)), the dust growth should proceed faster in resultant dusty rings. When the height of the lower layer is much larger than the dust scale height,

one has $\Sigma_d \simeq \Sigma_{d,\text{tot}}$. Because Σ_g insignificantly changes during the growth of secular GI, $\Sigma_{g,\text{tot}}$ will be also almost constant in time. Thus, the enhancement of $\Sigma_{d,\text{tot}}/\Sigma_{g,\text{tot}}$ will be similar to that of Σ_d/Σ_g . In the case of Q4a10 run, if the initial total dust-to-gas ratio is 0.05 and increases as well as Σ_d/Σ_g by a factor of 9.3 as expected from Equation (3.69), we have $t_{\text{grow}} \simeq 199$ yr at $r = 73.6$ au. Thus, coagulation also proceeds within one Keplerian period although the coagulation timescale is still longer than the freefall time.

In Q5a8L run, Σ_d/Σ_g becomes an order of magnitude larger than the initial value at $r \simeq 80$ au (Figure 3.24). The coagulation timescale in the dust ring is about 209 yr, which is much shorter than the radial drift timescale. Thus, the dust grains in the ring will grow and decouple from gas before the dust ring drifts into the inner stable region. This combination of dust ring formation and coagulation will also prevent the ring from being transient. Thus, to consider both ring fragmentation and dust growth is important for further discussion on ring and planetesimal formation. More quantitative analyses require multidimensional simulations with the dust growth, which is our future work. Nevertheless, we can expect the subsequent planetesimal formation via either ring fragmentation or accelerated coagulation if the significant dust concentration occurs via secular GI.

3.4.4 Observational justification

Our simulations show that secular GI results in significant substructures only in a dust disk. This property is in contrast to a planet-based scenario in which Jupiter-mass planets carve gaps in both dust and gas disks (e.g., Gonzalez et al. 2015; Kanagawa et al. 2015; Zhang et al. 2018). Therefore, observations of a gas distribution near the midplane will enable us to discriminate between the proposed ring formation mechanisms: one requires gap-like profiles in a gas disk (i.e., hidden high-mass planet scenario) while another shows a relatively smooth gas profile (i.e., the secular-GI-based mechanism). We should note that if nonlinear growth of secular GI results in massive rocky objects, those large objects would create some substructures in the gas disk. If the gas gap is as wide as the dust gap, it might be difficult to distinguish the secular-GI-based mechanism and the planet-based mechanism. Even in this case, secular GI might explain the origin of the hypothetical planets in the gap.

In contrast to a high-mass planet, a low-mass planet can carve a gap only in a dust disk. A low-mass planet first creates prominent structures in a dust disk and takes a long time to carve a significant gas gap because the dust scale height is smaller

than the gas scale height (e.g., Yang & Zhu 2020). Thus, there is a possibility that observations only identify resolvable high-contrast dust gaps but cannot resolve low-contrast gas gaps. Thus, the low-mass-planet-based scenario and the secular-GI-based scenario can be degenerate. Nevertheless, those scenarios depend on the disk properties and dust sizes in different ways. Therefore, accurately observing a midplane gas density is important as well as observations of dust distributions.

As discussed above, dust growth to larger solid bodies can occur in resultant dust rings. If those objects are large enough, the rings would be dark at millimeter wavelengths. This indicates that resultant multiple spiky rings and adjacent gaps would be observed as a wide gap structure. Because collisional fragmentation of the resultant larger bodies would supply small grains that contribute to sub-mm emissions, the re-supplied dust grains will determine the “floor” intensity in the apparent gap. The re-supplied dust grains take part in the growth of secular GI and subsequent fragmentation supplies small dust grains again. This recycling process indicates the existence of an equilibrium between dust-to-planetesimal conversion via secular GI and dust supply via planetesimal fragmentation. A similar process is investigated by Stammer et al. (2019) although they focus on a different instability called streaming instability (Youdin & Goodman 2005). Stammer et al. (2019) claims that planetesimal formation in dust rings via streaming instability stalls the growth of itself because dust grains are depleted as a result of planetesimal formation. Because the resultant planetesimals are not observed at sub-mm emission, this self-regulating process can limit the optical depth at sub-mm wavelengths. The DSHARP observations revealed that the optical depth in dust rings are limited to around $\simeq 0.2 - 0.5$ (see also, Dullemond et al. 2018, Huang et al. 2018). To consistently examine substructures and optical depth profiles resultant from secular GI, we have to explicitly include both dust growth and fragmentation in our simulations. Because self-gravitational ring fragmentation will occur simultaneously, nonaxisymmetric analyses and simulations are important to explore observational signatures. Those will be the scope of our future studies.

3.4.5 Effects on dust-to-gas ratio dependence on the dust coefficient

In our simulations, the dust diffusion coefficient D is given by a constant parameter α . However, numerical studies suggest that the dust diffusivity decreases when dust-to-gas mass ratio increases as in rings resultant from secular GI (see Figures 3.12). Schreiber & Klahr (2018) measured the dust diffusivity under the influence of turbulence driven by

3.4. DISCUSSION

streaming instability. They found that the turbulent diffusion weakens when the dust-to-gas mass ratio is larger than unity. If the turbulent diffusion in dust rings is driven by streaming instability, the saturated surface density of thin dense rings will be larger than that obtained from our simulations or estimated in Equation (3.69) with the constant diffusivity. It is also possible that the inefficient diffusion cannot support the thin dense ring and the ring just radially collapses. In either case, a timescale of planetesimal formation via gravitational collapse or accelerated dust growth will be shorter.

We can estimate the saturated surface density at a dense ring with the reduced diffusivity. We assume that the dust diffusion coefficient is proportional to power-law function of $\Sigma_{d,f}/\Sigma_{g,0}$

$$D = \alpha_1 \frac{c_s^2}{\Omega} \left(\frac{\Sigma_{d,f}}{\Sigma_{g,0}} \right)^{-\beta}, \quad (3.93)$$

where α_1 is dimensionless diffusion parameter when $\Sigma_{d,f}/\Sigma_{g,0} = 1$. Following the same way to derive Equation (3.69), we evaluate the dust surface density at its saturation:

$$\frac{\Sigma_{d,f}}{\Sigma_{d,0}} = f(\beta) \left(\frac{\Sigma_{d,0}/\Sigma_{g,0}}{0.1} \right)^{\frac{1+2\beta}{2-2\beta}} \left(\frac{\alpha_1}{1 \times 10^{-3}} \right)^{\frac{1}{\beta-1}} \left(\frac{Q}{4.5} \right)^{\frac{1}{2\beta-2}} \left(\frac{k_0 H}{8} \right)^{\frac{3}{2\beta-2}}, \quad (3.94)$$

$$f(\beta) \simeq (8.7 \times 10^{1-2\beta})^{\frac{1}{2-2\beta}}. \quad (3.95)$$

The equation has no solution and $f(\beta)$ diverges if $\beta = 1$. This indicates that the dust diffusion can not sustain the radial ring collapse if $\Sigma_{d,f}/\Sigma_{g,0}$ -dependence of D is steeper than $\beta = 1$. Although Equation (3.94) has a solution for $\beta > 1$, the situation is not achieved during the growth of perturbations because the diffusion timescale becomes shorter than the collapse timescale before the dust surface density reaches $\Sigma_{d,f}$.

The velocity dispersion of dust grains c_d is also expected to decrease as the dust-to-gas ratio increases beyond unity. If c_d decreases, the Coriolis force will be a unique repulsing force against self-gravity. The characteristic length scale λ_{crit} of such a system is

$$\lambda_{\text{crit}} \equiv \frac{4\pi^2 G \Sigma_d}{\Omega^2}. \quad (3.96)$$

Dust clumps smaller than λ_{crit} will self-gravitationally collapse. Adopting $\Sigma_d = 9.5 \text{ g/cm}^2$ at $r = 73.6 \text{ au}$ taken from the ring properties in Q4a10 run, one obtains $\lambda_{\text{crit}} \simeq 17.7 \text{ au}$, which is much larger than the resultant ring width (see Figure 3.12). A circumference of a ring with $r = 73.6 \text{ au}$ is about 462 au, which is 6 times longer than λ_{crit} . This indicates that non-axisymmetric modes with an azimuthal wavenumber m larger than 6 will grow and result in azimuthal fragmentation. Because higher m modes have larger growth rates, sizes of resultant dust clumps can be much smaller. If the dust ring in

Q4a10 run whose mass is $M_{\text{ring}} = 49.7M_{\oplus}$ and radius is $r \simeq 73.6$ au fragments, the mass of the dust clump M_{clump} is

$$M_{\text{clump}} = \frac{M_{\text{ring}}}{m} \simeq 8.2M_{\oplus} \left(\frac{m}{6}\right)^{-1}. \quad (3.97)$$

The above clump mass for $m = 6$ gives upper limit because the non-axisymmetric modes with $m < 6$ are expected to be stable. For further studies, non-axisymmetric simulations are necessary.

3.5 Summary

In Chapter 3, we show numerical simulations of secular GI in radially extended disks. Because dust grains suffer radial drift toward a central star, exploring the growth of secular GI with a radially wide region is essentially important to discuss formation of dust substructures and planetesimals in a protoplanetary disk. Numerical simulations are powerful tools to investigate such a problem. However, numerical diffusion prevents the slow growth of secular GI. Motivated by this issue, we develop the Lagrangian-cell method utilizing the symplectic integrator. The Lagrangian-cell method is free from numerical diffusion due to advection, and the symplectic integrator reduces the accumulation of errors due to time integration. Combining the method with the piecewise exact solution for dust-gas friction, we performed numerical simulations of linear/nonlinear secular GI.

Nonlinear growth of secular GI shows the gravitational collapse of dust rings whose timescale is characterized by the freefall time. As a result, the dust surface density increases by an order of magnitude while the gas surface density insignificantly changes. This results in high dust-to-gas ratio in thin dense rings. The dust enrichment suppresses dust drift through the backreaction to the gas and saves dust grains in a disk. If a growth timescale of secular GI is too long, secular GI only creates low-contrast rings. Such rings eventually drift into an inner stable region and start to decay. Thus, resultant substructures are transient. Because rings smoothly decay, it seems possible that rings resultant from secular GI are observed even in the stable region. According to the above results, planetesimal formation requires dust enrichment up to $\Sigma_{\text{d}}/\Sigma_{\text{g}} \simeq 1$ via thin dense ring formation by secular GI.

We simply estimate the coagulation timescale and the freefall timescale and show that both ring fragmentation and accelerated coagulation will proceed within one Keplerian period once secular GI develops into the nonlinear phase. Thus, secular GI can be an efficient process to cause planetesimal formation.

3.5. SUMMARY

The mass conversion from dust grains to planetesimals will make resultant rings darker at sub-mm wavelengths. This indicates that resultant multiple spiky rings will be observed as a single wide gap substructure. Planetesimal fragmentation after its formation will re-supply small dust grains that continue to accumulate via secular GI. This recycling of dust grains indicates the existence of a state at which dust depletion via planetesimal formation and dust supply via planetesimal fragmentation are in equilibrium. Such a self-regulating process might explain the observed marginally optically thin substructures as discussed in Stammler et al. (2019).

In contrast to the ring-gap formation by high-mass planets, secular GI creates prominent substructures only in a dust disk. Therefore, observations of a midplane gas density profile will provide the key to understand what process actually operates and forms substructures in the observed disks. We should note that low-mass planets carve prominent dust gaps and low-contrast gas gaps, which might observationally degenerate with the secular-GI-based scenario if observations cannot resolve the low-contrast gas gaps.

For further quantitative studies, we need to perform multidimensional simulations with dust coagulation and fragmentation.

Chapter 4

Coagulation Instability: Self-Induced Dust Concentration

This chapter is based on a paper submitted to The Astrophysical Journal, Tominaga, Inutsuka, & Kobayashi (2021).

4.1 Short introduction

As discussed in the previous chapters, secular GI has the potential to locally concentrate dust grains and accelerate further dust growth toward planetesimals in resultant rings. The numerical simulations in Chapter 3 show that dust surface density increases by an order of magnitude once secular GI develops into nonlinear regime.

The unstable condition of secular GI is given by Equation (2.60). In terms of the dust-to-gas surface density ratio, disks satisfying the following condition become unstable to secular GI:

$$\varepsilon > 0.016 \left(\frac{D}{10^{-4} c_s^2 / \Omega} \right) \left(\frac{\tau_s}{0.1} \right)^{-1} \left(\frac{Q}{4} \right)^2, \quad (4.1)$$

where $\tau_s = t_{\text{stop}} \Omega$ is dimensionless stopping time and we assume $\varepsilon \ll 1$ to reduce Equation (2.60). The above condition means that the dust-to-gas ratio for dust with $\tau_s = 0.1$ should be higher than 0.016 for secular GI to operate. Assuming that dust grains of a size a are in the Epstein regime

$$\tau_s = \frac{\pi \rho_{\text{int}} a}{2 \Sigma_g}, \quad (4.2)$$

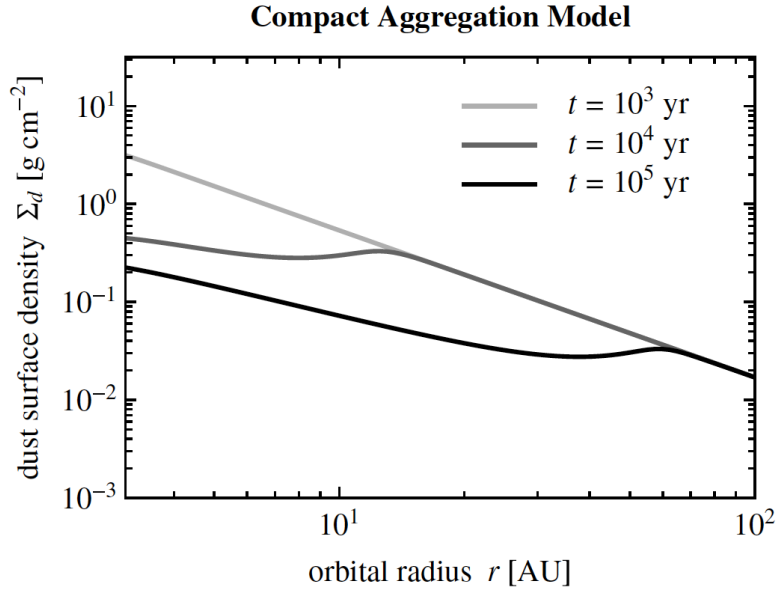


Figure 4.1: Time evolution of dust surface density via direct coagulation in the minimum mass solar nebula (MMSN) disk. The combination of inside-out dust growth and radial drift decreases dust surface density by an order of magnitude. This figure is originally from Figure 3 of Okuzumi et al. (2012).

one obtains

$$a = \frac{2}{\pi^2} \frac{\tau_s}{\rho_{\text{int}}} \frac{H}{r} \frac{M_*}{r^2} \quad (4.3)$$

$$\simeq 0.6 \text{ cm} \left(\frac{\tau_s}{0.1} \right) \left(\frac{\rho_{\text{int}}}{1.4 \text{ g/cm}^3} \right)^{-1} \left(\frac{Q}{4} \right)^{-1} \left(\frac{H/r}{0.05} \right) \left(\frac{r}{50 \text{ au}} \right)^{-2} \left(\frac{M_*}{1M_\odot} \right). \quad (4.4)$$

Thus, for secular GI to grow in a disk, Equation (4.1) should be satisfied for mm- or cm-sized dust grains although the required dust size depends on the other parameters and the radial location. Collisional coagulation will grow dust grains up to the required sizes (~ 1 cm).

However, according to numerical studies on coagulation in an isolated disk, dust surface density significantly decreases as dust grows into the size of ~ 1 cm ($\tau_s \simeq 0.1$) unless the surrounding envelope supplies dust grains to the disk (e.g., Brauer et al. 2008; Okuzumi et al. 2012). In other words, pure coagulation that provides large dust tends to violate the condition on the dust density (i.e., dust-to-gas ratio, Equation(4.1)). Figure 4.1 shows a dust surface density evolution via compact dust coagulation presented by Okuzumi et al. (2012). Dust coagulation proceeds in the inside-out manner because its timescale is proportional to the Keplerian orbital period $2\pi/\Omega \propto r^{3/2}$ (see Equation (A.3)). As a result of the inside-out coagulation, an inner region hosts larger grains

4.1. SHORT INTRODUCTION

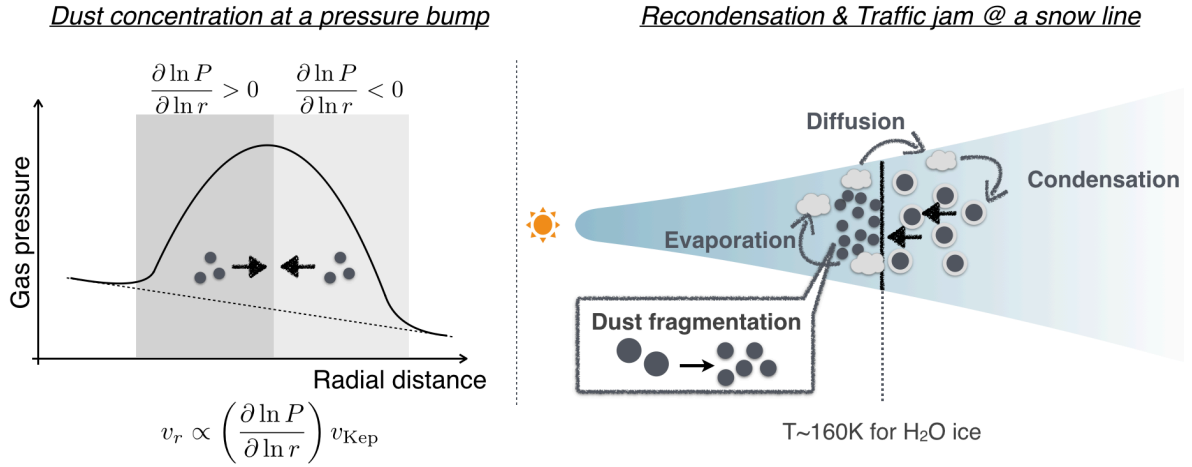


Figure 4.2: Currently proposed mechanisms for dust retention: (1) concentration at a pressure bump (e.g., Whipple 1972) and (2) combination of recondensation and traffic jam of dust grains (e.g., Stevenson & Lunine 1988). A pressure bump concentrates dust grains at its center because the radial drift velocity is proportional to the pressure gradient $\partial \ln P / \partial \ln r$ (see, Equation (1.14)). The second mechanism takes place at a H₂O snow line where water ice on grain’s surface evaporates. If silicate grains inside the snow line is fragile enough, inner dust grains fragment into smaller solids and pile up.

that have larger drift velocity, leading to the decrease in the dust surface density. They assumed that there is no dust supply to the disk from its outside, which corresponds to the very last stage of the disk evolution. The tendency for dust density to decrease as a result of coagulation may hold in the early disk although the density decrease may be less prominent because of gas and dust accretion from the envelope.

This “discrepancy” is problematic not only for secular GI but also for other dust-gas instabilities expected as a promising mechanism to form planetesimals. Streaming instability is one example (e.g., Youdin & Goodman 2005; Youdin & Johansen 2007; Johansen & Youdin 2007; Jacquet et al. 2011). Streaming instability has the potential to cause dust clumping at much smaller scales than secular GI, and resultant clumps eventually collapse self-gravitationally once those mass densities exceed Roche density (e.g., Johansen et al. 2007; Simon et al. 2016). The validity of streaming instability also depends on dust-to-gas ratio $\varepsilon = \Sigma_d / \Sigma_g$ and dimensionless stopping time (e.g., Johansen et al. 2009b; Carrera et al. 2015; Yang et al. 2017). Carrera et al. (2015) and Yang et al. (2017) numerically investigated conditions of dust clumping via streaming instability. They found the required dust-to-gas ratio larger than 0.02 for dust of $\tau_s = 0.1$, which is similar to secular GI (Equation (4.1)). Higher dust-to-gas ratio is required for smaller dust ($\tau_s = 10^{-2} - 10^{-3}$). In the presence of turbulent diffusion, strong clumping

via streaming instability will require much higher dust abundances (Chen & Lin 2020; Umurhan et al. 2020; Gole et al. 2020).

Therefore, reaccumulation of large dust grains resultant from coagulation is necessary for the dust-gas instabilities to operate and lead to planetesimal formation. Because of their growth wavelength of $\lesssim H$, a spatial scale of reaccumulation should be $\lesssim H$ at least. Pressure bumps or zonal flows in a gas disk are possible sites of dust reaccumulation (e.g., Whipple 1972; Kretke & Lin 2007; Johansen et al. 2009a; Bai & Stone 2014; Flock et al. 2015). If a “bump” structure in a gas pressure profile, dust grains at an inner region of the bump move outward while those at an outer region fall inward because their drift velocity is proportional to $\partial \ln P / \partial r$ (Equation (1.14)). Thus, dust grains pile up at the center of the bump (see Figure 4.2). Streaming instability in pressure bumps has been investigated both analytically (Auffinger & Laibe 2018) and numerically (Taki et al. 2016; Carrera et al. 2020). Auffinger & Laibe (2018) and Carrera et al. (2020) showed that streaming instability develops for dust-to-gas ratio of 0.01 if a relative amplitude of a pressure bump is larger than 10-20%. However, we should note that deformation of a bump due to frictional backreaction potentially inhibits subsequent gravitational collapse (Taki et al. 2016). Gas vortices also trap dust particles (e.g., Barge & Sommeria 1995; Chavanis 2000; Lyra & Lin 2013; Raettig et al. 2015). Although some disks are considered to host a vortex (Fukagawa et al. (2013); van der Marel et al. (2013); Casassus et al. 2015), other disks hosting annular substructures show few evidences that vortices are present.

A combination of recondensation of water vapor and dust traffic jam near a water snow line is another possible process for reaccumulating dust grains (e.g., Stevenson & Lunine 1988; Drążkowska & Dullemond 2014; Drążkowska & Alibert 2017; Schoonenberg & Ormel 2017; Schoonenberg et al. 2018). A water snow line is a location where water ice on grain’s surface evaporates. Resultant bare silicate grains are relatively fragile and fragment into smaller grains. The radial speed decreases inward across the snow line, leading to traffic jam. Because vaporized water diffuses outward and recondenses onto dust grains outside the snow line and they become larger, dust grains successively pile up around the snow line (see Figure 4.2). The process however is highly dependent on a critical velocity at which collisional fragmentation becomes efficient. It is found that dust grains efficiently pile up around the snow line if water vaporization inside the snow line provides fragile silicate grains whose critical velocity is \sim a few m/s. However, experiments suggest that dry silicate grains are less fragile than previously considered (a critical velocity $\gtrsim 10$ m/s, Kimura et al. 2015; Steinpilz et al. 2019). If this is the case in protoplanetary disks, the dust reaccumulation around the snow line may not operate

(see discussion in Drążkowska & Alibert 2017).

In this chapter, we propose another mechanism for retention and reaccumulation of mm- and cm-sized dust grains. We find that the inside-out coagulation itself triggers an instability that we call “coagulation instability”. Coagulation instability grows even when dust is highly depleted and dust-to-gas ratio is of the order of 10^{-3} . In contrast to the above mechanisms that operate at a specific location in a disk (e.g., a snow line), coagulation instability can operate and reaccumulate dust grains throughout a disk.

We first describe basic equations for linear analyses in Section 4.2 and show results in Section 4.3. Discussion and summary are present in Sections 4.5 and 4.6.

4.2 Moment method for dust coagulation

Dust coagulation is described by the Smoluchowski equation for a column number density $N(r, m)$ per unit dust particle mass m (Smoluchowski 1916; Schumann 1940; Safronov 1972):

$$\begin{aligned} \frac{\partial mN}{\partial t} = & \frac{m}{2} \int_0^m dm' K(r, m', m - m') N(r, m') N(r, m - m') \\ & - mN(r, m) \int_0^\infty dm' K(r, m, m') N(r, m') dm' - \frac{1}{r} \frac{\partial}{\partial r} (rv_r(r, m)mN(r, m)), \end{aligned} \quad (4.5)$$

where $K(r, m_1, m_2)$ is a collision kernel representing a vertically integrated collision rate between dust particles of masses $m_1 = 4\pi\rho_{\text{int}}a_1^3/3$ and $m_2 = 4\pi\rho_{\text{int}}a_2^3/3$ ¹. The expression of the collision kernel is (e.g., Brauer et al. 2008)

$$K(r, m_1, m_2) \equiv \frac{\sigma_{\text{coll}}}{2\pi H_d(m_1)H_d(m_2)} \int_{-\infty}^{\infty} \Delta v_{\text{pp}} \exp \left[-\frac{z^2}{2} \left(\frac{1}{H_d(m_1)^2} + \frac{1}{H_d(m_2)^2} \right) \right] dz, \quad (4.6)$$

where Δv_{pp} is collision velocity and σ_{coll} is a cross section:

$$\sigma_{\text{coll}} \equiv \pi(a_1 + a_2)^2. \quad (4.7)$$

Note that the radial velocity v_r and the dust scale height H_d depend on dust particle mass.

In this thesis, we describe dust growth using moment equations of Equation (4.5) because analytical treatments of the Smoluchowski equation are difficult (see Estrada &

¹In this thesis, we focus on collisional growth of compact spherical dust grains for simplicity. Collisional growth of porous dust aggregates are investigated in Okuzumi et al. (2012).

Cuzzi 2008; Ormel & Spaans 2008; Sato et al. 2016; Taki et al. 2020). Following Sato et al. (2016), we define the i th moment $M_i(r)$ as

$$M_i(r) \equiv \int_0^\infty m^{i+1} N(r, m) dm, \quad (4.8)$$

and the i th moment equation is

$$\begin{aligned} \frac{\partial M_i}{\partial t} &= \frac{1}{2} \int_0^\infty dm \int_0^\infty dm' K(r, m, m') N(m) N(m') [(m + m')^{i+1} - (m^{i+1} + m'^{i+1})] \\ &\quad - \frac{1}{r} \frac{\partial}{\partial r} (r \langle m^i v_r \rangle_m \Sigma_d), \end{aligned} \quad (4.9)$$

where

$$\langle m^i v_r \rangle_m \equiv \frac{1}{\Sigma_d} \int_0^\infty m^{i+1} v_r(m) N(r, m) dm. \quad (4.10)$$

Note that the dust surface density Σ_d is equivalent to 0th moment M_0 . Thus, the 0th moment equation yields the continuity equation

$$\frac{\partial \Sigma_d}{\partial t} + \frac{1}{r} \frac{\partial}{\partial r} (r \langle v_r \rangle_m \Sigma_d) = 0. \quad (4.11)$$

The 1st moment equation gives an evolutionary equation of a ‘‘peak mass’’, $m_p \equiv M_1$ (Ormel & Spaans 2008):

$$\frac{\partial m_p \Sigma_d}{\partial t} = \int_0^\infty dm \int_0^\infty dm' m m' K(r, m, m') N(m) N(m') - \frac{1}{r} \frac{\partial}{\partial r} (r \langle m v_r \rangle_m \Sigma_d). \quad (4.12)$$

To solve the 0th and 1st moment equations, we assume the following closure relation (see Sato et al. 2016; Taki et al. 2020):

$$m_p v_r(m_p) = m_p \langle v_r \rangle_m = \langle m v_r \rangle_m. \quad (4.13)$$

Sato et al. (2016) found that the moment equation can reproduce full-size calculations (Equation (4.5)) if one approximate the first term as the equal-sized kernel $K(m_p, m_p)$:

$$\begin{aligned} \int_0^\infty dm \int_0^\infty dm' m m' K(r, m, m') N(m) N(m') \\ \simeq K(m_p, m_p) = \frac{2a^2}{H_d(m_p)} \int_{-\infty}^\infty \Delta v_{pp} \exp\left(-\frac{z^2}{H_d(m_p)^2}\right) dz, \end{aligned} \quad (4.14)$$

where we use $m_p = 4\pi\rho_{\text{int}}a^3/3$. Although the integrand includes z -dependent collision speed, they approximately put the term outside of the integral

$$\int_0^\infty dm \int_0^\infty dm' m m' K(r, m, m') N(m) N(m') \simeq \frac{2\sqrt{\pi}a^2\Delta v_{pp}}{H_d(m_p)}. \quad (4.15)$$

Sato et al. (2016) also showed that adopting a collision speed with a dust size ratio of 1:2 for Δv_{pp} show better agreement between the moment calculations and full-size calculations. Based on these assumptions and the closure relation, we obtain the basic equations for coagulating dust grains:

$$\frac{\partial \Sigma_{\text{d}}}{\partial t} + \frac{1}{r} \frac{\partial}{\partial r} (r v_r \Sigma_{\text{d}}) = 0, \quad (4.16)$$

$$\frac{dm_{\text{p}}}{dt} = \frac{\partial m_{\text{p}}}{\partial t} + v_r \frac{\partial m_{\text{p}}}{\partial r} = \frac{2\sqrt{\pi} a^2 \Delta v_{\text{pp}} \Sigma_{\text{d}}}{H_{\text{d}}}, \quad (4.17)$$

where $v_r = v_r(m_{\text{p}})$ and $H_{\text{d}} = H_{\text{d}}(m_{\text{p}})$. Although Equation (4.16) is apparently the same as the usual continuity equation (Equation (2.1)), we should note that the surface density Σ_{d} in Equation (4.16) denotes total surface mass density of various sized dust particles and the velocity v_r denotes the representative velocity $v_r(m_{\text{p}})$.

Further simplification and equations at the local frame

In this chapter, we assume dust particles in the Epstein regime, and calculate the dimensionless stopping time $\tau_{\text{s}} \equiv t_{\text{stop}} \Omega$ using the size of the-peak-mass dust $a = (3m_{\text{p}}/4\pi\rho_{\text{int}})^{1/3}$:

$$\tau_{\text{s}} = \sqrt{\frac{\pi}{8}} \frac{\rho_{\text{int}} a}{\rho_{\text{g}} c_{\text{s}}} \Omega. \quad (4.18)$$

We also use the midplane value of τ_{s} and v_r because most of the dust particles are distributed near the midplane. For a vertical gas density profile, $\rho_{\text{g}}(z=0)$ is given by $\Sigma_{\text{g}}/\sqrt{2\pi}H$ (Equation (1.9)), and thus one obtains

$$\tau_{\text{s}} = \frac{\pi}{2} \frac{\rho_{\text{int}} a}{\Sigma_{\text{g}}}. \quad (4.19)$$

Equations (4.17) and (4.19) yield

$$\frac{\partial \tau_{\text{s}}}{\partial t} + v_x \frac{\partial \tau_{\text{s}}}{\partial r} = \frac{\sqrt{\pi}}{4} \left(\frac{\Sigma_{\text{d}}}{\Sigma_{\text{g},0}} \right) \left(\frac{\Delta v_{\text{pp}}}{\tau_{\text{s}} H_{\text{d}}} \right) \tau_{\text{s}}. \quad (4.20)$$

In this chapter, we mainly focus on turbulent-induced collisions at which dust particles collide with a relative velocity $\Delta v_{\text{pp}} = \sqrt{C\tau_{\text{s}}\alpha}c_{\text{s}}$ (Ormel & Cuzzi 2007), where C is a numerical factor and $C \simeq 2.3$ for dust grains with a size ratio of 0.5. We also use the simplified expression for the dust scale height: $H_{\text{d}} = \sqrt{\alpha/\tau_{\text{s}}}H$. These simplifications reduce Equation (4.20) as follows:

$$\frac{\partial \tau_{\text{s}}}{\partial t} + v_r \frac{\partial \tau_{\text{s}}}{\partial r} = \frac{\Sigma_{\text{d}}}{\Sigma_{\text{g}}} \frac{\tau_{\text{s}}}{3t_0} + \frac{\tau_{\text{s}}}{\Sigma_{\text{g}}} \frac{1}{r} \frac{\partial}{\partial r} (r \Sigma_{\text{g}} u_r) - \frac{\tau_{\text{s}}}{\Sigma_{\text{g}}} v_r \frac{\partial \Sigma_{\text{g}}}{\partial r}, \quad (4.21)$$

where $t_0 \equiv (4/3\sqrt{C\pi})\Omega^{-1} \simeq 0.49\Omega^{-1}$.

In the following sections, we perform linear analyses in the Cartesian local shearing sheet (Goldreich & Lynden-Bell 1965b) whose radial distance from a star is R and Keplerian orbital frequency is Ω . In the local frame, the basic equations for dust are summarized as follows:

$$\frac{\partial \Sigma_d}{\partial t} + \frac{\partial \Sigma_d v_x}{\partial x} = 0, \quad (4.22)$$

$$\frac{\partial \tau_s}{\partial t} + v_x \frac{\partial \tau_s}{\partial x} = \frac{\Sigma_d}{\Sigma_g} \frac{\tau_s}{3t_0} + \frac{\tau_s}{\Sigma_g} \frac{\partial \Sigma_g u_x}{\partial x} - \frac{\tau_s}{\Sigma_g} v_x \frac{\partial \Sigma_g}{\partial x}, \quad (4.23)$$

4.3 One-fluid linear analyses and results

We first perform one-fluid linear analyses considering only dust equations. We assume that the gas surface density is uniform at the local frame, $\Sigma_g = \Sigma_{g,0}$, and the radial dust velocity is given by the so-call drift velocity

$$v_x = -\frac{2\tau_s}{1 + \tau_s^2} \eta R \Omega. \quad (4.24)$$

The assumption of the steady uniform gas reduces Equation (4.23) as follows:

$$\frac{\partial \tau_s}{\partial t} + v_x \frac{\partial \tau_s}{\partial x} = \frac{\Sigma_d}{\Sigma_{g,0}} \frac{\tau_s}{3t_0}. \quad (4.25)$$

We set an unperturbed state with uniform surface densities for gas and dust. As shown below, a growth timescale of coagulation instability is shorter than a coagulation timescale $3t_0 \Sigma_{g,0} / \Sigma_d$. Thus, we can safely neglect the evolution of the background state via dust coagulation, and assume uniform dimensionless stopping time $\tau_{s,0}$ and the velocity $v_{x,0} = -2\tau_{s,0} \eta R \Omega / (1 + \tau_{s,0}^2)$.

Based on the above unperturbed state, we obtain the linearized equations from Equations (4.22), (4.24) and (4.25)

$$(n + ikv_{x,0})\delta \Sigma_d + ik\Sigma_{d,0}\delta v_x = 0, \quad (4.26)$$

$$\delta v_x = \frac{1 - \tau_{s,0}^2}{1 + \tau_{s,0}^2} \frac{\delta \tau_s}{\tau_{s,0}} v_{x,0}, \quad (4.27)$$

$$(n + ikv_{x,0})\delta \tau_s = \frac{\delta \Sigma_d}{\Sigma_{g,0}} \frac{\tau_{s,0}}{3t_0} + \frac{\Sigma_{d,0}}{\Sigma_{g,0}} \frac{\delta \tau_s}{3t_0}, \quad (4.28)$$

where we assume plane-wave perturbations as in the previous chapters, i.e., $\delta \Sigma_d \propto \delta v_x \propto \delta \tau_s \propto \exp(ikx + nt)$. Solving the eigenvalue problem with Equations (4.26) - (4.28), we

obtain the following dispersion relation

$$n = n_{\text{ap},\pm} \equiv -ikv_{x,0} + \frac{\varepsilon}{6t_0} \left(1 \pm \sqrt{1 - \frac{12t_0}{\varepsilon} \frac{1 - \tau_{s,0}^2}{1 + \tau_{s,0}^2} ikv_{x,0}} \right), \quad (4.29)$$

where $\varepsilon \equiv \Sigma_{\text{d},0}/\Sigma_{\text{g},0}$. There is one growing mode. For short-wavelength perturbations, the complex growth rate n of the growing mode can be approximated as

$$\begin{aligned} n_{\text{ap},+} &\simeq -ikv_{x,0} + \frac{\varepsilon}{6t_0} \left(1 + \sqrt{\frac{12t_0}{\varepsilon} \frac{1 - \tau_{s,0}^2}{1 + \tau_{s,0}^2} ik|v_{x,0}|} \right) \\ &= -ikv_{x,0} + \frac{\varepsilon}{6t_0} \left(1 + (1+i) \sqrt{\frac{6t_0}{\varepsilon} \frac{1 - \tau_{s,0}^2}{1 + \tau_{s,0}^2} k|v_{x,0}|} \right). \end{aligned} \quad (4.30)$$

Thus, the growth rate, i.e. the real part of n , at large k is

$$\begin{aligned} \text{Re}[n_{\text{ap},+}] &\simeq \frac{\varepsilon}{6t_0} \left(1 + \sqrt{\frac{6t_0}{\varepsilon} \frac{1 - \tau_{s,0}^2}{1 + \tau_{s,0}^2} k|v_{x,0}|} \right) \\ &\simeq \frac{\varepsilon}{3t_0} \sqrt{\frac{3t_0}{2\varepsilon} \frac{1 - \tau_{s,0}^2}{1 + \tau_{s,0}^2} k|v_{x,0}|}. \end{aligned} \quad (4.31)$$

Equation (4.31) is always positive, and thus a disk is unconditionally unstable. The growth rate is much larger than $\varepsilon/3t_0$ at $k \gg \varepsilon/t_0|v_{x,0}|$. Therefore, this instability develops faster than the unperturbed state that evolves at the timescale of $3t_0/\varepsilon$.

A characteristic length scale of coagulation instability is $L_{\text{gdI}} \equiv 3t_0|v_{x,0}|/\varepsilon$, which is called a growth-drift length in the following. The growth-drift length is a distance that dust moves at the unperturbed velocity within the e -folding time of its size. We find that L_{gdI} is comparable to the gas scale height H as follows:

$$\frac{L_{\text{gdI}}}{H} = 3 \left(\frac{t_0\Omega}{0.5} \right) \left(\frac{\varepsilon}{0.01} \right)^{-1} \left(\frac{|v_{x,0}|/c_s}{0.02} \right). \quad (4.32)$$

Using L_{gdI} to normalize a wavenumber $\tilde{k} \equiv kL_{\text{gdI}}$ and assuming $\tilde{k} \gg 1$, we obtain

$$n_{\text{ap},+} \simeq i \frac{\varepsilon}{3t_0} \tilde{k} + \frac{\varepsilon}{6t_0} \left(1 + (1+i) \sqrt{\frac{1 - \tau_{s,0}^2}{1 + \tau_{s,0}^2} 2\tilde{k}} \right). \quad (4.33)$$

Thus, we obtain

$$\text{Re}[n_{\text{ap},+}] \left(\frac{3t_0}{\varepsilon} \right) = \frac{1}{2} + \frac{1}{2} \sqrt{\frac{1 - \tau_{s,0}^2}{1 + \tau_{s,0}^2} 2\tilde{k}} \quad (4.34)$$

When dust particles are so small that the dimensionless stopping time satisfies $\tau_{s,0} \lesssim 0.1$ and $1 \pm \tau_{s,0}^2 \simeq 1$, we obtain

$$\text{Re}[n_{\text{ap},+}] \left(\frac{3t_0}{\varepsilon} \right) = \frac{1}{2} + \sqrt{\frac{\tilde{k}}{2}}. \quad (4.35)$$

We note that L_{gdl} depends on $\tau_{s,0}$. Equation (4.35) signifies that coagulation instability has the self-similarity. Thus, one can derive growth rates for different dust sizes scaling wavelengths \tilde{k} .

The amplitude of $\delta\tau_s/\tau_{s,0}$ is smaller than $\delta\Sigma_d/\Sigma_{d,0}$ for coagulation instability. At short wavelengths, the relative amplitude is approximately given as

$$\begin{aligned} \frac{\delta\tau_s/\tau_{s,0}}{\delta\Sigma_d/\Sigma_{d,0}} &\simeq (1-i) \frac{\varepsilon}{6t_0} \sqrt{\frac{6t_0}{\varepsilon k |v_{x,0}|} \frac{1+\tau_{s,0}^2}{1-\tau_{s,0}^2}}, \\ &= \exp\left(-i\frac{\pi}{4}\right) \sqrt{\frac{1}{kL_{\text{gdl}}} \frac{1+\tau_{s,0}^2}{1-\tau_{s,0}^2}}. \end{aligned} \quad (4.36)$$

This shows that the relative amplitude decreases as increasing k . For $kL_{\text{gdl}} = 100$, $\delta\tau_s/\tau_{s,0}$ is smaller than $\delta\Sigma_d/\Sigma_{d,0}$ by an order of magnitude.

Coagulation instability is triggered by a combination of dust coagulation and traffic jam. When there is a perturbation in dust surface density, dust particles grow more efficiently than those at nodes of the perturbation. On the other hand, dust growth is less efficient at a region of negative density perturbations. These spatially varying growth efficiencies result in $\delta\tau_s$ perturbation that is in phase with $\delta\Sigma_d$. Because non-zero $\delta\tau_s$ leads to radial variation of drift velocity δv_x , dust particles tend to concentrate at nodes where radial gradients of δv_x is negative. This concentration shifts the surface density perturbation toward the central star. Dust growth is enhanced in the shifted region of $\delta\Sigma_d > 0$, leading to amplification of $\delta\tau$. The amplification of $\delta\tau_s$ augments the velocity perturbation δv_x and results in more stronger traffic jam. This successive dust growth and traffic jam lead to coagulation instability.

4.4 Two-fluid linear analyses and results

Next, we perform two-fluid linear analyses and discuss effects of gas motion on coagulation instability. In this analysis, we do not assume the terminal velocity for dust and gas. Basic equations are summarized as follows

$$\frac{\partial \Sigma_{\text{g}}}{\partial t} + \frac{\partial \Sigma_{\text{g}} u_x}{\partial x} = 0, \quad (4.37)$$

$$\frac{\partial u_x}{\partial t} + u_x \frac{\partial u_x}{\partial x} = 3\Omega^2 x + 2\Omega u_y - \frac{1}{\Sigma_g} \frac{\partial c_s^2 \Sigma_g}{\partial x} + \frac{\Sigma_d}{\Sigma_g} \frac{v_x - u_x}{\tau_s} \Omega, \quad (4.38)$$

$$\frac{\partial u_y}{\partial t} + u_x \frac{\partial u_y}{\partial x} = -2\Omega u_x + \frac{\Sigma_d}{\Sigma_g} \frac{v_y - u_y}{\tau_s} \Omega, \quad (4.39)$$

$$\frac{\partial \Sigma_d}{\partial t} + \frac{\partial \Sigma_d v_x}{\partial x} = 0, \quad (4.22)$$

$$\frac{\partial v_x}{\partial t} + v_x \frac{\partial v_x}{\partial x} = 3\Omega^2 x + 2\Omega v_y - \frac{v_x - u_x}{\tau_s} \Omega, \quad (4.40)$$

$$\frac{\partial v_y}{\partial t} + v_x \frac{\partial v_y}{\partial x} = -2\Omega v_x - \frac{v_y - u_y}{\tau_s} \Omega, \quad (4.41)$$

$$\frac{\partial \tau_s}{\partial t} + v_x \frac{\partial \tau_s}{\partial x} = \frac{\Sigma_d}{\Sigma_g} \frac{\tau_s}{3t_0} + \frac{\tau_s}{\Sigma_g} \frac{\partial \Sigma_g u_x}{\partial x} - \frac{\tau_s}{\Sigma_g} v_x \frac{\partial \Sigma_g}{\partial x}. \quad (4.23)$$

As in the one-fluid analyses, we set a unperturbed state without using Equation (4.23). The unperturbed state is then derived from the following equations:

$$\frac{\partial \Sigma_{g,0} u_x}{\partial x} = 0, \quad (4.42)$$

$$u_x \frac{\partial u_x}{\partial x} = 3\Omega^2 x + 2\Omega u_y - \frac{1}{\Sigma_{g,0}} \frac{\partial c_s^2 \Sigma_{g,0}}{\partial x} + \frac{\Sigma_{d,0}}{\Sigma_{g,0}} \frac{v_x - u_x}{\tau_s} \Omega, \quad (4.43)$$

$$u_x \frac{\partial u_y}{\partial x} = -2\Omega u_x + \frac{\Sigma_d}{\Sigma_g} \frac{v_y - u_y}{\tau_s} \Omega, \quad (4.44)$$

$$\frac{\partial \Sigma_d v_x}{\partial x} = 0, \quad (4.45)$$

$$v_x \frac{\partial v_x}{\partial x} = 3\Omega^2 x + 2\Omega v_y - \frac{v_x - u_x}{\tau_s} \Omega, \quad (4.46)$$

$$v_x \frac{\partial v_y}{\partial x} = -2\Omega v_x - \frac{v_y - u_y}{\tau_s} \Omega. \quad (4.47)$$

Coagulation instability requires the drift motion in the unperturbed state. We thus consider non-zero radial gradient of the unperturbed gas surface density $\Sigma'_{g,0} \equiv \partial \Sigma_{g,0} / \partial x$ and gradient of gas pressure $(c_s^2 \Sigma_{g,0})' \equiv \partial (c_s^2 \Sigma_{g,0}) / \partial x$. Assuming small x/R , we approximate the physical variables as constants or linear functions in x :

$$u_x = u_{x,0} + u'_{x,0} x, \quad (4.48)$$

$$u_y = -\frac{3}{2} \Omega x + u_{y,0} + u'_{y,0} x, \quad (4.49)$$

$$\Sigma_d = \Sigma_{d,0} + \Sigma'_{d,0} x, \quad (4.50)$$

$$v_x = v_{x,0} + v'_{x,0} x, \quad (4.51)$$

$$v_y = -\frac{3}{2}\Omega x + v_{y,0} + v'_{y,0}x, \quad (4.52)$$

$$\tau_s = \tau_{s,0} + \tau'_{s,0}x. \quad (4.53)$$

The degree of freedom is 12 for given gas surface density and pressure gradients. We also assume that second- and higher-order terms of those gradients are small enough that we can neglect those terms.

Equation (4.42) gives

$$\Sigma'_{g,0}u_{x,0} + \Sigma_{g,0}u'_{x,0} + 2\Sigma'_{g,0}u'_{x,0}x = 0. \quad (4.54)$$

The first and second terms are the second order in $\Sigma'_{g,0}$ because $u_{x,0}$ should be proportional to $\Sigma'_{g,0}/\Sigma_{g,0}$ in the drift solution. The third term is the third-order in $\Sigma'_{g,0}$ because the spatial derivative of $u_{x,0}$ introduces $\Sigma'_{g,0}$. Therefore, Equation (4.54) is satisfied at the first order in Σ'_g . One also finds that Equation (4.45) is satisfied as well. The remaining equations (Equations (4.43), (4.44), (4.46) and (4.47)) introduce 8 equations to determine the coefficients of x^0 and x^1 for the unperturbed state variables. Because the number of variables (12) is larger than the number of equations (8), we can freely fix four coefficients. In the present analyses, we set $\Sigma'_{d,0} = v'_{x,0} = u'_{x,0} = \tau'_{s,0} = 0$. In this case, we find the following velocity fields from the equations of motion:

$$u_{x,0} = \frac{2\varepsilon\tau_{s,0}}{(1+\varepsilon)^2 + \tau_{s,0}^2} \left(-\frac{(c_s^2\Sigma_{g,0})'}{2\Omega\Sigma_{g,0}} \right), \quad (4.55)$$

$$u_{y,0} = -\left[1 + \frac{\varepsilon\tau_{s,0}^2}{(1+\varepsilon)^2 + \tau_{s,0}^2} \right] \left(-\frac{(c_s^2\Sigma_{g,0})'}{2\Omega\Sigma_{g,0}(1+\varepsilon)} \right), \quad (4.56)$$

$$v_{x,0} = -\frac{2\tau_{s,0}}{(1+\varepsilon)^2 + \tau_{s,0}^2} \left(-\frac{(c_s^2\Sigma_{g,0})'}{2\Omega\Sigma_{g,0}} \right), \quad (4.57)$$

$$v_{y,0} = -\left[1 - \frac{\tau_{s,0}^2}{(1+\varepsilon)^2 + \tau_{s,0}^2} \right] \left(-\frac{(c_s^2\Sigma_{g,0})'}{2\Omega\Sigma_{g,0}(1+\varepsilon)} \right), \quad (4.58)$$

We note that ε , $\Sigma'_{g,0}$, $(c_s^2\Sigma_{g,0})'$, and $\tau_{s,0}$ are parameters to be determined in advance. One finds that the above solution corresponds to the steady drift velocity given by Nakagawa et al. (1986) when relating $\Sigma'_{g,0}$ to η as follows:

$$-\frac{(c_s^2\Sigma_{g,0})'}{\Sigma_{g,0}} = 2\eta R\Omega^2. \quad (4.59)$$

Assuming the temperature profile, one obtains $\Sigma'_{g,0}$ from the following equation:

$$\frac{\Sigma'_{g,0}}{\Sigma_{g,0}} = -\frac{1}{R} \left(2\eta \frac{R^2\Omega^2}{c_s^2} + \frac{\partial \ln c_s^2}{\partial \ln R} \right). \quad (4.60)$$

Linearized equations

Using the above unperturbed state, we linearize the basic equations. Perturbations are assumed to be proportional to $\exp(ikx + nt)$. The amplitudes of the perturbations generally depend on x because the above unperturbed state has x -dependent gas surface density. In this thesis, we focus on short-wavelength perturbations with $kx \gg 1$ and neglect spatial gradients of the amplitudes based on WKB approximation. We also assume an isothermal disk and do not consider temperature perturbation. Under these approximations, the linearized equations are

$$(n + iku_{x,0})\delta\Sigma_g + \left(ik\Sigma_{g,\text{unp}} + \frac{\partial\Sigma_{g,\text{unp}}}{\partial x} \right) \delta u_x = 0, \quad (4.61)$$

$$(n + iku_{x,0})\delta u_x = 2\Omega\delta u_y + \frac{\delta\Sigma_g}{\Sigma_{g,\text{unp}}^2} \frac{\partial c_s^2 \Sigma_{g,\text{unp}}}{\partial x} - \frac{c_s^2}{\Sigma_{g,\text{unp}}} ik\delta\Sigma_g + \frac{\Sigma_{d,0}}{\Sigma_{g,\text{unp}}} \frac{v_{x,0} - u_{x,0}}{\tau_{s,0}} \Omega \left(\frac{\delta\Sigma_d}{\Sigma_{d,0}} - \frac{\delta\Sigma_g}{\Sigma_{g,\text{unp}}} + \frac{\delta v_x - \delta u_x}{v_{x,0} - u_{x,0}} - \frac{\delta\tau_s}{\tau_{s,0}} \right), \quad (4.62)$$

$$(n + iku_{x,0})\delta u_y = -\frac{\Omega}{2}\delta u_x + \frac{\Sigma_{d,0}}{\Sigma_{g,\text{unp}}} \frac{v_{y,0} - u_{y,0}}{\tau_{s,0}} \Omega \left(\frac{\delta\Sigma_d}{\Sigma_{d,0}} - \frac{\delta\Sigma_g}{\Sigma_{g,\text{unp}}} + \frac{\delta v_y - \delta u_y}{v_{y,0} - u_{y,0}} - \frac{\delta\tau_s}{\tau_{s,0}} \right), \quad (4.63)$$

$$(n + ikv_{x,0})\delta\Sigma_d + ik\Sigma_{d,0}\delta v_x = 0, \quad (4.64)$$

$$(n + ikv_{x,0})\delta v_x = 2\Omega\delta v_y - \frac{v_{x,0} - u_{x,0}}{\tau_{s,0}} \Omega \left(\frac{\delta v_x - \delta u_x}{v_{x,0} - u_{x,0}} - \frac{\delta\tau_s}{\tau_{s,0}} \right), \quad (4.65)$$

$$(n + ikv_{x,0})\delta v_y = -\frac{\Omega}{2}\delta v_x - \frac{v_{y,0} - u_{y,0}}{\tau_{s,0}} \Omega \left(\frac{\delta v_y - \delta u_y}{v_{y,0} - u_{y,0}} - \frac{\delta\tau_s}{\tau_{s,0}} \right), \quad (4.66)$$

$$(n + ikv_{x,0})\delta\tau_s = \frac{\Sigma_{d,0}}{\Sigma_{g,\text{unp}}} \frac{\tau_{s,0}}{3t_0} \left(\frac{\delta\Sigma_d}{\Sigma_{d,0}} - \frac{\delta\Sigma_g}{\Sigma_{g,\text{unp}}} + \frac{\delta\tau_s}{\tau_{s,0}} \right) + \frac{\tau_{s,0}}{\Sigma_{g,\text{unp}}} \left[\left(ik\Sigma_{g,\text{unp}} + \frac{\partial\Sigma_{g,\text{unp}}}{\partial x} \right) \delta u_x + iku_{x,0}\delta\Sigma_g \right] - \frac{\tau_{s,0}v_{x,0}}{\Sigma_{g,\text{unp}}} ik\delta\Sigma_g - \frac{\tau_{s,0}v_{x,0}}{\Sigma_{g,\text{unp}}} \frac{\partial\Sigma_{g,\text{unp}}}{\partial x} \left(\frac{\delta\tau_s}{\tau_{s,0}} + \frac{\delta v_x}{v_{x,0}} - \frac{\delta\Sigma_g}{\Sigma_{g,\text{unp}}} \right), \quad (4.67)$$

where $\Sigma_{g,\text{unp}} \equiv \Sigma_{g,0} + \Sigma'_{g,0}x$. We calculate the complex growth rate n for $x = 0$, i.e., $\Sigma_{g,\text{unp}} = \Sigma_{g,0}$.

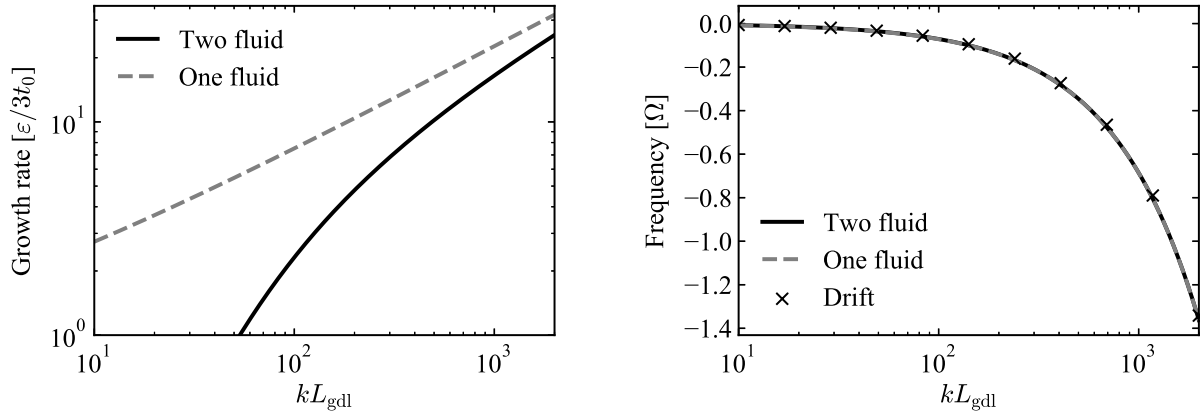


Figure 4.3: Growth rates and oscillation frequencies for $\tau_{s,0} = 0.1$, $\varepsilon = 10^{-3}$, and $R = 20$ au. In this case, one has $L_{\text{gdl}} \simeq 33.78H$. The grey dashed lines correspond to the growth rate and the oscillation frequency obtained from one-fluid analyses (Equation (4.29)). Cross marks on the right panel shows the oscillation frequency due to the dust drift $v_{x,0}k$.

Growth rate of coagulation instability in two-fluid disks

In the present analyses, we use the minimum mass solar nebula disk model (Hayashi 1981) with a solar-mass star to estimate $\Sigma'_{\text{g},0}$. The gas surface density and the temperature T are given by $\Sigma_{\text{g},0} = 1700(R/1 \text{ au})^{-3/2} \text{ g cm}^{-2}$ and $T = 280(R/1 \text{ au})^{-1/2} \text{ K}$. Assuming the midplane gas density $\rho_{\text{g}}(0) = \Sigma_{\text{g}}/\sqrt{2\pi}H$ and the mean molecular weight of 2.34, we obtain $\eta \simeq 1.8 \times 10^{-3}(R/1 \text{ au})^{1/2}$. We then calculate growth rates and phase velocities for a certain radius R .

Figure 4.3 shows the growth rate $\text{Re}[n]$ normalized by $\varepsilon/3t_0$ and the oscillation frequency $-\text{Im}[n]$ normalized by the Keplerian frequency Ω in the case of $\tau_{s,0} = 0.1$, $\varepsilon = 10^{-3}$, and $R = 20$ au. We also plot the growth rate and the frequency obtained from the one-fluid analyses (Equation (4.29)). The two-fluid analyses give lower growth rates, and the difference is significant especially at longer wavelengths. On the other hand, the oscillation frequencies show a good agreement between the one-fluid and two-fluid analyses. The frequencies from both analyses are well reproduced by the drift-induced frequency $v_{x,0}k$.

The quantitative differences come from the third term on the right hand side of Equation (4.23). The term represents that the stopping time decreases as dust drifts into the inner high gas density region. To show the effect on the dispersion relation, we perform “modified” one-fluid analyses using Equation (4.22) and the following equation:

$$\frac{\partial \tau_{\text{s}}}{\partial t} + v_x \frac{\partial \tau_{\text{s}}}{\partial x} = \frac{\Sigma_{\text{d}}}{\Sigma_{\text{g}}} \frac{\tau_{\text{s}}}{3t_0} - \frac{\tau_{\text{s}}}{\Sigma_{\text{g}}} v_x \frac{\partial \Sigma_{\text{g}}}{\partial x}, \quad (4.68)$$

4.4. TWO-FLUID LINEAR ANALYSES AND RESULTS

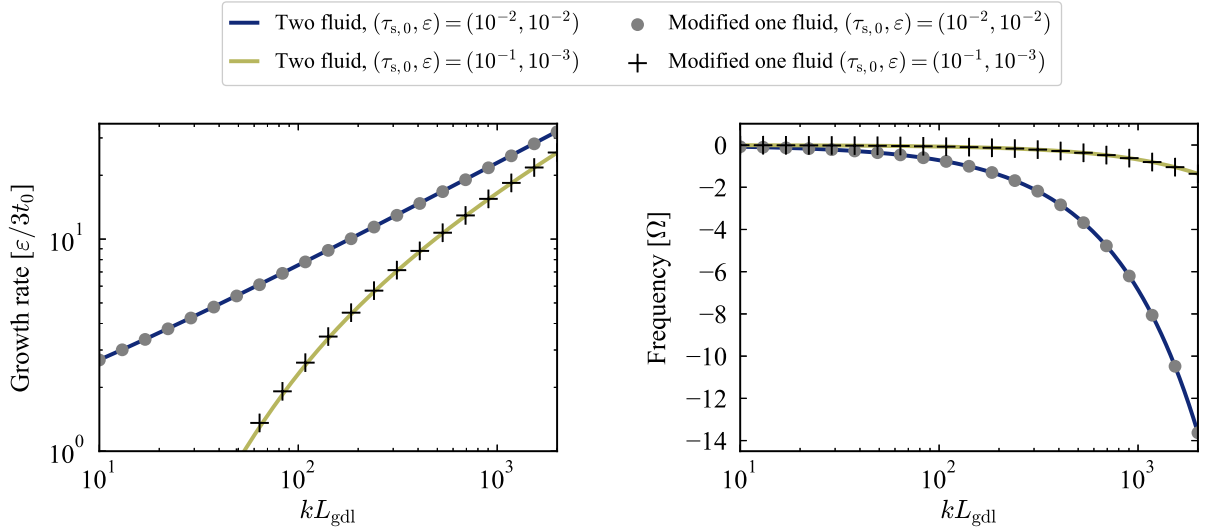


Figure 4.4: Growth rate and oscillation frequency at $R = 20$ au. Blue and yellow solid lines show the results for $(\tau_{s,0}, \varepsilon) = (10^{-2}, 10^{-2})$ and $(10^{-1}, 10^{-3})$, respectively. Filled circles and plus marks represent growth rates and phase velocities obtained from modified one-fluid analyses. We find that the results of the two-fluid analyses are well reproduced by the modified one-fluid analyses.

In the same way of the one-fluid linear analyses in the previous subsection, one can derive a dispersion relation of the growing mode:

$$n_{\text{ap}}(k, T) \equiv -ikv_{x,0} + \frac{\varepsilon}{6t_0} \left(T + \sqrt{T^2 - \frac{12t_0}{\varepsilon} \frac{1 - \tau_{s,0}^2}{1 + \tau_{s,0}^2} ikv_{x,0}} \right), \quad (4.69)$$

$$T \equiv 1 + \frac{2}{1 + \tau_{s,0}^2} \frac{L_{\text{gdl}}}{\Sigma_{g,0}/\Sigma'_{g,0}}. \quad (4.70)$$

Considering $\tau_{s,0} \ll 1$, one obtains

$$n_{\text{ap}}(k, T) \simeq -ikv_{x,0} + \frac{\varepsilon}{6t_0} \left(T + \sqrt{T^2 - \frac{12t_0}{\varepsilon} ikv_{x,0}} \right) \quad (4.71)$$

$$T \simeq 1 + 2 \frac{L_{\text{gdl}}}{\Sigma_{g,0}/\Sigma'_{g,0}}. \quad (4.72)$$

Figure 4.4 compares the modified one-fluid dispersion relation $n_{\text{ap}}(k, T)$ and two-fluid dispersion relation n for $(\tau_{s,0}, \varepsilon) = (10^{-2}, 10^{-2})$ and $(10^{-1}, 10^{-3})$. The two-fluid dispersion relations are well reproduced by the modified one-fluid dispersion relation, meaning that the decrease of the growth rates is responsible for the third term on the right hand

side of Equation (4.23). In other words, modes of gas are irrelevant to coagulation instability, and the only unperturbed gas structure ($\Sigma_{g,0}$) affects the growth rate. The newly introduced factor T is less than unity because of the negative gas surface density gradient, and thus the growth rate becomes smaller than in one-fluid analyses ($T = 0$). The oscillation frequencies are mainly determined by the drift velocity $v_{x,0}$, which depends on the dimensionless stopping time $\tau_{s,0}$ even in the modified one-fluid analyses.

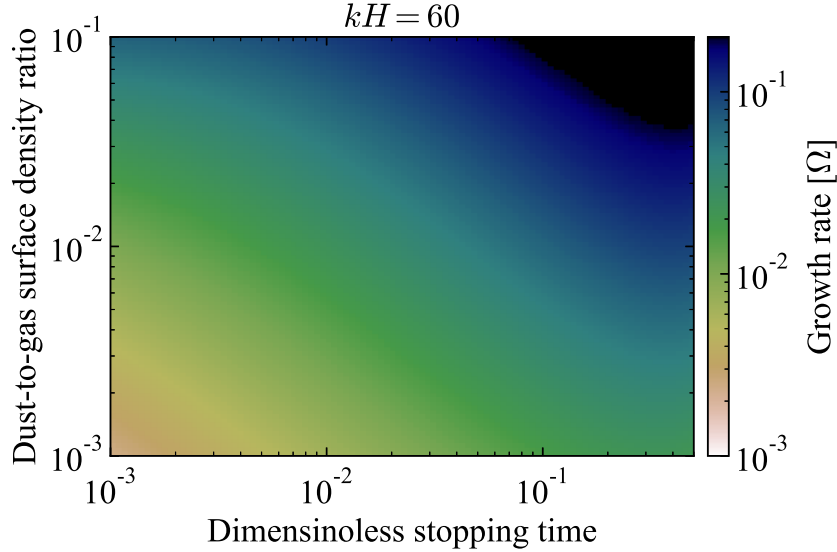


Figure 4.5: Growth rate for $kH = 60$ as a function of the dimensionless stopping time $\tau_{s,0}$ and the unperturbed dust-to-gas surface density ratio $\varepsilon = \Sigma_{d,0}/\Sigma_{g,0}$. Here we assume $R = 20$ au. The color shows the growth rate in the unit of Ω . Even for $\varepsilon \sim 10^{-3}$, the growth rates of coagulation instability can be $\sim 0.01\Omega$, which shows that the instability grows only within 20 Keplerian periods.

Figure 4.5 shows the two-fluid growth rate as a function of the dimensionless stopping time and the unperturbed dust-to-gas surface density ratio. We plot the growth rates at $kH = 60$ as the reference value. If one takes larger k , one will find larger growth rate (see Figure 4.4). We find that the growth rate increases as $\tau_{s,0}$ and ε increase. These trends are consistent with the ε - and $\tau_{s,0}$ -dependences of the one-fluid dispersion relation. As $\tau_{s,0}$ increases, one obtains larger dust drift speed $|v_{x,0}|$. Because the velocity perturbation is proportional to $v_{x,0}$ (Equation (4.27)), the faster drift speed leads to stronger traffic jam and thus larger growth rate. As ε increases, dust coagulation becomes effective and coagulation instability grows faster. According to Equation (4.72), the growth rate at short wavelengths ($12t_0k|v_{x,0}|/\varepsilon T^2 \gg 1$) is proportional to $\sqrt{k|v_{x,0}|t_0/\varepsilon} \propto \sqrt{\tau_{s,0}/\varepsilon}$. Therefore, the growth rates are constant along lines of constant $\tau_{s,0}/\varepsilon$, which can be seen in Figure 4.5.

4.5 Discussion

4.5.1 Stabilization due to dust diffusion

Gas turbulence drives not only collisional growth but also dust diffusion, which smooths out dust surface density perturbations. The diffusion will prevent coagulation instability especially at short wavelengths and limits its growth rate. In this subsection, we discuss to what extent the diffusion stabilizes the instability by simply performing one-fluid analyses.

As shown in Chapter 2, simply adding the diffusion term to the continuity equation violates the angular momentum conservation. We showed that replacing dust velocity by a sum of the mean-flow velocity and the diffusive-flow velocity recovers the angular momentum conservation. We thus simply replace v_x in Equations (4.22) and (4.68) as

$$v_x = \langle v_x \rangle - \frac{D}{\Sigma_d} \frac{\partial \Sigma_d}{\partial x}, \quad (4.73)$$

where D is a diffusion coefficient and $\langle v_x \rangle$ is the mean-flow component representing the collective drift and defined by

$$\langle v_x \rangle \equiv -\frac{2\tau_s}{1 + \tau_s^2} \eta R \Omega. \quad (4.74)$$

Some studies use another form of the diffusion flux proportional to gradient of dust-to-gas ratio, which corresponds to another closure relation between $\langle \Delta \Sigma_d \Delta v_r \rangle$ and $\langle \Sigma_d \rangle$. To check the difference, we thus consider another case where we use the following dust velocity:

$$v_x = \langle v_x \rangle - \frac{D \Sigma_g}{\Sigma_d} \frac{\partial}{\partial x} \left(\frac{\Sigma_d}{\Sigma_g} \right). \quad (4.75)$$

Substituting Equation (4.73) to the continuity equation gives

$$\frac{\partial \Sigma_d}{\partial t} + \frac{\partial \Sigma_d \langle v_x \rangle}{\partial x} = \frac{\partial}{\partial x} \left(D \frac{\partial \Sigma_d}{\partial x} \right) \quad (4.76)$$

$$\frac{\partial \tau_s}{\partial t} + \left(\langle v_x \rangle - \frac{D}{\Sigma_d} \frac{\partial \Sigma_d}{\partial x} \right) \frac{\partial \tau_s}{\partial x} = \frac{\Sigma_d}{\Sigma_g} \frac{\tau_s}{3t_0} - \frac{\tau_s}{\Sigma_g} \left(\langle v_x \rangle - \frac{D}{\Sigma_d} \frac{\partial \Sigma_d}{\partial x} \right) \frac{\partial \Sigma_g}{\partial x}. \quad (4.77)$$

When we use Equation (4.75), we obtain the following equations:

$$\frac{\partial \Sigma_d}{\partial t} + \frac{\partial \Sigma_d \langle v_x \rangle}{\partial x} = \frac{\partial}{\partial x} \left(D \Sigma_g \frac{\partial}{\partial x} \left(\frac{\Sigma_d}{\Sigma_g} \right) \right) \quad (4.78)$$

$$\frac{\partial \tau_s}{\partial t} + \left(\langle v_x \rangle - \frac{D \Sigma_g}{\Sigma_d} \frac{\partial}{\partial x} \left(\frac{\Sigma_d}{\Sigma_g} \right) \right) \frac{\partial \tau_s}{\partial x} = \frac{\Sigma_d}{\Sigma_g} \frac{\tau_s}{3t_0} - \frac{\tau_s}{\Sigma_g} \left(\langle v_x \rangle - \frac{D \Sigma_g}{\Sigma_d} \frac{\partial}{\partial x} \left(\frac{\Sigma_d}{\Sigma_g} \right) \right) \frac{\partial \Sigma_g}{\partial x}. \quad (4.79)$$

4.5. DISCUSSION

We perform linear analyses based on Equations (4.76) and (4.77) and those based on Equations (4.78) and (4.79). In both cases, we set unperturbed states with uniform dust surface density and uniform dimensionless stopping time. We take into account the dust growth equation (Equation (4.77) or (4.79)) only for perturbed quantities as in the one-fluid analyses.

First, we perform linear analyses using Equations (4.76) and (4.77). In this case, the unperturbed velocity is

$$v_{x,0} = \langle v_{x,0} \rangle = -2\tau_{s,0}\eta \frac{R\Omega}{1 + \tau_{s,0}^2}. \quad (4.80)$$

Based on the above unperturbed velocity with uniform $\Sigma_{d,0}$ and $\tau_{s,0}$, we obtain the following linearized equations:

$$(n + ik \langle v_{x,0} \rangle + Dk^2) \frac{\delta \Sigma_d}{\Sigma_{d,0}} + \frac{1 - \tau_{s,0}^2}{1 + \tau_{s,0}^2} ik \langle v_{x,0} \rangle \frac{\delta \tau_s}{\tau_{s,0}} = 0, \quad (4.81)$$

$$\left(n + ik \langle v_{x,0} \rangle - \frac{\varepsilon}{3t_0} + \frac{2 \langle v_{x,0} \rangle \Sigma'_{g,0}}{1 + \tau_{s,0}^2 \Sigma_{g,0}} \right) \frac{\delta \tau_s}{\tau_{s,0}} + \left(-\frac{\varepsilon}{3t_0} - ikD \frac{\Sigma'_{g,0}}{\Sigma_{g,0}} \right) \frac{\delta \Sigma_d}{\Sigma_{d,0}} = 0. \quad (4.82)$$

The full dispersion relation is

$$(n + ik \langle v_{x,0} \rangle)^2 + A_1(n + ik \langle v_{x,0} \rangle) + A_0 = 0, \quad (4.83)$$

$$A_1 = -\frac{\varepsilon}{3t_0} + \frac{2 \langle v_{x,0} \rangle \Sigma'_{g,0}}{1 + \tau_{s,0}^2 \Sigma_{g,0}} + Dk^2, \quad (4.84)$$

$$A_0 = ik \langle v_{x,0} \rangle \left(\frac{1 - \tau_{s,0}^2}{1 + \tau_{s,0}^2} \right) \left(\frac{\varepsilon}{3t_0} + ikD \frac{\Sigma'_{g,0}}{\Sigma_{g,0}} \right) + Dk^2 \left(-\frac{\varepsilon}{3t_0} + \frac{2 \langle v_{x,0} \rangle \Sigma'_{g,0}}{1 + \tau_{s,0}^2 \Sigma_{g,0}} \right). \quad (4.85)$$

The terms proportional to $\Sigma'_{g,0}$ come from the last term on the right hand side of Equation (4.77). Using $L_{\text{gdl}} = 3t_0 \langle v_{x,0} \rangle / \varepsilon$ and T defined by Equation (4.70), we obtain the dispersion relation of a growing mode

$$n \frac{3t_0}{\varepsilon} = i\tilde{k} + \frac{1}{2} (T - \beta \tilde{k}^2) + \frac{1}{2} \sqrt{(T + \beta \tilde{k}^2)^2 + 4i\tilde{k} \frac{1 - \tau_{s,0}^2}{1 + \tau_{s,0}^2} \left(1 + i\tilde{k} \beta L_{\text{gdl}} \frac{\Sigma'_{g,0}}{\Sigma_{g,0}} \right)}, \quad (4.86)$$

where $\beta = DL_{\text{gdl}}^{-2}(3t_0/\varepsilon)$ is a dimensionless diffusion coefficient. Assuming that dust particles are so small that they satisfy $\tau_{s,0} \ll 1$ and $D \simeq \alpha c_s^2 \Omega^{-1}$ (see Youdin & Lithwick 2007), we can relate β to often-used strength of turbulence α as follows (see also Equation (4.32)):

$$\begin{aligned} \beta &\simeq \alpha \left(\frac{H}{L_{\text{gdl}}} \right)^2 \frac{3t_0 \Omega}{\varepsilon} \\ &\simeq 6.6 \times 10^{-4} \left(\frac{\alpha}{1 \times 10^{-4}} \right) \left(\frac{t_0 \Omega}{0.5} \right)^{-1} \left(\frac{\varepsilon}{1 \times 10^{-3}} \right) \left(\frac{|v_{x,0}|/c_s}{0.01} \right)^{-2}. \end{aligned} \quad (4.87)$$

4.5. DISCUSSION

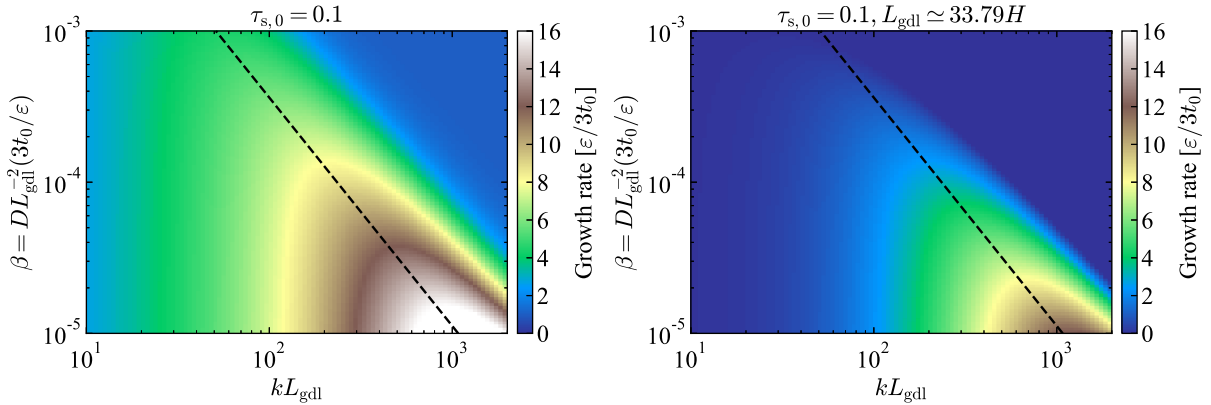


Figure 4.6: Growth rate with the dust diffusion. The left panel shows growth rates calculated without the terms proportional to $\Sigma'_{g,0}$ in Equation (4.86) while the right panel shows growth rate that we derive with all terms in Equation (4.86). The dashed line shows wavenumber estimated by Equation (4.88)

We note that β depends on dust sizes because the drift speed $|v_{x,0}|$ depends on the dimensionless stopping time. As in the comparison of the one-fluid and modified one-fluid analyses, we evaluate (1) growth rates without the terms proportional to $\Sigma'_{g,0}$ and (2) growth rates with all terms in Equation (4.86), separately.

Figure 4.6 shows growth rates as a function of kL_{gdl} and the dimensionless diffusion coefficient β for $\tau_s = 0.1$. On the left panel, we show growth rates calculated without the last term on the right-hand side of Equation (4.77) while on the right panel we show growth rates that we derived using all terms. In both cases, coagulation instability is stabilized at short wavelengths. As in the diffusion-free case, including the decrease of τ_s due to the gas surface density gradient $\Sigma'_{g,0}$ reduces the growth rate by a factor of a few for $L_{\text{gdl}} \simeq 33.79H$. One finds smaller growth rates for stronger diffusion, i.e., larger β . When a gas disk is less turbulent and β becomes less than 1×10^{-4} , coagulation instability grows 2-10 times faster than dust coagulates. Such a situation is realized in a region where $\alpha \times \epsilon \simeq 1.5 \times 10^{-8}$ (see Equation (4.87)).

As a result of diffusion, coagulation instability has the most unstable wavenumber k_{max} in contrast to the diffusion-free case. We find that the most unstable wavenumber is well described by the following relation:

$$k_{\text{max}}L_{\text{gdl}} \simeq \frac{1}{3} \left(\frac{4}{\beta^2} \frac{1 - \tau_{s,0}^2}{1 + \tau_{s,0}^2} \right)^{1/3}. \quad (4.88)$$

The dashed line in Figure 4.6 shows the wavenumber given by the right hand side of Equation (4.88). In both panels, Equation (4.88) well reproduces the most unstable

4.5. DISCUSSION

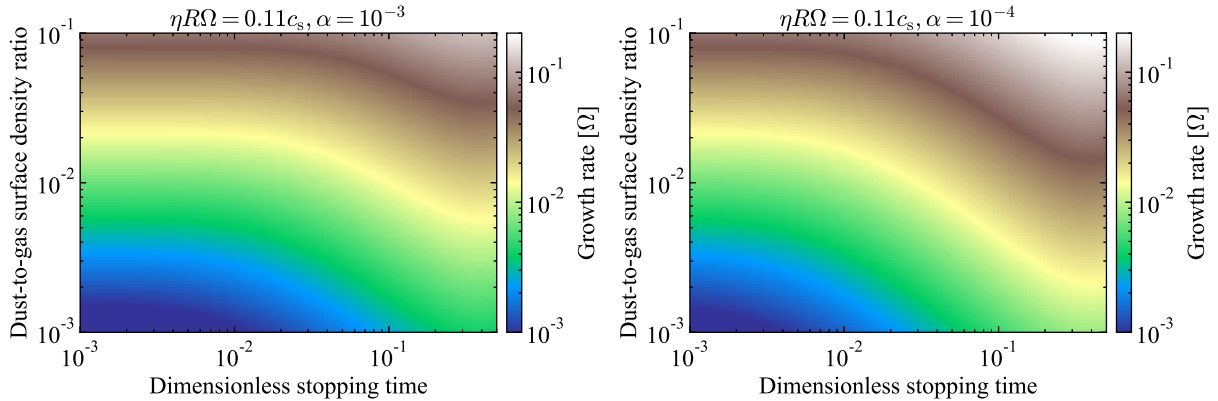


Figure 4.7: Growth rate at $kL_{\text{gdI}} = (4\beta^{-2}(1 - \tau_{\text{s},0}^2)/27(1 + \tau_{\text{s},0}^2))^{1/3}$ (Equation (4.88)) as a function of dimensionless stopping time $\tau_{\text{s},0}$ and unperturbed dust-to-gas surface density ratio $\varepsilon = \Sigma_{\text{d},0}/\Sigma_{\text{g},0}$. The left and right figures show the growth rate for $\alpha = 10^{-3}$ and $\alpha = 10^{-4}$, respectively.

wavenumber. Considering small dust particles with $1 \pm \tau_{\text{s},0}^2 \simeq 1$, one obtains the most unstable wavelength $\lambda_{\text{max}} \equiv 2\pi/k_{\text{max}}$ as follows:

$$\lambda_{\text{max}} \simeq 1.07H \left(\frac{\alpha}{1 \times 10^{-4}} \right)^{2/3} \left(\frac{t_0\Omega}{0.5} \right)^{1/3} \left(\frac{\varepsilon}{1 \times 10^{-3}} \right)^{-1/3} \left(\frac{|v_{x,0}|/c_s}{0.02} \right)^{-1/3} \quad (4.89)$$

Figure 4.7 shows the growth rate at a wavelength given by Equation (4.88). We neglect the last term on the right-hand side of Equation (4.77) because the global simulations of coagulation show radial constant τ_{s} (e.g., Okuzumi et al. 2012). Following Youdin & Lithwick (2007) and Youdin (2011), we calculate the diffusion coefficient as

$$D = \frac{1 + \tau_{\text{s},0} + 4\tau_{\text{s},0}^2}{(1 + \tau_{\text{s},0}^2)^2} \alpha c_s H. \quad (4.90)$$

The strength of turbulence α is assumed to be 10^{-3} on the left panel of Figure 4.7 and 10^{-4} on the right panel. In weakly turbulent disks with $\alpha = 10^{-4}$, coagulation instability can develop within $\simeq 10 - 30$ Keplerian period even when the dust-to-gas ratio is less than 0.01 if dust grains grow up to $\tau_{\text{s},0} \simeq 0.1$. The timescale is still tens of Keplerian periods even for $\alpha = 10^{-3}$.

Next, we perform linear analyses using Equations (4.78) and (4.79). We found little difference from the above analyses based on Equations (4.76) and (4.77). We thus simply show a dispersion relation.

The unperturbed state with uniform $\Sigma_{\text{g},0}$ has the dust drift velocity $v_{x,0} = \langle v_{x,0} \rangle + D\Sigma'_{\text{g},0}/\Sigma_{\text{g},0}$. Linearizing Equations (4.78) and (4.79), we obtain the following dispersion

relation:

$$(n + ikv_{x,0})^2 + B_1(n + ikv_{x,0}) + B_0 = 0, \quad (4.91)$$

$$B_1 = -\frac{\varepsilon}{3t_0} + \frac{2v_{x,0}}{1 + \tau_{s,0}^2} \frac{\Sigma'_{g,0}}{\Sigma_{g,0}} + Dk^2 - D \left(\frac{\Sigma'_{g,0}}{\Sigma_{g,0}} \right)^2 \frac{1 - \tau_{s,0}^2}{1 + \tau_{s,0}^2}, \quad (4.92)$$

$$B_0 = ikv_{x,0} \left(\frac{1 - \tau_{s,0}^2}{1 + \tau_{s,0}^2} \right) \left(\frac{\varepsilon}{3t_0} + ikD \frac{\Sigma'_{g,0}}{\Sigma_{g,0}} \right) + Dk^2 \left(-\frac{\varepsilon}{3t_0} + \frac{2v_{x,0}}{1 + \tau_{s,0}^2} \frac{\Sigma'_{g,0}}{\Sigma_{g,0}} \right) - \frac{ik\varepsilon D \Sigma'_{g,0}}{3t_0 \Sigma_{g,0}} \frac{1 - \tau_{s,0}^2}{1 + \tau_{s,0}^2}. \quad (4.93)$$

The differences from Equations (4.86)-(4.85) are (1) $\langle v_{x,0} \rangle$ is replaced with $v_{x,0}$, (2) the last terms on the right-hand side of Equations (4.92) and (4.93). The former is small for $|\langle v_{x,0} \rangle| > D|\Sigma'_{g,0}/\Sigma_{g,0}|$, which roughly corresponds to $\tau_{s,0} > \alpha$. We also find that the latter difference is also small as follows. The last term of Equation (4.92) is much smaller than the third term Dk^2 because coagulation instability grows at $kH \gg 1$. The last term on the right-hand side of Equation (4.93) is also smaller than the first term for $\tau_{s,0} > \alpha$ and $|v_{x,0}| > D|\Sigma'_{g,0}/\Sigma_{g,0}|$ are satisfied. Because of $H_d/H \simeq \sqrt{\alpha/\tau_{s,0}}$, the condition $\tau_{s,0} > \alpha$ is equivalent to $H_d < H$. This is what we usually expect for large grains.

4.5.2 Effects of other collision velocities

Although we consider turbulent-induced collisions in the above sections, the collision velocity in reality consists of multiple components:

$$\Delta v_{pp} = \sqrt{(\Delta v_t)^2 + (\Delta v_B)^2 + (\Delta v_r)^2 + (\Delta v_\phi)^2 + (\Delta v_z)^2}, \quad (4.94)$$

where Δv_t is the turbulent-induced velocity, Δv_B is a collision velocity due to Brownian motion, Δv_r , Δv_ϕ , and Δv_z are relative velocities due to the drift motion. Considering these collision velocities increases coagulation rate, and thus coagulation instability will grow faster.

In the following, we estimate how much coagulation instability is accelerated. For a collision of dust grains with masses of m_1 and m_2 , the collision velocity induced by the Brownian motion is

$$\Delta v_B = \sqrt{\frac{8k_B T(m_1 + m_2)}{\pi m_1 m_2}}. \quad (4.95)$$

According to Brauer et al. (2008), the Brownian motion is effective only for small dust grains that show insignificant drift. We can neglect the Brownian motion in the present discussion because coagulation instability grows when dust grains drift. In the absence

of frictional backreaction to gas, the radial, azimuthal, vertical relative velocities are

$$\Delta v_r = -\frac{2\tau_s(2 - \tau_s^2)}{(4 + \tau_s^2)(1 + \tau_s^2)}\eta R\Omega, \quad (4.96)$$

$$\Delta v_\phi = \frac{3\tau_s^2}{(4 + \tau_s^2)(1 + \tau_s^2)}\eta R\Omega \quad (4.97)$$

$$\Delta v_z = -\frac{\tau_s}{(2 + \tau_s)(1 + \tau_s)}z\Omega, \quad (4.98)$$

where we assume dust grains whose size ratio is 0.5. Assuming $\Delta v_t = \sqrt{C\alpha}\tau_s c_s$, one finds $\Delta v_r/\Delta v_t \propto \Delta v_z/\Delta v_t \propto \sqrt{\tau_s/\alpha}$ and $\Delta v_\phi/\Delta v_t \propto \tau_s\sqrt{\tau_s/\alpha}$ for leading-order terms. Thus, Δv_r and Δv_z are larger than Δv_ϕ for $\tau_s < 1$, and we approximate the collision velocity Δv_{pp} using the following equation:

$$\Delta v_{pp} \simeq \Delta v_t \sqrt{1 + f \frac{\tau_s}{\alpha}}, \quad (4.99)$$

where f is defined as

$$\begin{aligned} f &\equiv \frac{\alpha}{\tau_s} \left(\left(\frac{\Delta v_r}{\Delta v_t} \right)^2 + \left(\frac{\Delta v_z}{\Delta v_t} \right)^2 \right), \\ &= \frac{4}{C} \left(\frac{2 - \tau_s^2}{(4 + \tau_s^2)(1 + \tau_s^2)} \right)^2 \left(\frac{\eta R\Omega}{c_s} \right)^2 + \frac{1}{C(2 + \tau_s)^2(1 + \tau_s)^2} \left(\frac{z}{H} \right)^2 \end{aligned} \quad (4.100)$$

Substituting Equation (4.99) into Equation (4.20) gives

$$\frac{\partial \tau_s}{\partial t} + v_x \frac{\partial \tau_s}{\partial x} = \sqrt{1 + f \frac{\tau_s}{\alpha}} \frac{\Sigma_d}{\Sigma_{g,0}} \frac{\tau_s}{3t_0}. \quad (4.101)$$

We thus expect that growth rates of coagulation instability becomes larger by a factor of $\sqrt{1 + f\tau_{s,0}/\alpha}$. If the dust scale height is determined by turbulent stirring ($z \simeq H_d \simeq \sqrt{\alpha/\tau_s}H$), one obtains $\sqrt{1 + f\tau_{s,0}/\alpha} \simeq 5$ for $\tau_{s,0} = 0.1$, $\alpha = 10^{-4}$, $C = 0.49$, and $\eta R\Omega = 0.11c_s$ that corresponds to a value at $R = 20$ au in the minimum-mass solar nebula. In such a case, coagulation instability will grow five times faster than shown in the previous sections.

4.5.3 Comparison with the drift timescale

Exponentially growing perturbations due to coagulation instability move inward at a phase velocity $\simeq v_{x,0}$ as shown in the above sections. Thus, coagulation instability

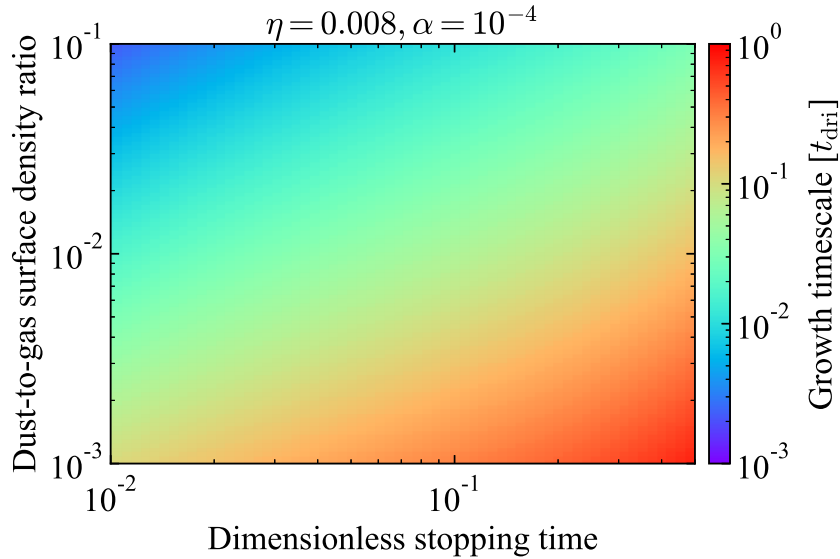


Figure 4.8: Growth timescale in the unit of drift timescale t_{dri} at the most unstable wavelength. The vertical and horizontal axes show the unperturbed dust-to-gas surface density ratio $\varepsilon = \Sigma_{\text{d},0}/\Sigma_{\text{g},0}$ and dimensionless stopping time $\tau_{\text{s},0}$. The strength of turbulence is assumed to be $\alpha = 10^{-4}$.

significantly affects the disk and dust evolution only if its growth timescale is shorter than the drift timescale:

$$t_{\text{dri}} = \frac{R}{|v_{x,0}|} = \frac{1 + \tau_{\text{s}}^2}{2\tau_{\text{s},0}\eta\Omega}. \quad (4.102)$$

One finds $t_{\text{dri}}\Omega \simeq 631$ for $\tau_{\text{s},0} = 0.1$ and $\eta = 0.008$. Thus, perturbations reach a central star within one hundred orbital periods. Figure 4.8 shows the growth timescale of coagulation instability normalized by t_{dri} at the most unstable wavelength. The vertical and horizontal axes are dust-gas ratio $\varepsilon = \Sigma_{\text{d},0}/\Sigma_{\text{g},0}$ and dimensionless stopping time $\tau_{\text{s},0}$, respectively. The growth timescale is basically shorter than the drift timescale in plotted region. Including the relative drift speed in the collision speed, one will find shorter growth timescales of the instability. Thus, we expect coagulation instability operates and affects the disk and dust evolution.

4.5.4 Effects of fragmentation and erosion

In the above sections, we neglect collisional fragmentation of dust grains that takes place when the collision speed is larger than a critical speed (e.g., Wada et al. 2013 2009). Erosive collisions will reduce growth efficiency of peak-mass dust particles (Krijt et al. 2015). We discuss whether coagulation instability operates in the presence of collisional fragmentation and erosion. In this thesis, we simply modify Equation (4.25) introducing

a sticking efficiency ϵ_{eff} as in previous studies (e.g., Okuzumi & Hirose 2012, Okuzumi et al. 2016, Ueda et al. 2019):

$$\frac{\partial \tau_s}{\partial t} + v_x \frac{\partial \tau_s}{\partial x} = \epsilon_{\text{eff}} \frac{\Sigma_d}{\Sigma_{g,0}} \frac{\tau_s}{3t_0}. \quad (4.103)$$

Replacing t_0 with $t_0/\epsilon_{\text{eff}}$ in Equation (4.29), we obtain one-fluid dispersion relation in the presence of fragmentation:

$$n_{\text{ap},\pm} \equiv -ikv_{x,0} + \epsilon_{\text{eff}} \frac{\varepsilon}{6t_0} \left(1 \pm \sqrt{1 - \epsilon_{\text{eff}}^{-1} \frac{12t_0}{\varepsilon} \frac{1 - \tau_{s,0}^2}{1 + \tau_{s,0}^2} ikv_{x,0}} \right). \quad (4.104)$$

When fragmentation or erosion results in imperfect sticking ($0 < \epsilon_{\text{eff}} < 1$), the growth rate of coagulation instability decreases. At short wavelengths, the growth rate is proportional to $\sqrt{\epsilon_{\text{eff}}}$.

When catastrophic fragmentation ($\epsilon_{\text{eff}} < 0$) occurs, we find that a mode with a complex growth rate $n_{\text{ap},-}$ becomes unstable while coagulation instability becomes stable (i.e., $\text{Re}[n_{\text{ap},+}] < 0$). The growth rate $\text{Re}[n_{\text{ap},-}]$ at short wavelengths is

$$\text{Re}[n_{\text{ap},-}] \simeq |\epsilon_{\text{eff}}| \frac{\varepsilon}{6t_0} \sqrt{|\epsilon_{\text{eff}}|^{-1} \frac{6t_0}{\varepsilon} \frac{1 - \tau_{s,0}^2}{1 + \tau_{s,0}^2} k|v_{x,0}|}. \quad (4.105)$$

At short wavelengths, the relative amplitude of $\delta\tau_s$ and $\delta\Sigma_d$ is approximately given by

$$\frac{\delta\tau_s/\tau_{s,0}}{\delta\Sigma_d/\Sigma_{d,0}} \simeq -\exp\left(i\frac{\pi}{4}\right) \sqrt{\frac{|\epsilon_{\text{eff}}|\varepsilon}{3t_0k|v_{x,0}|} \frac{1 + \tau_{s,0}^2}{1 - \tau_{s,0}^2}}. \quad (4.106)$$

Although Equation (4.106) shows negative correlation except for $\exp(i\pi/4)$ in contrast to coagulation instability, its physical mechanism is similar to coagulation instability. Dust particles are subject to more significant fragmentation at high density regions ($\delta\Sigma_d >$), leading to a radial variation of $\delta\tau_s$ and δv_x . The resultant radial gradient of δv_x leads to traffic jam in the radial direction and promotes further fragmentation at dust-piling-up regions. This positive feedback results in the “fragmentation-driven” instability.

4.5.5 Coevolution with other dust-gas instabilities

Because coagulation instability is triggered by dust coagulation, the instability is entirely different from any other dust-gas instabilities previously studied, including secular GI and TVGI discussed in Chapters 2 and 3. For example, one will find that $\text{Re}[n_{\text{ap},+}]$ in Equation (4.29) goes to zero when taking the limit of $t_0 \rightarrow \infty$, meaning that dust coagulation is the essential process for the instability.

The previous studies on dust coagulation showed dust depletion if a disk is isolated and there is no mass infall (e.g., Brauer et al. 2008; Okuzumi et al. 2012). In such a dust-depleted region, the previously-studied dust-gas instabilities can not grow. On the other hand, coagulation instability can grow even when dust-to-gas surface density ratio is 10^{-3} . Development of coagulation instability leads to dust concentration at small scale $\sim k^{-1}$. In the presence of dust diffusion, we can expect such a dust concentration at a spatial scale of $\sim H$ (see Equation (4.89)). Nonlinear development will result in significant increase in dust surface density by an order of magnitude, which will be briefly shown in the next chapter. If such a nonlinear development is achieved, coagulation timescale becomes short and collisional growth toward planetesimals might be expected. If coagulation instability increases dust sizes and dust-to-gas ratio from 10^{-3} to 0.02 or even higher, secular GI will subsequently operate in the resultant dust-piling-up region. Therefore, we expect that coagulation instability is a powerful mechanism to connect the first bottom-up coagulation and planetesimal formation via secular GI.

It is also possible that streaming instability operates in dust-rich regions resultant from coagulation instability. Because unstable wavelengths of streaming instability are much shorter than the gas scale height, streaming instability will create azimuthally elongated filaments in a dust-rich region. However, recent studies show that streaming instability is substantially stabilized when there is a power-law dust size distributions (Krapp et al. 2019; Zhu & Yang 2020; Paardekooper et al. 2020). Therefore, how coagulation instability affects dust size distribution is an issue to address in the context of the coevolution of coagulation instability and streaming instability. We will also explore this issue in future studies.

4.6 Summary

Planetesimal formation via dust-gas instabilities has a problem in their growth conditions. Secular GI requires larger dust-to-gas ratio (> 0.01) for large dust grains ($\tau_{s,0} \simeq 0.1$; see Chapters 1 and 2). The other dust-gas instabilities (e.g., streaming instability) also require such enrichment of large dust grains. On the other hand, the first coagulation and the radial drift lead to depletion of such large dust grains in the absence of dust supply from the infalling envelope. Thus, the previous dust-gas instabilities require some dust retention mechanisms.

In this chapter, we present an instability driven by coagulation (“coagulation instability”) as a mechanism of dust retention. Coagulation instability operates as a result of a positive feedback between coagulation and traffic jam: coagulation is accelerated

4.6. SUMMARY

at dust-rich regions and amplifies dust size perturbations while traffic jam due to the size perturbations locally amplifies dust density perturbations. In the absence of dust diffusion, coagulation instability grows faster at shorter wavelengths, which is because a timescale of traffic jam is shorter at shorter wavelengths. For example, the growth timescale of the instability is tens Keplerian periods for $(\tau_{s,0}, \varepsilon) = (10^{-1}, 10^{-3})$, which is 20-30 times shorter than the coagulation timescale $(\varepsilon/3t_0)^{-1}$ (see Figures 4.3 and 4.5).

In the presence of dust diffusion, short-wavelength perturbations are stabilized, and thus the dispersion relation of coagulation instability shows the most unstable wavelength at $\sim H$ (see Equation (4.89)). Coagulation instability still grows only within a few tens of the Keplerian periods regardless of the stabilization due to dust diffusion. Therefore, coagulation instability can be a promising mechanism for reaccumulating dust grains, and bridge the gap between the first coagulation and planetesimal formation via the dust-gas instabilities.

Chapter 5

Summary and Future Prospects

5.1 Summary of this thesis

Planetesimal formation from dust grains in a protoplanetary disk is the first step in the planet forming processes. However, the formation mechanism is still unrevealed and controversial because of the difficulties due to the radial drift and fragmentation (e.g., Weidenschilling 1977; Weidenschilling & Cuzzi 1993; Brauer et al. 2008). Recent ALMA observations have been showing some clues for revealing planetesimal formation. One of the most highlighted results of the observations is the discovery of ubiquitous annular substructures in dust distributions, i.e., rings and gaps. The existence of multiple dust rings in disks are in contrast to the classical theories that showed fast depletion of mm-sized dust because of the radial drift. Therefore, investigating the origin of multiple rings and connections to planetesimal formation will provide the key to reveal planetesimal formation and unify the disk evolution theory and planet formation theory.

In this thesis, we focus on disk evolution via secular GI, which is one possible mechanism of ring and planetesimal formation. Secular GI is one of the dust-gas instabilities and originally proposed as a mechanism of planetesimal formation (e.g., Ward 2000; Youdin 2005a, 2005b). Takahashi & Inutsuka (2014) and Takahashi & Inutsuka (2016) showed that secular GI can create multiple dust rings with a width of $\simeq H$, which is consistent of the observed rings. However, the previous studies have some issues:

1. their equations with dust diffusion violate angular momentum conservation,
2. the previous studies focused on the locally linear growth but nonlinear growth in a radially extended disk is important to explore ring and planetesimal formation
3. secular GI requires high dust-to-gas ratio for mm- or cm-sized grains although the

first bottom-up coagulation toward those sizes results in dust depletion.

This thesis addresses these issues.

In Chapter 2, we first reformulate equations describing dust diffusion while not violating the momentum conservation. Our formulation is based on the Reynold averaging, which divides physical properties into mean-flow parts and fluctuating parts due to turbulent motion. Averaging the usual hydrodynamic equations naturally reproduce the diffusion equation (see also Cuzzi et al. 1993) and simultaneously introduces a new term: momentum advection along diffusion flow. We found that including such an advection term in momentum equations recovers the momentum conservation.

Based on the reformulated equations, we perform linear analyses of secular GI. In contrast to the previous studies that showed overstability, our results show that secular GI is an exponentially growing mode without oscillation. The overstability in the previous studies was found to be due to the nonconservation of angular momentum. We also found another unstable mode that we name two-component viscous GI (TVGI). TVGI is triggered by a combination of friction and turbulent gas viscosity. Although the linear analyses in Chapter 2 show that TVGI grows for wider parameter space than secular GI, including dust drift stabilizes TVGI as shown in Chapter 3. Thus, TVGI can be a powerful mechanism for forming planetesimals at a region where dust insignificantly drifts.

In Chapter 3, we first develop numerical methods for long-term simulations of secular GI. Secular GI has long growth timescales, $\simeq 100$ orbital periods, and thus one needs long-term integrations. However, the dust drift throughout a gas disk potentially introduces significant numerical diffusion due to advection, which numerically prevents the growth of secular GI. Motivated by this issue, we develop the Lagrangian-cell method, which is free from the numerical diffusion. We also utilizing the symplectic integrator and reduces the accumulation of errors due to time integration. Test simulations with local radial domain show that combining the method with the piecewise exact solution for dust-gas friction enables simulations of linear/nonlinear secular GI.

We perform numerical simulations of secular GI in radially extended disks while assuming uniform profile of dimensionless stopping time for simplicity. We found that non-linear growth of secular GI shows the gravitational collapse of dust rings whose timescale is well represented in terms of the freefall time. As a result, the dust surface density increases by an order of magnitude. On the other hand, the gas surface density insignificantly changes, leading to high dust-to-gas ratio in thin dense rings. If the dust-to-gas ratio increases enough, the dust drift is suppressed because of strong backreaction to the gas. Thus, dust grains are saved in a disk once secular GI grows into the highly nonlinear

regime. If the growth of secular GI is too small to create high-contrast rings and gaps, those substructures enter the inner stable region and finally become transient. According to those results, planetesimal formation via secular GI requires dust enrichment toward around the gas density, i.e., dust-to-gas ratio $\simeq 1$.

Simple estimates of the coagulation timescale and the freefall timescale indicate that accelerated coagulation and ring fragmentation will result in planetesimals within one Keplerian period at the ring location. This implies that multiple rings resultant from secular GI are dark at mm wavelengths and would be observed as a single wide gap structure. Subsequent fragmentation of planetesimals will supply smaller dust grains that determine a floor intensity at the wide gap. Because secular GI creates only insignificant substructures in a gas disk, observations of gas profiles around the midplane will provide hints to understand which ring-forming process actually operates in the observed disks.

In Chapter 4, we address the third issue: secular GI requires reaccumulation of mm- and cm-sized dust grains. Although previous studies already proposed some dust retention mechanisms including dust-piling-up near the water snow line and the dead-zone inner boundary, those operate at a specific location. However, traffic jam around the snow line is not operational for less fragile silicate that recent experiments suggest (e.g., Kimura et al. 2015; Steinpilz et al. 2019). In addition, those mechanisms operate at inner regions ($r \lesssim$ a few au) and do not explain the origin of outer planetesimals and asteroids. We propose a new instability as another mechanism for reaccumulating dust grains. The instability is triggered by a combination of dust coagulation and small scale traffic jam, and thus we call it “coagulation instability”. In the absence of dust diffusion, coagulation instability shows larger growth rate at shorter wavelengths, which is because a timescale of traffic jam becomes shorter at shorter wavelengths. Even in the presence of dust diffusion and in a dust-depleted region, coagulation instability grows at a wavelength comparable to the gas scale height. Its growth timescale is about a few tens of the Keplerian periods. Therefore, coagulation instability efficiently accumulates mm- and cm-sized dust grains, connecting the first coagulation to the top-down planetesimal formation via secular GI investigated in Chapters 2 and 3.

5.2 Future prospects

Simulations of coagulation instability

In this thesis, we only explore the linear growth of coagulation instability. Nonlinear simulations of coagulation instability are necessary to investigate to what extent the

5.2. FUTURE PROSPECTS

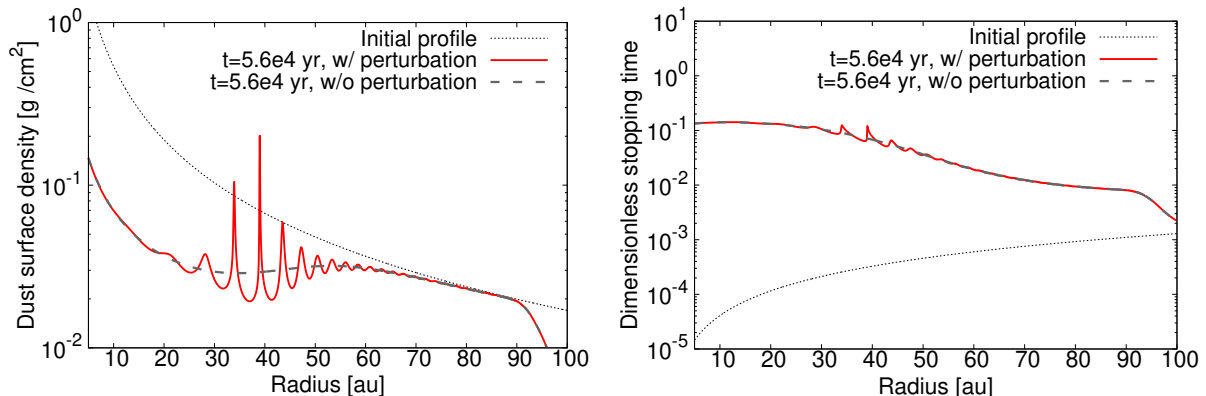


Figure 5.1: Preliminary results of a numerical simulation of coagulation instability. The left panel shows dust surface density evolution while the right panel shows evolution of dimensionless stopping time. In both panel, black dotted line shows initial profile, and the red solid and gray dashed lines show profiles at $t = 5.6 \times 10^4$ yr obtained from simulations with and without initial perturbations, respectively.

instability reaccumulates dust grains. In addition, its growth in a radially extended disk is important to discuss the resultant disk morphology.

We have been doing simulations of coagulation instability using one-fluid code based on the symplectic method presented in Chapter 3. Figure 5.1 shows a preliminary result. We here assumed MMSN disk model with initial dust-to-gas ratio of 0.01 and initial dust sizes of $10 \mu\text{m}$. Turbulence strength is set to be $\alpha = 10^{-4}$ and dust diffusion is taken into account in the simulations. We input sinusoidal perturbations with a wavelength of 2 au for $r \geq 50$ au. We also show the results of a simulation without initial perturbation (the grey dashed lines). Inside-out coagulation lets inner dust grains drift inward, resulting in dust depletion as seen in Figure 4.1. The initially perturbed simulation (the red lines) shows spiky structures resultant from linear/nonlinear coagulation instability. The dust surface density locally increases by a factor of 10. Note that we do not include self-gravity in these simulations. Because the initial dust-to-gas surface density ratio is 0.01, the dust-to-gas ratio in one dust-rich region at $r \simeq 40$ au is about 0.03. We just stopped simulations once the time step becomes smaller than $10^{-2}/(2\pi)$ yr, and thus further dust enrichment can be expected. The right panel of Figure 5.1 indicates a slightly larger dust size in dust-rich regions. Dust enrichment by an order of magnitude accelerates dust coagulation and increases dust sizes, which is another property of nonlinear coagulation instability. As time proceeds, the accelerated dust coagulation will increase dimensionless stopping time above unity. In such a case, slightly outer dust grains of $\tau_s < 1$ are going to overtake the forward dust of $\tau_s > 1$, and thus single-size approximation becomes invalid.

For further discussions, we need to directly solve the Smoluchowski equation with a dust size distribution (Equation (4.5)).

One can see that the separation of the adjacent dust-rich region ($\simeq 5$ au) is larger than the wavelength of initial perturbations ($= 2$ au). This is due to the global dust evolution. Inner dust grains are larger and drift faster, and thus the phase speed is larger in the inner region, leading to an increase in the separation. Numerical investigation of this separation evolution will be important for observational implications on disk substructures.

Coagulation instability at the early disk-evolution stage

If turbulence is not so strong, coagulation instability always grows because a disk is unconditionally unstable (see Chapter 4). On the other hand, as mentioned in Chapter 1, secular GI grows in relatively massive disks, for example, $Q \lesssim 6$, although the required disk mass depends on the other parameters. Thus, it is worthwhile to investigate whether coagulation instability grows and sets up conditions preferable for secular GI at the early disk-evolution stage where a disk is thought to be massive (see Figure 1.2).

Coagulation instability in young disks is also important in the context of substructure formation. Some works reported that young disks with an age of $\lesssim 1$ Myr already host dust ring structures (e.g., ALMA Partnership et al. 2015; Sheehan & Eisner 2017; Dipierro et al. 2018; Sheehan & Eisner 2018; Nakatani et al. 2020). These observations may indicate that dust grains have grown up to millimeter sizes. Coagulation instability will be operational for those dust grains and create some substructures as shown in Figure 5.1.

Because coagulation instability accelerates dust coagulation at the nonlinear growth phase, the instability potentially creates the first-generation planetesimals directly. Such an early planetesimal formation will support the hypothesis that planets already form in Class II disks and carve gaps (e.g., Gonzalez et al. 2015; Kanagawa et al. 2015; Zhang et al. 2018). Therefore, investigating coagulation instability at the very early stage is important for both planet-based and secular-GI-based ring formation scenarios.

Secular GI with dust growth and multidimensional analyses

In Chapter 3, we showed that secular GI can create multiple thin dense rings, where one can expect dust growth or planetesimal formation via ring fragmentation within one Keplerian period. Thus, we expect that those multiple rings would be observed as a dark gap. To obtain further observational implications, we have to implement dust growth in simulations of secular GI. Collisional fragmentation is also necessary because it supplies

small dust grains that we can observe at the ALMA bands. The equilibrium between dust supply due to fragmentation and dust depletion due to planetesimal formation via secular GI will determine the intensity at the wide gap. In future studies, we will explore the coevolution of secular GI and dust growth and also perform synthetic observations aiming at direct comparison with the observed intensity profiles.

Multidimensional analyses including simulations are also important to understand the disk evolution via secular GI. Introducing the azimuthal direction, we can directly treat ring fragmentation and quantify planetesimal formation rates. Numerical simulations with radial and azimuthal directions will be necessary because planetesimal formation occurs at the nonlinear stage. The inclusion of the vertical motion is also important. As mentioned in Chapters 2 and 3, secular GI will be operational around the midplane. It is however unclear to what vertical extent we have to consider dust and gas because gas at the upper layer will interact with midplane dust through gravity. Multidimensional linear analyses will reveal the vertical extent. These are the scope of our future studies.

Appendix A

Drift-Limited Stopping Time

This chapter is based on a published paper, Tominaga, Takahashi, & Inutsuka 2020, *The Astrophysical Journal*, Volume 900, pp. 182-198 (Tominaga et al. 2020).

We estimate the drift-limited stopping time based on our disk model. The drift-limited stopping time in different disk models was derived in (Birnstiel et al. 2012) and Okuzumi et al. (2012). Following those studies, we compare two timescales: dust growth timescale t_{grow} within which dust size becomes twice larger, and drift timescale t_{drift} within which dust drifts and falls onto the central star.

The dust growth timescale for spherical grains is given by

$$t_{\text{grow}} = 3m \left(\frac{dm}{dt} \right)^{-1} = \frac{3m}{\rho_d \sigma \Delta v}, \quad (\text{A.1})$$

where m is mass of a single dust grain. The cross section and the relative velocity of dust grains are denoted by σ and Δv , respectively. For compact spherical dust grains with the radius of a and the internal density of ρ_{int} , Equation (A.1) yields

$$t_{\text{grow}} = \frac{\rho_{\text{int}} a}{\rho_d \Delta v}. \quad (\text{A.2})$$

Assuming turbulence-driven collisions with $\Delta v = \sqrt{3t_{\text{stop}}\Omega\alpha c_s}$ (Ormel & Cuzzi 2007), the Epstein drag regime, and vertically Gaussian profiles for dust and gas disks gives the following dust growth timescale at the midplane ($z = 0$):

$$t_{\text{grow}}\Omega \simeq 2\sqrt{\frac{2}{3\pi}} \frac{\Sigma_{\text{g,tot}}}{\Sigma_{\text{d,tot}}}. \quad (\text{A.3})$$

Note that the growth timescale depends not on $\Sigma_{\text{d}}/\Sigma_{\text{g}}$ but on $\Sigma_{\text{d,tot}}/\Sigma_{\text{g,tot}}$.

The drift timescale $t_{\text{drift}}\Omega$ is given by

$$t_{\text{drift}}\Omega = \frac{r\Omega}{|v_{r,\text{drift}}|}. \quad (\text{A.4})$$

The denominator $v_{r,\text{drift}}$ is the steady drift velocity given by Equation (1.14) (Nakagawa et al. 1986). Assuming that the radial profile of $\Sigma_{g,\text{tot}}$ has the same power law index q as Σ_g (see Equation (3.63)), Equation (1.11) at the midplane ($\rho_g(r, z = 0) = \Sigma_{g,\text{tot}}(r)/\sqrt{2\pi}H(r)$) becomes

$$\eta = \frac{H^2}{2r^2} \left(\frac{7}{4} + q + \frac{r}{100\text{au}} \right) \simeq 2 \times 10^{-3} \left(\frac{9}{4} + \frac{r}{100\text{ au}} \right) \left(\frac{r}{100\text{au}} \right)^{\frac{1}{2}}, \quad (\text{A.5})$$

where we use $q = 1/2$. We approximate the radial drift velocity with $v_{\text{drift}} \simeq -2\eta r \Omega t_{\text{stop}} \Omega$ and obtain

$$t_{\text{drift}} \Omega \simeq \frac{1}{2\eta t_{\text{stop}} \Omega}. \quad (\text{A.6})$$

According to Okuzumi et al. (2012), dust grains will grow in size without significant radial drift when they satisfy $t_{\text{grow}} \lesssim t_{\text{drift}}/10$ ¹. Thus, using Equations (A.3), (A.5) and (A.6), we obtain the drift-limited stopping time

$$t_{\text{stop}} \Omega \simeq 0.13 \left(\frac{\Sigma_{d,\text{tot}}/\Sigma_{g,\text{tot}}}{0.01} \right) \left(\frac{\eta}{4 \times 10^{-3}} \right)^{-1}. \quad (\text{A.7})$$

Our assumption $t_{\text{stop}} \Omega = 0.6$ for $\Sigma_{d,\text{tot}}/\Sigma_{g,\text{tot}} = 0.05$ is almost consistent with the above value in $30 \text{ au} \leq r \leq 100 \text{ au}$.

¹In Okuzumi et al. (2012), t_{grow} denotes the mass doubling timescale, and thus the coefficient of t_{drift} is different by a factor of three.

References

- Adachi, I., Hayashi, C., & Nakazawa, K. 1976, *Progress of Theoretical Physics*, 56, 1756
- Alexiades, V., Amiez, G., & Gremaud, P. A. 1996, *CNME*, 12, 31
- ALMA Partnership, Brogan, C. L., Pérez, L. M., et al. 2015, *ApJL*, 808, L3
- Andre, P., & Montmerle, T. 1994, *ApJ*, 420, 837
- Andre, P., Ward-Thompson, D., & Barsony, M. 1993, *ApJ*, 406, 122
- Andrews, S. M., Wilner, D. J., Zhu, Z., et al. 2016, *ApJL*, 820, L40
- Andrews, S. M., Huang, J., Pérez, L. M., et al. 2018, *ApJL*, 869, L41
- Auffinger, J., & Laibe, G. 2018, *MNRAS*, 473, 796
- Avenhaus, H., Quanz, S. P., Garufi, A., et al. 2018, *ApJ*, 863, 44
- Bae, J., Zhu, Z., & Hartmann, L. 2017, *ApJ*, 850, 201
- Bai, X.-N., & Stone, J. M. 2014, *ApJ*, 796, 31
- Balbus, S. A., & Hawley, J. F. 1991, *ApJ*, 376, 214
- . 1998, *Reviews of Modern Physics*, 70, 1
- Barge, P., & Sommeria, J. 1995, *A&A*, 295, L1
- Bate, M. R. 1998, *ApJL*, 508, L95
- Beckwith, S. V. W., Sargent, A. I., Chini, R. S., & Guesten, R. 1990, *AJ*, 99, 924
- Benisty, M., Juhasz, A., Boccaletti, A., et al. 2015, *A&A*, 578, L6
- Birnstiel, T., Dullemond, C. P., & Brauer, F. 2009, *A&A*, 503, L5

REFERENCES

- Birnstiel, T., Klahr, H., & Ercolano, B. 2012, *A&A*, 539, A148
- Blandford, R. D., & Payne, D. G. 1982, *MNRAS*, 199, 883
- Bohlin, R. C., Savage, B. D., & Drake, J. F. 1978, *ApJ*, 224, 132
- Brauer, F., Dullemond, C. P., & Henning, T. 2008, *A&A*, 480, 859
- Carballido, A., Fromang, S., & Papaloizou, J. 2006, *MNRAS*, 373, 1633
- Carrera, D., Johansen, A., & Davies, M. B. 2015, *A&A*, 579, A43
- Carrera, D., Simon, J. B., Li, R., Kretke, K. A., & Klahr, H. 2020, arXiv e-prints, arXiv:2008.01727
- Casassus, S., Wright, C. M., Marino, S., et al. 2015, *ApJ*, 812, 126
- Chavanis, P. H. 2000, *A&A*, 356, 1089
- Chen, K., & Lin, M.-K. 2020, *ApJ*, 891, 132
- Chiang, E. I., & Goldreich, P. 1997, *ApJ*, 490, 368
- Cuzzi, J. N., Dobrovolskis, A. R., & Champney, J. M. 1993, *Icar*, 106, 102
- Dipierro, G., Ricci, L., Pérez, L., et al. 2018, *MNRAS*, 475, 5296
- Drążkowska, J., & Alibert, Y. 2017, *A&A*, 608, A92
- Drążkowska, J., & Dullemond, C. P. 2014, *A&A*, 572, A78
- Dubrulle, B., Morfill, G., & Sterzik, M. 1995, *Icar*, 114, 237
- Dullemond, C. P., & Penzlin, A. B. T. 2018, *A&A*, 609, A50
- Dullemond, C. P., Birnstiel, T., Huang, J., et al. 2018, *ApJL*, 869, L46
- Estrada, P. R., & Cuzzi, J. N. 2008, *ApJ*, 682, 515
- Fedele, D., Carney, M., Hogerheijde, M. R., et al. 2017, *A&A*, 600, A72
- Flock, M., Ruge, J. P., Dzyurkevich, N., et al. 2015, *A&A*, 574, A68
- Fukagawa, M., Tsukagoshi, T., Momose, M., et al. 2013, *PASJ*, 65, L14
- Gammie, C. F. 1996, *ApJ*, 462, 725

REFERENCES

- . 2001, *ApJ*, 553, 174
- Gaustad, J. E. 1963, *ApJ*, 138, 1050
- Goldreich, P., & Lynden-Bell, D. 1965a, *MNRAS*, 130, 97
- . 1965b, *MNRAS*, 130, 125
- Goldreich, P., & Ward, W. R. 1973, *ApJ*, 183, 1051
- Gole, D. A., Simon, J. B., Li, R., Youdin, A. N., & Armitage, P. J. 2020, arXiv e-prints, arXiv:2001.10000
- Gonzalez, J. F., Laibe, G., Maddison, S. T., Pinte, C., & Ménard, F. 2015, *MNRAS*, 454, L36
- Goodman, J., & Pindor, B. 2000, *Icar*, 148, 537
- Hashimoto, J., Tsukagoshi, T., Brown, J. M., et al. 2015, *ApJ*, 799, 43
- Hastings, C., Hayward, J. T., & Wong, J. P. 1955, *Approximations for digital computers*
- Hayashi, C. 1981, *Progress of Theoretical Physics Supplement*, 70, 35
- Hu, X., Zhu, Z., Okuzumi, S., et al. 2019, *ApJ*, 885, 36
- Huang, J., Andrews, S. M., Dullemond, C. P., et al. 2018, *ApJL*, 869, L42
- Ilgner, M., & Nelson, R. P. 2006, *A&A*, 445, 205
- Inoue, T., & Inutsuka, S.-i. 2008, *ApJ*, 687, 303
- Inutsuka, S.-i., Machida, M. N., & Matsumoto, T. 2010, *ApJL*, 718, L58
- Isella, A., Guidi, G., Testi, L., et al. 2016, *Physical Review Letters*, 117, 251101
- Jacquet, E., Balbus, S., & Latter, H. 2011, *MNRAS*, 415, 3591
- Johansen, A., Oishi, J. S., Mac Low, M.-M., et al. 2007, *Nature*, 448, 1022
- Johansen, A., & Youdin, A. 2007, *ApJ*, 662, 627
- Johansen, A., Youdin, A., & Klahr, H. 2009a, *ApJ*, 697, 1269
- Johansen, A., Youdin, A., & Mac Low, M.-M. 2009b, *ApJL*, 704, L75

REFERENCES

- Kanagawa, K. D., Muto, T., Tanaka, H., et al. 2015, *ApJL*, 806, L15
- Kataoka, A., Tsukagoshi, T., Pohl, A., et al. 2017, *ApJL*, 844, L5
- Kataoka, A., Muto, T., Momose, M., et al. 2015, *ApJ*, 809, 78
- Kimura, H., Wada, K., Senshu, H., & Kobayashi, H. 2015, *ApJ*, 812, 67
- Kitamura, Y., Momose, M., Yokogawa, S., et al. 2002, *ApJ*, 581, 357
- Klahr, H., & Hubbard, A. 2014, *ApJ*, 788, 21
- Kobayashi, H., Tanaka, H., & Krivov, A. V. 2011, *ApJ*, 738, 35
- Kobayashi, H., Tanaka, H., Krivov, A. V., & Inaba, S. 2010, *Icar*, 209, 836
- Kokubo, E., & Ida, S. 1998, *Icar*, 131, 171
- Koyama, H., & Inutsuka, S.-I. 2000, *ApJ*, 532, 980
- Krapp, L., Benítez-Llambay, P., Gressel, O., & Pessah, M. E. 2019, *ApJL*, 878, L30
- Kretke, K. A., & Lin, D. N. C. 2007, *ApJL*, 664, L55
- Krijt, S., Ormel, C. W., Dominik, C., & Tielens, A. G. G. M. 2015, *A&A*, 574, A83
- Kusaka, T., Nakano, T., & Hayashi, C. 1970, *Progress of Theoretical Physics*, 44, 1580
- Lada, C. J. 1987, in *Star Forming Regions*, ed. M. Peimbert & J. Jugaku, Vol. 115, 1
- Larson, R. B. 1969, *MNRAS*, 145, 271
- Latter, H. N., & Rosca, R. 2017, *MNRAS*, 464, 1923
- Lin, D. N. C., & Papaloizou, J. 1980, *MNRAS*, 191, 37
- Lin, M.-K., & Kratter, K. M. 2016, *ApJ*, 824, 91
- Long, F., Pinilla, P., Herczeg, G. J., et al. 2018, *ApJ*, 869, 17
- Lynden-Bell, D., & Pringle, J. E. 1974, *MNRAS*, 168, 603
- Lyra, W., & Lin, M.-K. 2013, *ApJ*, 775, 17
- Machida, M. N., Inutsuka, S.-i., & Matsumoto, T. 2010, *ApJ*, 724, 1006

REFERENCES

- Machida, M. N., Inutsuka, S.-I., & Matsumoto, T. 2011, PASJ, 63, 555
- Machida, M. N., Inutsuka, S.-i., & Matsumoto, T. 2014, MNRAS, 438, 2278
- Machida, M. N., Matsumoto, T., Hanawa, T., & Tomisaka, K. 2006, ApJ, 645, 1227
- Masunaga, H., & Inutsuka, S.-i. 2000, ApJ, 531, 350
- Mestel, L., & Spitzer, L., J. 1956, MNRAS, 116, 503
- Michikoshi, S., Kokubo, E., & Inutsuka, S.-i. 2012, ApJ, 746, 35
- Mizuno, H. 1980, Progress of Theoretical Physics, 64, 544
- Momose, M., Morita, A., Fukagawa, M., et al. 2015, PASJ, 67, 83
- Mori, S., Bai, X.-N., & Okuzumi, S. 2019, ApJ, 872, 98
- Mouschovias, T. C., & Paleologou, E. V. 1979, ApJ, 230, 204
- Muto, T., Grady, C. A., Hashimoto, J., et al. 2012, ApJL, 748, L22
- Nakagawa, Y., Sekiya, M., & Hayashi, C. 1986, Icar, 67, 375
- Nakano, T., Nishi, R., & Umebayashi, T. 2002, ApJ, 573, 199
- Nakatani, R., Liu, H. B., Ohashi, S., et al. 2020, ApJL, 895, L2
- Nelson, R. P., Gressel, O., & Umurhan, O. M. 2013, MNRAS, 435, 2610
- Oka, A., Nakamoto, T., & Ida, S. 2011, ApJ, 738, 141
- Okuzumi, S., & Hirose, S. 2012, ApJL, 753, L8
- Okuzumi, S., Momose, M., Sirono, S.-i., Kobayashi, H., & Tanaka, H. 2016, ApJ, 821, 82
- Okuzumi, S., Tanaka, H., Kobayashi, H., & Wada, K. 2012, ApJ, 752, 106
- Ormel, C. W., & Cuzzi, J. N. 2007, A&A, 466, 413
- Ormel, C. W., & Spaans, M. 2008, ApJ, 684, 1291
- Paardekooper, S.-J., McNally, C. P., & Lovascio, F. 2020, MNRAS, 499, 4223
- Pérez, S., Casassus, S., Baruteau, C., et al. 2019, AJ, 158, 15

REFERENCES

- Pérez, S., Casassus, S., Hales, A., et al. 2020, *ApJL*, 889, L24
- Pinte, C., Price, D. J., Ménard, F., et al. 2018, *ApJ*, 860, L13
- Pinte, C., van der Plas, G., Ménard, F., et al. 2019, *Nature Astronomy*, 3, 1109
- Pinte, C., Price, D. J., Menard, F., et al. 2020, arXiv e-prints, arXiv:2001.07720
- Pollack, J. B., Hubickyj, O., Bodenheimer, P., et al. 1996, *Icar*, 124, 62
- Raettig, N., Klahr, H., & Lyra, W. 2015, *ApJ*, 804, 35
- Riols, A., & Lesur, G. 2019, *A&A*, 625, A108
- Safronov, V. S. 1969, *Evolutsiia doplanetnogo oblaka*.
- . 1972, *Evolution of the protoplanetary cloud and formation of the earth and planets*.
- Sano, T., Miyama, S. M., Umebayashi, T., & Nakano, T. 2000, *ApJ*, 543, 486
- Sato, T., Okuzumi, S., & Ida, S. 2016, *A&A*, 589, A15
- Schmit, U., & Tscharnuter, W. M. 1995, *Icar*, 115, 304
- Schoonenberg, D., & Ormel, C. W. 2017, *A&A*, 602, A21
- Schoonenberg, D., Ormel, C. W., & Krijt, S. 2018, *A&A*, 620, A134
- Schreiber, A., & Klahr, H. 2018, *ApJ*, 861, 47
- Schumann, T. E. W. 1940, *Quarterly Journal of the Royal Meteorological Society*, 66, 195
- Sekiya, M. 1998, *Icar*, 133, 298
- Shakura, N. I., & Sunyaev, R. A. 1973, *A&A*, 24, 337
- Shariff, K., & Cuzzi, J. N. 2011, *ApJ*, 738, 73
- Sheehan, P. D., & Eisner, J. A. 2017, *ApJL*, 840, L12
- . 2018, *ApJ*, 857, 18
- Shu, F. H. 1984, in *IAU Colloq. 75: Planetary Rings*, ed. R. Greenberg & A. Brahic, 513–561

REFERENCES

- Shu, F. H. 1992, *The physics of astrophysics. Volume II: Gas dynamics.* (University Science Books)
- Simon, J. B., Armitage, P. J., Li, R., & Youdin, A. N. 2016, *ApJ*, 822, 55
- Smoluchowski, M. V. 1916, *Zeitschrift fur Physik*, 17, 557
- Stammler, S. M., Drażkowska, J., Birnstiel, T., et al. 2019, *ApJL*, 884, L5
- Steinpilz, T., Teiser, J., & Wurm, G. 2019, *ApJ*, 874, 60
- Stephens, I. W., Yang, H., Li, Z.-Y., et al. 2017, *ApJ*, 851, 55
- Stevenson, D. J., & Lunine, J. I. 1988, *Icar*, 75, 146
- Stolker, T., Dominik, C., Avenhaus, H., et al. 2016, *A&A*, 595, A113
- Strom, K. M., Strom, S. E., Edwards, S., Cabrit, S., & Skrutskie, M. F. 1989, *AJ*, 97, 1451
- Suriano, S. S., Li, Z.-Y., Krasnopolsky, R., & Shang, H. 2018, *MNRAS*, 477, 1239
- Suriano, S. S., Li, Z.-Y., Krasnopolsky, R., Suzuki, T. K., & Shang, H. 2019, *MNRAS*, 484, 107
- Takahashi, S. Z., & Inutsuka, S.-i. 2014, *ApJ*, 794, 55
- . 2016, *AJ*, 152, 184
- Taki, T., Fujimoto, M., & Ida, S. 2016, *A&A*, 591, A86
- Taki, T., Kuwabara, K., Kobayashi, H., & Suzuki, T. K. 2020, arXiv e-prints, arXiv:2004.08839
- Teague, R., Bae, J., Bergin, E. A., Birnstiel, T., & Foreman-Mackey, D. 2018, *ApJL*, 860, L12
- Tomida, K., Machida, M. N., Hosokawa, T., Sakurai, Y., & Lin, C. H. 2017, *ApJL*, 835, L11
- Tominaga, R. T., Inutsuka, S.-i., & Takahashi, S. Z. 2018, *PASJ*, 70, 3
- Tominaga, R. T., Takahashi, S. Z., & Inutsuka, S.-i. 2019, *ApJ*, 881, 53
- . 2020, *ApJ*, 900, 182

REFERENCES

- Tomisaka, K. 1998, *ApJL*, 502, L163
- . 2002, *ApJ*, 575, 306
- Toomre, A. 1964, *ApJ*, 139, 1217
- Tsukagoshi, T., Nomura, H., Muto, T., et al. 2016, *ApJL*, 829, L35
- Ueda, T., Flock, M., & Okuzumi, S. 2019, *ApJ*, 871, 10
- Umurhan, O. M., Estrada, P. R., & Cuzzi, J. N. 2020, *ApJ*, 895, 4
- Urpin, V. 2003, *A&A*, 404, 397
- Urpin, V., & Brandenburg, A. 1998, *MNRAS*, 294, 399
- van Boekel, R., Henning, T., Menu, J., et al. 2017, *ApJ*, 837, 132
- van der Marel, N., van Dishoeck, E. F., Bruderer, S., et al. 2013, *Science*, 340, 1199
- Vandervoort, P. O. 1970, *ApJ*, 161, 87
- Wada, K., Tanaka, H., Okuzumi, S., et al. 2013, *A&A*, 559, A62
- Wada, K., Tanaka, H., Suyama, T., Kimura, H., & Yamamoto, T. 2009, *ApJ*, 702, 1490
- Ward, W. R. 2000, *On Planetesimal Formation: The Role of Collective Particle Behavior*, ed. R. M. Canup, K. Righter, & et al. (Tucson, AZ: Univ. Arizona Press), 75–84
- Weidenschilling, S. J. 1977, *MNRAS*, 180, 57
- Weidenschilling, S. J., & Cuzzi, J. N. 1993, in *Protostars and Planets III*, ed. E. H. Levy & J. I. Lunine, 1031
- Wetherill, G. W., & Stewart, G. R. 1989, *Icar*, 77, 330
- Whipple, F. L. 1972, in *From Plasma to Planet*, ed. A. Elvius, 211
- Wolfire, M. G., Hollenbach, D., McKee, C. F., Tielens, A. G. G. M., & Bakes, E. L. O. 1995, *ApJ*, 443, 152
- Wolniewicz, L. 1995, *The Journal of Chemical Physics*, 103, 1792
- Yang, C. C., Johansen, A., & Carrera, D. 2017, *A&A*, 606, A80
- Yang, C.-C., & Zhu, Z. 2020, *MNRAS*, 491, 4702

REFERENCES

- Yang, H., Li, Z.-Y., Looney, L., & Stephens, I. 2016, *MNRAS*, 456, 2794
- Youdin, A., & Johansen, A. 2007, *ApJ*, 662, 613
- Youdin, A. N. 2005a, *ArXiv Astrophysics e-prints*, astro-ph/0508659
- . 2005b, *ArXiv Astrophysics e-prints*, astro-ph/0508662
- . 2011, *ApJ*, 731, 99
- Youdin, A. N., & Goodman, J. 2005, *ApJ*, 620, 459
- Youdin, A. N., & Lithwick, Y. 2007, *Icar*, 192, 588
- Zhang, K., Blake, G. A., & Bergin, E. A. 2015, *ApJL*, 806, L7
- Zhang, S., Zhu, Z., Huang, J., et al. 2018, *ApJL*, 869, L47
- Zhu, Z., & Yang, C.-C. 2020, *arXiv e-prints*, arXiv:2008.01119
- Zhu, Z., Zhang, S., Jiang, Y.-F., et al. 2019, *ApJL*, 877, L18